

Lecture Notes in Civil Engineering

Kasinathan Muthukkumaran
C. N. V. Satyanarayana Reddy
Anil Joseph
S. Senthamilkumar *Editors*

Foundation and Forensic Geotechnical Engineering

Proceedings of the Indian Geotechnical
Conference 2021 Volume 2

 Springer

Lecture Notes in Civil Engineering

Volume 295

Series Editors

Marco di Prisco, Politecnico di Milano, Milano, Italy

Sheng-Hong Chen, School of Water Resources and Hydropower Engineering,
Wuhan University, Wuhan, China

Ioannis Vayas, Institute of Steel Structures, National Technical University of
Athens, Athens, Greece

Sanjay Kumar Shukla, School of Engineering, Edith Cowan University, Joondalup,
WA, Australia

Anuj Sharma, Iowa State University, Ames, IA, USA

Nagesh Kumar, Department of Civil Engineering, Indian Institute of Science
Bangalore, Bengaluru, Karnataka, India

Chien Ming Wang, School of Civil Engineering, The University of Queensland,
Brisbane, QLD, Australia

Lecture Notes in Civil Engineering (LNCE) publishes the latest developments in Civil Engineering—quickly, informally and in top quality. Though original research reported in proceedings and post-proceedings represents the core of LNCE, edited volumes of exceptionally high quality and interest may also be considered for publication. Volumes published in LNCE embrace all aspects and subfields of, as well as new challenges in, Civil Engineering. Topics in the series include:

- Construction and Structural Mechanics
- Building Materials
- Concrete, Steel and Timber Structures
- Geotechnical Engineering
- Earthquake Engineering
- Coastal Engineering
- Ocean and Offshore Engineering; Ships and Floating Structures
- Hydraulics, Hydrology and Water Resources Engineering
- Environmental Engineering and Sustainability
- Structural Health and Monitoring
- Surveying and Geographical Information Systems
- Indoor Environments
- Transportation and Traffic
- Risk Analysis
- Safety and Security

To submit a proposal or request further information, please contact the appropriate Springer Editor:

- Pierpaolo Riva at pierpaolo.riva@springer.com (Europe and Americas);
- Swati Meherishi at swati.meherishi@springer.com (Asia—except China, Australia, and New Zealand);
- Wayne Hu at wayne.hu@springer.com (China).

All books in the series now indexed by Scopus and EI Compendex database!

Kasinathan Muthukkumaran ·
C. N. V. Satyanarayana Reddy · Anil Joseph ·
S. Senthamilkumar
Editors

Foundation and Forensic Geotechnical Engineering

Proceedings of the Indian Geotechnical
Conference 2021 Volume 2

 Springer

Editors

Kasinathan Muthukkumaran
Department of Civil Engineering
National Institute of Technology,
Tiruchirappalli
Tiruchirappalli, Tamil Nadu, India

Anil Joseph
Geostructurals Pvt. Ltd.
Cochin, Kerala, India

C. N. V. Satyanarayana Reddy
College of Engineering
Andhra University
Visakhapatnam, Andhra Pradesh, India

S. Senthamilkumar
Periyar Maniammai Institute of Science
and Technology
Thanjavur, Tamil Nadu, India

ISSN 2366-2557

ISSN 2366-2565 (electronic)

Lecture Notes in Civil Engineering

ISBN 978-981-19-6358-2

ISBN 978-981-19-6359-9 (eBook)

<https://doi.org/10.1007/978-981-19-6359-9>

© The Editor(s) (if applicable) and The Author(s), under exclusive license to Springer Nature Singapore Pte Ltd. 2023

This work is subject to copyright. All rights are solely and exclusively licensed by the Publisher, whether the whole or part of the material is concerned, specifically the rights of translation, reprinting, reuse of illustrations, recitation, broadcasting, reproduction on microfilms or in any other physical way, and transmission or information storage and retrieval, electronic adaptation, computer software, or by similar or dissimilar methodology now known or hereafter developed.

The use of general descriptive names, registered names, trademarks, service marks, etc. in this publication does not imply, even in the absence of a specific statement, that such names are exempt from the relevant protective laws and regulations and therefore free for general use.

The publisher, the authors, and the editors are safe to assume that the advice and information in this book are believed to be true and accurate at the date of publication. Neither the publisher nor the authors or the editors give a warranty, expressed or implied, with respect to the material contained herein or for any errors or omissions that may have been made. The publisher remains neutral with regard to jurisdictional claims in published maps and institutional affiliations.

This Springer imprint is published by the registered company Springer Nature Singapore Pte Ltd. The registered company address is: 152 Beach Road, #21-01/04 Gateway East, Singapore 189721, Singapore

Preface

The Indian Geotechnical Society, Trichy (IGS-Trichy) Chapter, and National Institute of Technology (NIT) Tiruchirappalli, India, organized the Indian Geotechnical Conference (IGC-2021) at Trichy during 16–18 December 2021. The main theme of the conference was “**GEO-INDIA**”—**GEOTECHNICS FOR INFRASTRUCTURE DEVELOPMENT AND INNOVATIVE APPLICATIONS**.

The sub-themes of the conference included:

1. Soil Behaviour and Characterization of Geomaterials
2. Geotechnical, Geological and Geophysical Investigation
3. Foundation Engineering
4. Ground Improvement Techniques
5. Geo-environmental Engineering
6. Soil Dynamics and Earthquake Geotechnical Engineering
7. Earth Retaining Structures, Dams and Embankments
8. Slope Stability and Landslides
9. Transportation Geotechnics
10. Geosynthetics Application
11. Computational, Analytical and Numerical Modelling
12. Rock Engineering, Tunnelling, Deep Excavations and Underground Constructions
13. Forensic Geotechnical Engineering and Case Studies
14. Others: Behaviour of Unsaturated Soils, Offshore & Marine Geotechnics, Remote Sensing & GIS, Instrumentation & Monitoring, Retrofitting of Geotechnical Structures, Reliability in Geotechnical Engineering, Geotechnical Education, Codes & Standards, & any other relevant topic

The proceedings of this conference consists of selected papers presented at the conference. The proceedings is divided into six volumes. A special issue on IGC-2021 keynote and theme lecture presentations were published by Indian Geotechnical Journal.

We sincerely thank all the authors who have contributed their papers to the conference proceedings. We also thank all the theme editors and reviewers who have been

instrumental in giving their valuable inputs for improving the quality of the final papers. We greatly appreciate and thank all the student volunteers for their unwavering support that was instrumental in preparation of this proceedings. Finally, thanks to Springer team for their support and full cooperation for publishing six volumes of this IGC-2021 proceedings.

Trichy, India

Kasinathan Muthukkumaran
Chairman IGC-2021

Contents

1	Analysis and Design of Foundation System for the Horizontal Solar Axis Tracker	1
	Sreyashrao Surapreddi, G. Santhoshkumar, and Priyanka Ghosh	
2	Bidirectional and Conventional Static Load Test on Bored Piles in Soil: A Field Comparison	13
	Anil Cherian	
3	The Ultimate Bearing Capacity of Ring Footing with Inclined Base	23
	Jitesh T. Chavda	
4	Comparative Study of Geotechnical Design of Foundations as Per Indian Standards and Eurocode 7	33
	V. S. Sowmiyaa	
5	Parametric Study of the Behavior of Large Piled Raft Foundation on Stiff Clay	43
	Rajib Modak and Baleshwar Singh	
6	Estimation of Shaft-Base Initial Stiffness and Ultimate Resistance of O-Cell Piles	55
	Nayakam Venkatesh, Kadali Srinivas, and Madhav Madhira	
7	A Numerical Study of Performance of Large Piled Raft Foundation on Sand Under Vertical Loading	65
	Banchiva K. Marak and Baleshwar Singh	
8	Effect of Compressibility on Bearing Pressure of Soft Ground	75
	J. Y. V. Shiva Bhushan, Madhav Madhira, and G. V. Narasimha Reddy	
9	Raft Foundation Analysis for a 135-m High-Rise Residential Tower in Noida	81
	Ravi Sundaram, Sorabh Gupta, and Gyan Chand	

10	Model Study on Single Pile Subjected to Axial and Inclined Load Embedded in Contaminated Soil	93
	Rutvik K Kalthiya, Jay Dave, and Manish V. Shah	
11	Behavior of Combined Piled-Raft Foundation Under Eccentric Loading	107
	Hannanur Rahaman, Plaban Deb, and Sujit Kumar Pal	
12	Shape Optimization of Onshore Wind Turbine Foundations	117
	M. Deva Kumar, Rajesh Katyal, Anil Kumar Sharma, and M. K. Haridharan	
13	Analysis of Load Distribution Coefficient of Piled Raft System: A Numerical Approach	129
	Plaban Deb and Sujit Kumar Pal	
14	Effect of Slope Inclination on $V-H$ and $V-M$ Capacity Envelope of Strip Foundation on Undrained Clay Slope	139
	Ayushi Goyal, Aarushi Maurya, Dhiraj Raj, and M. Bharathi	
15	Wind Turbine Foundation Using PHC Piles in Problematic Soil ...	147
	Shirlin Charles, Sunil Ranjan Mohapatra, and Sudhansu Bhusan Prusty	
16	Effect of Super Structural Symmetry on Pile Foundations Under Pseudo-static Loading	157
	Aniket Chanda, Saumitro Mandal, and Arghadeep Biswas	
17	Behavior of Pile in Sloped Grounds Under the Influence of Surcharge Loads	165
	Jegatheeswaran Boompani, K. Muthukkumaran, and R. Manjula	
18	Influence of Flexural Rigidity of Footing and Shear Strength of Supporting Soil on Internal Stresses in Foundation	177
	Aleena Sam, A. Arunima Anil, Smitha Anna Kurian, Sujina Kabeer, J. Jayamohan, and Swathy Pushpan	
19	Influence of Oil Spill on the Load–Settlement Behavior of Footings of Adjacent Structures	191
	S. B. Ardra, H. A. Athira, J. P. Janu, S. Parvathy, J. Jayamohan, and Shruthi Johnson	
20	Behavior of Vertical and Battered Piles Under Combined Axial and Lateral Load	203
	Poulami Ghosh, Shilak Bhaumik, and Sibapriya Mukherjee	
21	Footing Resting on Clayey Slopes	217
	Rajesh P. Shukla and Ravi S. Jakka	

22 A Comparison of Solutions of Laterally Loaded Long Piles Using Subgrade Modulus Approach 229
 Rupam Mahanta

23 An Overview of Large Capacity Pile Load Test: A Case Study 241
 B. Vani and Madan Kumar Annam

24 Influence of Soil Cover on Lateral Response of Rock-Socketed Piles 249
 C. R. Neeraj, K. T. Saikumar, and Sudheesh Thiyyakandi

25 Analysis of Foundation System of the Taj Mahal 261
 Leonardo Souza, Yeshwant Chodnekar, and Purnanand Savoikar

26 Heritage Impact Assessment of the Subordinate Court Complex Near the David Yale and Joseph Hyner’s Tomb 273
 Angel Paul, K. V. Aishwarya, M. Keerthana, T. Satyamurthy, and Jitesh T. Chavda

27 Numerical Investigation on the Influence of Different Parameters on a Vegetated Slope—A Case Study 287
 G. Vishnu and Tadikonda Venkata Bharat

28 A Geotechnical Study on Failed Base Slab of Molasses Tank 299
 Nandyala Darga Kumar and C. Lavanya

29 Geotechnical Design and Execution of Driven Spun Piles in Estuarine Geology 311
 Gouri Krishna, M. Jeevan Reddy, and Adak Pinaki

About the Editors

Dr. Kasinathan Muthukkumaran is currently Professor in Civil Engineering at National Institute of Technology, Tiruchirappalli, India. He obtained Ph.D. in Soil-Structure Interaction and Marine Geotechnical Engineering from Indian Institute Technology Madras. He has published more than 150 papers in international and national journals and conferences. He has completed 5 R&D (including ISRO—**Chandrayaan-2 Mission project**) and 70 major consultancy projects in Geotechnical Engineering and published two patent including “**Moon Soil**” (A Method for Manufacture of Highland Lunar Soil Simulant). He has guided 10 Ph.D. scholars and six more are in progress, five MS (by research) and more than 40 M.Tech. students in Geotechnical and allied research areas. He is the **Founder Chairman** of Indian Geotechnical Society (IGS-Trichy) Trichy Chapter. He is a member of Technical Committee (TC-301 on “**Preservation of Historic Sites**”) of International Society for Soil Mechanics and Geotechnical Engineering. Prof. Muthukkumaran area of research is in geotechnical engineering, which includes pile foundation, soil-structure interaction, marine geotechnics and foundations, field instrumentation, geotechnical physical modeling, ground improvement and forensic geotechnical engineering. He has received DST Young Scientist Award, IGS-Smt. Indra Joshi Biennial Award and Keynote Paper Award—GEOMATE Conference 2015 at Osaka, Japan. He is an Associate Editor of *Australian Journal of Civil Engineering and Serving* editorial board member of several journals. Prof. Muthukkumaran has significant administrative contribution as Estate Officer, Associate Dean (Planning and Development), Member of Buildings and Works Committee and Member of **Board of Governors (BoG)** of National Institute of Technology, Tiruchirappalli and Member of Buildings and Works Committee, IIM Trichy. He has received **NIT Trichy Achiever Awards** for research publications, research projects, maximum citation and consultancy projects.

Dr. C. N. V. Satyanarayana Reddy is professor of civil engineering at College of Engineering, Andhra University, India and has over 29 years of teaching, research and consultancy experience. His expertise and research interests are in the areas of reinforced soils, ground improvement, landfills, soil retention in excavations, deep foundations and forensic geotechnical engineering. He obtained his B.Tech.

(Civil Engineering) degree securing first Rank from Nagarjuna University, M.Tech (Geotechnical Engineering) degree from Indian Institute of Technology (IIT) Madras, M.E (Structures) from Andhra University and Ph.D. from National Institute of Technology (NIT) Warangal. He has guided nine Ph.D. scholars and 97 M.Tech. dissertations so far. He has more than 110 publications in various national and international journals and seminars/conference proceedings. He served as Director of Andhra University Development Centre during the period 2013–2017. He is a recipient of “Andhra Pradesh Scientist Award 2020” in the discipline of civil Engineering from Government of Andhra Pradesh and Andhra Pradesh State Council of Science and Technology, Dr. Sarvepalli Radhakrishnan “Best Academician Award 2014” from Andhra University and “Engineer of the Year 2006 Award” from Government of Andhra Pradesh, and the Institution of Engineers (India) Andhra Pradesh State Centre. He handled research projects funded by Department of Science and Technology, New Delhi, and University Grants Commission. He is a life fellow of Indian Geotechnical Society, the Institution of Engineers (India) and is life member of Indian Roads Congress, Indian Concrete Institute, Indian Society for Technical Education.

Dr. Anil Joseph is Managing Director of Geostructurals (P) Ltd., a leading foundation and structural consultancy firm based at Cochin, India. He has provided foundation and structural consultancy for more than 2000 high rise structures including many land mark multistoried and infrastructure projects in India and abroad in the last 28 years. His field of interests are deep foundations, ground improvement, forensic geotechnical analysis, structural design, offshore structures and soil structure interaction. He is also the Managing Director of CECONS (P) Ltd. a construction firm specialized in the execution of pile foundations and Director of Engineers Diagnostic Centre (P) Ltd. a firm specialized in Geotechnical investigation and Retrofitting works. He was awarded Ph.D. from National Institute of technology (NIT), Calicut on his work on “Precompression of Soft Marine Clays” and from Open International University, on his work on “Prestressing and Hollow Shell Technology in Earth Quake Resistant Construction.” He was a National Executive Committee member of the Indian Geotechnical Society from 2012 to 2020. He is serving as the Honorary Secretary of Indian Geotechnical Society, Kochi Chapter. He has numerous publications in various journals of national and international repute.

Dr. S. SenthamilKumar is working as Professor at Periyar Maniammai Institute of Science and Technology, Tamil Nadu, India. He received his Ph.D. in Earthquake Geotechnical Engineering from Anna University, Chennai, and M.E. in Geotechnical Engineering from Annamalai University, Tamil Nadu. He has 26 years of teaching and research experience and four years of industrial experience. He has exposure in geotechnical engineering, soil dynamics and earthquake engineering, project management, sustainable construction technology, green building concept, solid and liquid waste management, FEM, water resources, GIS and remote sensing. He has published 43 journal papers, 36 conference papers, eight books and book chapters. He was awarded with best faculty and best consultancy service provider. Under his supervision, eight Ph.D. degrees were awarded. He completed nine funded

projects and many consultancy works. He organized 27 workshops, conferences and seminars. He is life member in six technical professional societies including Indian Geotechnical Society.

Chapter 1

Analysis and Design of Foundation System for the Horizontal Solar Axis Tracker



Sreyashrao Surapreddi , G. Santhoshkumar , and Priyanka Ghosh 

Introduction

Green energy, often known as renewable energy, has drawn considerable attention in recent years. Solar energy is one of the most important renewable energy sources that can be utilized as an efficient alternative to generate electricity. Solar panels with photovoltaic (PV) modules are generally used to serve the purpose [1, 2]. The efficiency of a solar panel is primarily dependent on the intensity of the sun. However, it is observed that a static PV module cannot completely utilize the intensity of the sun due to the change in the position of the sun during a day. Hence, introducing the solar tracking system in solar panels is beneficial in increasing the exposure time of the solar panels toward the solar radiation and thereby improving the efficiency of the PV module [3]. A solar tracker, which is widely used in the PV module of the solar cell, constantly navigates as per the optimal angle of the sunlight exposure and propels the solar panels toward the direction of the sunlight in a day to maximize the power output. With the aid of servo-controlled motors or actuators connected with a sensor, the solar panel positions itself in synchronization with the movement of the sunlight throughout the day. As a result, it can extract maximum solar energy by keeping the maximum possible angle of incidence for the solar radiation.

It is planned to utilize a barren land parcel of Kutch, Gujarat, by large-capacity renewable power project. The proposed power project would be of the hybrid type, i.e., power would be generated by using the PV-based solar panel and wind turbine generators. This ambitious project would require extensive capital investment from

S. Surapreddi · P. Ghosh (✉)

Department of Civil Engineering, Indian Institute of Technology Kanpur, Kanpur 208016, India
e-mail: priyog@iitk.ac.in

G. Santhoshkumar

Department of Civil Engineering, Amrita School of Engineering, Amrita Vishwa Vidyapeetham, Coimbatore 641112, India

the developers, and hence, the safety of the structures is of paramount importance. The present study deals with the design of the pile foundations for the HSAT shown in Fig. 1.1. The pile foundations are subjected to different magnitudes of load as per the location of the solar trackers, i.e., exterior, interior, and far-interior, as shown in Table 1.1. Case-I refers to the service loads considering a loading combination of 1.0 DL + 1.0 WL, where DL and WL represent the dead load and the wind load, respectively, whereas, for Case-II, a load factor of 1.3 is considered. An extensive investigation is carried out in the present investigation using the theoretical approaches [4–6] followed by the finite element (FE) analysis to provide an economically viable and functionally suitable pile foundation based on the soil condition and the loading configuration. In addition, the seismic analysis based on the pseudo-static approach is also carried out to evaluate the performance of the proposed pile foundation system under seismic conditions.

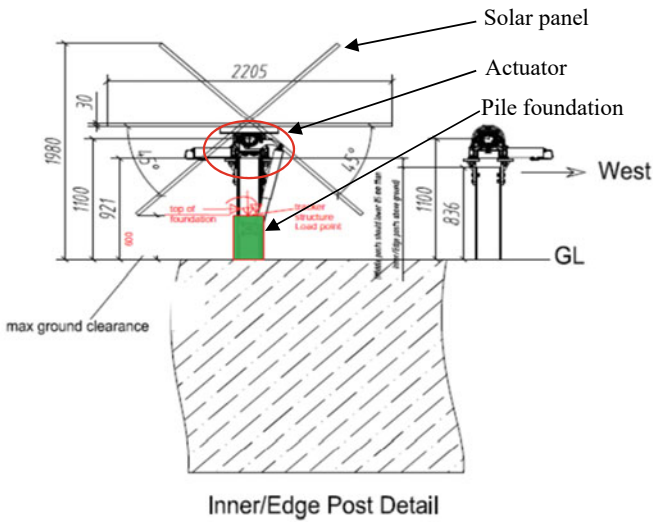


Fig. 1.1 Typical cross section of a horizontal solar axis tracker (HSAT) system

Table 1.1 Load cases considered for the design of the pile foundation

Load cases	Tracker type	Compression (kN)	Uplift (kN)	Lateral (kN)	Moment (kN-m)
Case-I	Exterior	24.75	9.7	20.25	26.0
	Interior	19.25	4.2	14.65	16.3
	Far-interior	16.4	1.65	8.25	8.4
Case-II	Exterior	32.4	12.7	26.6	33.8
	Interior	25.0	5.5	18.9	21.2
	Far-interior	21.3	2.15	10.66	10.9

Table 1.2 Soil profile considered for the design of piles using the theoretical approach

Borehole	Soil type	SPT N value	c (kN/m ²)	ϕ (°)	Unit weight (kN/m ³)	E (kN/m ²)
BH101	CH	12	46	5	18.84	5400
BH102	CH	11	42	5	18.44	5100
BH105	CH	10	44	5	17.66	4800
BH107	CI	12	40	5	16.87	5400
BH109	CH	10	47	6	19.03	4800
BH110	(SM-SC)	18	8	25	17.46	7200
BH111	CH	12	50	4	17.66	5400
BH112	CH	10	42	5	17.27	4800
BH113	CH	10	45	5	17.27	4800
BH114	CH	9	31	4	16.78	4500

Geotechnical Investigation

The soil parameters were evaluated from the detailed subsoil investigation report. The subsoil investigation report comprised of field exploration, laboratory tests, and analysis of the test results. The subsoil investigation report was prepared based on ten boreholes with the depth ranging from 80 to 100 m. The elastic properties of different soil layers were estimated from the parameters available in the geotechnical investigation report. From the SPT N values, the elastic modulus (E) of different soil types and the magnitude of the Poisson's ratio were determined by following the standard recommendation of Bowles [7]. While performing the analysis based on the theoretical approaches, the soil properties were considered up to the embedment/termination depth of the piles. The piles having a diameter ranging from 0.3 to 0.45 m and length ranging from 2 to 4.5 m were considered for the calculation purposes. The summary of the soil properties considered for the theoretical approaches for boreholes BH 101–BH 114 is shown in Table 1.2. The soil profiles were characterized as per IS 1498:1970 [8] and are reported in Table 1.2. The groundwater table at the borehole locations was encountered at depths ranging from 2.2 to 3.4 m below the existing ground level (EGL), which might arise during heavy rains. Hence, for the analysis of the foundations, the water table was considered to be at the ground level. The data depicted in Table 1.2 show that the nature of the soil in the boreholes (BH 101–BH 114) is primarily cohesive, except BH 110, where the soil is described as silty sand.

Analysis of Pile Foundations

The loads coming from the superstructure to the piles are reported in Table 1.1. The optimum geometry of the pile foundations (length and diameter) for different boreholes under different loading conditions was obtained. The analysis of the piles was carried out in two stages:

- *Stage I*—design of piles as per Brom’s method [4] and the IS code method [5, 6] satisfying the lateral displacement criterion.
- *Stage II*—check for the piles designed in *Stage I* using the FE analysis and propose suitable modifications, if needed.

The results are then compared to understand the adequacy of the piles based on the theoretical approaches [4–6] and the FE analysis. For each borehole, the ultimate load-carrying capacity of a single pile was obtained from both theoretical [4–6] and numerical (FE analysis) approaches, as discussed in the following sections.

Theoretical Approaches

To obtain the ultimate load-carrying capacity of a single bored cast in-situ (BCS) and driven pile, the IS code [5, 6] provides the following recommendations based on the static formulae. Further, the displacement of the piles was also estimated to satisfy the displacement criteria.

Static Formulae: As per the static formulae [5, 6], the safe load-carrying capacity of a single pile under compression (F_C), uplift (F_U), and lateral (F_L) can be expressed as:

$$Q_{ub} = (c_b N_c + \sigma' N_q + 0.3\gamma D N_\gamma) A_b \quad (1.1)$$

$$Q_{uf} = (K_p \sigma'_{avg} \tan \delta + \alpha c_f) A_f \quad (1.2)$$

$$F_C = \frac{(Q_{ub} + Q_{uf} - W_p)}{FS} \quad (1.3)$$

$$F_U = \frac{Q_{uf}}{FS} \quad (1.4)$$

$$F_L = \frac{Q_{uL}}{FS} \quad (1.5)$$

where Q_{ub} and Q_{uf} are the end bearing and the skin friction capacities of a single pile, respectively; N_c , N_q and N_γ are the bearing capacity factors obtained from IS 6403:2002 [9]; A_b and A_f are the cross-sectional and the surface areas of the pile respectively; γ is the unit weight of the soil at the bearing stratum; D is the diameter of the pile; σ' is the effective stress; σ'_{avg} is the average effective stress; K_p is the earth pressure coefficient for the soil layer. The value of K_p was taken as 0.7 for the bored pile and 1.0 for the driven pile as recommended by Nayak [10]; δ is the angle of interface friction between the soil and the pile stem, and its magnitude was taken as the 2/3rd of the friction angle of the soil layer; c_b and c_f are the cohesion at

the bearing stratum and the surface respectively; α is the adhesion factor for the soil layer which was taken as 0.3–0.5. FS is the factor of safety taken as 2 in the present analysis; W_p refers to the weight of the pile; Q_{uL} refers to the ultimate lateral load, which can be calculated using Brom's method [4] and the IS code method [5, 6]. The lever arm (X_0) and the moment capacity (M) can be calculated as recommended by Prakash and Sharma [11]

$$X_0 = \frac{Q_{uL}}{9c_b D} \quad (1.6)$$

$$M = \frac{Q_{uL}(e + 1.5D + 0.5X_0)}{FS} \quad (1.7)$$

where e is the unsupported length of the pile.

Check for Lateral Displacement: The lateral displacement of BCS piles was estimated using Brom's method [4] and the IS code method [5, 6] for short and long piles. As per IS 2911: 2010 [5], the short piles and the long piles behave as rigid and elastic members, respectively. Hence, the increase in the pile capacity of short piles does not yield a significant reduction in the lateral displacement as in long piles. The stiffness factor (R) can be estimated using Eq. (1.8).

$$R = \sqrt[4]{\frac{EI}{KD}} \quad (1.8)$$

where K can be calculated from Clause-2.2 [5], EI is the flexural rigidity of the pile, which depends on the grade of concrete and the geometry of the pile. If $L \leq 2R$, it is considered as a short pile, whereas for a long pile, it is $L \geq 3.5R$. The Brom's length factor (β) can be expressed as

$$\beta = \sqrt[4]{\frac{k_1 D}{4EI}} \quad (1.9)$$

where k_1 is the modulus of subgrade reaction. If $\beta L < 2.5$, it can be termed as a short pile. For a given value of unsupported length (e), length of the pile (L), and Brom's length factor (β), the lateral displacement y for short piles can be determined.

Finite Element (FE) Analysis

To obtain a comprehensive understanding of the load-carrying capacity and the settlement characteristics of BCS and driven piles designed as per Brom's method [4] and the IS code method [5, 6], a detailed FE analysis was conducted using PLAXIS 3D [12]. In general, the theoretical approaches considered the critical load cases

separately (compression, uplift, lateral and moment) in the analysis. While calculating the displacement under lateral load, the pile was considered to be a cantilever beam neglecting the contribution of the soil surrounding the embedded length of the pile. Further, the settlements under compression and uplift are not addressed by the theoretical approaches. However, the FE analysis takes into account all the limitations described above. In addition, the load–settlement curves and the displacement contours could also be obtained using the FE analysis. Hence, a three-dimensional FE analysis was performed using PLAXIS 3D [12]. The input parameters pertaining to the soil are obtained from Table 1.2 and based on the subsoil investigation report. Piles were modeled separately for each borehole (BH 101–BH 114). The maximum value of the bearing resistance and the traction values adopted in the modeling of the pile element were obtained from the static formulae recommended by IS 2911: 2010 [5]. The soil domain considered for the FE analysis was three times the embedment/termination depth of the piles. The pile and the soil were modeled using an embedded pile element and 15-noded triangular element, respectively (Fig. 1.2). The physical properties of reinforced concrete used in the analysis are given in Table 1.3. The FE analysis was carried out in three load sets—(a) compressive, (b) uplift, (c) lateral load and moment.

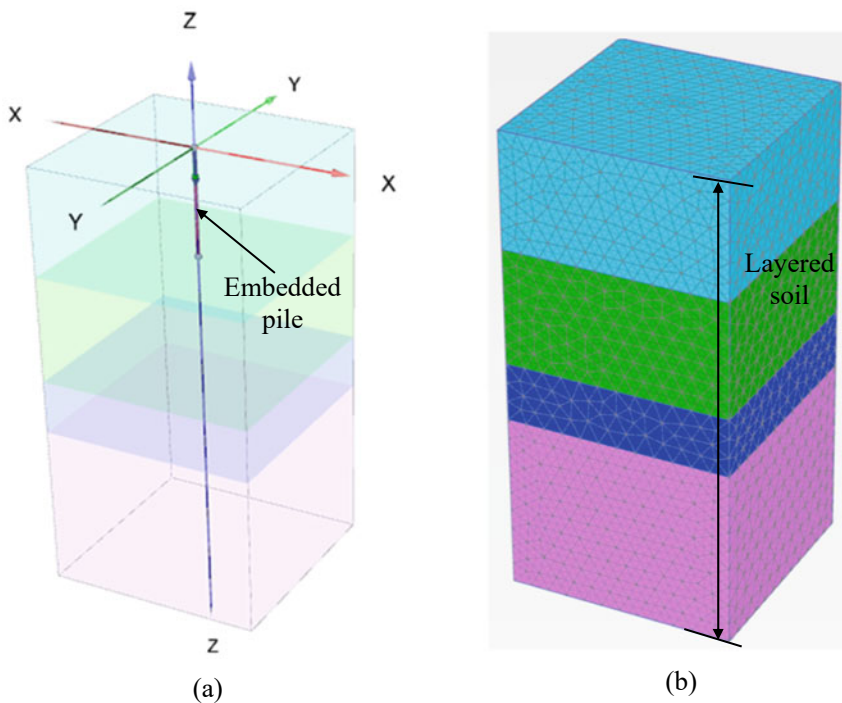


Fig. 1.2 Finite element model generated in PLAXIS 3D showing **a** pile model and **b** meshing scheme

Table 1.3 Properties of reinforced concrete adopted in FE analysis

Properties	Value
Unit weight (kN/m ³)	25
Young’s modulus (kN/m ²)—bored piles	27.5 × 10 ⁶
Young’s modulus (kN/m ²)—driven piles	45.0 × 10 ⁶
Poisson’s ratio	0.2

Results and Discussion

Pile Geometry and Serviceability Criteria

Based on the load cases given in Table 1.1, the BCS and driven piles were designed using the theoretical approaches [4–6], followed by the numerical analysis [12]. The permissible serviceability criteria (displacement) were adopted as 12 mm (compression), 5 mm (uplift), and 10 mm (lateral) as per the project requirements. The corresponding displacements were captured in the FE analysis by gradually imposing the compressive, uplift and lateral loads on the piles. The ultimate load carrying capacity was determined from the generated load–settlement curves corresponding to the permissible displacement. The safe loads were obtained by increasing the diameter from 0.3 m with an increment of 0.05 m for every trial. Under such a process, the range of pile diameter and embedded pile length for the BCS piles were obtained as 0.3 m to 0.45 m and 2 m to 4.5 m, respectively, using the theoretical and FE approaches. Similarly, the BCS and the driven piles for different boreholes were extensively investigated using the theoretical and FE approaches. The summary of the pile geometry obtained is reported in Tables 1.4 and 1.5, respectively.

Table 1.4 Recommendation of pile geometry based on the soil condition for the BCS piles

Load cases	Tracker type	Theoretical approach		FE analysis	
		Diameter (m)	Length (m)	Diameter (m)	Length (m)
Case-I	Exterior	0.35	2.5, 3.0, 3.5	0.35	2.5, 3.0, 3.5
		Interior	0.30	2.5	0.30
	0.35		2.5, 3.0	0.35	2.5, 3.0
	Far Interior	0.30	2.0	0.30	2.0
		0.35	2.5	0.35	2.5
Case-II	Exterior	0.35	3, 4.5	0.35	3.0, 4.0, 4.5
		0.45	4.0		
	Interior	0.35	2.5, 3, 3.5	0.35	2.5, 3.0, 3.5
		Far Interior	0.30	2.0	0.30
	0.35		2.0, 3.0	0.35	2.0, 3.0

Table 1.5 Recommendation of pile geometry based on the soil condition for the precast driven piles

Load cases	Tracker type	Theoretical approach		FE analysis	
		Diameter (m)	Length (m)	Diameter (m)	Length (m)
Case-I	Exterior	0.35	2.5, 3.0, 3.5	0.35	2.5, 3.0, 3.5
	Interior	0.30	2.5	0.30	2.5
		0.35	2.5, 3.0	0.35	2.5, 3.0
	Far interior	0.30	2.0	0.30	2.0
		0.35	2.5	0.35	2.5
Case-II	Exterior	0.35	3, 4.5	0.35	3.0, 4.0, 4.5
		0.40	4.0		
	Interior	0.35	2.5, 3.0, 3.5	0.35	2.5, 3.0, 3.5
	Far interior	0.30	2.0	0.30	2.0
		0.35	2.0, 3.0	0.35	2.0, 3.0

Seismic Analysis

Considering the location of the site (Zone V), the seismic analysis was also performed to provide a better insight into the analysis. During the static analysis of piles, it was observed that the boreholes BH 107 and BH 110 exhibit different soil types. Hence, the seismic analysis was only carried out for these boreholes using the pseudo-static approach. The effect of earthquakes was considered in terms of additional seismic inertial forces [13, 14]. The pseudo-static module available in PLAXIS 3D [12] was utilized to serve the intended purpose. As per IS 1893:2014 [15], the horizontal seismic acceleration (A_h) can be determined using Eq. (1.10).

$$A_h = \frac{Z}{2} \cdot \frac{I}{R} \cdot \frac{S_a}{g} \quad (1.10)$$

where Z is the zone factor, I is the importance factor, R is the response reduction factor and S_a/g is the average acceleration coefficient for the site. The seismic analysis was performed by adopting the horizontal and the vertical seismic accelerations as 0.3 and 0.2, respectively. The seismic load-carrying capacities of different piles at the boreholes mentioned above are reported in Tables 1.6, 1.7, 1.8 and 1.9.

From Tables 1.6, 1.7, 1.8 and 1.9, it can be seen that the load-carrying capacities of the piles under seismic conditions are more significant than the load configurations mentioned in Table 1.1. The driven piles have a higher load-carrying capacity than the BCS piles, as shown in Tables 1.6, 1.7, 1.8 and 1.9. However, apart from BH 110, where the soil is described as silty sand, the nature of the soil in other boreholes (BH 101–BH 114) is primarily cohesive. In general, the driven piles are not recommended for clayey deposits due to the generation of excess pore water pressure and a decrease in the frictional resistance during the pile driving operation [16, 17]. To reduce the

Table 1.6 Seismic load-carrying capacity of the BCS piles (BH 107)

Load cases	Tracker type	Compression (kN)	Uplift (kN)	Lateral (kN)
Case-I	Exterior	45.1	32.2	51.2
	Interior	40.2	30.4	48.1
	Far interior	28.4	19.1	43.5
Case-II	Exterior	62.0	40.0	58.0
	Interior	45.1	32.2	51.2
	Far interior	28.4	19.1	43.5

Table 1.7 Seismic load-carrying capacity of the driven piles (BH 107)

Load cases	Tracker type	Compression (kN)	Uplift (kN)	Lateral (kN)
Case-I	Exterior	46.2	32.5	52.0
	Interior	40.7	31.1	50.8
	Far interior	28.8	19.7	44.2
Case-II	Exterior	63.5	40.5	60.3
	Interior	46.2	32.5	52.0
	Far interior	28.8	19.7	44.2

Table 1.8 Seismic load-carrying capacity of the BCS piles (BH 110)

Load cases	Tracker type	Compression (kN)	Uplift (kN)	Lateral (kN)
Case-I	Exterior	42.4	22.2	70.1
	Interior	29.2	15.1	60.4
	Far interior	27.6	10.2	55.7
Case-II	Exterior	63.1	40.2	72.2
	Interior	42.4	22.2	70.1
	Far interior	29.2	15.1	60.4

Table 1.9 Seismic load-carrying capacity of the driven piles (BH 110)

Load cases	Tracker type	Compression (kN)	Uplift (kN)	Lateral (kN)
Case-I	Exterior	45.4	26.2	74.1
	Interior	31.3	18.5	63.7
	Far interior	29.3	12.2	56.1
Case-II	Exterior	70.2	48.5	80.1
	Interior	45.4	26.2	74.1
	Far Interior	31.3	18.5	63.7

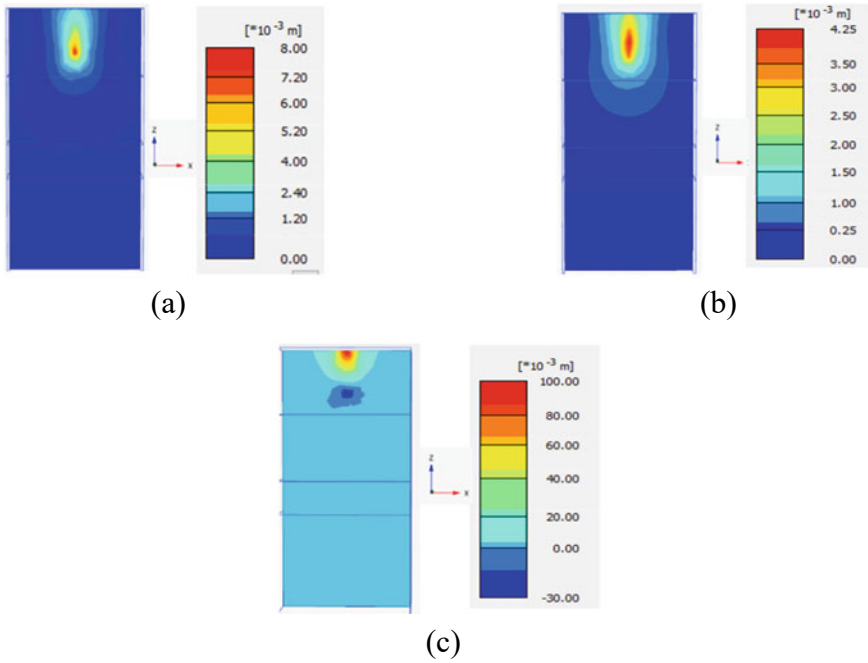


Fig. 1.3 Displacement contours for the BCS pile under the pseudo-static condition (BH107—interior, 0.3 m diameter and 2 m length) **a** vertical displacement (compression), **b** vertical displacement (uplift) and **c** lateral displacement

developed excess pore pressure, suitable ground improvement techniques such as granular columns may be adopted [18, 19]. Representative displacement contours for the BCS pile under the pseudo-static condition at BH 107 (Interior, 0.3 m diameter and 2 m length) are shown in Fig. 1.3. It can be ensured from Fig. 1.3 that the lateral displacement is more critical for designing the pile foundation for the proposed HSAT system. The significance of lateral load capacity in designing several marine structures is also reported by several researchers [20, 21].

Conclusions

The optimum geometry of the pile foundation (length and diameter) for a proposed HSAT system is obtained using the theoretical and FE approaches. The results obtained are compared to obtain a safe and economical design of pile foundations for the solar axis tracker system. Some of the significant conclusions revealed from the present study can be listed as

- The lateral load is found to be the critical parameter influencing the pile geometry for the HSAT system.
- The range of pile diameter and embedded pile length are obtained as 0.3–0.45 m and 2–4.5 m for the given soil conditions.
- The piles are found to perform well under the action of the given loads and satisfy the recommended serviceability criteria.
- The pile geometries recommended by the theoretical approaches are verified with the FE analysis, and suitable modifications are proposed.
- The proposed geometry of the piles is verified under the seismic condition as well.
- Though the performance of the driven piles is found to be better in the silty sand, the BCS piles are recommended for the cohesive soil, especially under the seismic condition.

Acknowledgements The authors would like to acknowledge the financial support provided by Adani Green Energy Limited (AGEL) to carry out the present work (Ref. No. AGEL/IITK/C/SK/670/20).

References

1. Hammoumi AE, Motahhir S, Ghzizal AE, Chalh A, Derouich A (2018) A simple and low-cost active dual-axis solar tracker. *Energy Sci Eng* 6(5):607–620
2. Rabaia MK, Abdelkareem MA, Sayed ET, Elsaid K, Chae KJ, Wilberforce T, Olabi AG (2021) Environmental impacts of solar energy systems: a review. *Sci Total Environ* 754:141989
3. Awasthi A, Shukla AK, Manohar SR, Dondariya C, Shukla KN, Porwal D, Richhariya G (2020) Review on sun tracking technology in solar PV system. *Energy Rep* 6:392–405
4. Broms BB (1964) Lateral resistance of piles in cohesionless soils. *J Soil Mech Found Div* 90(3):123–156
5. IS 2911-Part 1 (2010) Design and construction of pile foundation—concrete piles—bored cast in-situ piles. Bureau of Indian Standards, New Delhi
6. IS 2911-Part 4 (2010) Design and construction of pile foundation—concrete piles—driven precast concrete piles. Bureau of Indian Standards, New Delhi
7. Bowles JE (1997) *Foundation analysis and design*, 5th edn. McGraw-Hill Companies, Singapore
8. IS 1498 (1970) Classification and identification of soils for general engineering purposes. Bureau of Indian Standards, New Delhi
9. IS 6403 (1981) Code of practice for determination of bearing capacity of shallow foundations. Bureau of Indian Standards, New Delhi
10. Nayak NN (1996) *Foundation design manual*, 4th edn. Dhanpat Rai Publications, New Delhi
11. Prakash S, Sharma HD (1990) *Pile foundations in engineering practice*. Wiley, Canada
12. Brinkgreve RBJ, Kumarswamy S, Swolfs WM, Waterman D, Chesaru A, Bonnier PG (2016) PLAXIS 2016. Reference Manual. PLAXIS bv, Netherlands
13. Tabesh A, Poulos HG (2001) Pseudostatic approach for seismic analysis of single piles. *J Geotech Geoenviron Eng* 127(9):757–765
14. Liyanapathirana DS, Poulos HG (2005) Pseudostatic approach for seismic analysis of piles in liquefying soil. *J Geotech Geoenviron Eng* 131(12):1480–1487
15. IS 1893-Part 3 (2014) Criteria for earthquake resistant design of structures—bridges and retaining walls. Bureau of Indian Standards, New Delhi

16. Clark JI, Meyerhof GG (1972) The behavior of piles driven in clay. I. An investigation of soil stress and pore water pressure as related to soil properties. *Can Geotech J* 9(4):351–373
17. Hwang JH, Liang N, Chen CH (2001) Ground response during pile driving. *J Geotech Geoenviron Eng* 127(11):939–949
18. Ben Salem Z, Frikha W, Bouassida M (2016) Effect of granular-column installation on excess pore pressure variation during soil liquefaction. *Int J Geomech* 16(2):04015046
19. Badanagki M, Dashti S, Kirkwood P (2018) Influence of dense granular columns on the performance of level and gently sloping liquefiable sites. *J Geotech Geoenviron Eng* 144(9):04018065
20. Rao SN, Ramakrishna VGST, Rao MB (1998) Influence of rigidity on laterally loaded pile groups in marine clay. *J Geotech Geoenviron Eng* 124(6):542–549
21. Rathod D, Krishnanunni KT, Nigitha D (2020) A review on conventional and innovative pile system for offshore wind turbines. *Geotech Geol Eng* 38(4):3385–3402

Chapter 2

Bidirectional and Conventional Static Load Test on Bored Piles in Soil: A Field Comparison



Anil Cherian 

Introduction

The success of any high-rise building foundation design primarily depends on the accuracy of estimating the shaft and bearing capacity of soil/rock beneath them [1]. Performing load tests using sacrificial hydraulic jacks by dividing foundation elements into sections is suitable for high-capacity piles. For such high load tests, the traditional top-down test using huge anchors, reaction piles, kentledge systems, etc., is challenging both technically and commercially.

In most of the deep foundation infrastructure projects, BDSLT has been demonstrated to have advantages as compared to the conventional pile load testing method in many aspects [2]. Due to the rising use of high load large-diameter piled foundations in recent years, a conventional static load test is occasionally inadequate to assess the shaft and bearing capacity of bored piles, and hence, BDSLT has been increasingly used in the contemporary foundation industry. In this test method, specially designed sacrificial hydraulic jacks, a loading device, are installed at the desired depth or pile toe. The lower shaft and toe resistance provide the reaction force to mobilize the upper shaft resistance and vice versa. The BDSLT divides the toe and shaft resistances, mobilizing them in opposite directions, whereas the traditional static load test combines them in the same downward direction [3]. Therefore, an equivalent top-down load–movement curve is made from the BDSLT pile data to obtain the settlement behavior.

The first application of BDSLT started in the early 1970s [4, 5]. Later, this method was used commercially in the Brazilian piling industry [6] and then in USA [7]. This testing method was effectively implemented in the Middle East foundation industry for the last two decades [8–13]. These test methods are very well-recognized and

A. Cherian (✉)

Strainstall Middle East LLC (James Fisher and Sons plc, UK), Dubai, United Arab Emirates
e-mail: dranilct@gmail.com

are mentioned in the standards [14–18]. Although there are some uncertainties in foundation engineering related to the comparability of results between BDSLT and conventional static load tests, there are studies that endorse the consistency between the two testing methods [19, 20]. BDSLT as compared to the traditional static load test is a cost-effective substitute for high-capacity test piles [20, 21].

Due to the lack of extensive field studies, there is a general notion that BDSLT and traditional static load test results are not comparable, and therefore BDSLT cannot be used as an alternative method in bore pile capacity evaluation in soil conditions. Hence, the purpose of this article is to share the load test results of both techniques from the same study area in Multa City, Kuwait, to enable a practical comparison of the testing methods that can be applied in other countries like India having similar soil conditions.

General Geological Setting

The State of Kuwait is situated in the northwestern corner of the Arabian Peninsula, between Longitudes 46° 30' and 48° 30' East and Latitudes 28° 30' and 30° 08' North and includes ten offshore islands. The majority of the northern parts of the country have been covered by deflation to lag gravels that protect the removal of fine sediments from wind action [22]. The vegetated sand sheets in the western and southern parts have deteriorated due to anthropogenic activities [23, 24]. Kuwait can be divided according to its morphological characteristics into several geomorphic zones. Information from previous studies, field inspection, study of topographic maps and interpretation, and analysis of aerial photographs were used in the delineation of these zones. Most of these geomorphic zones originated during the Late Tertiary–Quaternary periods were due to the tectonic, erosion or depositional processes or their combination [25].

The subsurface formation consists of light brownish gray, medium grained, sand with silt encountered at depth 0.0–5.0 m below ground surface (Layer 1). From 5.00 to 15.0 m depth, light brownish beige, medium grained, clayey sand was identified (Layer 2). Light brownish gray, medium grained, poorly graded sand with silt was observed at 15.0–35.0 m below ground surface (Layer 3). The water table was encountered at around 7.00 m depth below ground surface at the time of site investigation. The general soil parameters with depth (mRL—meter Reduce Level) is presented in Table 2.1.

Methodology

Static load testing is important for the execution of a successful deep foundation project. The load-carrying capacity of piles has usually been assessed by static load

Table 2.1 General soil parameters

Layer	Depth range (m)	Depth (mRL)	Thickness (m)	Average SPT	Design unit shaft friction (kN/m ²)
1	0.00–5.00	102.60–97.60	5.00	15	45
2	5.00–15.00	97.60–87.60	10.00	50	150
3	15.00–35.00	87.60–67.60	20.00	50	150

tests using either concrete blocks or reaction piles or anchor systems. In these traditional methods, the pile is loaded using a test frame either in compression or in tension. Generally, test piles are instrumented with load cells, jacks, vibrating wire strain gauges and displacement transducers. Due to the local authority regulations and safety concerns, the test frames must be designed and approved and incorporated with the above electronic devices with an automatic data logging system and data will be analyzed to obtain the required load and settlement parameters (Fig. 2.1).

A traditional top-down test utilizes an overhead reaction system or weight to load the bored pile in compression at its top. Side shear and end bearing combine to resist the top total load. In a conventional method, load measured at the pile head through an external reaction system, mobilizing skin friction and the end bearing parameters [26]. On the other hand, BDSLT method loads the bored pile in compression from the middle or tip section. As the hydraulic jack expands, the bottom shaft and tip resistances provide reaction for the upper side shear, and conversely, until reaching the one of the pile capacity components or ultimate jack capacity. The end bearing component is directly measured using the jacks placed at the toe of the pile.



Fig. 2.1 Typical static load setup



Fig. 2.2 BDSLT pile installation

BDSLTs are executed using sacrificial calibrated hydraulic jack assembly embedded within the test pile. In this test, jack assembly contains of two 6000 kN bidirectional hydraulic jacks located between upper and lower bearing plates (Fig. 2.2). Six levels of vibrating wire Geokon model 4200 concrete embedment strain gauges (four units at each level, a total of 24 nos.) were installed to understand the pile shaft resistance behavior. Jack level is calculated from the geotechnical parameters available in the soil data and local experience to equalize the bidirectional forces in the pile to avoid any early single direction failure and will aid to complete the load test as per the project requirements [12].

The test shaft was instrumented with vibrating wire strain gauges, tell-tales and displacement transducers to better understand the geotechnical behavior of the test pile under applied loading circumstances. Strain gauges mounted along the shaft help determine the internal load distribution by measuring the stresses associated with each applied load. At the top and bottom of the hydraulic cell, tell-tales and displacement transducers monitor displacement. Two displacement transducers will be fitted at the testing platform level to measure pile top movement during the test (Fig. 2.3). The load test will be performed once the pile has reached full strength, which is usually 14 days following casting [10, 12]. Table 2.2 lists the details of the preliminary test piles (PTP1 and PTP2).

Results and Discussion

The bidirectional displacement data obtained from the load tests was analyzed to obtain the equivalent top-loading (ETL) settlement plot [12]. This plot is a good

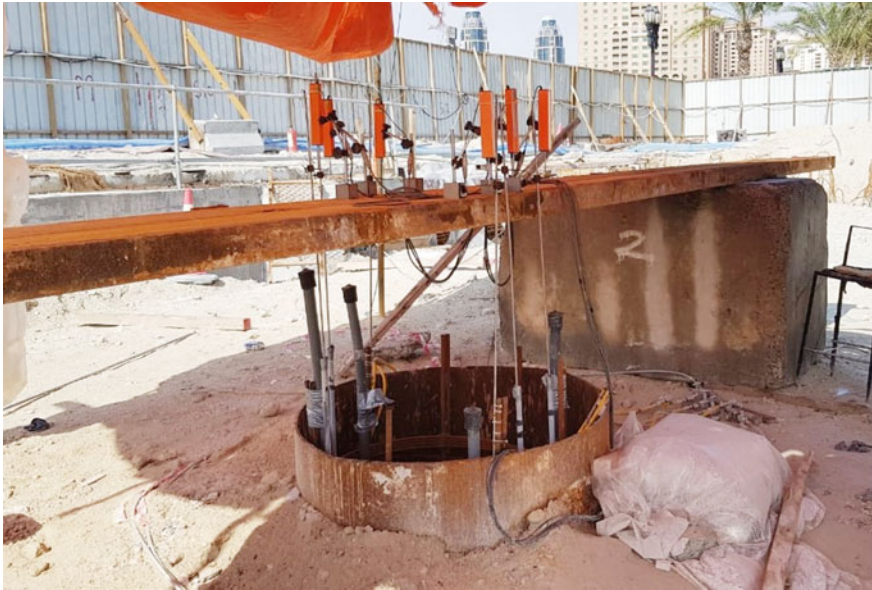


Fig. 2.3 BDSLT setup

Table 2.2 Details of preliminary test piles

Pile ID	Diameter (mm)	Cut-off level (m RL)	Toe level (m RL)	Working load (kN)	Test load (kN)	Strain gauge levels (mRL)
PTP1 (BDSLT)	1500	99.70	73.70	8360	20,900	99.20, 93.00, 86.90, 82.90, 78.60 and 74.20 jack level at 84.90
PTP2 (static)	1500	99.70	73.70	8360	20,900	99.20, 93.00, 86.90, 82.90, 78.60 and 74.20

assessment of the pile top load–displacement behavior that would occur from a traditional top-down load test. Since the load application in BDSLT is at some specific depth within the foundation element, such load–displacement relationships are not measured directly, but must be constructed to compare with the traditional load–settlement [19]. The upper section of the jack assembly is governed by shaft resistance developed in the upper pile section and that section below the jack assembly denotes the shaft and tip resistance developed in the pile lower segment. The equivalent top loading method analyzes the upper and lower jack displacement data to identify the elastic settlement curve [12, 27]. The settlement obtained from both testing methods

is provided in Table 2.3. The comparison settlement plot is presented in Fig. 2.4. The strain obtained from strain gauges during the load tests at ultimate load from different segments of the pile was used to calculate the unit shaft friction distribution (Table 2.4).

In both test methods, the loading test continued until 250% of the load and not reached the failure load. The settlement obtained from BDSLT at ultimate load was 10.30 mm, and that from the static load test was 9.80 mm. The maximum average



Fig. 2.4 Load—settlement comparison plot

Table 2.3 Load and settlement values

Applied load (kN)	Applied load (%)	Settlement (BDSLT)	Settlement (Static)
0	0	0.00	0.00
8360	100	3.50	3.80
12,540	150	5.70	6.00
16,720	200	7.90	7.70
20,900	250	10.30	9.80

Table 2.4 Ultimate unit shaft friction obtained from BDSLT and static (kN/m²)

Strain gauge level (mRL)	BDSLT	Static
99.20–93.00	61	96
93.00–86.90	182	232
86.90–82.90	302	242
82.90–78.60	205	162
78.60–74.20	138	92

shaft resistance mobilized from BDSLT ranges from 61 to 302 kN/m² and from static load test was 92–242 kN/m² at the normalized pile settlement values. The pile shaft friction kept increasing linearly and had not reached its maximum stress, even at the ultimate test load. It could be due to the fact that the majority of the load is consumed by the deeper comparatively stiff layers as expected from the geotechnical information. This designates that the ultimate shaft friction and settlement are still not achieved after the load test. The load tests were not able to mobilize any tip resistance. As the skin friction obtained from the load test was more than sufficient to resist the applied loads, and hence, there was no mobilization of tip resistance occurred. Based on the results, it was identified that the load test outcomes symbolize the soil characteristics in the study area and the shaft friction determined are higher than the values assumed during the initial pile design.

The two test methods differ in their loading arrangement location in the pile. The observed settlement behavior and unit shaft friction of the tested piles show slight deviation. The unit shaft friction calculated at the opposite ends of the pile section shows variations as expected. However, the behavior in the middle section of the tested piles looks more or less similar [28]. These differences are perhaps due to the apparent stiffness of the soil–pile system, interaction of reaction piles, load transfer behavior, etc., with the two test procedures. In the traditional compression test, the shaft undergoes downward vertical penetration, while in BDSLT, the shaft operates bidirectionally upward and downward. The top-down equivalent curve calculated from the BDSLT results is approximately equal to that obtained from the traditional top-down load test. However, differences in results may arise in terms of pile construction defects, and hence, proper construction quality checks are the necessary to minimize the errors and overall foundation risk.

Based on the analysis, it is confirmed that both test methods are accurate enough to assess the geotechnical behavior of the pile. Hence, it is identified that the BDSLT is an alternate feasible, innovative replacement of the traditional static load test to determine the ultimate static performance of deep foundations, with the benefit of having the separation of pile shaft and tip resistance.

Conclusion

A comparative pilot study of instrumented BDSLT and conventional static load tests in the same soil conditions is discussed in this article. The study confirmed that both methods are practically accurate enough to estimate the pile design parameters. Moreover, BDSLT is an innovative engineered system that is readily acquiescent to any soil conditions without the use of any external loading system at the ground level. Hence, BDSLT is a true full-scale static load test using automatic data acquisition techniques to provide valuable information to geotechnical engineers. It is recommended that further similar field studies using strain gauge instrumented piles in different soil conditions are required to comprehend the ground influence on pile performance.

References


1. Amir HA, Ehsan S (2016) New design equations for estimation of ultimate bearing capacity of shallow foundations resting on rock masses. *Geosci Front* 7(1):91–99
2. Kwon OS, Choi Y, Kwon O, Kim MM (2005) Comparison of the bidirectional load test with the top-down load test. *Transp Res Record: J Transp Res Board* 1936:108–116
3. Kim SR, Chung SG (2012) Equivalent head-down load vs. movement relationships evaluated from bi-directional pile load tests. *KSCE J Civ Eng* 16:1170–1177
4. Gibson GL, Devenny DW (1973) Concrete to bedrock testing by jacking from the bottom of a borehole. *Can Geotech J* 10(2):304–306
5. Amir JM (1983) Interpretation of load tests on piles in rock. In: *Proceedings of the 7th Asian regional conference on soil mechanics and foundation engineering*, Haifa, pp 235–238, Israel
6. Elisio, PCA (1983) *Celula Expansiva Hidrodinamica—Uma nova maneira de executar provas de carga* (Hydrodynamic expansive cell. A new way to perform loading tests). Independent publisher, Brazil
7. Osterberg JO (1984) A new simplified method for load testing drilled shafts. *Foundation Drilling*, XXIII ADSC
8. Cherian A (2018) Value engineering of foundation design using bidirectional static load test (BDSLTL): a case study from Dubai, United Arab Emirates. *Int J Earth Sci Eng* 11:270–273
9. Cherian A (2020a) Geotechnical and geological aspects of structural health monitoring in high-rise buildings. *J Indian Geophys Union* 24:10–24
10. Cherian A (2020b) Assessment of pile capacity using bidirectional static load test (BDSLTL). *Indian Geotech J* 51:369–375
11. Cherian A (2020c) Characterization of Simsima limestone for foundation design in Qatar: a case study. *J Rock Mech Tunneling Technol* 26:109–122
12. Cherian A (2021a) Geotechnical evaluation of multilayered Simsima limestone using bidirectional static load test. *J Geol Soc India* 97:670–674
13. Cherian A (2021b) Bidirectional static load test using instrumented pile: an innovative testing method in the construction industry. In: *Proceedings of the 7th ICRAGEE (seismic design and performance)*. Springer Singapore, pp 361–364
14. ASTM D8169/8169-18 (2018) Standard test methods for deep foundations under bi-directional static axial compressive load. ASTM International, West Conshohocken, PA
15. ASTM D1143 / D1143M-20 (2020) Standard test methods for deep foundation elements under static axial compressive load. ASTM International, West Conshohocken, PA
16. ICE (2012) *Manual of geotechnical engineering*. 1458–1460
17. Federation of Piling Specialists (2006) *Handbook on pile load testing*. Federation of Piling Specialists, Beckenham
18. IRC 78 (2014) *Standard specifications and code of practice for road bridges*. Section VII parts 1 and 2, foundations and substructure
19. Osterberg JO (1998) The Osterberg load test method for bored and driven piles. The first ten years. In: *Proceedings of the seventh international conference and exhibition on piling and deep foundations*, Vienna, Austria
20. Schmertmann JH, Hayes JA (1997) The Osterberg cell and bored pile testing—a symbiosis. The third international geotechnical engineering conference, Cairo, Egypt
21. Osterberg JO (1989) Breakthrough in load testing methodology, vol 28, no 8. *Found Drill Ed ADSC*, p 13
22. England M (2003) Bi-directional static load testing—state of art. In: *Proceedings of 4th international geotechnical seminar on deep foundations on BAP*, Ghent, Belgium, pp 309–313
23. Abdal MS, Suleiman MK (1984) Kuwait desert soil properties and genesis. In: *Proceeding of soil congress*, Kuwait
24. Khalaf FI, Gharib IM, Al-Hashash MZ (1984) Types and characteristics of the recent surface deposits of Kuwait, Arabian Gulf. *J Arid Environ* 7:9–33
25. Al-Sulaimi JS, El-Rabaab SM (1994) Morphological and morphostructural features of Kuwait. *Geomorphology* 11(2):151–167

26. England M, Cheesman P (2018) Recent experiences of full scale static pile load testing in chalk. In: *Engineering in chalk*, ICE Publishing
27. Hoyoung S, Rozbeh BM, William DL (2016) Assessment of methods for construction of an equivalent top loading curve from O-cell test data. *Soils Found* 56(5):889–903
28. Russo G (2013) Experimental investigations and analysis on different pile load testing procedures. *Acta Geotechnica* 8:17–31

Chapter 3

The Ultimate Bearing Capacity of Ring Footing with Inclined Base



Jitesh T. Chavda 

Introduction

The ring foundations are adopted for an isolated structure with circular geometry. The ring foundations are economical than circular footing, and they provide benefit effect of arching [5]. The bearing capacity of ring footings having flat base has been investigated widely using experimental and numerical approaches [1–9, 11–22]. However, the solution for the bearing capacity of ring footing with inclined base is not available in the literature. The ring footing with radii ratio = 0.25 has higher bearing capacity compared to radius ratio = 0, 0.5 and 0.75, and this may be due to beneficial effect of arching [4, 5]. The bearing capacity of cutting edge, also called tapered base of open caisson, reduced with an increase in the tapered angle or cutting angle of cutting edge [5]. It is noted from experimental results of Chavda and Dodagoudar [5] that the steeper cutting edge has higher bearing capacity than flatter cutting edge. The flatter cutting edge represents flat base ring footing, whereas the inclined cutting edge represents ring footing with inclined base. Therefore, there is a need to evaluate the effect of base inclination on the bearing capacity of the ring footing.

In the present study, the bearing capacity factors (BCF) of the ring footing with varying radii ratio ($r_i/r_o = 0-0.75$) and inclined base is evaluated using finite element (FE) method. The radii ratio is defined as the ratio of inner radius to the external radius of the ring footing. The inward base inclination of the ring footing is considered in the study, and the inclination angle (α) is varied from 0 to 20° with an increment of 5°, i.e., ($\alpha = 0, 5, 10, 15^\circ$). The present study FE results for ring footing with

J. T. Chavda (✉)

Department of Civil Engineering, Sardar Vallabhbhai National Institute of Technology,
Surat 395007, India

e-mail: jtc@amd.svnit.ac.in

flat base are compared with the numerical results of Hosseininia [12], Gholami and Hosseininia [9] and Chavda and Dodagoudar [4].

Problem Definition

The BCF of the ring footing is determined based on Griffiths [10] approach for strip footing using FE method. The bearing capacity Eq. (3.1) for ring footing is used as per Chavda and Dodagoudar [4]. The expression for bearing capacity of the ring footing is given as Eq. (3.1).

$$q_u = cN'_c + qN'_q + (r_o - r_i)\gamma N'_\gamma \quad (3.1)$$

The N'_c , N'_q and N'_γ are the modified BCF of the ring footing which considers the effect of shape of the footing, c is cohesion of soil, q is magnitude of surcharge acting at the base level of ring footing, γ is the unit weight of the soil, and r_i is the inner radius and r_o is the external radius of the ring footing. The ultimate bearing capacity of ring footing is determined for varying friction angles of the soil ($\varphi = 5-35^\circ$). First, the ultimate load is obtained from the load displacement chart for the ring footing corresponding to the different friction angles. The ultimate load is divided by the ring geometry to obtain the ultimate bearing pressure, i.e., the capacity of the ring footing with different base inclinations. Finally, the bearing capacity ratio (BCR) is obtained from the ultimate bearing capacity of the ring footings. The bearing capacity of the ring footing is evaluated corresponding to a finite value of cohesion of 20 kPa, a magnitude of surcharge of 20 kPa and a unit weight of the soil of 20 kN/m³. In order to quantify the effect of inclined base of the ring footing, BCR is evaluated. The BCR is defined as the ratio of the bearing capacity of ring footing with inclined base to the bearing capacity of ring footing with flat base. The BCR is plotted for increasing base inclination, friction angles and different radii ratio of the ring footing.

FE Model

The FE-based program PLAXIS 2D is used to examine the effect of inclined base on the bearing capacity of ring footing. The advantage of symmetry is taken in the analysis, and axisymmetric formulation is used. The Mohr–Coulomb material model is used in the FE analysis of ring footing. The Young's modulus of 200 MPa and Poisson's ratio of 0.3 are assigned to the soil in the FE analysis. Appropriate boundary conditions are assigned as shown in Fig. 3.1. Roller support is assigned for vertical boundaries, and fixed support is assigned for bottom boundary. The horizontal distance between the extreme ends of ring footing is kept constant as 1 m for the variations in the inclinations of the base of ring footing as shown in Fig. 3.1.

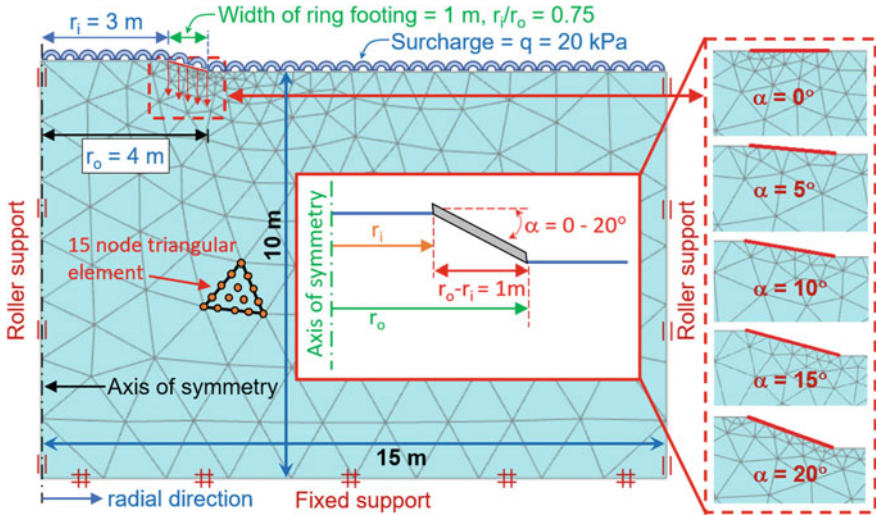


Fig. 3.1 Schematic of FE model of ring footing with mesh details, boundary conditions and representation of variation of base inclinations

For determination of ultimate bearing capacity, the vertical projection area of ring footing will remain constant as the horizontal projected width remains constant.

The FE mesh domains are finalized based on the development of plastic regions within the FE mesh domain for a ring footing with radii ratio = 0.75. The overall FE mesh dimension in radial direction is 15 m and in vertical direction is 10 m. The far boundary at 15 m away from axis of symmetry is placed such that it is away by minimum 5 times the width of ring footing from the external diameter of ring, i.e., $15\text{ m} > r_o + 5(r_o - r_i)$. In all cases, the width of ring is kept constant as recommended by Chavda and Dodagoudar [4], i.e., $r_o - r_i = 1\text{ m}$ for variations in the radii ratio (r_i/r_o) of ring footing from 0 to 0.75.

Mesh Convergence Study

The mesh size convergence study was performed for a case of ring footing ($r_i/r_o = 0$), i.e., circular footing resting soil having $c = 20\text{ kPa}$, $\gamma = 0$ and footing is surface footing, i.e., $q = 0$. The ultimate bearing capacity of the flat base circular footing resting on the surface of cohesive weightless soil was evaluated for very coarse, coarse, medium, fine and very fine mesh. The mesh convergence study results are shown in Fig. 3.2. It is observed from the figure that the ultimate bearing capacity of the circular footing reduces with reduction in the mesh size and reaches to a saturated value after fine mesh size. Hence, in the present study, the fine mesh is selected in all the FE analyses of circular and ring footings with flat and inclined base.

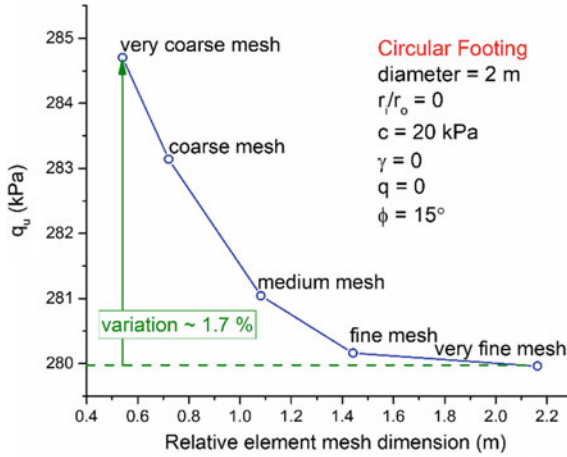


Fig. 3.2 Mesh convergence study for circular footing

Results and Discussion

Comparison of Bearing Capacity of Ring Footing

The bearing capacity of ring footing with flat base is evaluated and is compared with the published data from the available literature. The ring footing of width = 1 m having radii ratio = 0 represents the circular footing of diameter = 2 m. The bearing capacity of rough base circular footing ($r_i/r_o = 0$) and ring footing ($r_i/r_o = 0.25-0.75$) is evaluated using FE analysis and compared with the numerical solution of Hosseininia [12], Gholami and Hosseininia [9] and Chavda and Dodagoudar [4]. The comparison of FE-based ultimate bearing pressure of rough base circular and ring footings with the ultimate bearing capacity evaluated using the BCF N'_c , N'_q , N'_γ available in the published literature is depicted in Fig. 3.3. Based on the comparison, the present study results are found to match well with the published literature.

Bearing Capacity of Ring Footing with Inclined Base

The effect of inclined base of the ring footing is expressed in the form of normalized ratio as BCR. The BCR is the ratio of the bearing capacity of ring footings with inclined base to flat base. The BCR is plotted for increasing base inclination, friction angles and different radii ratio.

The BCR for ring footing with radii ratio = 0–0.75 with varying inclined base is depicted in Figs. 3.4a–d. It is observed from the figure that the BCR reduces with increase in the base inclination for the ring footing with radii ratio = 0, i.e., circular

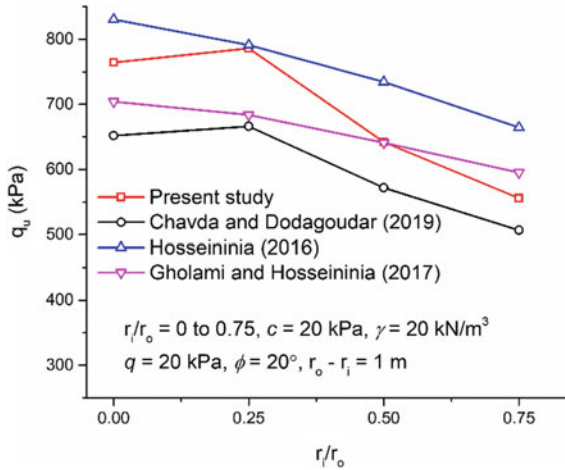


Fig. 3.3 Comparison of ultimate bearing capacity ring footing with varying radii ratio

footing, whereas the BCR increases with increase in the base inclination for ring footing with radii ratio = 0.25 and 0.50. In the case of ring footing with radii ratio = 0.75, the BCR reduces with increase with increase in the base inclination of the ring footing. This clearly shows that the ring footing with radii ratio = 0.25 and 0.5 shall be provided with the inclined base to get the benefits of increase in the ultimate bearing capacity. Moreover, there is need of further research to establish the fact on effect of inclined base of ring footing on the failure zone development in soil beneath footing, the experimental and numerical evaluation of evolution of arching in soil due to increase in the base inclination of ring footing, and finally the empirical relation can be proposed for the evaluation of bearing capacity of ring footing with inclined base using the ring footing results of flat base.

Conclusions

The bearing capacity of the ring footing with flat base ($\alpha = 0$) and varying inclined base ($\alpha = 0, 5, 10, 15^\circ$) is evaluated using FE-based program, PLAXIS 2D. The radii ratio is varied from 0 to 0.75. In the study, the bearing capacity of the ring footing is determined for the following parameters: $r_o - r_i = 1$ m, $c = 20$ kPa, $\gamma = 20$ kN/m³, $\varphi = 5-35^\circ$ and $q = 20$ kPa. The present study finite element results are compared with the numerical solutions of Hosseininia [12], Gholami and Hosseininia [9] and Chavda and Dodagoudar [4] for a specific $\varphi = 20^\circ$. Then the bearing capacity ratio is evaluated for varying radii ratio of the ring footing, different friction angles and different inward base inclination of the ring footing. Based on the present study results and comparisons, the following conclusions are drawn:

- The bearing capacity of circular footing ($r_i/r_o = 0$) with change in base angle, i.e., the conical shape, no major improvement in bearing capacity is observed.
- The bearing capacity of the ring footing ($r_i/r_o = 0.25$ and 0.50) increases with increase in the inward base inclination of the ring footing. The improvement was significant for $r_i/r_o = 0.25$ and 0.50 . This may be due to the benefit effect of arching is offered by the soil to the footing for narrow range of radii ratio of ring footing ($r_i/r_o = 0.25$ and 0.50). However, in the case of ring footing with higher $r_i/r_o = 0.75$, no major improvement in bearing capacity is observed. This may be due to the behavior of ring footing at higher radius ratio tends to that of strip footing.

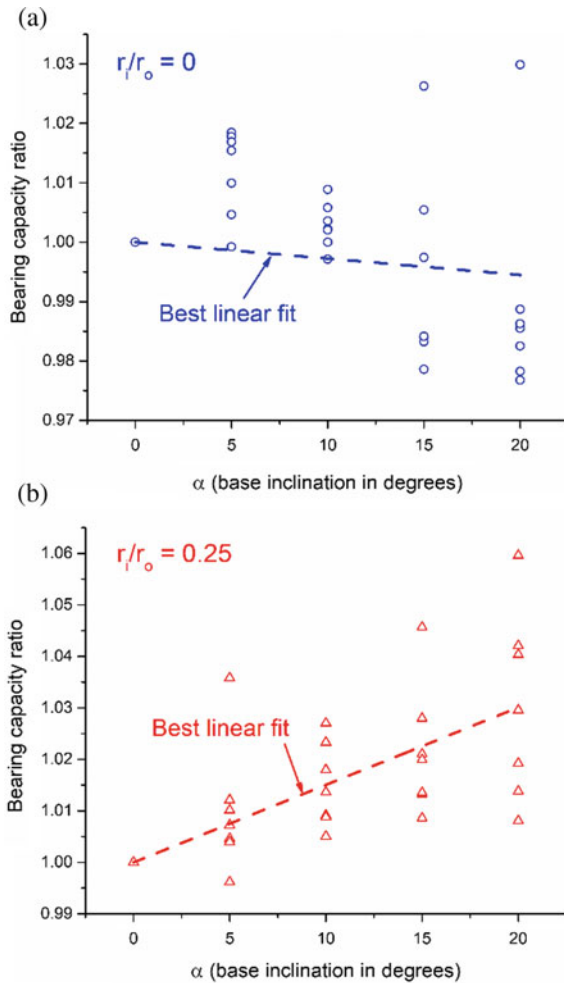


Fig. 3.4 BCR for varying base inclination of ring footing with different radii ratio: **a** radius ratio = 0, **b** radius ratio = 0.25, **c** radius ratio = 0.50, **d** radius ratio = 0.75

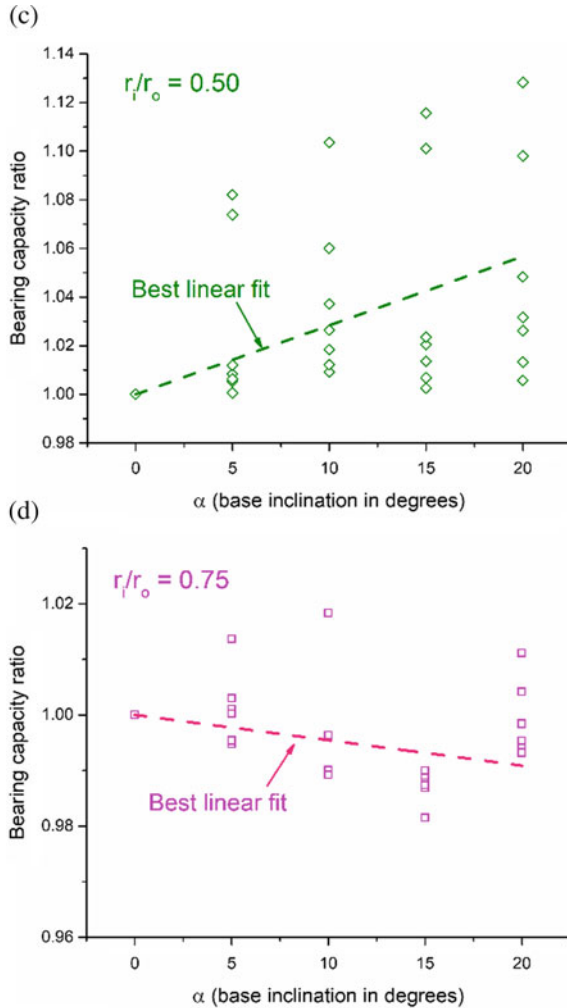


Fig. 3.4 (continued)

- Moreover, there is need of further research to establish the fact on effect of inclined base of ring footing on the failure zone development in soil beneath footing, the experimental and numerical evaluation of evolution of arching in soil due to increase in the base inclination of ring footing, and finally the empirical relation can be proposed for the evaluation of bearing capacity of ring footing with inclined base using the flat base ring footing.
- In order to take the benefit effect of base inclination of the ring footing, the ring footing to be adopted as foundation for structures with circular geometry like silos, circular towers, overhead water tank, etc. can be provided with the inclined base for a radii ratio = 0.25 to 0.50.

References

1. Benmebarek S, Saifi I, Benmebarek N (2017) Undrained vertical bearing capacity factors for ring shallow footings. *Geotech Geol Eng* 35(1):355–364. <https://doi.org/10.1007/s10706-016-0110-y>
2. Benmebarek S, Remadna MS, Benmebarek N, Belouar L (2012) Numerical evaluation of the bearing capacity factor N'_γ of ring footings. *Comput Geotech* 44:132–138. <https://doi.org/10.1016/j.compgeo.2012.04.004>
3. Boushehrian JH, Hataf N (2003) Experimental and numerical investigation of the bearing capacity of model circular and ring footings on reinforced sand. *Geotext Geomembr* 21(4):241–256. [https://doi.org/10.1016/S0266-1144\(03\)00029-3](https://doi.org/10.1016/S0266-1144(03)00029-3)
4. Chavda JT, Dodagoudar GR (2019) Finite element evaluation of vertical bearing capacity factors N'_c , N'_q and N'_γ for ring footings. *Geotech Geol Eng* 37(2):741–754. <https://doi.org/10.1007/s10706-018-0645-1>
5. Chavda JT, Dodagoudar GR (2021) Experimental evaluation of failure zone in sand beneath the ring footing and cutting edge of open caisson using image analysis. In: *Proceedings of the Indian geotechnical conference 2019: IGC-2019*, vol I. Springer Nature, p 273
6. Choobbasti AJ, Heshami S, Najafi A, Pirzadeh S, Farrokhzad F, Zahmatkesh A (2010) Numerical evaluation of bearing capacity and settlement of ring footing; case study of Kazeroon cooling towers. *Int J Res Rev Appl Sci* 4(2):263–271
7. Clark JI (1998) The settlement and bearing capacity of very large foundations on strong soils: 1996 R.M. Hardy keynote address. *Can Geotech J* 35:131–145. <https://doi.org/10.1139/t97-070>
8. El Sawwaf M, Nazir A (2012) Behavior of eccentrically loaded small-scale ring footings resting on reinforced layered soil. *J Geotech Geoenviron Eng* 138(3):376–384. [https://doi.org/10.1061/\(ASCE\)GT.1943-5606.0000593](https://doi.org/10.1061/(ASCE)GT.1943-5606.0000593)
9. Gholami H, Hosseininia ES (2017) Bearing capacity factors of ring footings by using the method of characteristics. *Geotech Geol Eng* 35(5):2137–2146. <https://doi.org/10.1007/s10706-017-0233-9>
10. Griffiths DV (1982) Computation of bearing capacity factors using finite elements. *Geotechnique* 32(3):195–202. <https://doi.org/10.1680/geot.1982.32.3.195>
11. Hataf N, Razavi MR (2003) Behavior of ring footing on sand. *Iran J Sci Technol Trans B: Eng* 27:47–56
12. Hosseininia ES (2016) Bearing capacity factors of ring footings. *Iran J Sci Technol Trans Civ Eng* 40(2):121–132. <https://doi.org/10.1007/s40996-016-0003-6>
13. Ismael NF (1996) Loading tests on circular and ring plates in very dense cemented sands. *J Geotech Eng* 122(4):281–287. [https://doi.org/10.1061/\(ASCE\)0733-9410\(1996\)122:4\(281\)](https://doi.org/10.1061/(ASCE)0733-9410(1996)122:4(281))
14. Kumar J, Chakraborty M (2015) Bearing capacity factors for ring foundations. *J Geotech Geoenviron Eng* 141(10):06015007. [https://doi.org/10.1061/\(ASCE\)GT.1943-5606.0001345](https://doi.org/10.1061/(ASCE)GT.1943-5606.0001345)
15. Kumar J, Ghosh P (2005) Bearing capacity factor N'_γ for ring footings using the method of characteristics. *Can Geotech J* 42(5):1474–1484. <https://doi.org/10.1139/t05-051>
16. Laman M, Yildiz A (2003) Model studies of ring foundations on geogrid-reinforced sand. *Geosynth Int* 10(5):142–152. <https://doi.org/10.1680/gein.2003.10.5.142>
17. Ohri ML, Purhit DGM, Dubey ML (1997) Behavior of ring footings on dune sand overlaying dense sand. In: *Proceedings of international conference of civil engineering*, Tehran, Iran, pp 4–6
18. Remadna MS, Benmebarek S, Benmebarek N (2017) Numerical evaluation of the bearing capacity factor N'_c of circular and ring footings. *Geomech Geoeng* 12(1):1–13. <https://doi.org/10.1080/17486025.2016.1153729>
19. Saran S, Bhandari NM, Al Smadi MMA (2003) Analysis of eccentrically obliquely loaded ring footings on sand. *Indian Geotech J* 33(4):422–446
20. Sargazi O, Hosseininia ES (2017) Bearing capacity of ring footings on cohesionless soil under eccentric load. *Comput Geotech* 92:169–178. <https://doi.org/10.1016/j.compgeo.2017.08.003>

21. Tang C, Phoon KK (2018) Prediction of bearing capacity of ring foundation on dense sand with regard to stress level effect. *Int J Geomech* 18(11):04018154. [https://doi.org/10.1061/\(ASCE\)GM.1943-5622.0001312](https://doi.org/10.1061/(ASCE)GM.1943-5622.0001312)
22. Zhao L, Wang JH (2008) Vertical bearing capacity for ring footings. *Comput Geotech* 35(2):292–304. <https://doi.org/10.1016/j.compgeo.2007.05.005>

Chapter 4

Comparative Study of Geotechnical Design of Foundations as Per Indian Standards and Eurocode 7



V. S. Sowmiyaa

Introduction

Various series of Indian Standards were formulated on design and construction of different types of foundations. IS 1904 gives general requirements of design and construction of foundation in soils. IS 1080 covers design and construction of spread foundations (strip and pad). IS 2950 covers spread foundations (raft). IS 12070 gives guidelines for the design and construction of shallow foundations on rocks. The design and construction of pile foundations in soil such as driven cast in-situ piles and bored cast in-situ piles are covered in IS 2911 (Part 1/Sec 1 & 2). IS 2911 Part 4 provides procedure and guidelines for pile load tests.

The purpose of foundation design is to propose the foundation dimensions such as length, breadth, thickness and embedment depth of foundation within the soil or rock stratum so that the net loading intensity on the foundation does not exceed the allowable bearing capacity. The allowable bearing capacity is the net capacity of the foundation required to resist shearing failure and settlements without exceeding allowable limits. IS 6403 covers the determination of bearing capacity of shallow foundations. IS 8009 covers methods of calculation of settlements of shallow foundations subjected to symmetric static vertical loading. IS 8009 (Part 2) covers calculation of settlements of deep foundations subjected to symmetrical static vertical loading. The verification of safe bearing capacities can be done by field tests like plate load tests (for spread foundation) and pile load tests (for pile foundation). IS 1888-1982 (Reaffirmed) covers the method of load tests on soils. IS 2911 (Part 4)-2013 covers load test on piles.

Eurocodes comprises ten basic codes starting from 0 to 9 covering various disciplines to design like structural design of concrete, timber, aluminum, steel structures,

V. S. Sowmiyaa (✉)
L&T Construction Heavy Civil Infrastructure IC, Chennai, India
e-mail: sowmiyaa.s1@lntecc.com

geotechnical design and designs for resisting earthquakes. BS EN 1997 also known as Eurocode 7 or simply EN 7 comprises of geotechnical design with two parts: Part 1 deals with general rules, and Part 2 deals with ground investigation and testing. The scope of this paper is limited to EN 7 Part 1.

EN 7 method of design is a limit state design method. The limit states are broadly categorized as ultimate limit state (ULS) and serviceability limit state (SLS). ULS is associated with collapse, structural failure, excessive deformation or loss of stability of the whole structure or any part of it. SLS corresponds to conditions beyond which specified service requirements are no longer met. EN7 deals with five different ultimate limit states such as EQU, STR, GEO, UPL, HYD.

STR and GEO are the most important ultimate limit states for spread and pile foundation design.

Both the limit states ULS and SLS shall be checked from the following methods.

1. Design based on calculation

Design based on calculation involves definition of actions, ground properties, geometry, deformations and resistances values. In EN 7, every geotechnical problem is considered as design situations and selected as per clause 2.2 of the EN 7. Actions/Loads like dead loads and imposed loads from superstructure, surcharges, soil weight, water weight, earth pressures, ground excavation and traffic loads. Calculation models can be analytical, semi-empirical or numerical model.

As per EN 7, the characteristic value is defined as the cautious estimate of the value affecting the occurrence of the limit state. Characteristic values for loads or actions, geotechnical parameters and geometrical data should be estimated based on relevant Eurocodes. The design values of loads/actions and geotechnical parameters are estimated from characteristic values by applying partial factors as defined in Annex A of EN 7 Part 1 or as set by National Annex of EN 7. Design value of geometric data can be derived from nominal values as given in EN 1990: 2002.

Design Approaches (STR/GEO): EC7 consists of three design approaches which uses different partial factors. The partial safety factors are grouped into A (actions and effect of actions), M (for geotechnical parameters) and R (for resistances).

Table 4.1 gives summary of design approaches and combination of partial factors.

In case of SLS, the partial factors taken as 1.0.

Table 4.1 Design approaches as per EC7

Design approach	Combination of partial factors
Design approach 1	Combination 1: A1 “+” M1 “+” R1 Combination 2: A2 “+” M2 “+” R1
Design approach 2	Combination: A1 “+” M1 “+” R2
Design approach 3	Combination: (A1* or A2 [†]) “+” M2 “+” R3

*On structural actions

†On geotechnical actions

2. **Design based on Prescriptive Measures:** This involves adopting conventional, conservative rules of design with specifications and control of materials, workmanship, protection and maintenance works.
3. **Load Tests and Tests on Experimental Model:** Load tests on small/large scale model can be used as a justification of design by giving consideration for differences in ground condition between test and actual construction, time effects and scale effects.
4. **Design based on Observational method.** Before start of construction, acceptable limits of behavior shall be established. A suitable instrumentation and monitoring plan shall be devised to check the behavior within the acceptable limits. Proper plan of contingency measures to be adopted if the behavior is beyond the acceptable limits.

Design Examples

Design of Spread Foundation (Design by Calculation)

A spread foundation of size $2\text{ m} \times 2\text{ m}$ with 0.5 m thick rests on a bearing stratum of very dense sand with friction angle 36° . The bulk unit weight of the soil is 18 kN m^{-3} . The permanent and variable action/loads are found to be 400 kN and 400 kN , respectively. The safety factors for spread foundations as per EN7 and global safety factor as per IS 6403 are summarized in Table 4.2.

The estimated loads/actions, effect of actions like design bearing pressure and soil parameters and the resistances after applying partial factors are listed in Table 4.3. In Design Approach 1, Combination 1, actions alone are factored while the ground conditions and resistances are unfactored making it the most optimistic approach and gives higher bearing resistance. In Design Approach 1, Combination 2 ground properties alone are factored. In Design Approach 2, actions and resistances are factored, whereas ground is not factored. In Design Approach 3, both actions and ground properties are factored making it the most conservative approach out of all 3. As per IS 6403 with overall factor of safety the bearing resistance is found to be very less and more conservative than EN 7. The utilization factor, i.e., ratio of design bearing pressure and design bearing resistance (q_{Ed}/q_{Rd}) is found to be in the range of 71–85% as per IS Method, whereas the ratio is found to be in the range of 25–58% as per EN Method. Thus EN 7 approach is found to be more economical design compared to IS Method. Among EN 7 three design approaches, Design Approach 1 Combination 1 is more optimistic design and Design Approach 3 is relatively conservative design.

Table 4.2 Safety factors for design of spread foundation as per EN 7, IS 6403

Partial factor as per EN 7		Design approaches				
Actions (A)		DA 1		DA2 (A1)	DA3	
		C1(A1)	C2 (A2)		Strut (A1)	Geo (A2)
Permanent, γ_G	Unfavorable	1.35	1.0	1.35	1.35	1.0
	Favorable	1.0	1.0	1.0	1.0	1.0
Variable, γ_Q	Unfavorable	1.5	1.3	1.5	1.5	1.3
	Favorable	0	0	0	0	0
Soil Parameters (M)		(M1)	(M2)	(M1)		(M2)
Angle of shearing resistance		1.0	1.25	1.0	1.25	
Effective cohesion		1.0	1.25	1.0	1.25	
Undrained shear strength		1.0	1.4	1.0	1.4	
Unconfined strength		1.0	1.4	1.0	1.4	
Weight density		1.0	1.0	1.0	1.0	
Resistances (R)		(R1)	(R1)	(R2)	(R3)	
Bearing resistance		1	1	1.4	1.0	
Sliding resistance		1	1	1.1	1.0	
Global Safety Factors as IS 6403						
As per clause 6.3, net ultimate bearing capacity shall be divided by a suitable factor of safety				FOS = 2.5–3 (generally recommended)		

Table 4.3 Actions, soil parameters and resistances as per EN 7 & IS 6403 for design of spread foundation

Parameters	EN 7 (by partial factors)				IS 6403 (by global factors)	
Design actions V_d (kN)	A1		A2		FOS = 1.5	
	1345		1082		1200	
Effect of actions, q_{Ed} Design bearing pressure, (kN/m ²)	A1		A2		300	
	302		243			
Soil parameters, Design friction angle, ϕ_d , degrees	M1		M2		36	
	36		30.2			
Resistances, q_{Rd} Design resistance, kN/m ²	DA1 Comb 1	DA1 Comb 2	DA2	DA3	FOS = 2.5	FOS = 3.0
	1212	513	866	513	352	422
Utilization factor (q_{Ed}/q_{Rd}) %	25	58	28	47	85	71

Design of Spread Foundation on Rock

A 5 m wide square footing to be built in a moderately weathered and moderately strong weathered basalt rock. The dry density of the rock is found to be 25.51 kN/m³ and the uniaxial compressive strength of rock (UCS) is found to be 35.3 MPa. The joint spacing is found to be 300 mm.

Design by Prescriptive Method as per EN 7: The type of rock is first grouped as per Table G.1 of EN 7. The rock considered for the study falls under group 2. Based on the UCS of rock 35.3 MPa and the spacing of discontinuities, the bearing resistance of rock is estimated from Figure G-1 of EN 7 (reproduced in Fig. 4.1). For Group 2 rock with UCS 35.3 MPa and spacing of discontinuities 300 mm, the allowable bearing resistance of rock is found to be around 10 MPa.

Design as per IS 12070: The safe bearing pressure is given by the equation:

$$q_s = q_c * N_j \text{ as per clause 6.2 of IS 12070.}$$

where,

q_c Uniaxial compressive strength, MPa.

N_j Empirical coefficient depending on spacing of discontinuities.

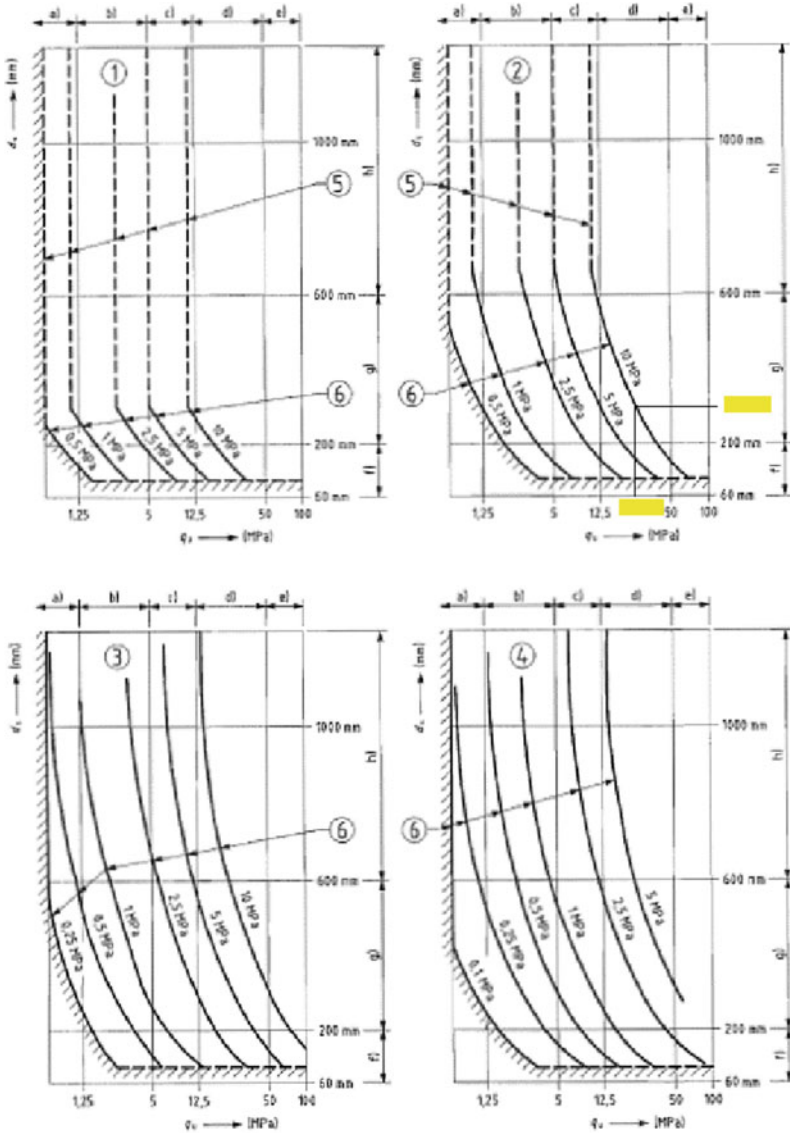
N_j 0.25 for 300 mm spacing of discontinuities.

Considering fully submerged condition, as per clause 9.2 of IS 12070, an allowance of 0.75 (3/4) is considered. The safe bearing pressure thus works out to 6.62 MPa. The summary of safe bearing resistance based on both EN 7 and IS 12070 is summarized in Table 4.4.

IS 12070 gives a more realistic value of bearing resistance compared to EN 7. IS 12070 considers spacing of discontinuities, allowances for water table, cavities and orientation of joints along with a global factor of safety of 3. However, EN 7 approach of prescriptive method using presumed bearing pressure considers broad grouping of rocks based on rock type and bearing resistance based on spacing of discontinuities. This presumed bearing pressure approach as per EN 7 can be used only as an indicative or preliminary design of bearing resistance of rock.

Pile Design by Pile Load Tests

Four numbers of initial vertical pile load tests TP1 to TP4 were conducted on 1500 mm diameter bored cast in-situ piles of length 30 m for a bridge project. The ultimate test load on the piles is 20,000 kN. The subsoil conditions at the initial test pile locations are given in Fig. 4.2. The load versus settlement curves of the initial vertical load tests are plotted in Fig. 4.3.



Abscissa: q_u (MPa); uniaxial compressive strength Ordinate: d_i (mm) discontinuity spacing
 1 Group 1 rocks, 2 Group 2 rocks, 3 Group 3 rocks, 4 Group 4 rocks,
 5 Allowable bearing pressure not to exceed uniaxial compressive strength of rock if joints are tight or 50 % of this value if joints are open,
 6 Allowable bearing pressures: a) very weak rock, b) weak rock c) moderately weak rock d) moderately strong rock, e) strong rock
 Spacings: f) closely spaced discontinuities g) medium spaced discontinuities h) widely spaced discontinuities

Fig. 4.1 Estimation of bearing resistance for spread foundation on rock (Figure G.1 of EN 7)

Table 4.4 Estimation of bearing resistance of spread foundation on rock

Method	Allowable bearing capacity, MPa
As per IS 12070	Safe bearing capacity = 6.62 MPa
As per EN 7	Allowable bearing capacity \approx 10 MPa

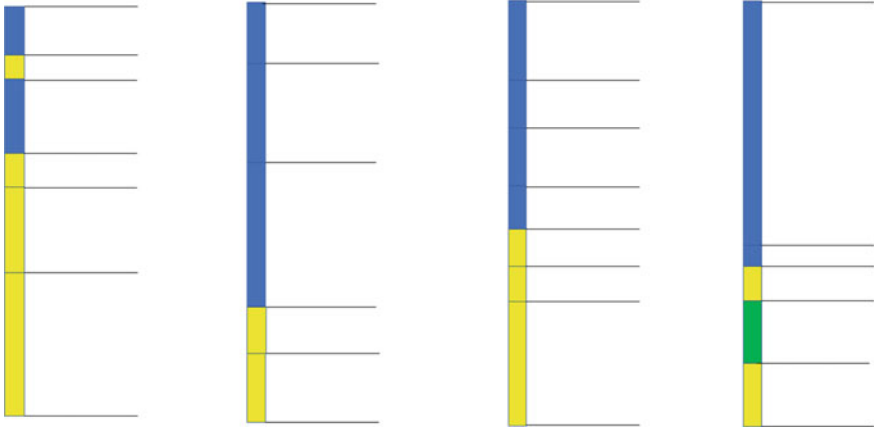
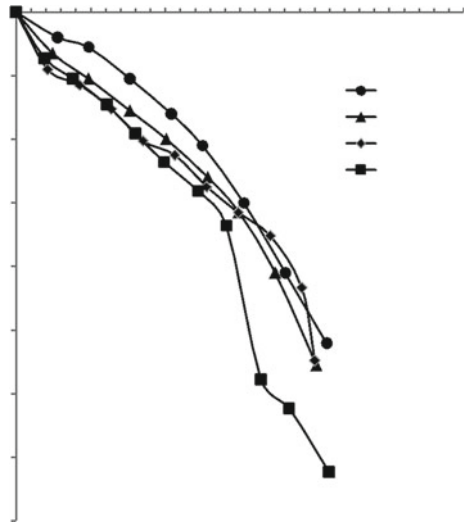


Fig. 4.2 Subsoil profile at initial test pile

Fig. 4.3 Load versus settlement curves of initial vertical pile load tests



The safe pile capacities are estimated as per IS 2911 Part 4 2013 for the initial test piles TP1 to TP4 and are summarized in Table 4.5.

Table 4.5 Safe pile capacity from pile load test and theoretical pile capacity (IS 2911 Part 4 & IS 2911 Part 1)

Test pile ID	2/3rd of final load, kN	Settlement at 2/3rd of final load, mm	50% of final load, kN	Settlement at 50% of final load, mm	Safe pile capacity, kN	Theoretical pile capacity, kN
TP1	13,880	5.1	10,410	3.2	10,410	10,146
TP2	13,413	5.5	10,060	4	10,060	10,760
TP3	13,333	5.7	10,000	4.36	10,000	10,657
TP4	13,978	6.6	10,484	4.95	10,484	10,781

As per EN 7, the ultimate capacity from pile load test is considered as maximum test load at which settlement is less than 10% of pile diameter. This involves determination of characteristic resistance $R_{c;k}$. $R_{c;k}$ is derived from R_{mean} (mean resistance from a number of load tests) and R_{min} (minimum resistance from a number of load tests). ξ_1 and ξ_2 are the correlation factors depending on the number and type of tests. The design resistance $R_{c;d}$ is then determined by applying partial safety factors based on the design approach as given in Table 4.6. Design Approach 3 is not applicable for design based on load test. The correlation factors as listed in Table A.9 of EN 7 are taken based on number of test piles. The estimation of safe pile capacity as per EN 7 from pile load test results is summarized in Table 4.6.

The average design pile capacity based on four initial test piles as per IS 2911 Part 4 is around 10,238 kN, whereas the average design pile capacity as per EN 7 is around 16,555 kN. The design capacity as per IS 2911 is more conservative than EN 7. The design pile capacity based on pile load test as per EN 7 is found to be 62% higher than IS 2911 Part 4 method. Thus, EN 7 is found to be more optimistic and economical for pile design based on static pile load tests.

Table 4.6 Safe pile capacity from pile load test as per EN 7

Determination of safe pile capacity as per EN7	
Mean ultimate pile capacity, $R_{c;mean}$ (average ultimate capacity from TP1 to TP4)	20,477 kN
Minimum ultimate pile capacity, $R_{c;min}$	20,000 kN
No of pile load tests	4 nos
Correlation factors	$\xi_1 = 1.1$ $\xi_2 = 1.0$
Characteristic pile capacity, $R_{c;k}$	18,615 kN
Partial safety factor, γ_t (from table A-7 of EN 7)	
R1—DA1 Comb 1 and Comb 2	1.15
R2—DA2	1.1
Design pile capacity, $R_{c;d}$ (Design approach 1 Comb 1 & 2)	16,187 kN
Design pile capacity, $R_{c;d}$ (design approach 2)	16,923 kN

Summary and Conclusions

An attempt has been made to compare the Indian Standards and EN 7 standard guidelines for the geotechnical design of foundations. Indian Standards of design involves the estimation of bearing capacity using bearing capacity equations with a suitable overall global factor of safety. EN 7 uses different design approaches by using partial factors for actions and its effect, ground properties and the bearing resistances. Eurocode 7 suggests four methods of foundation design. The conclusions based on the current study is listed below:

1. An example of spread foundation on soil is considered and the design methodology and design output are compared with IS 6403 & EN 7 approach. The utilization factor is found to be in the range of 71–85% as per IS Method and in the range of 25–58% as per EN Method. Thus, EN 7 partial factor approach is found to be more realistic and economical design compared to IS Method. Among three design approaches of EN 7, Design Approach 1 Combination 1 derives more optimistic bearing resistance and Design Approach 3 is relatively conservative design.
2. An example of prescriptive method of design approach as per EN 7 is considered for spread foundation design on rock and compared with IS 12070 Method. IS 12070 gives a more realistic value of bearing resistance compared to EN 7. IS 12070 considers spacing of discontinuities, allowances for water table, cavities, orientation of joints along with application of global factor of safety of 3. However, EN 7 approach of prescriptive method using presumed bearing pressure considers broad grouping of rocks based on rock type and estimation of bearing resistance based on spacing of discontinuities. This presumed bearing pressure approach as per EN 7 can be used only as an indicative or preliminary design for estimation of bearing resistance of rock.
3. Pile foundation design based on four pile load test results is considered and compared with IS 2911 Part 4 approach and EN 7 approach. The design capacity as per IS 2911 is more conservative than EN 7. The design pile capacity based on pile load test as per EN 7 is found to be 62% higher than IS 2911 Part 4 method. Thus, EN 7 is found to be more optimistic and economical.

References

1. IS 1904 (1986: Reaffirmed 2006) Code of practice for design and construction of foundations in soils: general requirements. Bureau of Indian Standards, New Delhi
2. IS 6403 (1981: Reaffirmed 2002) Code of practice for determination of bearing capacity of shallow foundations. Bureau of Indian Standards, New Delhi
3. IS 8009 (1976: Reaffirmed 2003) Code of practice for calculations of settlement of foundations part 1: shallow foundations subjected to symmetrical static vertical loads. Bureau of Indian Standards, New Delhi

4. IS 8009 (1980: Reaffirmed 2006) Code of practice for calculations of settlement of foundations part 2: deep foundations subjected to symmetrical static vertical loading. Bureau of Indian Standards, New Delhi
5. IS 2911 (2010) Design and construction of pile foundations—code of practice, part 1: concrete piles, section 1: driven cast in-situ concrete piles. Bureau of Indian Standards, New Delhi
6. IS 2911 (2010) Design and construction of pile foundations—code of practice, part 1: concrete piles, section 2: bored cast in-situ concrete piles. Bureau of Indian Standards, New Delhi
7. IS 2911 (2010) Design and construction of pile foundations—code of practice, part 4: load test on piles. Bureau of Indian Standards, New Delhi
8. IS 12070 (1987: Reaffirmed 2010) Code of practice for design and construction of shallow foundations on rocks. Bureau of Indian Standards, New Delhi
9. EN 1997 (1) Eurocode 7: geotechnical design—part 1: general rules [Authority: The European Union Per Regulation 305/2011, Directive 98/34/EC, Directive 2004/18/EC]

Chapter 5

Parametric Study of the Behavior of Large Piled Raft Foundation on Stiff Clay



Rajib Modak and Baleshwar Singh

Introduction

A piled raft is a compound structure comprising of raft, piles and subsoil. Unlike typical foundation design, in which loads are carried by the raft or by piles, the piled raft design considers both raft and piles contribution in load sharing [8, 9]. The raft shares the overcoming load employing raft–soil contact pressure and piles through friction and end bearing. The piled raft behavior is controlled by complex interactions between pile–soil, pile–pile, raft–soil and pile–raft [7]. Based on the pile and raft dimensions, the piled rafts are categorized as ‘small’ and ‘large’ piled rafts [18]. For small piled raft ($B_r/L < 1$), piles are added to provide sufficient bearing capacity and reduce average settlements, whereas, in the large piled raft ($B_r/L > 1$), piles are added essentially to minimize settlements and raft bending moments.

Poulos [14] proposed a three-stage design process for piled rafts and indicated that for the piled raft design on clayey soil, three-dimensional (3D) numerical modeling is the most reliable method. Also, it was suggested that soil profiles consisting of stiff clay are generally favorable for the application of piled rafts. Sanctis et al. [3] have offered some guidelines for optimum piled raft design. Maharaj [12] performed 3D analyses to understand the pile length and soil modulus effect on the piled raft behavior. It was reported that the piled raft ultimate capacity increased with increase in pile length and soil modulus. Maharaj and Gandhi [13] examined the behavior of piled raft when it is loaded up to failure. It was observed that the piles reached their ultimate capacities earlier than raft in the piled raft. Reul and Randolph [17]

R. Modak (✉) · B. Singh

Department of Civil Engineering, Indian Institute of Technology Guwahati, Guwahati 781039, India

e-mail: rmodak@iitg.ac.in

B. Singh

e-mail: baleshwar@iitg.ac.in

conducted a study to optimize piled rafts with non-uniform loading in the vertical direction. Several researchers have investigated the bearing [4, 10, 16] and settlement behavior [2, 15] of piled rafts in clayey soil through numerical modeling. Lee et al. [11] analyzed the nonlinear load sharing behavior as a settlement function for piled rafts found in clayey soil.

However, few parametric studies have been reported that evaluated the effect of various parameters on the large piled raft behavior founded on stiff clays through numerical modeling. In addition to that, few studies have addressed the structural response of the raft in large piled rafts in terms of bending moment. Thus, the present paper intends to understand the pile number, pile length, pile spacing and thickness of raft effect on the differential and average settlements, load sharing and raft's bending moment in large piled raft founded on stiff clay. To achieve the objectives, a series of numerical simulations were performed. The results presented can be used for the efficient and economical design of piled rafts on stiff clay.

Numerical Modeling

Meshing and Boundary Conditions

Finite element software PLAXIS 3D [1] has been selected for carrying out the numerical analyses. The meshing of the soil domain and the structural elements is presented in Fig. 5.1. The present study focused on understanding the piled raft behavior under drained conditions, and thereby, the long-term behavior of soil was considered. At the ground surface with hydrostatic pressure distribution, the water table is assumed, thus neglecting the effects of consolidation. The boundaries of the soil domain were reasonably large to avoid any boundary effects. In lateral directions, it was extended up to two times the raft width from the raft edges, with vertical movement being allowed and horizontal movement was restrained. The vertical boundary was set at four times the pile length distance from the base of raft and was restrained against both horizontal and vertical movements. In all directions, the ground surface was kept free. To identify the optimum mesh size, a convergence study was carried out and 'Fine' mesh with a relative element size of 0.7 has been adopted to model the soil domain. Nearby the raft and piles, finer mesh was generated by applying local mesh refinement.

Constitutive Modeling

Elastoplastic soil behavior was modeled using the soil material model. The Hardening model incorporates shear and compression hardening, occurring because of primary

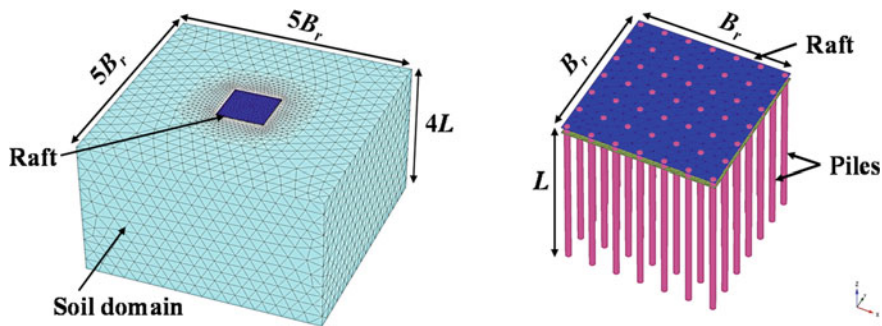


Fig. 5.1 Meshing of the soil domain and the structural elements

deviatoric loading and due to primary compression and isotropic loading, respectively. In Hardening Soil model, three parameters are required as input compared to a single parameter in the Mohr–Coulomb model to represent the elastic soil deformation. The three input parameters are the secant stiffness modulus (E_{50}^{ref}) from drained triaxial test (Eq. 5.1), nonlinear unloading/reloading stiffness modulus ($E_{\text{ur}}^{\text{ref}}$) (Eq. 5.2) and tangent stiffness modulus ($E_{\text{oad}}^{\text{ref}}$) from the oedometer test. All the stiffness modulus corresponds to 100 kPa (p^{ref}) reference stress level.

$$E_{50} = E_{50}^{\text{ref}} \left(\frac{c' \cot \phi' + \sigma_3'}{c' \cot \phi' + p^{\text{ref}}} \right)^m \quad (5.1)$$

$$E_{\text{ur}} = E_{\text{ur}}^{\text{ref}} \left(\frac{c' \cot \phi' + \sigma_3'}{c' \cot \phi' + p^{\text{ref}}} \right)^m \quad (5.2)$$

where E_{50} is primary loading stiffness modulus for; E_{ur} is unloading and reloading stiffness modulus; c' and ϕ' are the shear strength parameters; and m is the stress dependency factor.

Tetrahedral elements with 10-node were used for modeling the soil. Linear-elastic behavior of the raft and piles was considered as their elastic modulus is significantly greater than the modulus of soil. Rigid connection between piles and raft was considered. Modeling of raft was done as plate elements (6-node triangular) and the piles as embedded beam elements (3-node). To incorporate the interaction between pile and soil, embedded beam elements use special interface elements. The pile–soil interface was considered rigid ($R_{\text{inter}} = 1$), which indicates no strength reduction of the interface compared to the surrounding soil.

Model Validation

The validation of the present study in PLAXIS 3D was done by comparing with the results reported by Cho et al. [2] using the Mohr–Coulomb soil model in ABAQUS. A raft with dimensions of 10 m × 10 m and 1 m thick and piles 0.5 m diameter with pile length varying from 8–20 m was considered. The pile spacing considered was thrice the pile diameter, and over the entire raft area 55 MN load was applied uniformly. The properties of the materials used are given in Table 5.1. Figure 5.2 shows the results of the comparative study. The results obtained from PLAXIS 3D are in good agreement with those reported by Cho et al. [2]. However, in this paper, the Hardening Soil model has been used.

Table 5.1 Material properties for validation [2]

	Clay (stiff)	Bearing layer	Raft	Piles
Elasticity modulus, E' (MPa)	45	500	30,000	12,500
Cohesive strength, c' (kPa)	20	0.1	–	–
Angle of friction, ϕ' (°)	20	45	–	–
Poisson's ratio, ν'	0.3	0.3	0.2	0.25
Total unit weight, γ_t (kN/m ³)	19	20	25	25

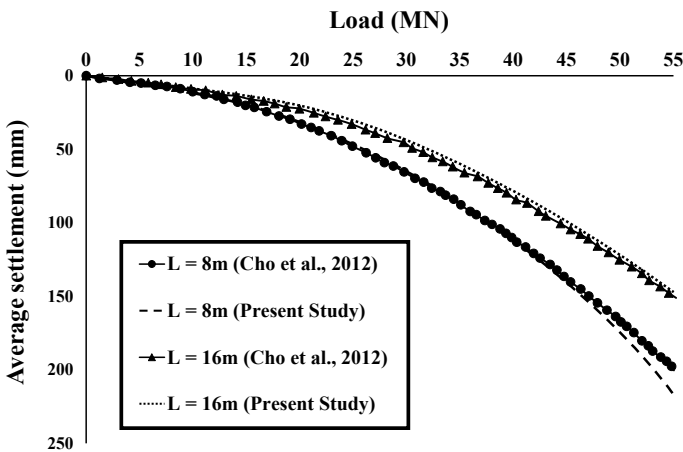


Fig. 5.2 Load–settlement behavior of PLAXIS 3D compared with results reported by Cho et al. [2]

Parametric Study

Numerical analyses are performed on piled rafts having different parameters, as shown in Table 5.2. The raft of 38 m × 38 m size, considered in the present study, has been selected from Reul and Randolph [17]. Table 5.3 shows the properties of the raft, pile and soil for this study. The Hardening Soil material input parameters for stiff clay are taken from Engin and Brinkgreve [5], and the raft and pile properties are selected from Reul and Randolph [17].

The pile number (n_p) is varied from 25 to 169 piles, ensuring the area enclosed by the pile group (A_g), measured from the center of the outermost piles, is the same

Table 5.2 Geometric configurations of piled raft

Parameters	Values
Width of raft, B_r (m)	38
Thickness of raft, t (m)	1, 2*, 3
Length of pile, L (m)	10, 20, 30*
Diameter of pile, D (m)	1
Number of piles, n_p	25, 49*, 81, 121, 169
Spacing between piles, s (m)	3, 4, 5, 6*
Area ratio corresponding to each pile spacing, A_g/A_r	0.2, 0.4, 0.6, 0.9*

*Standard value if not varied

Table 5.3 Material properties

Materials	Properties	Values
Soil	Unit weights $\gamma_{unsat}/\gamma_{sat}$ (kN/m ³)	20/20
	Ref. secant stiffness, E_{50}^{ref} (kN/m ²)	3.5×10^4
	Ref. oedometer stiffness, E_{oed}^{ref} (kN/m ²)	4.28×10^4
	Ref. stiffness for unloading reloading, E_{ur}^{ref} (kN/m ²)	1.05×10^5
	Stress dependency factor, m	1
	Poisson's ratio, ν_s	0.2
	Cohesive strength, c' (kN/m ²)	20
	Angle of friction ϕ' (°)	20
	Coefficient for lateral earth pressure (K_o)	0.8
Raft	Elasticity modulus, E_r (MN/m ²)	34,000
	Unit weight (kN/m ³)	25
	Poisson's ratio, ν_r	0.2
Piles	Elasticity modulus, E_p (MN/m ²)	30,000
	Unit weight (kN/m ³)	25
	Poisson's ratio, ν_p	0.2

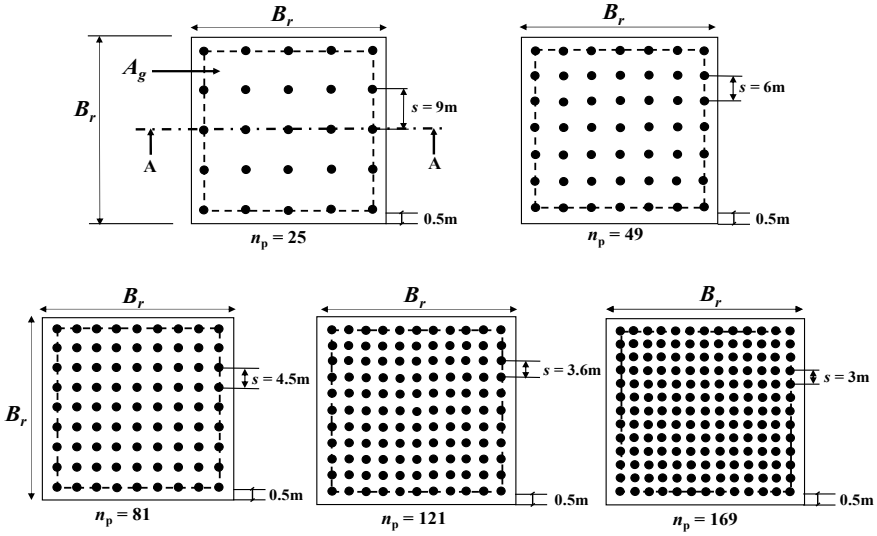


Fig. 5.3 Piled raft configurations

for all piled raft configurations as given in Fig. 5.3. The length of pile (L) is varied between 10 and 30 times the diameter (D) of pile. For the same number of piles, the pile spacings (s) are adopted such that the area ratio, i.e., the ratio of area enclosed by the group of piles (A_g) to the entire raft area (A_r), varied between 0.2 and 0.9. The thickness of the raft is varied to ensure that its stiffness changes from flexible to intermediate and to rigid, depending on the raft–soil stiffness ratio. All the piled rafts are subjected to a load of 300 kPa, applied over entire raft area.

Results in terms of the average and differential settlement are evaluated as per Eq. 5.3 [17] and Eq. 5.4 [2]. For both average (s_{avg}) and differential (s_{diff}) settlements, the raft’s center (s_{center}) and corner (s_{corner}) settlements are evaluated. As shown in Fig. 5.3, the bending moment is evaluated at the raft center, at section A-A, for all the configurations of the piled raft. For comparison of raft bending moment piled raft, an unpiled raft of size 38 m \times 38 m and 2 m thickness is considered. The load sharing behavior was represented as piled raft coefficient (α_{pr}). It is the ratio of load the piles carry (Q_p) to the total load (Q_{pr}) subjected on the piled raft (Eq. 5.5). $\alpha_{pr} = 0$ represents an unpiled raft whereas, $\alpha_{pr} = 1$ indicates a piled foundation. For piled rafts, piled raft coefficient range $0 < \alpha_{pr} < 1$. In the piled raft, the total load the piles carry is evaluated by adding the axial loads at each pile head.

$$s_{avg} = \frac{1}{3}(2s_{center} + s_{corner}) \tag{5.3}$$

$$s_{diff} = (s_{center} - s_{corner}) \tag{5.4}$$

$$\alpha_{pr} = \frac{Q_p}{Q_{pr}} \quad (5.5)$$

Results and Discussion

Effect of Pile Number

The pile numbers effect n_p (25, 49, 81, 121 and 169) on the large piled raft behavior in terms of average and differential settlement is shown in Fig. 5.4a, b. A decrease in both average and differential settlement was noted with an increase in pile number. However, the decrease rate of both the settlements beyond 81 piles becomes minimal. There is a decrease from 83 to 54 mm in average settlement and further to 43 mm, with pile number increasing from 25 to 49 and further 81, respectively. From 81 to 121 piles, the average settlement decreases only by 3 mm. Similarly, the differential settlement also decreases marginally by 3 mm with the increase in the pile number from 81 to 121 piles. A similar result has also been reported by Poulos [14]. Figure 5.4c shows the pile number effect on the raft bending moment. As pile number increases, the raft bending moment decreases; however, the decrease rate is marginal beyond 81 piles. The decrease in the bending moments is due to the increase in pile support underneath the raft, with the increase in pile number. It is noted that at the locations where piles are present, the raft moments sag, and at the raft spans, it peaks. Compared to an unpiled raft, the addition of piles does not prove advantageous in reducing bending moments. The pile number effect (Fig. 5.4d) on the load sharing behavior is shown in terms of piled raft coefficient. With the increment in pile number, the piled raft coefficient increase; however, the increase rate is minimal beyond 81 piles.

Effect of Pile Spacing

The pile spacing effect on piled raft behavior is given in Fig. 5.5. A piled raft with 7×7 piles has been considered to understand the pile spacing effect. The spacings, s (3, 4, 5 and 6 m) considered in the study varied the area ratio (A_g/A_r) from 0.2 to 0.9. A decrease in the average settlement can be observed from Fig. 5.5a with increase in the spacing between piles. The reduction is due to the uniform pile support over the entire raft area as the pile spacing increases. However, the reduction in the average settlement is minimal past 5 m pile spacing. From 5 to 6 m increase in spacing, the reduction in the average settlement is only 2.5 mm. The differential settlement, as shown in Fig. 5.5b, initially reduced and then increased as the pile spacing increased. The differential settlement at 5 m pile spacing is minimum. Thus

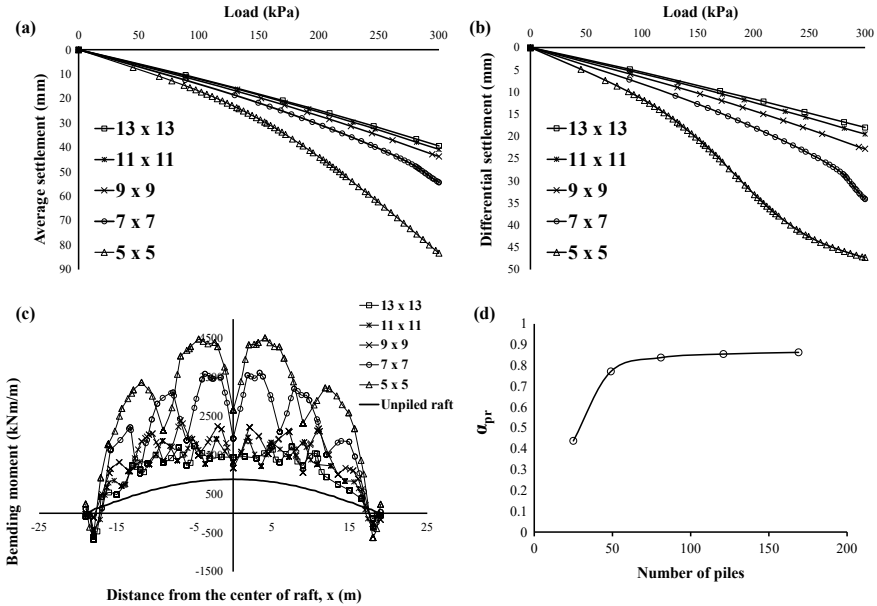


Fig. 5.4 Effect of pile number on the large piled raft behavior

adopting a pile spacing beyond 5 m may not be beneficial for minimizing both average and differential settlements. The pile spacing effect on the bending moment of the raft is shown in Fig. 5.5c. The behavior of the raft in piled raft changes from hogging (negative bending moments) to sagging (positive bending moments) with increased pile spacing. The piles are placed at the central portion of the raft for smaller pile spacing, and hence, adequate pile support over the entire raft area is not provided to carry the overcoming uniformly distributed load. Due to this reason, the raft tends to hog (structurally less stable) at smaller pile spacing. However, at larger pile spacing, adequate pile support is provided over the entire raft area. The raft bending moment is minimum and close to an unpiled raft bending moment at 5 m pile spacing. Figure 5.5d shows that as the spacing increase, the piled raft coefficient increases. Lower values of piled raft coefficient are observed at smaller pile spacing due to lesser mobilization of pile frictional resistance.

Effect of Pile Length

For understanding the pile length effect, a 7×7 piled raft configuration, with piles having 10, 20 and 30 m length and spaced at 6 m, has been considered. The average settlement decreases with increased pile length, as shown in Fig. 5.6a. This is because of the increase in pile frictional resistance with the increasing length of the pile. The

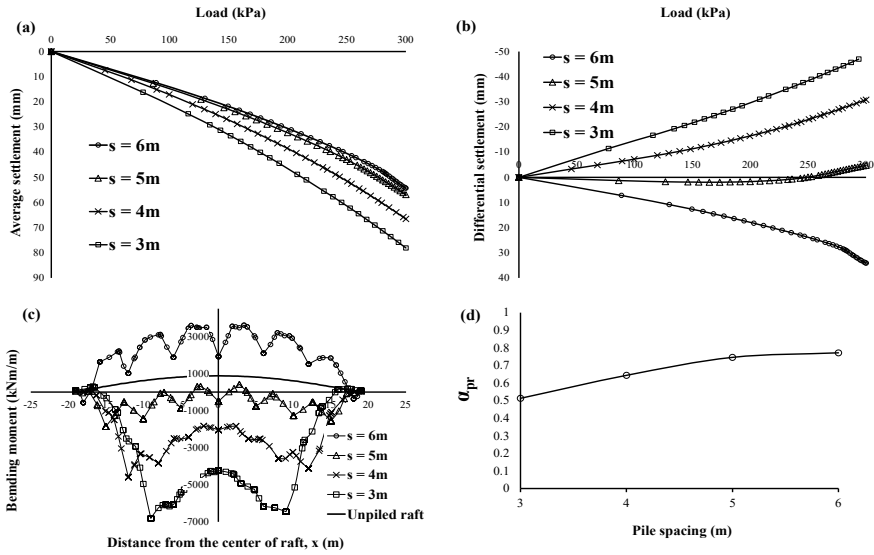


Fig. 5.5 Effect of pile spacing on the large piled raft behavior

differential settlement, as shown in Fig. 5.6b, doesn't vary consistently with the increasing pile length. The differential settlement depends on the intensity of load applied on the piled raft. At lower load level (up to 125 kPa), differential settlement is minimum for 30 m pile length and maximum for 10 m length pile, whereas, at greater level of load, the differential settlement is least for 10 m length. The effect of length on the bending moment of raft is given in Fig. 5.6c. The bending moment is minimum for 10 m pile length. However, compared to an unpiled raft, the bending moments are higher for piled rafts. Piled raft coefficient increases linearly as the pile length increases, as shown in Fig. 5.6d. The piled raft coefficient increases because of the increased frictional resistance with the longer length of the piles.

Effect of Raft Thickness

A 7×7 configuration piled raft with 30 m length piles and spaced at 6 m has been considered to understand the raft thickness effect. The raft thickness was varied to ensure that its stiffness changes from flexible to intermediate and to rigid. For estimating the raft's stiffness, the raft-soil stiffness ratio (K_{rs}) is evaluated as per Eq. 5.6 [6], where E_s and E_r are the soil and raft Young's modulus, respectively. $K_{rs} < 0.01$ indicates a fully flexible raft, K_{rs} value in the range 0.1–1 indicates a raft having intermediate flexibility, and for $K_{rs} > 1$, it indicates a rigid raft. 1 m, 2 m and 3 m thick raft are used, with corresponding K_{rs} values of 0.076, 0.61 and 2.06, respectively, in the present study.

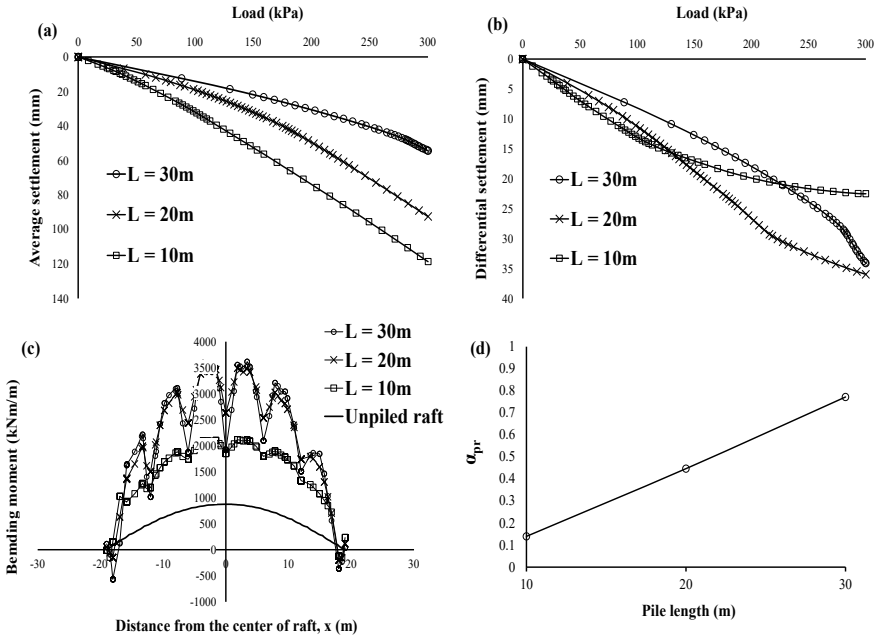


Fig. 5.6 Effect of pile length on the large piled raft behavior

$$K_{rs} = \frac{4E_r(1 - \nu_s^2)}{3E_s(1 - \nu_r^2)} \left(\frac{t}{B_r} \right)^3 \quad (5.6)$$

Figure 5.7a and d show that the raft thickness effect is not that significant for the average settlement and the percentage of load the piles carry. However, as shown in Fig. 5.7b, c, for differential settlement a substantial decrease was noted as the raft thickness increased, but at the cost of higher bending moments. These results are similar to those reported by Poulos [14].

Conclusions

In the present parametric study, numerical analyses were performed to understand the large piled raft behavior on stiff clays. The present study has shown that as the pile number increases, the differential and average settlements and bending moment decrease only up to a certain limit, beyond which the rate of change is minimal. Also, the increase in the percentage of load the piles carry is marginal beyond a certain pile number. The addition of piles does not prove beneficial in reducing the raft bending moments compared to an unpiled raft. Thus, from an economic point

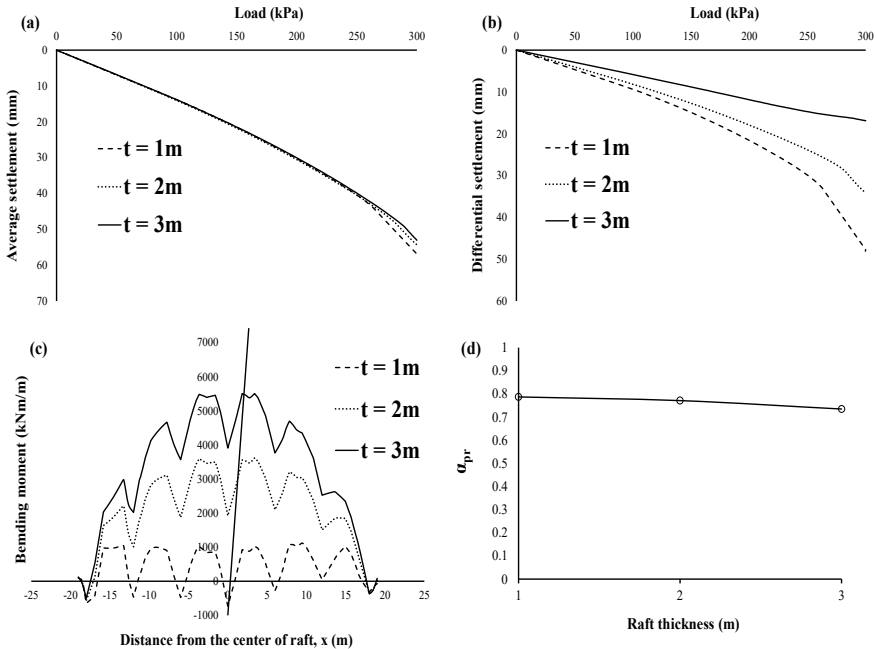


Fig. 5.7 Effect of raft thickness on the large piled raft behavior

of view, including more piles beyond a certain limit may not prove to be beneficial always.

The differential settlement decreases initially and then increases, whereas the average settlement decreases as the pile spacing increases. The behavior of the raft in piled raft changes from structurally less recommendable hogging to sagging with increase in spacing. The percentage of load the piles carry increases as the spacing increase.

As the pile length increases, the average settlement is found to decrease; however, the variation in the differential settlement is inconsistent and depends on the load level. For any length of pile considered, the raft bending moment in piled raft is higher than the unpiled raft. The percentage of load the piles carry increases linearly with increasing pile length. Thus, for an economical design, compromise can be made between pile spacing and pile length based on the requirements of the design criteria.

An increment in raft thickness does not significantly change the average settlement and load sharing behavior; however, the differential settlement decreases, and the bending moment increases with increasing raft thickness. Thus, from an economic point of view, a thinner raft can be suggested such that the raft bending moment is minimum but ensures that the differential settlement is within the permissible limit.

References

1. Brinkgreve R, Swolfs W, Engin E (2015) PLAXIS user's manual, version 6.1. Balkema, Rotterdam, The Netherlands
2. Cho J, Lee JH, Jeong S, Lee J (2012) The settlement behavior of piled raft in clay soils. *Ocean Eng* 53:153–163
3. de Sanctis L, Mandolini A, Russo G, Viggiani C (2002) Some remarks on the optimum design of piled rafts. In: *Deep foundations 2002: an international perspective on theory, design, construction, and performance*, pp 405–425
4. de Sanctis L, Mandolini A (2006) Bearing capacity of piled rafts on soft clay soils. *J Geotech Geoenviron Eng* 132(12):1600–1610
5. Engin HK, Brinkgreve RBJ (2009) Investigation of pile behaviour using embedded piles. In: *Proceedings of the 17th international conference on soil mechanics and geotechnical engineering*, vols 1, 2, 3 and 4. IOS Press, pp 1189–1192
6. Fraser RA, Wardle LJ (1976) Numerical analysis of rectangular rafts on layered foundations. *Geotechnique* 26(4):613–630
7. Katzenbach R, Arslan U, Moormann C (2000) Piled raft foundation projects in Germany. In: Hemsley JA (ed) *Design applications of raft foundations*. Thomas Telford, London, pp 323–392
8. Katzenbach R, Moormann C (2001) Recommendations for the design and construction of piled rafts. In: *International conference on soil mechanics and geotechnical engineering*, pp 927–930
9. Katzenbach R, Choudhury D (2013) ISSMGE combined pile-raft foundation guideline. Institute and Laboratory of Geotechnics. Technische Universität Darmstadt, Germany
10. Lee J, Kim Y, Jeong S (2010) Three-dimensional analysis of bearing behavior of piled raft on soft clay. *Comput Geotech* 37(1–2):103–114
11. Lee J, Park D, Choi K (2014) Analysis of load sharing behavior for piled rafts using normalized load response model. *Comput Geotech* 57:65–74
12. Maharaj DK (2003) Load settlement behavior of piled raft foundation by three dimensional non-linear finite element analysis. *Electron J Geotech Eng* 8:1257–1263
13. Maharaj DK, Gandhi SR (2004) Non-linear finite element analysis of piled-raft foundations. *Proc Inst Civ Eng-Geotech Eng* 157(3):107–113
14. Poulos HG (2001) Piled raft foundations: design and applications. *Geotechnique* 51(2):95–113
15. Prakoso WA, Kulhawy FH (2001) Contribution to piled raft foundation design. *J Geotech Geoenviron Eng* 127(1):17–24
16. Reul O (2004) Numerical study of the bearing behavior of piled rafts. *Int J Geomech* 4(2):59–68
17. Reul O, Randolph MF (2004) Design strategies for piled rafts subjected to nonuniform vertical loading. *J Geotech Geoenviron Eng* 130(1):1–13
18. Viggiani C (2001) Analysis and design of piled foundations. First Arrigo Croce Lecture. *Rivista Italiana Di Geotechnica*, pp 47–75

Chapter 6

Estimation of Shaft-Base Initial Stiffness and Ultimate Resistance of O-Cell Piles



Nayakam Venkatesh, Kadali Srinivas, and Madhav Madhira

Introduction

As the development in the construction of high-raised structures is increasing, for these structures to transfer the vertical load into deeper soil strata, a pile foundation is usually adopted. Piles derive their resistance by shaft and base actions when a pile is axially loaded according to these actions piles are classified as end bearing, friction and end-friction pile (combined piles), to estimate the ultimate capacity of these piles normally Kent-load test [1] is adopted in which the load application is from top of the pile which is economical only for marginal loads application but for the high-raised structure which requires high loads for testing of the pile to apply these aloft loads from the surface in the Kent-load form is difficult and uneconomical [2]. To test this type of large bored pile without any difficulty O-cell ring method is adopted nowadays. Osterberg ring (O-cell ring) is developed by Dr. George Osterberg, professor emeritus at Northwestern University. O-cell applies static load in bidirectionally, i.e., upward and downward directions in the form of hydraulic pressure, multiple O-cells can also be used in testing as per load requirement and placing of O-cell in reinforcement cage plays an important role, Lina et al. [3] investigated the placement of O-cell where the incorrect placement of O-cell will lead to failure of the upward or downward segments without reaching its ultimate capacity so the O-cell need to place at a location where the upward shaft capacity must equal to the downward shaft and base capacity not to cause any uncertainties in testing, mainly IS 2911-2015 part 4 [1] is adopted for testing of piles to estimate the ultimate capacity and allowable settlement of piles and for construction guidelines

N. Venkatesh (✉) · K. Srinivas · M. Madhira
VNR Vignana Jyothi Institute of Engineering and Technology, Hyderabad 500090, India
e-mail: venkateshpatel7320@gmail.com

K. Srinivas
e-mail: Srinivas_kadali@vnrvjiet.in

IS 2911-2010 sec 2 are adopted for bored piles. Some of the previous studies based on O-cell testing are Hussein et al. [4] analyzed the shaft and base resistance by developing a soil model varying relative density along with the diameter of piles, Fellinius and Minh [2] and Minh and Fellinius [5] estimated the ultimate capacity of two large bored piles of different length by using O-cell, and Abdelmalak and Riad [6] analyzed pile responses by using finite element method and compared with the normal testing method, along with this works some other works adopted in this analysis are Chin's [7] developed a simple method to estimate the ultimate capacity and stiffness of a pile from load–settlement curve and assumed it as a hyperbolic curve in which settlement—(settlement/load) curve is plotted the slope inverse of the straight portion of the curve will give the ultimate load and intercept inverse will give ultimate stiffness. Madhav and Vijay [8] proposed a new analytical solution from load–settlement curve to estimate the nonlinear response of shaft and base of a pile using a hyperbolic relationship.

Statement of Problem

Estimating ultimate resistances and initial stiffnesses of shaft and base of the pile using load–settlement curve from pile load test is important, as it enables verification of the prior predictions based on the geometry of pile (i.e., diameter, length and shape), method and mode of construction and other uncertainties involved during pile installation at the site. In this present study, two parameters of pile, i.e., ultimate resistance P_u and initial stiffness k_p , are estimated in two different methods for both downward and upward segments of the pile, the upward segment of pile resistance is only shaft action so, the ultimate resistances of the shaft, τ_{\max} and stiffnesses of shaft, k_τ are estimated directly by Chin's method [7], for the downward segment of pile the ultimate resistances of shaft, (τ_{\max}) and base, (q_u) and stiffnesses of shaft, (k_τ) and base, (k_b) are estimated by using a numerical solution by considering with different load combinations, i.e., P_1 and P_2 . The load–settlement is predicted by using estimated parameters and compared with real test load–settlement.

Methodology

A large bored pile of length L , diameter d and O-cell placed at a distance of L_d from the base of the pile, an axial load P is applied by O-cell in both directions as shown in Fig. 6.1. The application of load from O-cell in an upward segment of the pile is against the gravity (uplift action); it is resisted by shaft action only and downward segment of pile; it is along with the gravity which is similar to Kent-load test of the pile, resistances offered by both shaft and base actions. By O-cell testing on a pile, two different load–settlement curves are obtained in upward and downward directions as shown in Fig. 6.2. In this present analysis, both upward and downward segments

are considered separately, the initial slope of downward and upward load–settlement curves will represent the initial stiffness of pile, k_p , and initial shaft stiffness, k_τ , as shown in Figs. 3a, b, respectively. Ultimate capacity, P_u , and initial stiffness, k_p , of the pile are the two key known parameters required to estimate the four parameters, k_τ , τ_{max} , k_b and q_u of the base and shaft responses which are estimated from Chin's method.

Fig. 6.1 Schematic load distribution of pile from O-cell

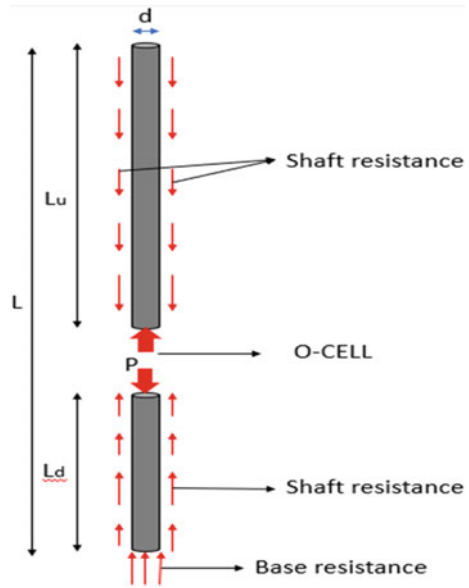
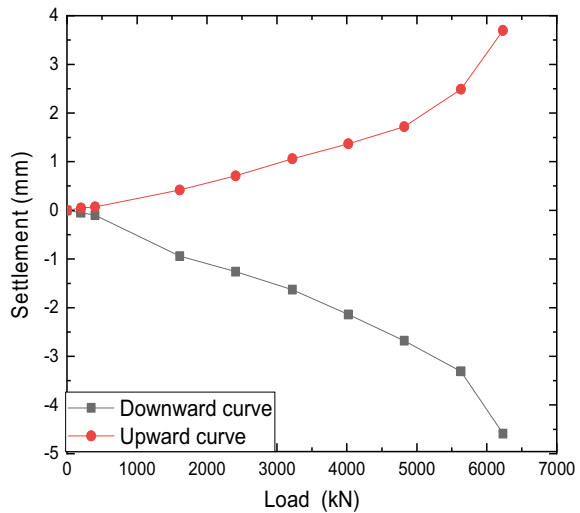


Fig. 6.2 Load–settlement response curve



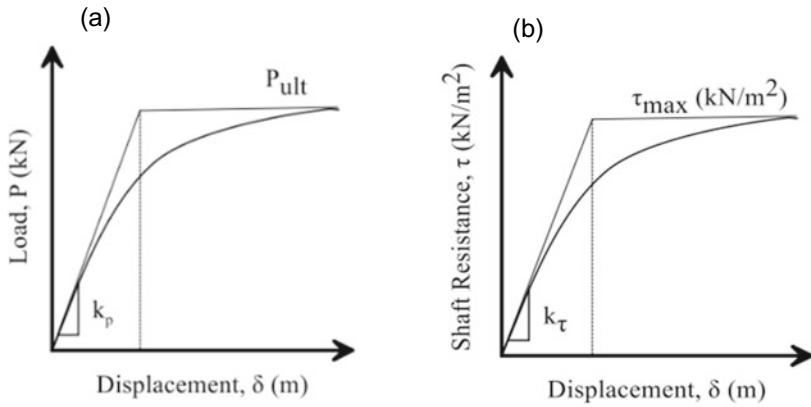


Fig. 6.3 Load–displacement response of piles **a** downward segment **b** upward segment

Chin’s [7] method is based on hyperbolic response between load and settlement which is adopted to estimate P_u and k_p ; according to Chin’s method, a fitting graph is plotted between settlement/load (δ/P) versus settlement (δ) as shown in Fig. 6.4; the slope of fitting line C_1 inverse gives ultimate capacity, P_u , and intercept of fitting line C_2 inverse gives initial stiffness of pile k_p . In this analysis, intercept of fitting line is considered in two different methods, i.e., set 1: Chin’s method intercept of the fitting line, set 2: first term from δ/P data as intercept, and a fitting curve is plotted for the remaining terms by ignoring first term data to estimate ultimate resistance P_u of set 2.

The δ/P versus δ is plotted is shown in Fig. 6.4, and an equation of fitting curve is shown below

$$\delta/P = C_1\delta + C_2 \tag{6.1}$$

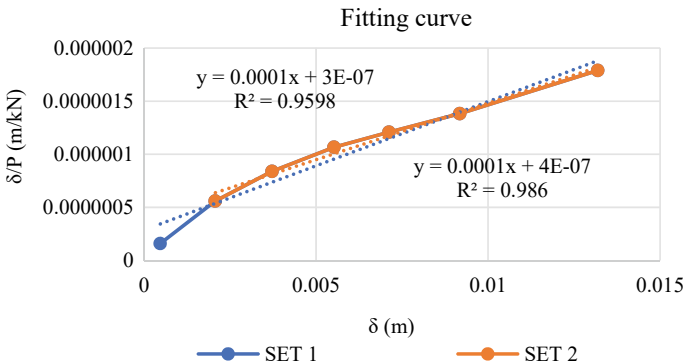


Fig. 6.4 Chin’s method for estimating P_u and K_p

where intercept $C_1 = 1/P_u$ and the slope $C_2 = 1/K_p$.

From Fig. 6.4, the ultimate resistance P_u and initial stiffness k_p are obtained for both sets of upward and downward segments of the pile, the ultimate resistance P_u remains the same in both sets, so only initial stiffnesses, k_p variation are considered in further analysis for both sets, i.e., k_{p1} and k_{p2} of set 1 and set 2, respectively. For an upward segment of the pile, the resistance offered is purely shaft so only ultimate shaft resistance, τ_{\max} , and shaft stiffness k_τ , are obtained directly by dividing the surface area of the pile with ultimate resistance P_u and initial stiffness k_p with respective sets, i.e., set 1 and set 2. For the downward segment of the pile to obtain four unknown parameters k_τ , τ_{\max} , k_b and q_u , numerical solution is adopted with different load combinations for both sets, A set of nonlinear coupled equations derived by Madhav and Vijay [8] to estimate the parameters of a downward segment of the pile are given below

1. Equation for k_b :

$$k_b = k_p^* - (4L/d)k_\tau \quad (6.2)$$

2. Equation for k_τ :

$$k_\tau = (C_4d_1 - C_2d_2)/(C_1C_4 - C_2C_3) \quad (6.3)$$

3. Equation for q_u :

$$q_u = P_u^* - (4L/d)\tau_{\max} \quad (6.4)$$

4. Equation for τ_{\max} :

$$\tau_{\max} = \frac{\{P_2^* \cdot A_2 - [(k_p^*/k_\tau) - (4.L/d)].P_u^* \cdot k_\tau \cdot \delta_2\}}{\{(4.L/d) \cdot [A_2 - k_p^* \cdot \delta_2 + (4.L \cdot k_\tau \cdot \delta_2/d)]\}} \quad (6.5)$$

where $k_p^* = k_p/(\pi d^2/4)$ —normalized stiffness of the pile, k_τ and k_b are shaft and base stiffnesses, respectively. $P_u^* = P_u/(\pi d^2/4)$ —normalized P_u of the pile, τ_{\max} and q_u are maximum shaft and base resistances, respectively.

$d_1, d_2, A_1, A_2, C_1, C_2, C_3, C_4$ are parameters used in equations as

$$d_1 = (P_1^*/\delta_1) - \left[\frac{(k_p^* \cdot P_u^*)}{A_1} \right] \quad (6.6)$$

$$d_2 = (P_2^*/\delta_2) - \left[\frac{(k_p^* \cdot P_u^*)}{A_2} \right] \quad (6.7)$$

$$A_1 = [P_u^* - (4.L \cdot \tau_{\max}/d)] + [k_p^* - (4.L \cdot k_\tau)/d] \cdot \delta_1 \quad (6.8)$$

$$A_2 = [P_u^* - (4.L \cdot \tau_{\max}/d)] + [k_p^* - (4.L \cdot k_\tau)/d] \cdot \delta_2 \quad (6.9)$$

$$C_1 = (4.L/d). \{(\tau_{\max}/\tau_{\max} + k_{\tau}.\delta_1) - (P_u^*/A_1) + (4.L.\tau_{\max}/d.A_1)\} \quad (6.10)$$

$$C_2 = -\left(4.L.k_p^*/d.A_1\right) \quad (6.11)$$

$$C_3 = (4.L/d). \{(\tau_{\max}/\tau_{\max} + k_{\tau}.\delta_2) - (P_u^*/A_2) + (4.L.\tau_{\max}/d.A_2)\} \quad (6.12)$$

$$C_4 = -\left(4.L.k_p^*/d.A_2\right) \quad (6.13)$$

The equations were obtained for 1/3rd and 2/3rd of P_u and if a certain load combination doesn't exist so tried with different load combinations as per suitable, pile parameters are estimated by substituting appropriate load combinations of P_1 and P_2 in Eqs. 6.2–6.5. A set of τ_{\max} values are estimated using Eq. 6.5 assuming k_{τ} . Similarly, another set of k_{τ} are estimated using Eq. 6.3 assuming τ_{\max} , and τ_{\max} was plotted against k_{τ} , for obtained results and the intersection point of the two curves which give the τ_{\max} and k_{τ} values for the pile under consideration. τ_{\max} and k_{τ} are substituted in Eqs. 6.2 and 6.4 to obtain the values of k_b and q_u , respectively; the numerical solution is solved by using MATLAB software, and this procedure is repeated for set 1 and set 2.

Note: The proposed analytical solution is only adopted for a pile where the O-cell is placed at a distance from the base of the pile because if an O-cell is placed at the base the resistance is purely base and above will be purely shafted resistance.

Results

The proposed method is adopted for five large bored piles of length 76 m, 25.15 m, 18.2 m, 73.5 m, 73 m with a diameter of 1.5 m, 1.2 m, 1.2 m, 2 m, 1.5 m where the O-cell placed at 16 m, 1 m, 6.3 m, 11.4 m, 11.6 m from base of the piles, respectively, and further, the details of piles are listed in Table 6.1 for which both upward and downward load–displacement curves are plotted as shown in Fig. 6.5 which are tested up to a maximum load of 7240 kN, 7360 kN, 11,965 kN, 16,560 kN, 8840 kN with maximum downward settlement of 4.59 mm, 13.19 mm, 31.2 mm, 56 mm, 110.4 mm in the field respectively.

The ultimate resistance, P_u , and initial stiffness, k_p , are estimated from Chin's method [7] for upward and downward segments of piles for both sets, i.e., set 1 and set 2; the estimated ultimate resistance for both sets is similar, and only initial stiffness variation is considered for further analysis which is listed in Table 6.2. For an upward segment of the pile, the ultimate shaft resistance τ_{\max} and initial shaft stiffness k_{τ} are directly estimated, and for the downward segment of the pile, the

Table 6.1 Geometrical details of piles

	TBP 1	TBP 2	TBP 3	TBP 4	TBP 5
Length of pile (m)	76	25.15	18.2	73.5	73
Diameter of pile (m)	1.5	1.2	1.2	2	1.5
Downward length (m)	16	1	6.3	11.4	11.6
Upward length (m)	60	24.15	11.9	62.1	61.4
Location of O-cell from toe (m)	16	1	6.3	11.4	11.6

four unknown parameters of each pile (k_τ , τ_{\max} , k_b and q_u) are estimated by using different load combinations from the analytical solution. As the analytical solution is obtained for load combinations of 1/3rd and 2/3rd of ultimate capacity as P_1 and P_2 , respectively, but in this present analysis different combinations are considered such as 0.33, 0.66 and 0.25, 0.5 of ultimate resistance P_u for set 1 and set 2, respectively, for pile TBP 1 and load combinations of other piles are listed in Table 6.3 which are less than or equal to 0.33 and 0.66 of ultimate resistance P_u and load combination along with their respect displacements δ are considered as per their suitability and availability of load–displacement data from the field test.

The estimated parameters k_τ , τ_{\max} , k_b and q_u for upward and downward segments of piles are summarized in Tables 6.4 and 6.5 for both sets. The upward shaft stiffnesses k_τ 18 MN/m³, 223 MN/m³, 85 MN/m³, 35 MN/m³ are additional than downward shaft stiffnesses k_τ of 9 MN/m³, 76 MN/m³, 18 MN/m³, 4.3 MN/m³ of piles TBP 1, TBP 3, TBP 4 and TBP 5, respectively, and for pile TBP 2 the upward shaft stiffness k_τ 67 MN/m³ less than downward shaft stiffness k_τ of 732 MN/m³ from Tables 6.4 and 6.5 which indicates the settlement of pile in both directions for a given load application and load distribution from O-cell in both direction will be different, from this estimated parameters k_τ , τ_{\max} , k_b and q_u load–displacement are predicated for a downward segment of the pile for both sets as shown in Fig. 6.5. The piles TBP 1, TBP 3 and TBP 5 maximum field settlement of 4.59 mm, 31.2 mm 110.4 mm which is closer to the set 2 (1st term as intercept) maximum predicated settlement of 4.7 mm, 37.7 mm, 115.8 mm for a maximum load of 7240 kN, 11,965 kN, 8840 kN, respectively, for pile TBP 2 the maximum field settlement of 13.19 mm is closer with set 1 (Chin’s method) maximum predicated settlement of 13.6 mm for a maximum load of 7630 kN, respectively, and for pile, TBP 4 field settlement is an approximately closer predicated settlement of 58 mm and 57 mm of set 1 and set 2, respectively, for a maximum load of 16,560 kN, from this analysis set 2 (first term as intercept) method obtains closer estimation of shaft and base resistance from O-cell testing of piles.

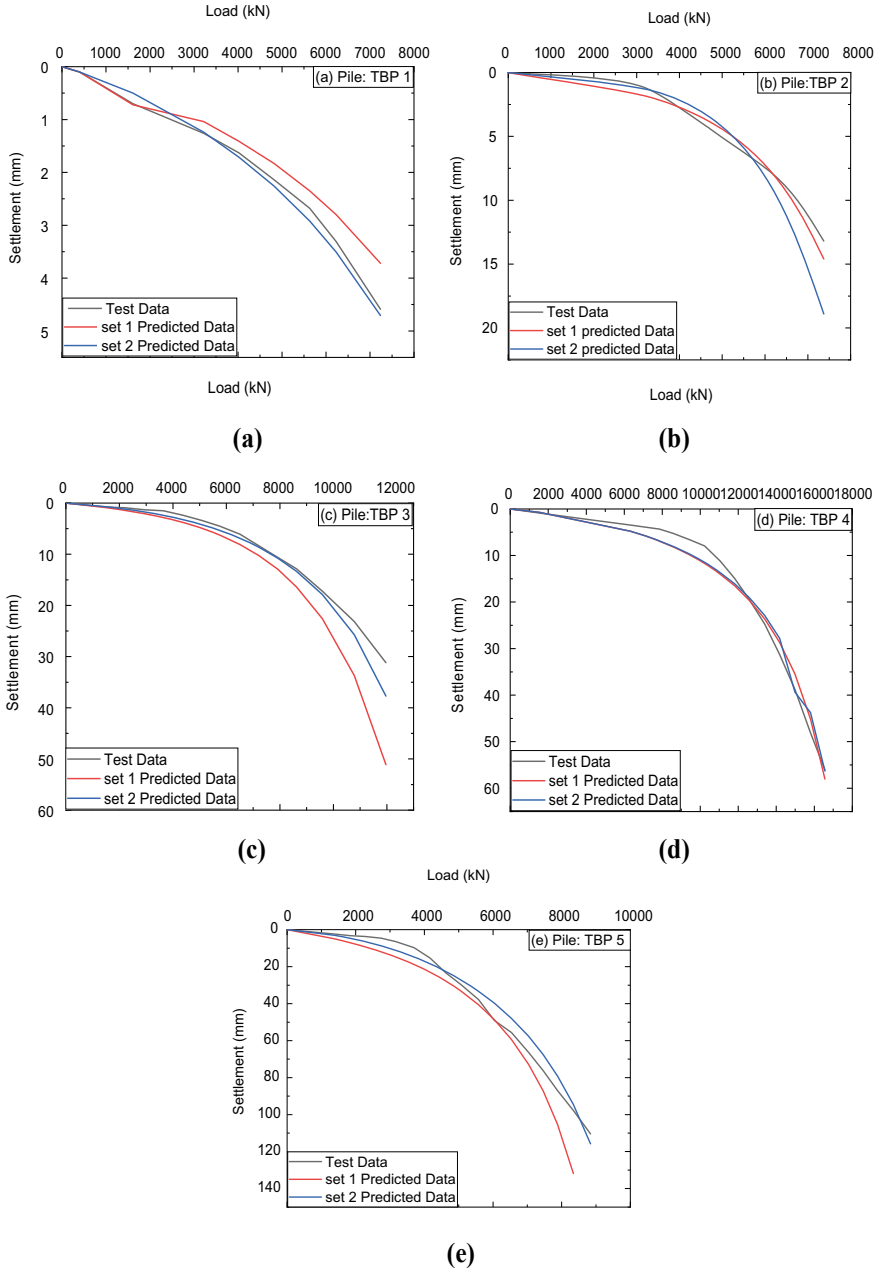


Fig. 6.5 Measured and predicted load–settlement curves of piles **a** TBP 1, **b** TBP 2, **c** TBP 3, **d** TBP 4, **e** TBP 5

Table 6.2 Ultimate load and initial stiffness of piles

TBP	Downward curve			Upward curve		
	P_u (MN) both sets	k_{p1} (MN/m)	k_{p2} (MN/m)	P_u (MN) both sets	k_{p1} (MN/m)	k_{p2} (MN/m)
1	12.5	3333.3	4000	20	5000	4000
2	10	3333.3	6250	10	10,000	6135
3	16.6	2000	2500	11.1	10,000	6993
4	20.0	2500	1754	20	33,333.3	23,094
5	12.5	333.3	625	11.1	10,000	5434

Table 6.3 Load combination of piles

Pile	Set 1		Set 2	
	P_1	P_2	P_1	P_2
TBP 1	$0.33 * P_u$	$0.66 * P_u$	$0.25 * P_u$	$0.5 * P_u$
TBP 2	$0.4 * P_u$	$0.66 * P_u$	$0.3 * P_u$	$0.6 * P_u$
TBP 3	$0.48 * P_u$	$0.66 * P_u$	$0.5 * P_u$	$0.6 * P_u$
TBP 4	$0.25 * P_u$	$0.66 * P_u$	$0.5 * P_u$	$0.6 * P_u$
TBP 5 ara>	$0.33 * P_u$	$0.66 * P_u$	$0.4 * P_u$	$0.66 * P_u$

Table 6.4 Initial stiffnesses and ultimate resistances of shaft and base of upward segment

Pile	Upward segment			
	τ_{max} (kPa)		k_τ (MN/m ³)	
	SET 1	SET 2	SET 1	SET 2
TBP 1	71	71	18	20
TBP 2	110	110	67	67
TBP 3	248	248	223	155
TBP 4	51	51	85	59
TBP 5	38	38	35	19

Table 6.5 Initial stiffnesses and ultimate resistances of shaft and base of downward segment

Downward segment							
τ_{max} (kPa)		k_τ (MN/m ³)		k_b (MN/m ³)		q_u (kPa)	
SET 1	SET 2	SET 1	SET 2	SET 1	SET 2	SET 1	SET 2
22	10	9	17	1866	1534	7146	7658
1201	1239	732	1569	507	295	4842	4712
342	253	76	87	164	374	7562	9424
42	26	18	15	385	457	5409	5749
85	44	4.3	8.5	55	90	3658	5700

Conclusion

This paper attains a simple numerical approach to estimate ultimate resistances and initial stiffnesses of shaft and base parameters for the O-cell pile load test. This approach is applied for five different O-cell piles using suitable load combinations for two different sets of stiffnesses. The estimated parameters are used to predict the load–settlement responses for both sets and compared with field load–settlement

- The set 2 approach gives closer to field test data, which is the best method to obtain accurate shaft and base resistance from O-cell testing.
- The estimated shaft stiffness k_{τ} is differing in both upward and downward segments of the pile which is additional to the upward segment of the pile indicating load distribution and settlement of pile will differ for an applied load from O-cell.

References

1. IS 2911-Part 4 (2015) Design and construction of pile foundations—code of practice—load test on piles. Bureau of Indian Standards, New Delhi
2. Fellinius BH, Minh NH (2013) Large diameter long bored pile in Mekong Delta. *Int J Geoenvironment Case Histories* ISSMGE 2(3):207
3. Lina XU, Guo X, Nie L, Qian Y (2016) Simulation study of the load-settlement behavior of a single pile using the osterberg-cell test based on the load transfer theory. *Open Civ Eng J* 10
4. Hussein HM, Abdou Abdel-Naiem M, Rushdy TA (2007) Investigation of shaft and base resistance of a single bored pile using osterberg cell. *J Eng Sci* 35(4):853–867
5. Minh NH, Fellinius BH (2014) Bidirectional cell tests on two 70 m long bored piles in Vietnam. In: ASCE geotechnical special publication GSP 233, pp 482–496
6. Abdelmalak R, Riad B (2016) Finite element modelling of Osterberg cell pile load test. Case history: St. Croix River crossing bridge, USA. In: International conference on structural and geotechnical engineering, Ain Shams University (ICSGE)
7. Chin FK (1971) Estimation of the ultimate load of piles not carried to failure. In: Proceeding of the South East Asian conference on soil engineering, pp 81.90
8. Madhav M, Vijay K (2019) A method to estimate shaft and base responses of a pile from pile load test results. *Geotech Eng J SEAGS AGSSEA* 50(3)

Chapter 7

A Numerical Study of Performance of Large Piled Raft Foundation on Sand Under Vertical Loading



Banchiva K. Marak and Baleshwar Singh

Introduction

Piled-raft foundation is a hybrid foundation system composed of two structural components, that is, the raft and the piles. This foundation type design takes into account of both the raft and pile bearing capacity making it an alternative economical option when used in suitable geotechnical conditions, as compared to the pile foundation designed in conventional way in which the capacity of the raft is not taken into consideration. Due to the combined action of both the structural components, various interactions take place between the structural components, that is the piles and raft and subsoil making the overall response of piled raft system complex. The piled-raft foundations are classified as small piled-rafts and large piled-rafts from the viewpoint of settlement control according to Viggiani et al. [1]. For small piled-raft foundation, the unpiled raft alone does not have required bearing capacity, and hence, the piles are added to attain required safety factor (F.O.S) with the width of raft ranging from 5 to 15 m and the width of raft is small compared to pile length ($B_r/L_p < 1$). Large piled-raft foundation is those where the unpiled raft has an adequate F.O.S. but it undergoes excessive settlement, and therefore, the inclusion of piles is intended for settlement reduction. In this case, the raft width is comparatively large with respect to the length of piles ($B_r/L_p > 1$). Therefore, settlement is a problem, and more importantly, the differential settlement poses a major problem in case of large piled-raft foundations. The number of piles to be added underneath the raft

B. K. Marak (✉) · B. Singh
Department of Civil Engineering, IIT Guwahati, Guwahati 781039, India
e-mail: k.banchiva@iitg.ac.in

B. Singh
e-mail: baleshwar@iitg.ac.in

in a piled-raft design should be such that ultimate load and settlement criteria are satisfied [2]. One of the important factors that need to be considered for the design of piled raft system to be optimum is to properly assess the total load shared between the raft and piles.

The introduction of piles underneath the raft is first proposed by Burland et al. [3]. For analyzing piled-raft foundations, various approaches are available ranging from analytical approaches [2, 4], physical modeling and centrifuge tests [5–8] to 3D numerical studies [2, 9–12]. The performance of raft on settlement reducing piles is investigated. It is found to observe that raft relative stiffness influences significantly on differential settlement [13]. The piled raft performance was evaluated using a 3D nonlinear verified model. The distribution of load between raft and piles depends on factors like the pile length, thickness of raft, pile arrangement and pile diameter [14]. Load sharing behavior and the load response of piled rafts in sand are investigated by Lee et al. [15].

The aim of present analysis is to understand the large piled raft foundations performance on sandy subsoil subjected to vertical load condition. The numerical simulations were carried out by considering the effect of geometric parameters like the pile length and pile spacing, and thickness of raft on differential and average settlements, load sharing ratio and bending moment of this foundation system. The raft thickness was varied such that its stiffness ranged from extremely flexible to extremely rigid case. The numerical simulations were conducted with the finite element software PLAXIS 3D.

Numerical Modeling

In this section, the numerical modeling procedure and the validation study of large piled-raft foundation system on sand are described. A commercial software PLAXIS 3D, which is finite element based, is used to carry out the three-dimensional numerical modeling [16]. A suitable mesh size is considered for analyzing the model on the basis of mesh convergence study. The numerical model is verified with the centrifuge test results of Park and Lee [8] by modeling the foundation in prototype scale.

Domain Size and Mesh Convergence

The size of the soil model is fixed at a lateral distance of $2.5B_r$ from the raft edge on all the four sides restraining the horizontal movement and allowing for the vertical movement. The soil domain vertical depth is taken as $5L_p$ from base of the raft and the soil bottom boundary is fixed meaning the horizontal movement and vertical movement are not allowed. The boundaries of the soil model are selected keeping in mind that the piled-raft influence zone is well within the soil domain to avoid any

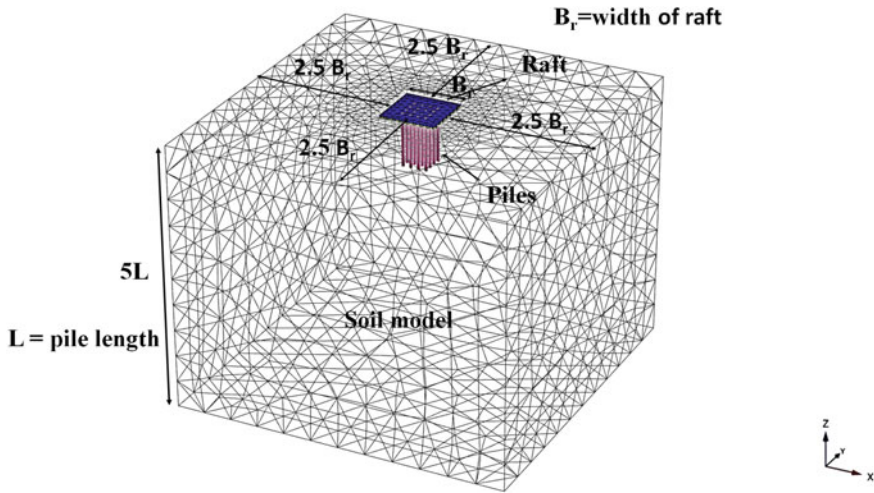


Fig. 7.1 Numerical model geometry and meshing

undesirable boundary effects. Figure 7.1 show the numerical model with the selected boundaries used for the study along with piled-raft geometry.

Mesh convergence study is performed to find out the optimal mesh required to perform the numerical analysis accurately by considering the available five different meshing options in PLAXIS library. Coarser meshes are unable to take into account of the important soil and structure behavioral characteristics, while very fine meshes take excessive computational time for the analysis. The element size according to different meshes is identified by non-dimensional length of element which is defined as the ratio of length of element to maximum dimension of the model geometry. The result of the mesh convergence study is shown in Fig. 7.2. It is found that the piled raft load carrying capacity varies a lot when the mesh is changed from very coarse to coarse and also from coarse to medium. The results almost converge beyond the medium meshing, and hence, medium mesh is adopted for carrying out the numerical study. Meshes are refined locally nearby the structural elements.

Material Modeling

The simulated volume of soil consists of tetrahedral elements which is 10 nodes, and the behavior of sandy soil considered in the study is simulated using Hardening Soil material model. The raft component is modeled considering a plate element which is a triangular element of 6 nodes, and the pile component is modeled considering the embedded beam element which has a special interface element. The behavior of both piles and raft is considered to be linear elastic. The interaction between the subsoil and the structural components is considered with the help of 12-node

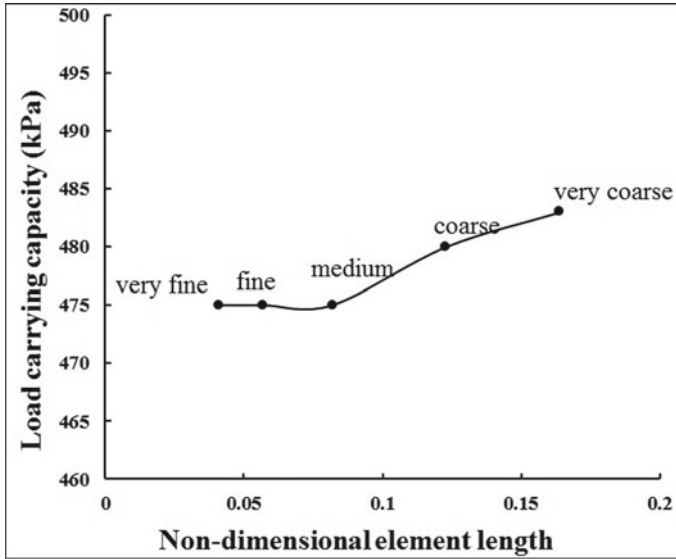


Fig. 7.2 Mesh convergence curve

interface element. The reduced shear strength at the soil–structure interface is taken into account by the Interface Reduction Factor (R_{int}).

For the present study, the soil properties of the homogeneous medium sand are considered from Nguyen et al. [7] and are shown in Table 7.1. Both the raft and piles are considered to be concrete material having modulus of elasticity equal to 30,000 MPa with Poisson’s ratio of 0.15.

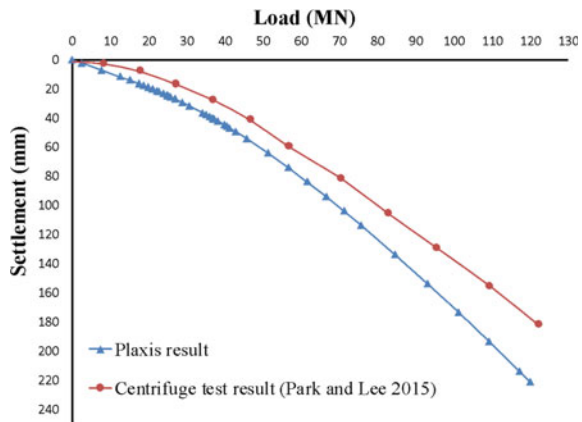
Model Validation Study

The present numerical model used for the study is validated with the results of centrifuge tests performed by Park and Lee [8] by modeling the foundation in prototype scale with the centrifuge acceleration of 60 g. The piled raft foundation of 9×9 m square raft with thickness of 1.2 m and 4×4 pile configuration with pile spacing of 2.4 m and pile of 0.6 m diameter and 15 m length are considered. Silica sand with 84% relative density having the elastic modulus of 50 MPa and friction angle of 43° is used for the analyses. The results of the obtained load–settlement curve for piled-raft system for both numerical analysis and centrifuge test are compared and shown in Fig. 7.3. The results obtained from numerical study and centrifuge tests show that centrifuge test result appears to predict a bit higher stiffness value; however, the overall response shows a reasonably close match with load–settlement curve having similar trend. This validated numerical model is then further used for the numerical modeling of the present analysis.

Table 7.1 Input parameters for PLAXIS 3D

Soil properties	Medium sand
Relative density (%)	40
Dry unit weight, γ_d (kN/m ³)	13.7
Secant Young's modulus, E_{50}^{ref} (MPa)	19.21
Oedometer stiffness, E_{oed}^{ref} (MPa)	19.21
Unloading/reloading stiffness, E_{ur}^{ref} (MPa)	57.63
Friction angle, ϕ (°)	40
Cohesion, c (kPa)	0
Poisson's ratio, ν	0.25
Dilatancy angle, ψ (°)	8
Raft and pile properties	
Modulus of elasticity, E (MPa)	30,000
Poisson's ratio, ν	0.15
Unit weight, γ (kN/m ³)	25

Fig. 7.3 Validation of the numerical model with the result of centrifuge test



Results and Discussion

The effect of L/d ratio, s/d ratio and thickness of raft on average and differential settlement, load sharing ratio and induced bending moment of piled-raft on medium sand condition is evaluated. The various parameters of the structural elements considered for the study are shown in Table 7.2. The uniformly distributed load of 250 kPa is applied on the foundation. The differential settlements (W_{diff}) and average settlement (W_{avg}) are calculated by considering the settlement at the center (W_{center}) and the settlement at the corner (W_{corner}) and are calculated by Eq. 7.1 [17] and Eq. 7.2 [18]. The load shared between the raft and piles is measured by load sharing ratio which is defined as the pile load share to the total load on the foundation.

Table 7.2 Raft and pile parameters considered for the present study [11]

Raft parameters	Values
Raft width, B_r (m)	25 × 25
Raft thickness, t_r (m)	0.206, 0.705*, 2.061, 4.679
Relative raft–soil stiffness ratio, K_{rs}	0.01, 0.4*, 10, 117
Pile parameters	
Pile diameter, d (m)	0.5
Pile length, L (m)	10, 15*, 20, 25
Pile spacing, s (m)	2, 3, 4, 5*, 6, 7, 8

*Standard value if not changed

$$W_{\text{avg}} = \frac{1}{3}(2W_{\text{center}} + W_{\text{corner}})W_{\text{avg}} = \frac{1}{3}(2W_{\text{center}} + W_{\text{corner}}) \quad (7.1)$$

$$W_{\text{diff}} = W_{\text{center}} - W_{\text{corner}} \quad W_{\text{diff}} = W_{\text{center}} - W_{\text{corner}} \quad (7.2)$$

Influence of L/d Ratio and s/d Ratio on the Behavior of Piled Flexible Raft Foundation

The influence of s/d ratio and L/d ratio on differential settlement and average settlement, load sharing ratio and induced bending moment behavior of foundation is carried out in this section. The s/d ratio considered for the study is 4, 6, 8, 10, 12, 14 and 16, and the L/d ratio considered is 20, 30, 40 and 50. The thickness of the raft considered is such that its behavior is flexible. Figure 7.4a presents the differential settlement variation for different s/d and L/d ratios taken for the present study. It is seen that for all the considered pile lengths, the increase in the s/d ratio led to the decrease in differential settlement initially and then attains minimum, and thereafter, it increases. For longer piles, the differential settlement attains minimum at a spacing of 10–12 times the pile diameter. However, for L/d ratio of 20 the differential settlement attains a minimum value at s/d ratio of around 8. This means that the piles should be placed at certain pile spacing in order to achieve minimum differential settlement. It is also observed that at a lower pile spacing (s/d ratio of 4 and 6), the differential settlement varies as the length of pile increases, whereas there is no variation in the differential settlement at a higher pile spacing. The change in average settlement with pile spacing is negligible for any pile length. The average settlement decreases with the increase in pile length for lower pile spacing as seen from Fig. 7.4b. From Fig. 7.4c, it can be seen that the rate of increase in the load carried by the piles decreases toward higher pile spacing for all pile lengths except for L/d ratio of 50 where the rate of increase starts decreasing at lower pile spacing. The reason for the decrease in the rate of increase of the load carried by the piles

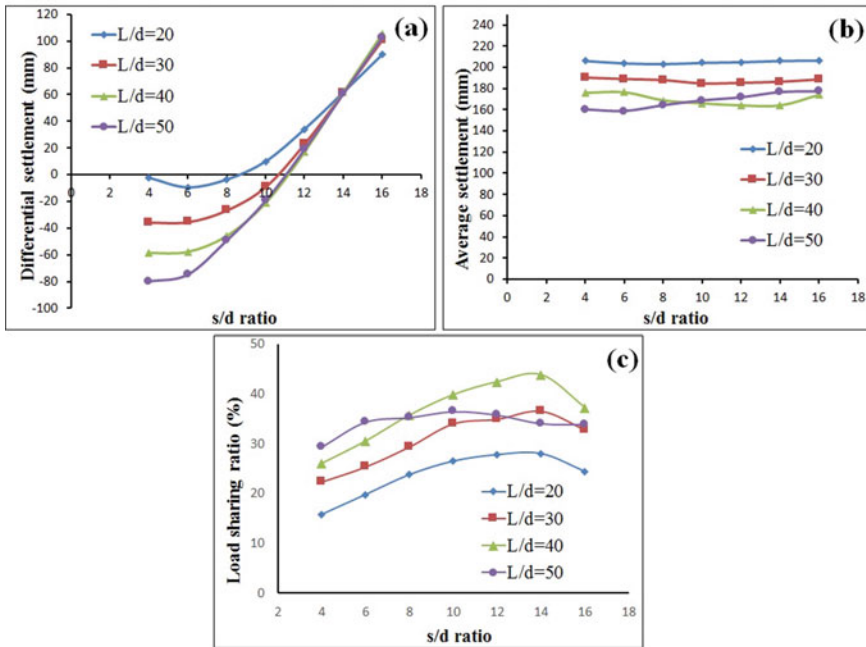


Fig. 7.4 Variation of **a** differential settlement, **b** average settlement and **c** load sharing ratio with the s/d and L/d ratio

toward higher pile spacing may be because of more raft–soil interaction (raft–soil contact stress) at a higher pile spacing compared to lower pile spacing. The load taken by the piles increases with increase in the length of pile; however, this behavior is not observed, for L/d ratio of 50. From Fig. 7.5, it is seen that the negative bending moment (hogging) in flexible raft is observed at lower s/d ratio (s/d ratios of 4, 6 and 8) for all the L/d ratios. However, the positive bending moment (sagging) is noticed at higher s/d ratios. It is found that higher pile lengths yielded more bending moment.

Influence of Raft Thickness and s/d Ratio on Piled Raft Behavior

This section discusses the effect of thickness of raft and s/d ratio on differential settlement and average settlement, load sharing behavior and induced bending moment behavior of foundation which are evaluated. The raft thickness considered for study is 0.206 m, 0.705 m, 2.061 m and 4.679 m which corresponds to raft–soil stiffness ratios of extremely flexible, flexible, rigid and extremely rigid case, respectively. Figure 7.6a shows the differential settlement variation for increase in s/d ratio for different raft thicknesses. It is seen that for thicker rafts, the differential settlement

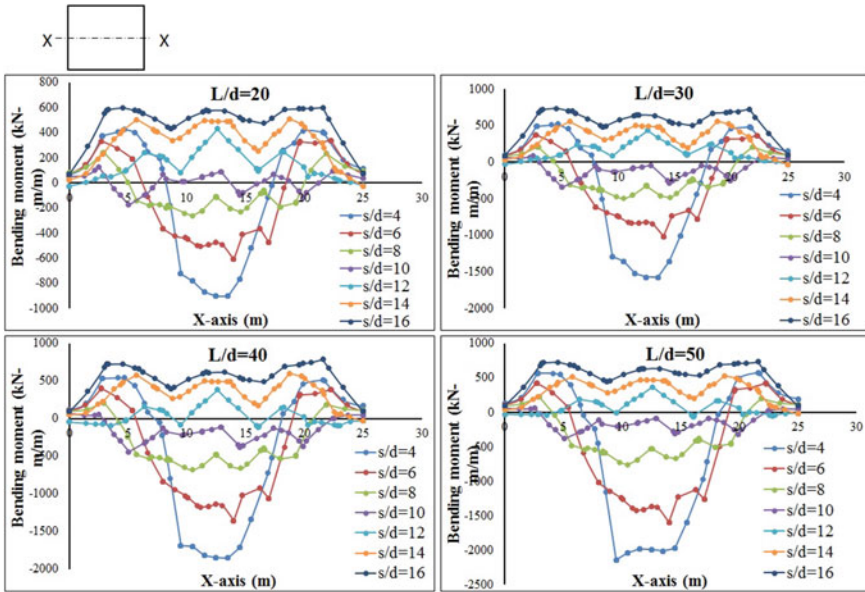


Fig. 7.5 Bending moment variation along section XX for different L/d ratios and s/d ratios

becomes negligible at all pile spacing. However, for lower raft thicknesses differential settlement initially reduces for lower pile spacing and attains minimum and then increases for higher pile spacing. From an economical perspective, thinner rafts can be used for minimizing differential settlement by optimally placing piles at certain pile spacing. Figure 7.6b shows that the average settlement increases with increase in the raft thickness for lower pile spacing; however, for higher pile spacing there is no significant change in the average settlement with variation in raft thickness. For rigid and extremely rigid rafts, the reduction in the average settlement is seen with the increase in the spacing of piles, whereas for flexible raft the average settlement is seen to be constant. From Fig. 7.6c, it is seen that the increase in the raft thickness does not significantly affect the load taken by piles. The load taken by the piles increases initially as the spacing of piles increases, may be due to the lesser interactions among piles as spacing increases, which then later decreases due to more raft–soil interaction. Figure 7.6d shows the bending moment variation along section XX passing through the center of the raft which can be seen that as the raft thickness increased from extremely flexible to extremely rigid case, it yielded a higher negative bending moment.

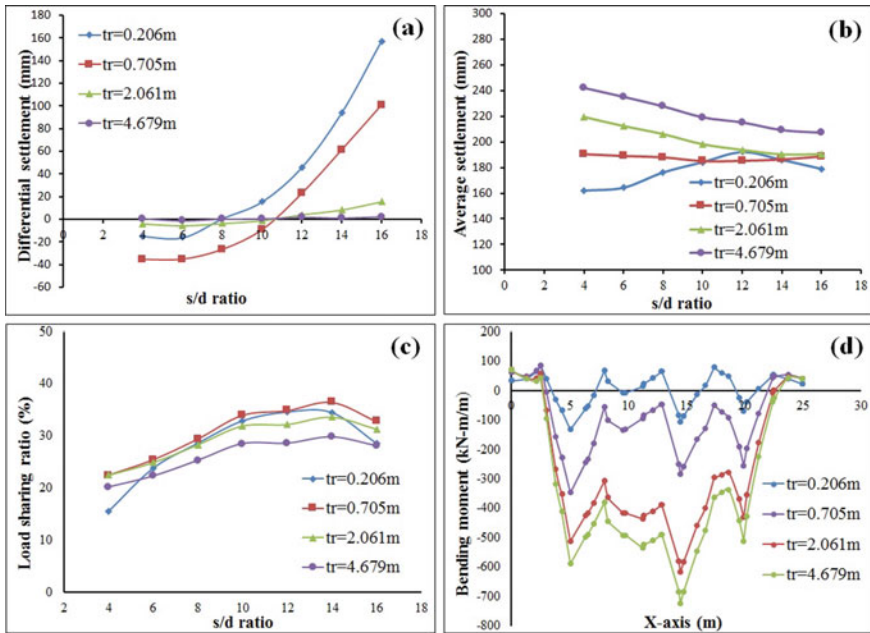


Fig. 7.6 Variation of **a** differential settlement, **b** average settlement, **c** load sharing ratio with s/d ratio and raft thickness and **d** variation of bending moment along section AA for different raft thicknesses

Conclusions

The 3D numerical simulations have been performed to understand the behavior of large piled-raft foundation on sand by considering the influence of geometric parameters like the length and spacing of piles, and thickness of raft on differential and average settlements, load sharing ratio and bending moment of large piled raft foundation. On the basis of the results obtained, it is concluded that the piles should be placed at certain pile spacing in order to achieve minimum differential settlement. The change in average settlement with spacing of pile is found to be negligible for any pile lengths. The rate of increase in the load carried by the piles decreases toward higher pile spacing for all pile lengths except for L/d ratio of 50 because of more raft-soil interaction (raft-soil contact stress) at a higher pile spacing compared to lower pile spacing. From an economical perspective, thinner rafts can be used for minimizing differential settlement by optimally placing piles at certain pile spacing. The decrease in average settlement is observed with the increase in spacing of pile for rigid and extremely rigid rafts, whereas for flexible raft the average settlement is seen to be constant. The increase in the raft thickness does not significantly affect the load sharing ratio. The load carried by piles increases initially with the increase in the spacing of pile, may be due to the lesser interactions among piles as spacing increases, which then later decreases due to more raft-soil interaction. The increase

in the raft thickness yielded higher bending moments in raft. This higher bending moment is also seen for increasing pile length with flexible raft.

References

1. Viggiani C, Mandolini A, Russo G (2012) *Piles and pile foundation*, 1st edn. Spon Press, London & New York
2. Oh EYN, Huang M, Surarak C, Adamec R, Balasurbamian AS (2008) Finite element modeling for piled raft foundation in sand. In: Eleventh East Asia-Pacific conference on structural engineering and construction (EASEC-11) "Building a Sustainable Environment", Taipei, Taiwan, vol 8
3. Burland JB, Broms BB, De Mello VB (1978) Behaviour of foundations and structures. In: Proceedings of the 9th ICSMFE, Tokyo, vol 2, pp 496–546
4. Poulos HG, Davis EH (1980) *Pile foundation analysis and design* (No. Monograph)
5. Horikoshi K, Randolph MF (1996) Centrifuge modelling of piled raft foundations on clay. *Geotechnique* 46(4):741–752
6. Long PD (1993) Footings with settlement-reducing piles in non-cohesive soil. Dissertation
7. Nguyen DDC, Jo SB, Kim DS (2013) Design method of piled-raft foundations under vertical load considering interaction effects. *Comput Geotech* 47:16–27
8. Park D, Lee J (2015) Comparative analysis of various interaction effects for piled rafts in sands using centrifuge tests. *J Geotech Geoenviron Eng* 141(1):04014082
9. Halder P, Manna B (2020) Performance evaluation of piled rafts in sand based on load-sharing mechanism using finite element model. *Int J Geotech Eng* 1–18
10. Mali S, Singh B (2018) Behavior of large piled-raft foundation on clay soil. *Ocean Eng* 149:205–216
11. Nguyen DDC, Kim DS, Jo SB (2014) Parametric study for optimal design of large piled raft foundations on sand. *Comput Geotech* 55:14–26
12. Reul O (2004) Numerical study of the bearing behavior of piled rafts. *Int J Geomech* 4(2):59–68
13. El-Garhy B, Galil AA, Youssef AF, Raia MA (2013) Behavior of raft on settlement reducing piles: experimental model study. *J Rock Mech Geotech Eng* 5(5):389–399
14. Alnuaim AM, El Naggar H, El Naggar MH (2017) Evaluation of piled raft performance using a verified 3D nonlinear numerical model. *Geotech Geol Eng* 35(4):1831–1845
15. Lee J, Park D, Park D, Park K (2015) Estimation of load-sharing ratios for piled rafts in sands that includes interaction effects. *Comput Geotech* 63:306–314
16. Brinkgreve R, Swolfs W, Engin E (2015) *PLAXIS user's manual*, version 6.1. Balkema, Rotterdam, The Netherlands
17. Randolph MF (1994) Design methods for pile groups and piled rafts. In: International conference on soil mechanics and foundation engineering, pp 61–82
18. Cho J, Lee JH, Jeong S, Lee J (2012) The settlement behavior of piled raft in clay soils. *Ocean Eng* 53:153–163

Chapter 8

Effect of Compressibility on Bearing Pressure of Soft Ground



J. Y. V. Shiva Bhushan, Madhav Madhira, and G. V. Narasimha Reddy

Introduction

Bearing capacity of shallow foundations, the most important design aspect for structures, is estimated most commonly considering the soil as incompressible and rigid plastic. Prandtl assumed soil to be perfectly plastic and gave bearing capacity factor, N_c , as 5.14 for strip footing on clays. Terzaghi [5] assumed the soil as rigid plastic and derived an equation for ultimate bearing capacity. Most of the soft soils especially undrained clays experience a nonlinear behavior even from small strains (less than 2%). Menard [3] has given an expression for the limit/maximum pressure in clays for expansion of cylindrical cavity as

$$p_l = c_u N_c^* + \sigma_h \quad (8.1)$$

where $N_c^* = 1 + \ln(G/c_u)$, G and c_u are shear modulus and undrained strength of the soft soil, respectively, and σ_h is the total horizontal stress at the corresponding depth. Vesic [6, 7] applied the cavity expansion theory accounting for the volume change in the plastic zone, in the computation of ultimate bearing capacity of shallow foundations. He proposed compressibility factors for cohesive soils accounting for rigidity index, $I_r (= G/c_u)$ a function of stiffness and shear strength of soil.

J. Y. V. Shiva Bhushan (✉) · M. Madhira
Department of Civil Engineering, VNR Vignana Jyothi Institute of Engineering and Technology,
Hyderabad 500090, India
e-mail: jyvshivabhushan@gmail.com

G. V. Narasimha Reddy
Department of Civil Engineering, JNT University, Hyderabad 500085, India
e-mail: gvnreddy@jntuh.ac.in

McMohan et al. [2] developed an ellipsoidal cavity expansion model using FEA to obtain load–settlement responses for shallow foundations on soils with different rigidities. They proposed a relation between footing load based on settlement and rigidity of soil as

$$\frac{\sigma_f}{c_u} = 4.45 + 1.34 \ln\left(\frac{\delta}{D} \frac{G}{c_u}\right) \quad (8.2)$$

where σ_f/c_u is the normalized footing pressure and δ/D is normalized settlement. The application of cylindrical cavity expansion theory in estimating the bearing pressure factor of compressible soil at different settlement ratios is presented in this study.

Problem Description

A rigid rough circular footing with a diameter, $D = 2$ m is considered. A uniform circular load is applied on compressible homogenous soft ground. An isotropic and homogeneous clay with unit weight, γ of 15 kN/m³ having an undrained shear strength, c_u of 15 kPa, and Poisson's ratio $\mu = 0.495$ is modeled as linear perfectly plastic behavior following Mohr–Coulomb failure criteria. Rigidity indices, $I_r (= G/c_u)$ are taken as 50, 100, 200, 500, 1000, 2000 and 5000. Stress–settlement responses of footings on soft soils for a range of I_r values [50–5000] are obtained and analyzed from the nonlinear elastic to perfectly rigid plastic (incompressible) conditions.

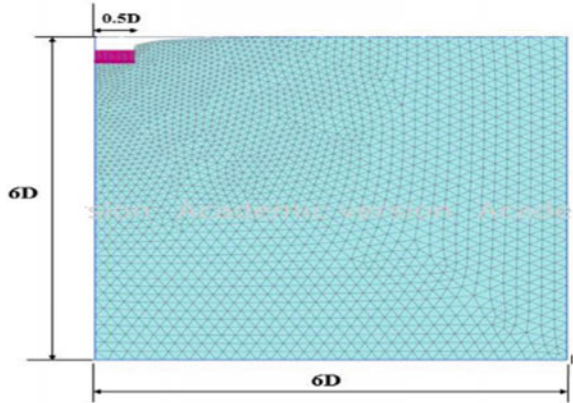
Finite Element Model

Finite element software—PLAXIS 2D, 2020—was used to analyze the problem. The axisymmetric model was chosen to simulate the circular shape of footing. 15-noded triangular elements were used to discretize the geometry. Boundary convergence was achieved for both the radial and vertical boundaries positioned 6D away from the center and beneath the footing (Fig. 8.1).

Mesh convergence was also checked and the mesh size was fixed as medium fine. Refinement of mesh discretized into 4209 elements with an average element size equal to about 271 mm for all the rigidity indices, I_r . The default boundary conditions option chosen were the bottom boundary is fixed in both radial and vertical directions, while the side boundaries are fixed in the radial direction and the top boundary is free.

To study the effect of compressibility on undrained bearing pressure of soft soil, a circular footing of diameter, $D = 2$ m is considered along which prescribed vertical displacement is applied and stress responses are analyzed. For soils with I_r more

Fig. 8.1 Axisymmetric finite element model showing deformed mesh for uniform displacement



than 500, 1 cm of displacement is applied; for soils with I_r less than 500, 10 cm displacement is applied till it reaches the near ultimate stress.

Results

Bearing pressure of soft ground, q , is obtained as a function of settlement s , for different compressibilities. Bearing pressure is normalized with undrained strength, c_u , and the ratio of bearing pressure to undrained strength of soil is defined as bearing pressure factor, $N_{cf}(= q/c_u)$. Settlements are normalized with footing diameter, D , as settlement ratio, SR %, ($=100 s/D$).

Effect of Rigidity Index, I_r

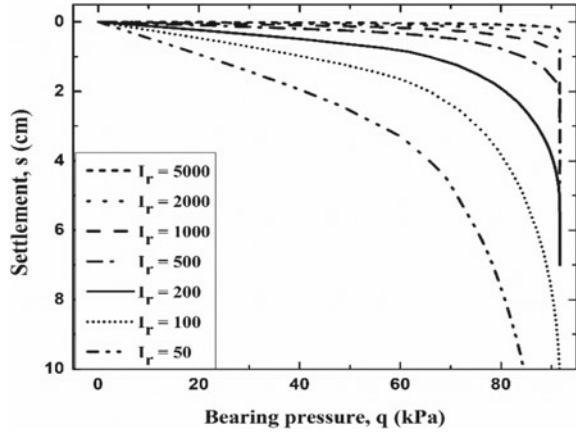
Pressure–settlement curves obtained for the circular foundation on soft ground with different rigidity indices are shown in Fig. 8.2. Undrained ultimate bearing capacity factor, N_c obtained for stiff ground ($I_r = 5000$) from FEA is

$$N_c = \frac{q_u}{c_u} = \frac{91.69}{15} = 6.11 \tag{8.3}$$

where q_u is ultimate load and c_u is the undrained shear strength of soft soil. Based on plasticity theory, Skempton [4] and Meyerhof [1] obtained undrained bearing capacity factors for circular footing resting on clays are 6 and 6.05, respectively. Soft ground with $G/c_u = 5000$ behaves as perfectly rigid plastic material, with the ultimate load of 91.7 kPa, reached at 3 mm displacement or settlement ratio, SR_f of 0.15%.

Responses of footings on soft ground with different I_r are shown in Fig. 8.2. Pressure–settlement curves are for $I_r = 5000, 2000$ and 1000 are close to rigid plastic behavior as I_r decreases, The stress–settlement responses become increasingly

Fig. 8.2 Bearing pressure–settlement response: effect of rigidity index, I_r



nonlinear for I_r less than 1000. The nonlinearity of the responses is very significant for $I_r = 100$ and 50. The bearing stress continues to increase with settlement and does not reach the ultimate value even at a vertical displacement of 10 cm for highly compressible soil with $I_r = 50$.

Figure 8.3 shows the variation of bearing pressure factor, N_{cf} with settlement ratio, SR for different rigidity indices of soft ground. Bearing pressure factor, N_{cf} increase with settlement ratio, SR of soft soil for a given rigidity index. Footings on soils with high rigidity, N_{cf} , reach the ultimate value at small SR; SR for $I_r = 1000$ and 100 are respectively 1% and 5%.

Effect of Rigidity Index on Bearing Pressure Factor

To estimate the degree of influence on the variation of bearing pressure of circular footing on compressible soil as a function of settlement and rigidity index, N_{cf} is normalized with bearing capacity factor, N_c for footing on incompressible ground.

Fig. 8.3 Variations of N_{cf} with SR (%) for different I_r

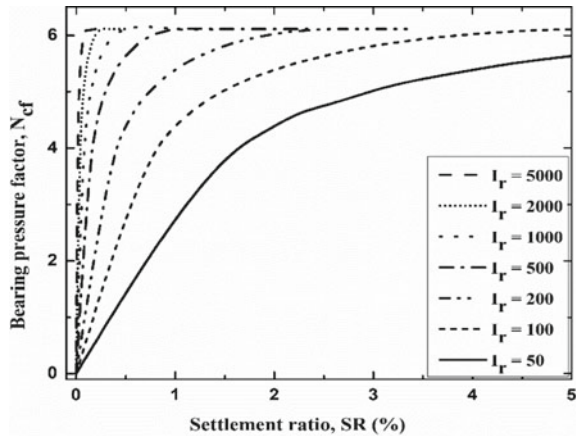
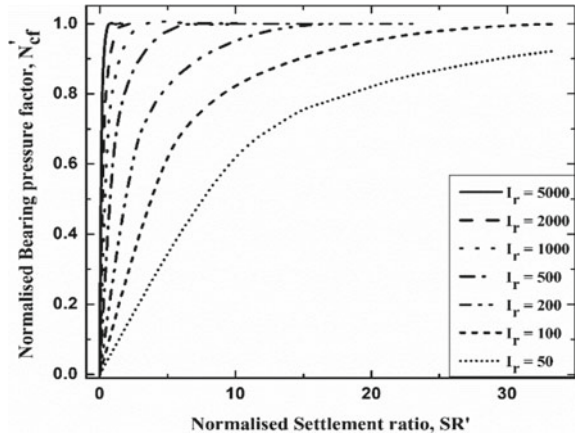


Fig. 8.4 Variations of N'_{cf} with SR' for different I_r



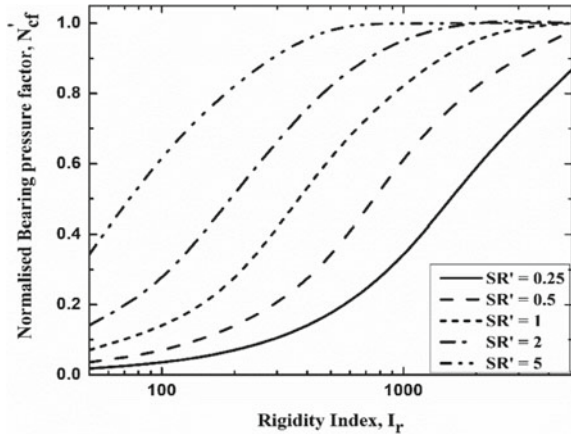
Normalized bearing pressure factor, N'_{cf} is $= N_{cf}/N_c$. Normalized settlement ratio, SR' , is defined as ratio of settlement ratio of compressible soil to settlement ratio of incompressible soil, $SR_f = 0.15\%$.

Variations of normalized bearing pressure factor with normalized settlement ratio for different rigidity is shown in Fig. 8.4. The point of maximum curvature in these curves depicts the limiting stage of linear behavior of compressible soils. Footings on compressible soils exhibit highly a nonlinear response with no marked yielding. For $SR' = 5$, N'_{cf} are respectively, 0.35, 0.6, 0.8 and 0.97, for compressible soils for $I_r = 50, 100, 200$ and 500 . Thus, limiting bearing pressures of footings on compressible soils are 35, 60, 80 and 97% of ultimate load corresponding to rigid plastic behavior of Terzaghi and Vesic at SR of 5%. The difference in normalized bearing pressure, N'_{cf} decreases with the increase of SR' .

Variation of undrained bearing pressure factor, N'_{cf} with rigidity index I_r , for different SR' is shown in Fig. 8.5 to illustrate the effect of compressibility. Normalized bearing pressure factor, N'_{cf} , increases with the rigidity of ground and settlement ratio. The bearing pressure factors, N'_{cf} for $I_r = 50, 200, 500$ and 1000 are respectively 4%, 14%, 34% and 98% of ultimate bearing capacity factor, N_c corresponding to SR of 0.15%.

For a soft ground with $I_r = 100$, the values of N'_{cf} at $SR' = 0.25, 0.5, 1, 2$ and 5 are respectively 0.03, 0.07, 0.14, 0.28 and 0.61. This implies that for footings on compressible soils with $I_r = 100$, the bearing pressure is limited to 3.5%, 7%, 14%, 28% and 61.5% of ultimate load at settlement ratios of 0.03%, 0.075%, 0.15%, 0.3% and 0.75%, respectively.

Fig. 8.5 N'_{cf} versus I_r at different SR'



Conclusions

Footings on soft compressible ground are analyzed to study the effect of compressibility on undrained bearing pressure factor, accounting for rigidity index, which is a function of stiffness and undrained shear strength of the soil. Bearing pressure factors as a function of settlement are presented to quantify the influence of compressibility on undrained bearing pressure of soft ground. The proposed plots of normalized bearing pressure factors can be used to estimate the limiting bearing capacity of circular footings for a given settlement.

References

1. Meyerhof GG (1951) The ultimate bearing capacity of foundations. *Geotechnique* 2:301–322
2. McMahon BT, Haigh SK, Bolton MD (2013) Cavity expansion model for the bearing capacity and settlement of circular shallow foundations on clay. *Geotechnique* 63(9):746–752. <https://doi.org/10.1680/geot.12.P.061>
3. Menard L (1957) In situ measurements of the physical properties of soils. *Ann Ponts Chausdes* 127:357–377
4. Skempton AW (1951) The bearing capacity of clays. *Proceedings Building Research Congress*, London, pp 180–189
5. Terzaghi K (1943) *Theoretical soil mechanics*. Wiley, New York, USA
6. Vesic AS (1972) Expansion of cavities in infinite soil mass. *J Soil Mech Found Div ASCE* 98(3):265–290
7. Vesic AS (1973) Analysis of ultimate loads of shallow foundations. *J Soil Mech Found Div* 99(1):45–73

Chapter 9

Raft Foundation Analysis for a 135-m High-Rise Residential Tower in Noida



Ravi Sundaram, Sorabh Gupta, and Gyan Chand

Introduction

Project Details

Three adjoining high-rise residential towers, 135 m high with ground + 35 storeys + 2 basements are under construction in Noida. The high-end construction includes large open area, swimming pool and other facilities. The foundation was planned at a depth of 10 m below the ground level.

Geotechnical investigation for the project revealed that the soils in the area are alluvial deposits consisting primarily of alternating strata of sandy silt of low plasticity and silty sand. In general, SPT values below foundation level ranged from 25 to 40 to 22 m depth, increasing gradually with depth.

Initial foundation analysis using the SPT data suggested that piled-raft may be required to support the tower. An artist's impression of the proposed building is illustrated in Fig. 9.1.

R. Sundaram (✉) · S. Gupta
Cengrs Geotechnica Pvt. Ltd, Noida, Uttar Pradesh 201309, India
e-mail: ravi@cengrs.com

S. Gupta
e-mail: sorabh@cengrs.com

G. Chand
Gulshan Homz Pvt. Ltd, Indrapuram, Uttar Pradesh 201014, India

Fig. 9.1 An artist's impression of the proposed building



Geotechnical Assessment

To develop a geotechnical model for the project site, the engineering properties of the various soil layers have to be effectively incorporated. In-situ tests can ensure that the design parameters selected for the are realistic. Poulos [1] states that reliable quantitative data for tall buildings can be generated by conducting field tests such as cone penetrometer, pressuremeter, dilatometer tests and other specialized tests.

To economize the design, pressuremeter tests and cross-hole seismic tests were performed and the design profile was updated. The actual column-loads and the soil parameters were input into a PLAXIS 3D model to assess the stresses and displacements of the raft foundation. For evaluating the settlement, the serviceability limit-state loadings (or the working loads) are applied to the foundation system.

The paper describes the geotechnical investigation performed and the results of the soil–structure interaction analysis that could justify the use of raft foundation without need for piles.

Geological Setting

The site overlooks the Hindon River and covers an area of about 3.5 acres. The soils in Noida are alluvial deposits of the Yamuna and Hindon Rivers and their tributaries.

The alluvial tract (Krishnan [2]) is in the nature of a synclinal basin formed concomitantly with the rise of the Himalayas. The Pleistocene and recent deposits of the Indo-Gangetic Basin are composed of gravels, sands, silts and clays with remains of animal and plants.

The area is a part of the Ganga-Yamuna Doab [3] in the vicinity of the River Yamuna. The soils range from clean sands (*Bhur*) and silts to stiff clays (*Matiar*).

The mixture of sands, silts and clays, usually sandy silt of low plasticity, locally called *Dumat* or loam is a good agricultural soil.

Geotechnical Investigation

Boreholes

The scope of the initial geotechnical investigation included six boreholes to 40 m depth and one borehole to 20 m depth. A layout plan showing the location of borehole and other test locations is illustrated in Fig. 9.2.

Typical bore profiles are illustrated in Fig. 9.3.

The soils consist primarily of alternating strata of sandy silt of low plasticity and silty sand/fine sand. Groundwater was encountered at about 6.5 m depth.

Field SPT values range from 6 to 12 from the ground level to 3–5 m depth, 14 to 25 to 9 m depth and from 21 to 34 to 24 m depth with a few higher values. Below this, the SPT values generally range from 40 to 65 to 40 m depth.

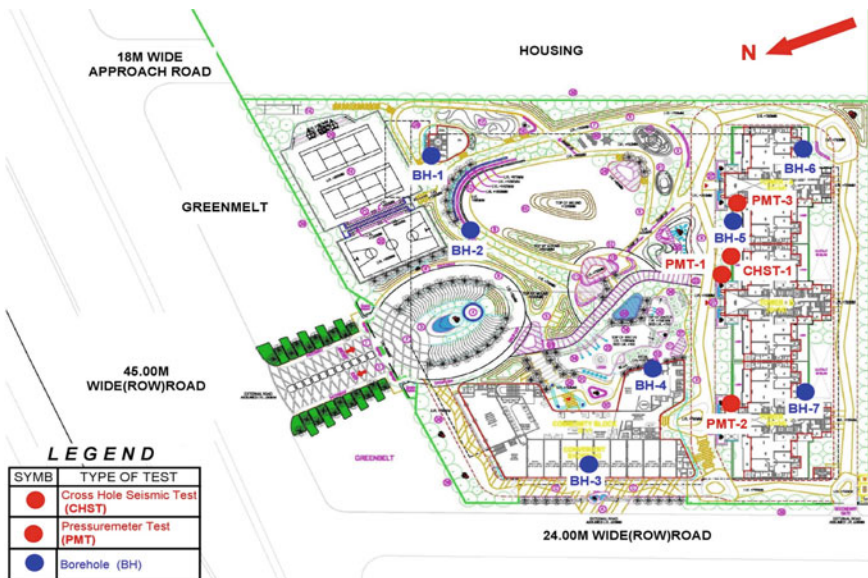


Fig. 9.2 Plan of field investigation

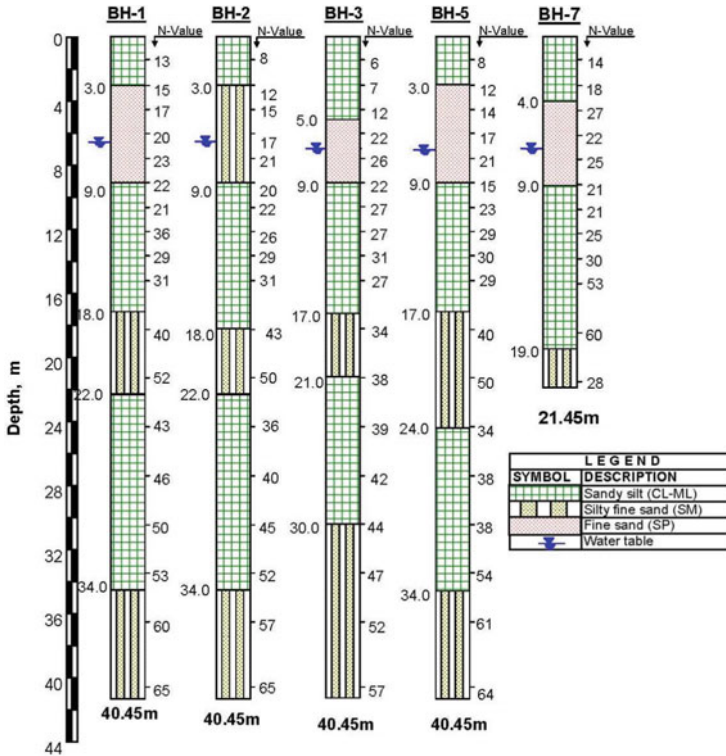


Fig. 9.3 Typical borehole profiles

Based on analysis of the borehole data, the geotechnical investigation agency suggested a safe net bearing pressure of 26.3 T/m² and corresponding gross bearing pressure of 410 kN/m² for raft foundation for a permissible total settlement of 75 mm.

Since the pressure at foundation level was somewhat higher, there was concern that piled-raft may have to be provided. After review of the data, it was decided to perform specialized tests such as pressuremeter tests and cross-hole seismic tests to update the design profile for foundation analysis (Sundaram et al. [4]). The intention was to confirm that raft foundation is a suitable option and to assess the feasibility of economizing the foundation cost.

Pressuremeter Tests

The site had been excavated to 1.5–2 m depth at the time of the study. Pressuremeter tests were performed using a Menard’s GA pressuremeter of 80-bars capacity at three points at locations as illustrated in Fig. 9.2. At each location, the tests were performed at every 5 m depth interval between 10 and 40 m depth. Figure 9.4 show

Fig. 9.4 Pressuremeter test in progress



the tests in progress at site. Typical results (plots of pressure versus volume change) from one borehole are presented in Fig. 9.5.

Based on the pressuremeter data, Fig. 9.6 presents the following plots:

- limit pressure versus depth and
- deformation modulus versus depth.

The design values were selected based on the data.

Cross-Hole Seismic Tests

One cross-hole seismic test (CHST) was performed to 40 m depth at the location illustrated in Fig. 9.2. The test was performed at every 1.5 m-depth interval in the borehole. Test results (plots of primary wave velocity and shear wave velocity versus depth and dynamic Young's modulus and dynamic shear modulus versus depth) are presented in Fig. 9.7.

Haberfield [5] has demonstrated that elastic modulus values obtained from geophysical tests can be correlated to those from pressuremeter tests considering the influence of strain level. He proposed that small-strain modulus values derived from CHST results be reduced by a factor of 0.2 to for static loading condition.

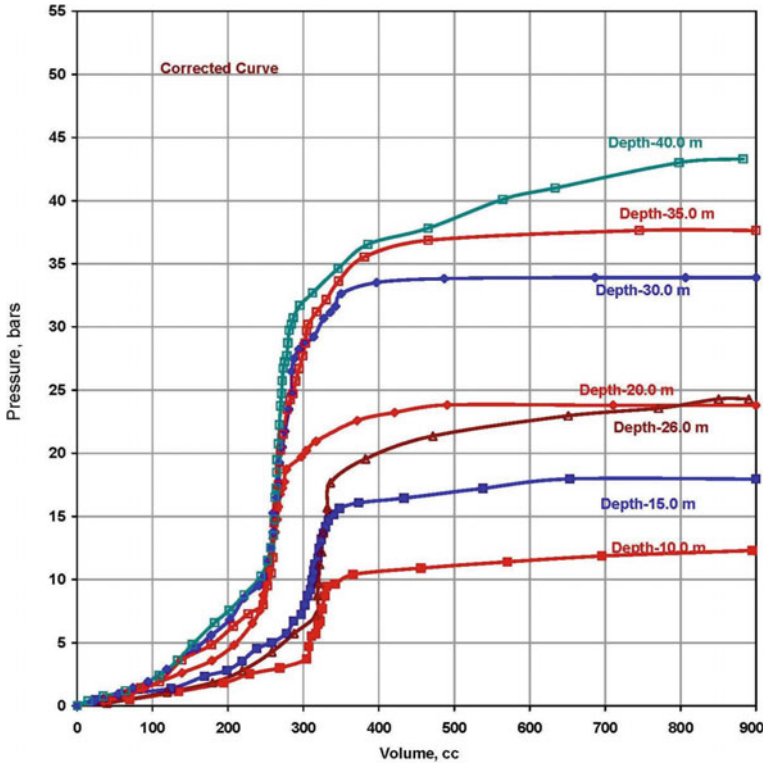


Fig. 9.5 Typical pressuremeter data (PMT-1)

Design Profile

The subsurface profile generally primarily consists of sandy silt and silty sand strata to the maximum explored depth of 40 m. In general, the sandy silt deposits have low plasticity and tend to behave as a granular material. Relative density of the granular soils is typically medium-dense to 18-m depth and dense to 34 m depth below which the sand is very dense in condition.

Reviewing the results of the field tests, the design profile selected for the foundation analysis is presented in Table 9.1.

The groundwater level was considered at 3 m depth for design purpose.

IS: 16700-2017 [6] specifies that total settlement to 125 mm is permissible for rafts and piled-rafts provided that angular distortion of the raft does not exceed 1/500.

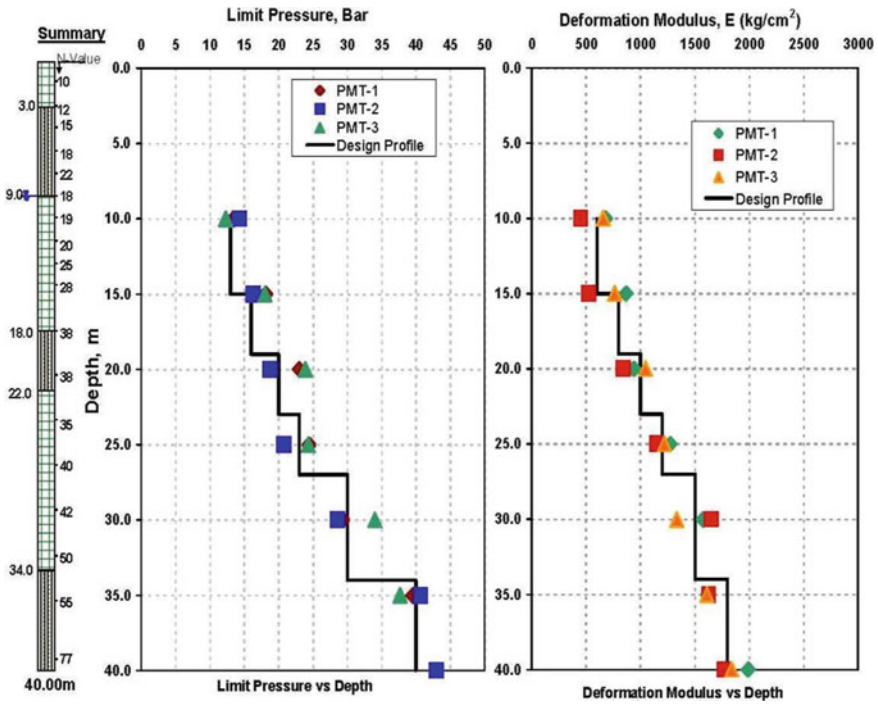


Fig. 9.6 Pressuremeter parameters (limit pressure and deformation modulus) versus depth

Katzenbach et al. [7] divide buildings from a geotechnical standpoint into three categories, designated as GC-1, GC-2 and GC-3 as described below:

- GC-1 comprises construction of buildings with low level of difficulty with regard to the soil such as simple/uniform predictable soil conditions with minimal lateral variations, medium to compact soils with deep groundwater and stable under seismic loads, etc.
- GC-3 comprises complex deposits with soft/weak zones that may experience excessive settlement under foundation loads, cohesive soils that may undergo long-term consolidation, organic soils prone to creep behavior, weathered rock with unfavorable joints or rocks that tend to dissolve or decay, mining sinkholes, etc.
- GC-2 comprises deposits with medium complexity which do not fall under GC-1 or GC-3.

As per our assessment of the strata conditions and groundwater level, the authors are of the opinion that the building planned may be considered in Category GC-2, a project of medium level of complexity.

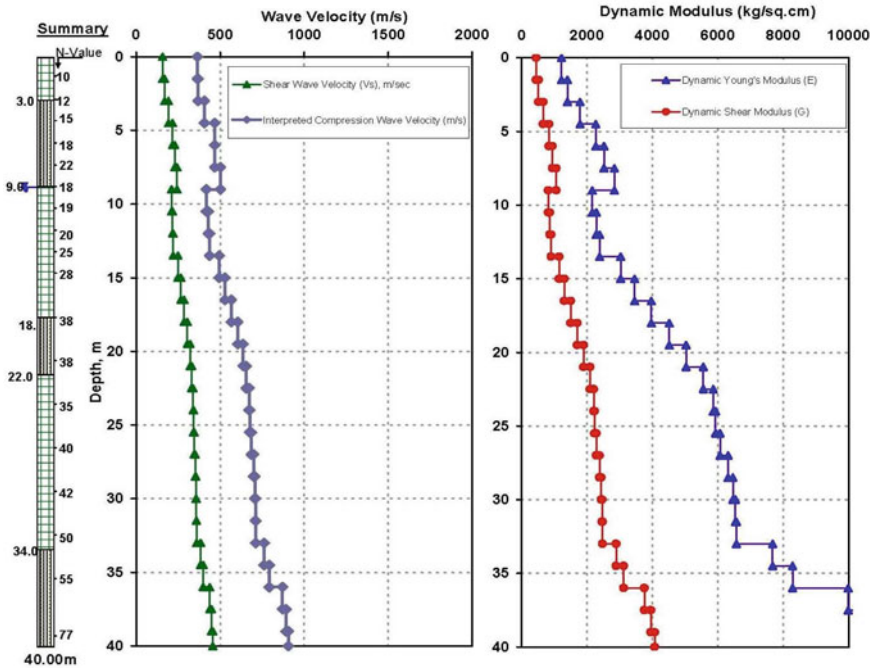


Fig. 9.7 Wave velocity and dynamic moduli versus depth

Table 9.1 Design profile for foundation analysis

Depth, m		Soil classification	γ , kN/m ³	c , kN/m ²	φ°	Field SPT-N values	E , kN/m ²
From	To						
0.0	3.0	Sandy silt	17.2	0	30	11	30,000
3.0	9.0	Silty sand	17.5	0	31	18	50,000
9.0	15.0	Sandy silt	17.8	0	30	20	54,000
15.0	18.0		31	22	59,000		
18.0	22.0	Silty sand	18.4	0	32	38	64,000
22.0	27.0	Sandy silt	18.8	0	33	40	100,000
27.0	34.0		19.0	0	33	45	110,000
34.0	40.0	Silty sand	19.2	0	34	55	140,000

Soil–Structure Interaction

Structure Properties

The structure properties input into the PLAXIS 3D model are as follows:

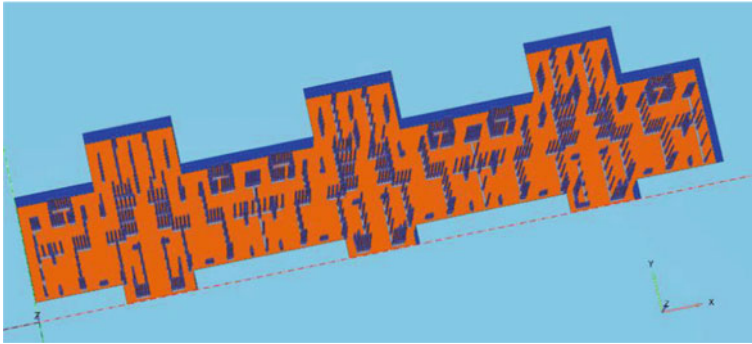


Fig. 9.8 Foundation model

Depth of foundation: 10 m depth
 Raft Thickness, D : 2.0 m
 Raft Modulus of Elasticity, E : 2.7×10^7 kN/m²
 Unit Weight of raft concrete, γ_c : 25 kN/m³
 Poisson's Ratio of raft, μ : 0.15.

The foundation model is illustrated in Fig. 9.8.

Results of Analysis

After performing detailed analysis, the authors proposed that the building be supported on raft foundation as per the configuration in Fig. 9.9. The settlement of the raft foundation and the contact pressure at the soil-raft interface are summarized in Table 9.2.

The computed maximum total settlement is within the permissible value of 125 mm. Also, the differential settlement or angular distortion is less than permissible value of $L/500$. Figure 9.10 presents contours of settlement at the raft-soil interface. The soil-raft contact pressure distribution is presented in Fig. 9.11.

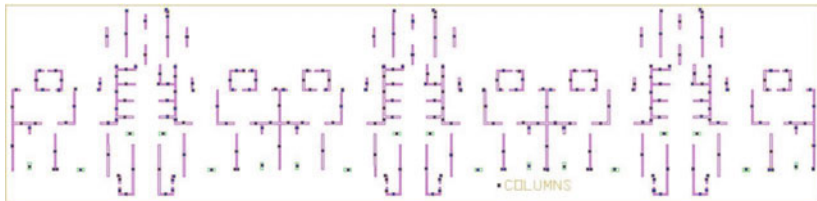


Fig. 9.9 Column configuration

Table 9.2 Summary of raft settlement and pressure

Load combination	DL + LL
Maximum total settlement of raft	80 mm
Maximum pressure on raft	460 kN/m ²
Maximum differential settlement of raft	L/523

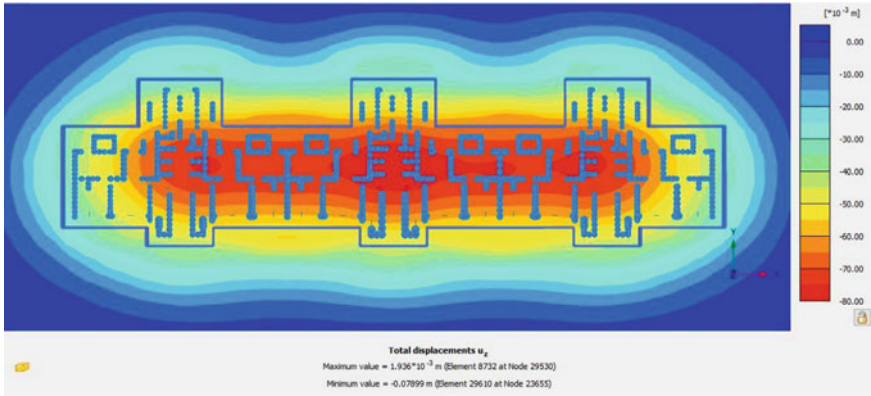


Fig. 9.10 Contours of settlement of raft



Fig. 9.11 Pressure contours at soil–raft interface

The soil spring constants in the different zones of the raft, computed as contact pressure divided by settlement are presented in Figs. 9.12 which were used by the structural engineer to design the raft foundation.

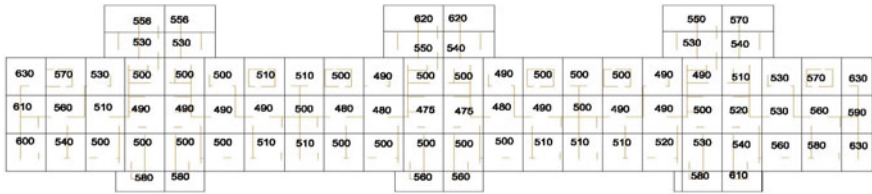


Fig. 9.12 Zoned spring constants



Fig. 9.13 Building under construction

Savings in Cost

The initial assessment based on the permissible settlement of 75 mm as per IS: 1904-1986 [8] suggested that piles may be required. Although detailed assessment was not done, the conventional analysis may have resulted in a piled raft with about 50–60 piles of 1-m diameter. The estimated savings in cost exceeded Rs. 4–5 crores (Indian Rupees 40–50 million). A photograph of the building under construction is presented in Fig. 9.13.

Concluding Remarks

To optimize the foundation design for a 135 m high residential tower planned with Ground + 35 storys + 2 basements in Noida, the borehole data were supplemented with pressuremeter tests and cross-hole seismic tests.

Using the updated design profile, a soil–structure interaction analysis was performed using PLAXIS 3D finite element software used to assess the stresses and settlement of the raft foundation. The analysis justified the elimination of need

for piles and the building was constructed on raft foundations. Zoned spring constants from the analysis were used for the structural analysis.

The reliability of the design could be enhanced by the use of advanced tests and soil–structure interaction. The savings that can be achieved by such an approach was substantial.

References

1. Poulos HG (2012) Foundation design for tall buildings. In: GEOCONGRESS 2012. Geotechnical Special Publication
2. Krishnan MS (1986) Geology of India and Burma, 6th edn. CBS Publishers, Delhi
3. Central Groundwater Board (2009) Groundwater brochure of Ghaziabad District, U.P. CGWB Northern Region, Prepared by R.C. Verma
4. Sundaram R, Gupta S, Gupta S (2019) Foundations for tall buildings on alluvial deposits—geotechnical aspects. In: Latha M (ed) Frontiers in geotechnical engineering. Developments in geotechnical engineering. Springer Nature, Singapore
5. Haberfield CM (2013) Tall tower foundations—from concept to construction. In: Phoon KK et al (eds) Advances in foundation engineering. Research Publishing Services, pp 33–65
6. IS: 16700 (2017) Criteria for structural safety of tall concrete buildings. Bureau of Indian Standards, New Delhi
7. Katzenbach R, Leppla S, Choudhury D (2017) Foundation systems for high rise structures. CRC Press, Boca Raton, FL
8. IS: 1904 (1986 Reaffirmed 2006) Design and construction of foundations in soils: general requirements. Bureau of Indian Standards, New Delhi

Chapter 10

Model Study on Single Pile Subjected to Axial and Inclined Load Embedded in Contaminated Soil



Rutvik K Kalthiya, Jay Dave, and Manish V. Shah

Introduction

Due to the illicit practices of disposing waste without proper treatment by chemical industries, large amounts of land has not only detorited for agriculture purposes, but also has severely impacted the engineering properties of soil. In Nandesari region located on the outskirts of Vadodara, vast amounts of land present there could be eventually used for the expansion of the city, or to meet the growing energy demands of the city by repurposing the land to harness the solar or wind energy. However, rapid economic growth in the past decades has given rise to many industries in this region. And unfortunately, the chemical waste generated by these industries has been blatantly discharged into nearby land, which has not only polluted the soil but has also infiltrated groundwater. On site visit, discoloration of soil and groundwater is conspicuously visible. Large quantities of toxic waste present in the soil and groundwater might have affected the engineering properties of soil. Hence, before any development can take place, a thorough investigation is indispensable to study the changes in soil behavior and avoid any catastrophes.

Since this land would be far more suited for wind and solar farms, pile foundation should be adopted as it aids in increasing the bearing capacity and reducing the settlement of the structure. Additionally, suitable analysis must be carried out which encompasses various load cases such as horizontal loads generated by wind and the vertical loads of the structure. Conventionally, the analysis of vertical and lateral components is carried out separately, and the combined effect of these components is not taken into consideration.

R. K. Kalthiya (✉) · J. Dave · M. V. Shah
L.D. Engineering College, Ahmedabad, Gujarat, India
e-mail: kalthiya.rutvik@gmail.com

M. V. Shah
e-mail: drmvshah@ldcee.ac.in

Although several researchers like Broms (1964), J.B. Hansen (1970), Meyerhof and Ranjan (1973) have tried to establish empirical relationships by experimental results; the variation in these values has befuddled engineers to adopt one method over the other. Also, the effect of contaminated soil on pile capacity subject to axial and inclined compressive loads has been rarely studied. This is the primary impetus behind the focus of the present research paper, where model tests are conducted on a single pile to study the interaction of the pile with both contaminated and non-contaminated soil.

Experimental Investigation

Foundation Medium

In this model study, contaminated soil is procured from Nandesari District, Gujarat State, where industrial pollution is more pronounced. For comparison purposes, a non-contaminated soil of similar classification is collected within 4 km of the site. The properties of the contaminated and non-contaminated soil are determined as per the I.S code, and results obtained are shown in Table 10.1.

Table 10.1 Index and engineering properties of soil

S. No.	Properties of soil	Contaminated soil	Non-contaminated soil
1	Type of soil	SP-SM	SP-SM
2	Specific gravity (G)	2.33	2.67
3	Cohesion (c)	6	4
4	Angle of internal friction (Φ)	30	34
5	Angle of wall friction(δ)	25	28
6	Relative density (D_r)	60	60
7	Density of soil (γ)	16.6	17.2
8	Optimum moisture content (OMC) (%)	11	13
9	Maximum dry density (MDD)	18.8	19.6
10	Liquid limit (%)	27	21
11	pH value of soil	8.0	7.2

Industrial Wastewater

Since industries are not abiding by the regulations of proper treatment of wastewater before discharging in surroundings, it becomes crucial to investigate the water to check for any lethal contaminants. Additionally, the chemicals present in the wastewater could potentially impact engineering properties of soil, so it becomes necessary to analyze the water to determine contaminants and its concentration present. The results of chemical analysis of effluent (industrial wastewater) are given in Table 10.2.

Table 10.2 Chemical analysis of industrial wastewater [1]

S. No.	Parameters	Value
1	pH	7.73
2	Organic matter	4747 mg/l
3	Oil and grease	22 mg/l
4	Chlorides	11,360 mg/l
5	Sulfates	3014 mg/l
6	Magnesium	87.7 mg/l
7	Sodium	2225 mg/l

Tests on Contaminated Soil

Although the contaminated water is chemically tested to determine the pollutant present, it is necessary to find out the changes in the composition of soil in presence of this contaminated water. Hence, X-ray diffraction (XRD) test and EDAX test were conducted on the contaminated soil to analyze the chemicals and elements present in the soil which are present in Tables 10.3 and 10.4 (Fig. 10.1).

Table 10.3 XRD test results

S. No.	Chemical name	Formula
1	Alumina	$K_2Al_{24}O_{37}$
2	Calcium chloride dihydrate	$C_aCl_2 \cdot 2(H_2O)$
3	Aluminum phosphate	$AlPO_4$
4	Silicon dioxide	SiO_2
5	Alunite	$KAl_3(SO_4)_2(OH)_6$
6	Magnesium calcium carbonate	$(C_a, M_g)CO_3$

Table 10.4 EDAX test results

Elements	Weight %	Elements	Weight %
Ca	5.75	K	1.26
Na	1.87	Ti	0.89
Al	9.39	Cr	4.32
S	1.12	Fe	12.34
Cl	0.45	O	43.67

Fig. 10.1 Contaminated soil



Experimental Setup

Model tank of 0.75 m × 0.75 m × 0.75 m is adopted for this test. The dimension of the model tank is determined by taking the pressure bulb of the pile into account. Soil samples for contaminated and non-contaminated model tests are procured from Nandesari District near Vadodara. Engineering properties of soils are mentioned in Table 10.1 (Fig. 10.2).

Two concrete piles having 360 mm and 450 mm embedded length are used in the test procedure having *L/D* ratio of 8 and 10, respectively. The piles of 45 mm diameter are casted from a PVC pipe, and 6 mm of steel reinforcement is provided at the center of the pile. The piles were cured for 28 days to achieve its optimum strength. Mechanical screw jack (5 ton capacity) and a proving ring of 50 kN capacity were used to apply load on the pile.

Experimental assembly consisted of a C section loading frame with capability of applying 30°, 45° and 60° inclined loads at the top of the pile cap as shown in Fig. 10.3. Steel chains were used to place the pile in center, equidistant from all four sides and its head extending 10 cm above the soil surface. After the pile was carefully supported with the help of chains, the tank was filled with soil with 60%

Fig. 10.2 X-ray diffraction peaks contaminated soil

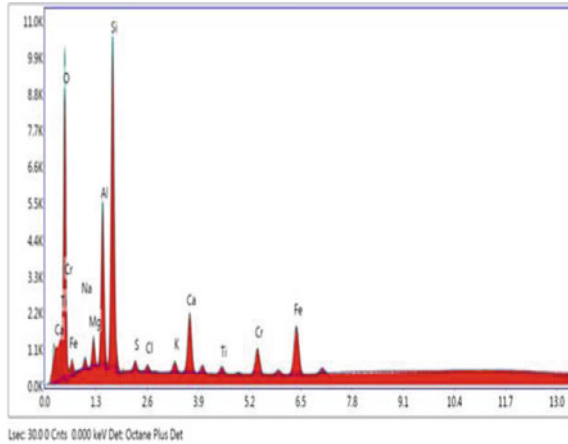


Fig. 10.3 Experimental setup for inclined load



relative density in five layers of 150 mm thickness. Round bottom hammer of 0.15 m diameter and 50 N weight was used to compact the soil to achieve the intended density of 16.6 kN/m³ for contaminated soil and 17.2 kN/m³ for non-contaminated soil. Two dial gauge of sensitivity 0.01 mm were placed on the top and the side of pile cap to measure vertical and lateral displacement.

Research Methodology

As per I.S.2911 (part 4) [2] maintained load test method (MLT) was adopted. The failure load was taken to be that load at which the load versus pile head displacement curve passes into a steep and fairly straight tangent.

Theoretically, the value of vertical load carrying capacity of the pile is calculated using the I.S 2911 Code method:

$$Q_u = A_p \left(C N_c + \frac{1}{2} N_\gamma \gamma D + P_D N_q \right) + (K P_{Di} \tan \delta + \alpha C) A_s \quad (10.1)$$

where

Q_u	ultimate bearing capacity,
A_p	c/s area of pile toe,
D	diameter of pile,
γ	effective unit weight of soil,
P_D	effective overburden pressure at pile toe,
N_c, N_q, N_γ	bearing capacity factors,
P_{Di}	effective overburden pressure for pile shaft,
δ	angle of wall friction between pile and soil,
A_s	surface area of pile.

The theoretical value of lateral load carrying capacity of the pile is calculated using the Broms [3] method for short restrained pile.

$$Q_H = 1.5 Y L^2 D K_p \quad (10.2)$$

where

K_p	coefficient of passive earth pressure,
L	length of the pile.

The pile rigidity is related to a stiffness factor T [4] which is expressed as,

$$T = \sqrt[3]{\frac{EI}{yh}} \quad (10.3)$$

where EI = stiffness of the pile and h = coefficient of subgrade reaction. The stiffness factor is used to determine the behavior of the pile. If $L \geq 4T$ then the pile behaves as a long flexible pile and for $L \leq 2T$ then the pile behaves as a short rigid pile. Because either piles of L/D ratio 8 and 10 are not less than $2T$ or greater than $4T$, the behavior of the pile is intermediate pile.

Since the length of the pile was closer to $2T$ than $4T$ and rotational failure was more dominant than formation of plastic hinges, lateral load carrying capacity was calculated as a short rigid pile.

The ultimate inclined load carrying capacity Q_{ui} of a vertical pile subjected inclined load can be expressed by the interaction equation of Meyerhof [5–7] given as

$$\left(\frac{Q_u \cos \alpha}{Q_a} \right)^2 + \left(\frac{Q_u \sin \alpha}{Q_n} \right)^2 = 1 \quad (10.4)$$

where α = inclination of the load with respect to the vertical axis of pile, Q_a and Q_n are the vertical and lateral ultimate capacity of pile, respectively. The theoretical value of vertical and inclined ultimate load carrying capacity of pile are compared with the experimental value of ultimate load carrying capacity of pile.

Inclined loads can be divided into two components: vertical and lateral. With increase in angle of load inclination, analysis of lateral load becomes important since it is responsible for the failure of the pile. Hence, P - Y curves under static conditions were theoretically developed using methodology proposed by Reese and Matlok (1974). The py curve then is used to determine the deflection and moment across the pile for design purposes. From the lateral component of the obtained experimental inclined load, the maximum moment and maximum deflection (displacement) are calculated using the py curve.

P - Y curves constructed for both contaminated and non-contaminated soil are primarily used to estimate the resistance offered by the soil subject to lateral loading. This numerical approach can be used to analyze the interaction of a pile with soil with varying depth and soil type. Ideally the P - Y curve should be generated from a full-scale model test using an instrumented pile; however, this method is not cost-effective. Using the P - Y curve other parameters such as moment and deflection can be determined. The following equations were used to estimate the ultimate resistance of soil per unit length of pile.

For Soil close to the ground surface

$$P_{st} = vx \frac{K_0 x \tan \phi \sin \beta}{\tan(\beta - \phi) \cos \alpha} + \frac{\tan \beta}{\tan(\beta - \phi)} (d + x \tan \beta \tan \alpha) + K_0 X \tan \beta (\tan \phi \sin \beta - \tan \alpha) - K_A d \quad (10.5)$$

For Soil well below ground surface

$$P_{sd} = K_A d \gamma x (\tan^8 \beta - 1) + K_0 d \gamma x \tan \phi \tan^4 \beta \quad (10.6)$$

where $\alpha = \frac{\phi}{2}$, $\beta = 45^\circ + \frac{\phi}{2}$, $K_0 = 0.4$, $K_A = \tan^2(45^\circ - \frac{\phi}{2})$ and γ = effective unit weight of soil.

Results and Discussions

Load Versus Vertical Displacement

Vertical displacement of the pile having L/D ratio 8 and 10 is shown in Figures 10.4 and 10.5.

The vertical load tests indicate greater load carrying capacity for non-contaminated soil for both the piles. Additionally, with increase in L/D ratio subsequent increase in load carrying capacity is observed. Experimentally, failure load is

Fig. 10.4 Load versus settlement curve for $L/D = 8$

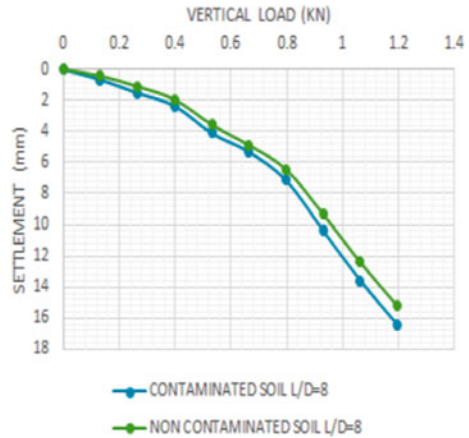
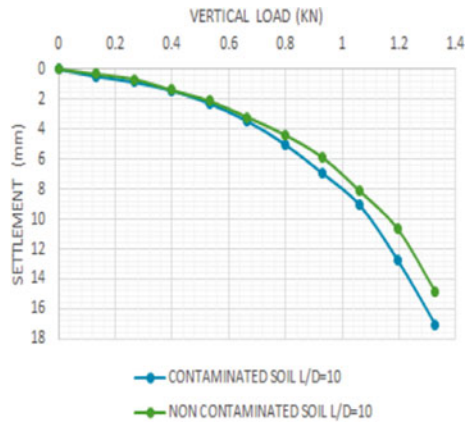


Fig. 10.5 Load versus settlement curve for $L/D=10$



calculated by plotting two tangent lines along the initial and latter portions of the load–displacement curves [8–10]. Although non-contaminated soil has a greater load carrying capacity, the difference in the value is less.

Effect of Angle of Load Inclination and L/D Ratio

Of the two components of inclined load, the lateral component is the governing load for the model tests conducted at 30°, 45° and 60° angles of inclination from the vertical axis. Also, from Fig. 10.7, we can clearly deduce the increase in bearing capacity with increase in L/D ratio. However, from Fig. 10.6, an increase in angle of load inclination from 30° to 60° and decrease in ultimate lateral load carrying capacity are observed.

For the lateral carrying capacity, passive resistance offered by the soil plays a considerable role in determining the effect of soil on the pile. Horizontal modulus of subgrade reaction is dependent on many factors such as the behavior of pile–soil and

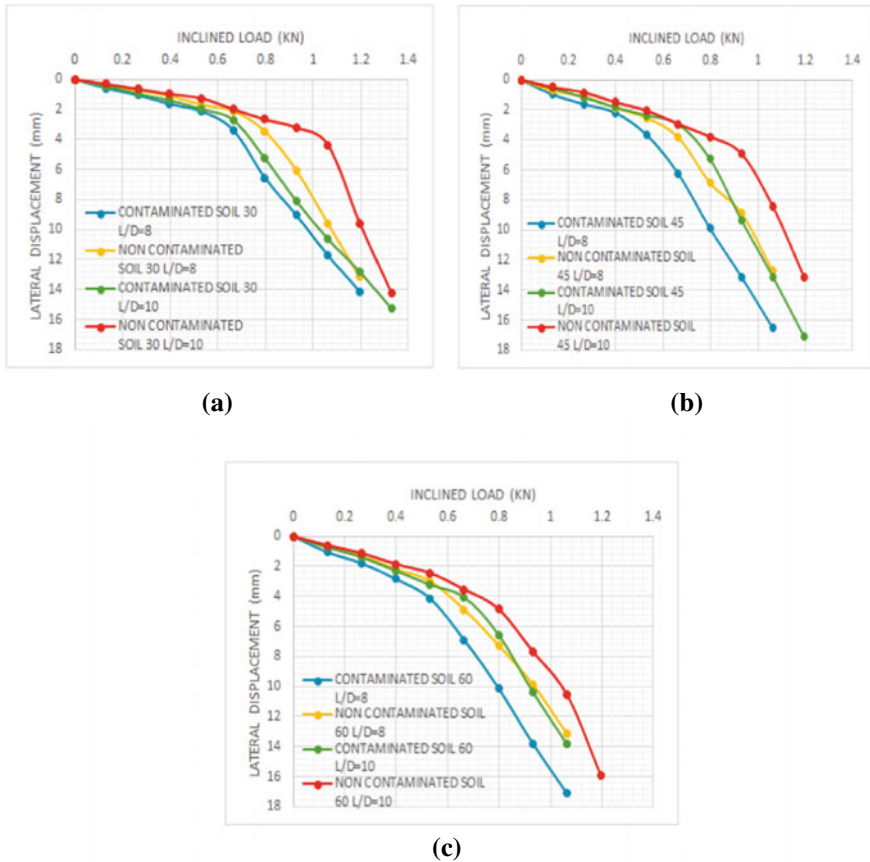


Fig. 10.6 Inclined load versus lateral displacement for 30°, 45° and 60° load inclination. **a** 30° load inclination. **b** 45° load inclination. **c** 60° load inclination

size of pile. Since the length of the pile is greater for L/D ratio 10, more surface area is available for soil to resist the movement of the pile. This increase in mobilization of passive resistance is responsible for the increase in ultimate load carrying capacity of the pile. Furthermore, horizontal modulus of subgrade reaction for contaminated soil differs from non-contaminated soil. From the experimental results of model tests and soil tests, it is evident that the resistance offered by non-contaminated soil is greater compared to contaminated soil.

Effect of Chemicals on Index and Engineering Properties of Soil

The index and engineering properties of the contaminated and non-contaminated soil are determined as per the Indian standard code. Specific gravity of soil is an important characteristic in determining how much heavier or lighter soil particles are compared to waters at 25 °C. As shown in Table 10.1, specific gravity of soil

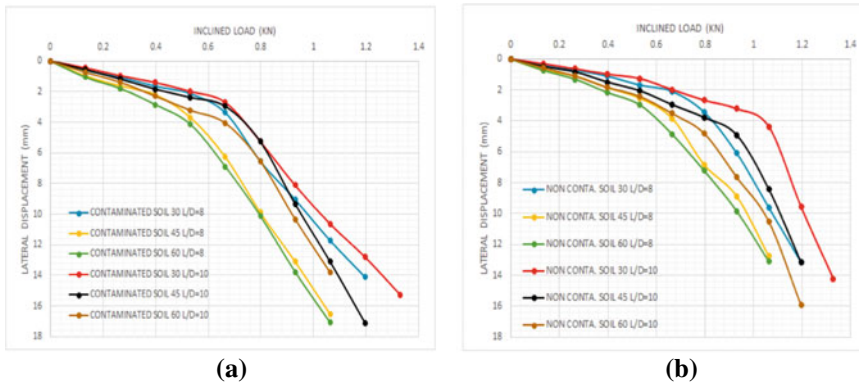


Fig. 10.7 Inclined load versus lateral displacement for $L/D = 8$ and 10. **a** For $L/D = 8$ and 10 contaminated soil. **b** For $L/D = 8$ and 10 non-contaminated soil

clearly decreases in the presence of contaminants [11]. Moreover, angle of internal friction is also found to decrease, which directly affects the behavior of pile as seen in the experimental results. This is mainly caused due to seepage of contaminated water in the pore spaces of sand and by assuming the formation of hydrate sulfates in the presence of excess water. Hydrate sulfate undermines the bonds between the soil particles, thus decreasing the soil strength. Other engineering properties are also affected in similar ways.

Analysis of Soil Pile Interaction Using P–Y Curve

Using P – Y curves, deflection is determined along the depth of the pile. Figure 10.8 shows the deflection pattern observed along the end of the pile theoretically. Deflection is determined using the ultimate lateral load carrying capacity of the pile and the P – Y curve constructed for both the soil which are shown in Fig. 10.8 [12–14]. Since the ultimate lateral load carrying capacity of both contaminated and non-contaminated soil is different under the similar loading conditions, observed deflection also varies significantly. Though pile resisting in non-contaminated soil shows more deflection as shown in Fig. 10.8, the value of ultimate lateral load for which deflection is determined is also significantly larger. Additionally, the deflection pattern of the pile along the depth for both contaminated and non-contaminated soil reveals that the behavior of the pile is intermediate (Fig. 10.9).

Comparison of Experimental Results with Theoretical Results of Ultimate Load Carrying Capacity of Pile

From Tables 10.5 and 10.6, we can ascertain that the experimental value of ultimate inclined load carrying capacity is validated with the theoretical value of ultimate inclined load carrying capacity calculated using Meyerhof interaction equation without any significant discrepancies in values. As shown in table, for the pile

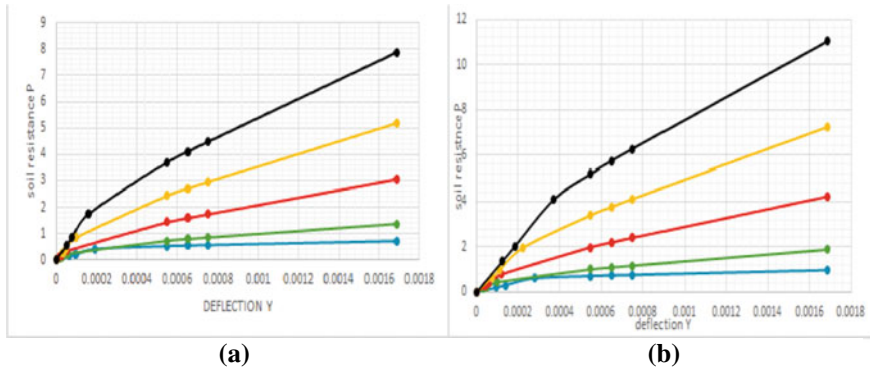


Fig. 10.8 a P - Y curve for contaminated soil, b P - Y curve for non-contaminated soil

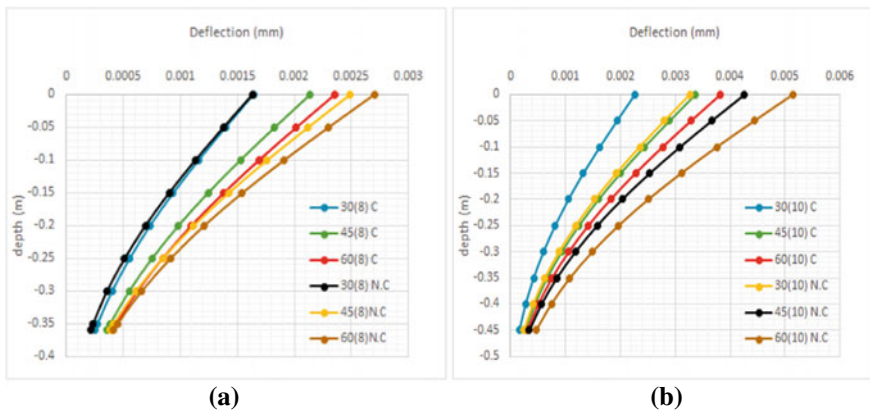


Fig. 10.9 Deflection pattern of pile calculated using P - Y curve. a For $L/D = 8$. b For $L/D = 10$

subjected to inclined loading at 60° of L/D ratio 10 the theoretical value is over-estimated by 4.75%, which isn't a considerable deviation. Also, with subsequent increase in angle of inclination, reduction in the ultimate bearing capacity of the pile is observed. Maximum ultimate bearing capacity of 1.04 kN is observed for a pile of L/D ratio 10 subject to axial load resting in non-contaminated soil. Maximum deviation of 35% is observed between the values of contaminated and non-contaminated soil subjected to similar loading conditions.

From Tables 10.7 and 10.8, it becomes apparent that the experimental value of deflection from the model test is comparable to the theoretical value of deflection determined from the P - Y curve without significant variation. For design purposes, values of moments along the pile depth are also determined using the P - Y curve. Maximum moment and deflection of 0.1361 kN m and 5.8 mm are

Table 10.5 Theoretical and experimental ultimate bearing capacity value of pile in contaminated soil

Degree of loading	<i>L/D</i> ratio	Theoretical value (kN)	Experimental value (kN)
0	8	0.582	0.67
0	10	0.746	0.885
30	8	0.532	0.61
30	10	0.728	0.75
45	8	0.493	0.52
45	10	0.711	0.73
60	8	0.461	0.45
60	10	0.695	0.68

Table 10.6 Theoretical and experimental ultimate bearing capacity value of pile in non-contaminated soil

Degree of loading	<i>L/D</i> ratio	Theoretical value (kN)	Experimental value (kN)
0	8	0.746	0.81
0	10	0.964	1.04
30	8	0.670	0.70
30	10	0.925	1.05
45	8	0.613	0.65
45	10	0.891	0.93
60	8	0.568	0.58
60	10	0.859	0.82

obtained for piles of *L/D* ratio 10 subjected to 60° load inclination resting in non-contaminated soil. Difference of maximum deflection and moment in contaminated and non-contaminated soil is approximately 20% and 25%, respectively. Moreover, 12% difference in value is observed between theoretical and experimental values deflection.

Table 10.7 Theoretical and experimental value of displacement of pile in contaminated soil

Degree of loading	L/D ratio	Theoretical value of displacement from P - Y curve (mm)	Experimental value of lateral displacement from inclined load test (mm)	Theoretical value of max. moment from P - Y curve (kN m)
30	8	1.64	2.2	0.0511
30	10	2.26	2.7	0.06486
45	8	2.13	2.6	0.06279
45	10	3.4	3.5	0.09292
60	8	2.35	3.1	0.06746
60	10	3.82	3.8	0.1054

Table 10.8 Theoretical and experimental value of displacement of pile in non-contaminated soil

Degree of loading	L/D ratio	Theoretical value of displacement from P - Y curve (mm)	Experimental value of displacement from inclined load test (mm)	Theoretical value of max. moment from P - Y curve (kN m)
30	8	1.63	2.1	0.05674
30	10	3.26	3.8	0.09205
45	8	2.49	2.9	0.0772
45	10	4.26	4.9	0.1176
60	8	2.70	3.2	0.08413
60	10	5.14	5.8	0.1361

Conclusion

- Tests on contaminated soil are clearly indicative of the changes in the engineering properties of soil in Nandesari District. The contaminated soil was found to have lower angle of internal friction, lower specific gravity and lower maximum dry density. Formation of hydrate sulfate is potentially the reason behind the decrease in soil strength. Consequently, horizontal modulus of subgrade reaction value is more for non-contaminated soil than contaminated soil.
- There is no significant variation observed in the ultimate load carrying capacity of the pile subject to axial load for both contaminated and non-contaminated soil.
- With increase in L/D ratio, both vertical and inclined load carrying capacities are found to increase. With increase in pile length, more skin friction and passive resistance are mobilized on the pile subject to axial and inclined loading. Additionally, there is a direct correlation between increase in angle of load inclination and reduction in ultimate load carrying capacity of pile.

- Experimental value of ultimate load carrying capacity of pile subjected to inclined loading is comparable with the theoretical values determined using Meyerhof's interaction equation.
- Also, the P - Y curve generated was successful in ascertaining the deflection observed in inclined model tests. Since the solution of P - Y curves rests on the assumption that governing load is lateral load and there is no effect of vertical component of load on lateral deflection, the deflection values estimated are not completely accurate. Approximate difference of 12% is observed in experimental and theoretical values determined using the P - Y curve.

Acknowledgements Authors are thankful to Prof. Dr. C. R. Sanghavi Head of Applied Mechanics Department and Prof. Dr. R. K. Gajjar Principal of L.D. College Of Engineering for providing all required research facilities for this project.

References

1. Resol DA, Karkush MO (2017) Geotechnical properties of sandy soil contaminated with industrial wastewater. *J Eng Sci Technol* 12(12):3136–3147
2. I.S.-2911, Part-4 (1985) Code of practice for design and construction of pile foundation
3. Poulos HG (1971), Broms (1964), Hansen (1970) Behaviour of laterally loaded piles: I—single piles. *J Soil Mech Found Div ASCE* 97(5)
4. Matlock H (1974), Reese LC (1970) Generalized solutions for laterally loaded piles. *J Soil Mech Found Div ASCE* 86:63–91
5. Meyerhof GG (1981a), Ranjan G (1972) The bearing capacity of rigid piles under inclined loads in sand. I: vertical piles. *Can Geotech J* 9:430–446
6. Issac S, Thomas S (2015) A model study on pile behaviour under inclined compressive loads in cohesion less soil. *Int J Eng Res Technol* 4(11)
7. Karkush MO (2016) Impact of soil contamination on the response of piles foundation under a combination of loading. *Eng Technol Appl Sci Res* 917–922
8. Bhardwaj S, Singh SK (2014) Pile capacity under oblique loads—evaluation from load—displacement curves. *Int J Geotech Eng*
9. Chari TR, Meyerhof GG (1983) Ultimate capacity of rigid single piles under inclined loads in sand. *Can Geotech J* 20
10. Issac S (2017) Comparative study of lateral pile behaviour in cohesion less soil under inclined compressive loading with P-Y curve method. *Int J Innovative Res Sci Eng Technol* 6(6)
11. Irfan M, Chen Y (2018) Geotechnical properties of effluent-contaminated cohesive soils and their stabilization using industrial by-products. *Processes*
12. Tomlinson MJ, Woodward J (2014) *Pile design and construction practice*, 6th edn. Taylor and Francis group, Oxford Shire. <https://doi.org/10.1201/b17526>
13. Murthy VNS (2007) *Advanced foundation engineering* 1st edn
14. Prakash S, Sharma HD *Pile foundation in engineering practice*

Chapter 11

Behavior of Combined Piled-Raft Foundation Under Eccentric Loading



Hannanur Rahaman, Plaban Deb, and Sujit Kumar Pal

Introduction

For the construction of any structure, raft foundation is generally used to transfer load to soil in the case when a soil layer is available at a near depth with adequate bearing capacity. Sometimes, if raft is placed over a soil with adequate bearing capacity, it also induced an excessive settlement. To minimize this excessive settlement, pile foundation along with this raft foundation can be used. In case of very tall building or structure, wind forces become a considerable design factor and due to this wind forces eccentric load will act on the structure which may result in differential settlement. Various researchers [1, 2] examine the behavior of pile while use as piled raft and pile groups in sand. The interaction behavior between pile and raft is a very important factor while designing piled-raft foundation [3]. Sawwaf [4] has reported the inclusion of short piles and pile arrangements are important factors on enhancing the maneuver of modeled raft loaded at an eccentricity on sand. The raft size, the raft thickness, the piles diameter and lengths are important design parameter of piled-raft foundation and the effect of which are studied by various researchers [5–7]. Soil type has considerable effect on capacity, changing it properties will change the utmost load carrying capacity of any particular foundation [8]. The raft thickness has insignificant effect on distribution of load on both raft and piles [9]. Patil et al. [10] studied addition of piles close to raft edges increase capacity and the settlement. The cushion layer thickness and spacing between piles in pile group effect on the load settlement behavior [11]. Deb and Pal [12] reported the differential settlement may be

H. Rahaman (✉) · S. K. Pal
Department of Civil Engineering, National Institute of Technology, Agartala 799046, India
e-mail: rahamanhr04@gmail.com

P. Deb
Department of Civil Engineering, G H Raisoni College of Engineering and Management,
Wagholi, Pune 412207, India

minimized by using raft and pile foundation together as combined foundation. Deb and Pal [13] studied the nonlinear behavior of piled-raft foundation and analyzed the effect of load acting vertically on the response in the lateral direction. Due to limited research work on the effect of eccentric load on piled-raft foundation an attempt has been made to analyze the behavior subjected to eccentric vertical loading. Therefore, the major objectives of this study are:

1. To evaluate the load settlement characteristics of connected piled-raft foundation under eccentric vertical loading.
2. To examine the piled-raft foundation behaviors due to the change of soil's Young's modulus.
3. To examine the load shared by pile under eccentric loading condition.

Numerical Modeling

Modeling of Piled-Raft-Soil System

In this study, ABAQUS/CAE software is used to create the three-dimensional model of pile, raft and soil continuum. Mohr–Coulomb plasticity is chosen for the nonlinear stress–strain characteristics of the soil, raft and pile. Deformable three-dimensional solid element with solid extrude feature is used to model pile and raft. Different datum planes are created in pile, raft and soil which are essential during assemble of all the parts. Material properties of all the parts are created in property module and assigned the properties. Raft is placed over the soil with surface to surface interface in the contact surface between them. Master–slave concept is used while modeling surface interface. For simulating the loading condition, at first geostress may be applied at the soil; at second stage own-weight of the pile and raft is considered and lastly the load is applied in the vertical direction.

Boundary Condition and Mesh Pattern

Boundary conditions are required to confine the soil in any particular direction. For all the bottom nodes, Encastre type of boundary condition is chosen so that translation and rotation movement of soil can be restricted. In the same way, two more boundary conditions are created in X–Y and Z–Y faces by choosing ZSYMM and XSYMM type of boundary condition. Mesh size should be chosen carefully as it has considerable effect on the results. In this modeling, fine meshes are used at the location where load is acting and coarse meshes are used over the remaining part of the soil and throughout same meshes are used in pile and raft. Triangular prism is applied in pile and linear brick element is chosen for soil and raft. The meshing pattern of the pile, soil continuum and raft is shown in Fig. 11.1.

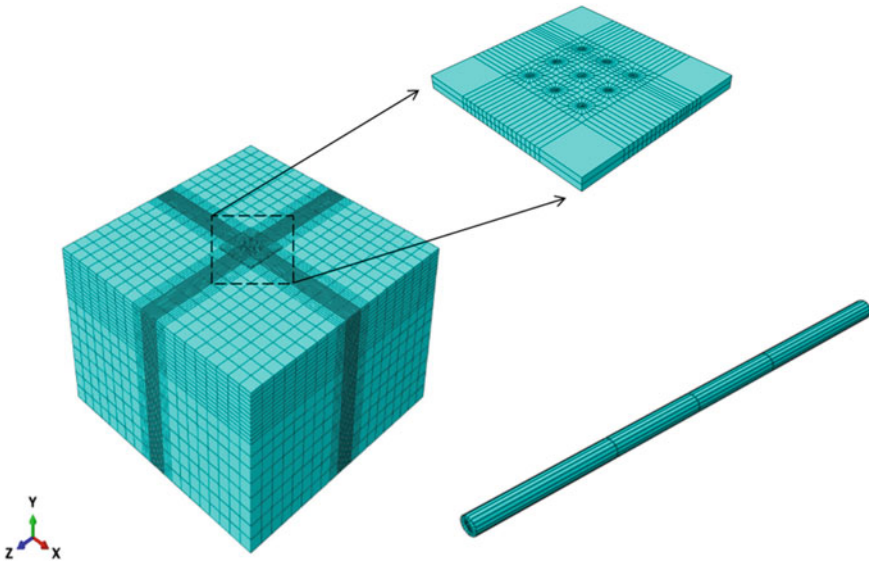


Fig. 11.1 Meshing pattern of the pile, raft and soil continuum

Test Program and Material Properties

Raft size of 14 m × 14 m × 1 m and pile of 15 m length and 0.6 m diameter is considered in this numerical modeling. Different spacing to dia. ratio (s/d) of pile such as 3, 4 and 5 is chosen for this analysis. Three type of pile group such as 3 × 3, 4 × 4 and 5 × 5 configuration are modeled for the analysis. For the effective analysis of settlement and load, the ultimate load is taken at 10% settlement of raft width, i.e., $w = 0.1B$ (where, w is settlement and B is raft width). Specifications of the piled-raft element and general properties of dry sand used for numerical modeling are presented in Table 11.1.

Table 11.1 Specifications of the piled-raft element and general properties of dry sand used for numerical modeling

Parameters	Prototype dimension	Properties of dry sand	Value
Width of raft (B)	14 m	Dry density (kN/m^3)	16.50
Thickness of raft (t)	1 m	Specific gravity	2.63
Dia. of pile (d)	0.6 m	Poisson's ratio	0.3
Length of concrete pile (L)	15 m	Friction angle	30°
Length to dia. ratio (L/d) of pile	25	Relative density	60%
Eccentricity to width ratio (e/B)	0, 0.1, 0.25, 0.4	E_P/E_S	1000

Note E_P = Young's modulus of pile = 22.4 GPa, E_S = Young's modulus of sand

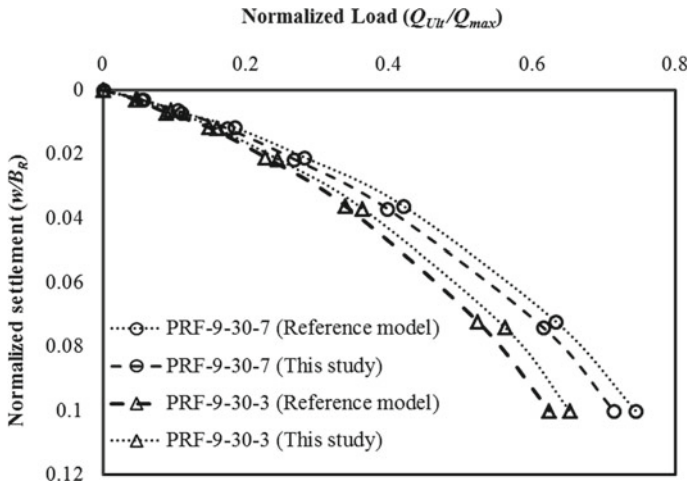


Fig. 11.2 Comparison of this model with the numerical model of Deb and Pal [12]

Validation

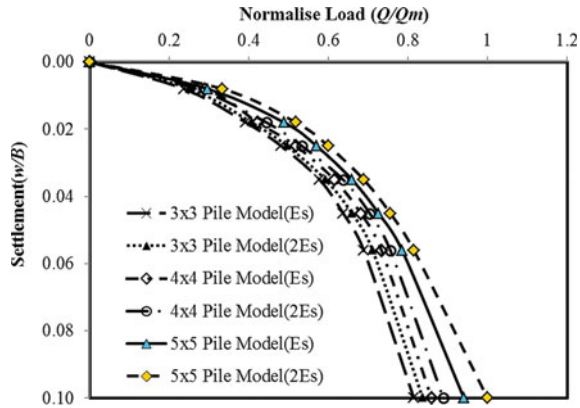
Better accuracy of any numerical model can be check by comparing it with other published numerical model. For the validation of the numerical model prepared in this study, the analysis is compared with the publish work of Deb and Pal [12]. A 3×3 pile configuration similar to reference model with raft width of 30 m and pile spacing to diameter ratio of 3 and 7 are prepared for comparison purpose. The load settlement response obtained from numerical analysis is compared with reference model and presented in Fig. 11.2. From the below figure, it can be ensured as load settlement responses obtained from this study matches very close to load settlement responses obtained from reference model.

Result and Discussion

Effect of Number of Pile and Young’s Modulus of Sand on Vertically Loaded Piled-Raft Foundation

Each model is analyzed for eccentric load with eccentricity of $e/B = 0, 0.1, 0.25, 0.4$ and the responses are recorded. The utmost load carrying capacity of all the configurations is obtained for the settlement of the foundation equal to 10% of raft width as per Deb and Pal [14]. The variation of normalized load settlement response for different pile configurations and Young’s modulus of dry sand in case of e/B of 0.1 are shown in Fig. 11.3. Figure reveals that with increase of number of pile

Fig. 11.3 Variation of load versus settlement curve for $e/B = 0.1$



from 9 to 25 in piled-raft foundation, the utmost load carrying capacity of foundation increases by 16%. With number of pile increases, contact surface between the pile and dry sand also increases which leads to enhance in capacity. It may also be found that the ultimate load carrying capacity increases with higher values of soil’s Young’s modulus as the stiffness of soil increases with increase in Young’s modulus. Load carrying capacity can be increases by 3–4% by changing the values of soil’s Young’s modulus from 1 to $2 E_s$.

Eccentric Vertical Load Carried by the Each Row Pile

Vertical load settlement curves are shown in Fig. 11.4 for different rows of pile group for s/d ratio of 4 and e/B ratio of 0.1. The capacity under eccentric vertical load subsequently reduces from row 3 to 1. From the figure, it is found that due to eccentric loading around 24%, more load is developed in the 3rd row of pile group as compare to the 1st row.

Variation of the Vertical Eccentric Load for the Different E_s Values

The normalized vertical eccentric load carrying capacity of different pile groups varies with Young’s modulus of dry sand used in this modeling. The variation of 3×3 pile group for different e/B ratios has shown in Fig. 11.5. It is found that the normalized vertical eccentric load carrying capacity increases with increase values of E_s and decreases when the e/B ratio increases. In case of eccentric load, the nearby piles take the maximum amount of load initially and get mobilized first, and after mobilization of nearby piles, the additional load takes by adjacent piles but in

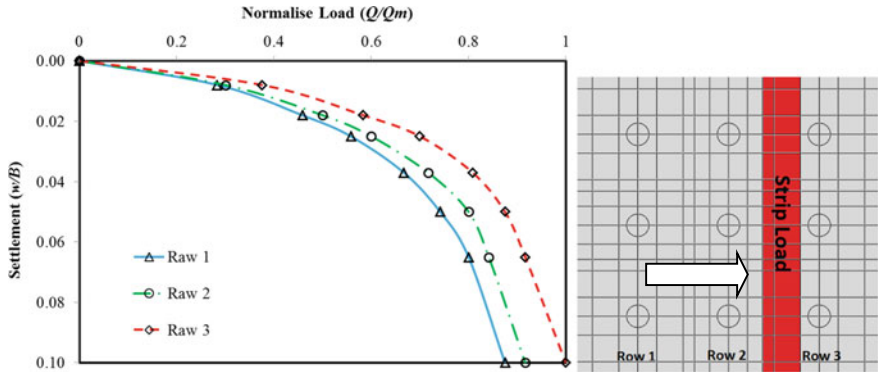


Fig. 11.4 Eccentric vertical load carried by the each row pile

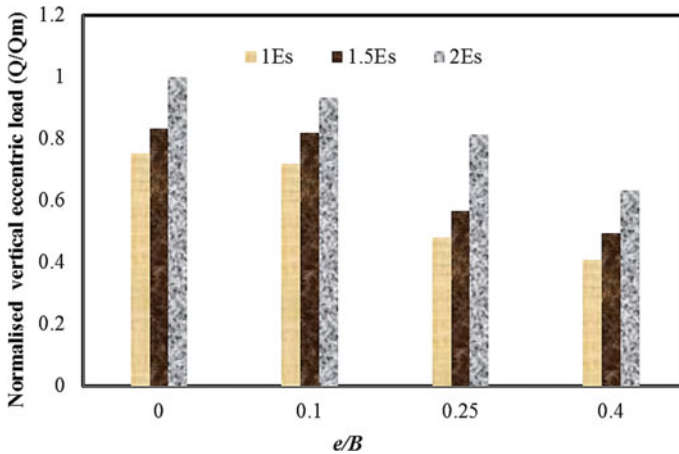


Fig. 11.5 Variation of vertical eccentric load for different E_s values

vertical load, all the piles mobilizes together. It is further observed that when the e/B ratio increases, the pile numbers which take the initial load become less and the normalized vertical eccentric load carrying capacity decreases.

Load Sharing Mechanism Under Eccentric Loading

The load transfer system of raft and piles as combined foundation is quite different from the individual raft and pile. In case of combined foundation of pile and raft, the total applied load is carried by both raft and pile. Eccentric load carried by pile group with different e/B ratios is shown in Fig. 11.6. Under eccentric loading, all the pile

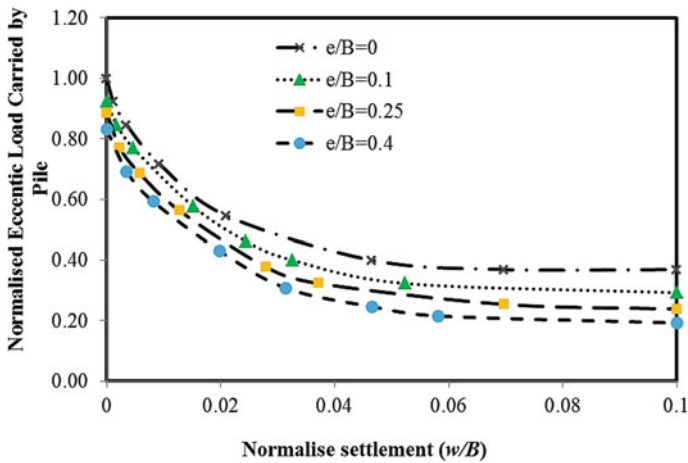


Fig. 11.6 Vertical eccentric load carried by 4 × 4 pile group with different e/b ratio

do not take equal load. Therefore, the maximum amount of loads are taken by nearby piles, where eccentric load is developed and the average load share by all the piles in case of eccentric loading becomes lower as compare to uniform vertical loading. After some period of eccentric loading, the piles near the vicinity of the eccentric loading get mobilized, and the remaining amount of loads are shared by raft. Due to this, the load shared by piles becomes lower with the eccentricity increases.

The normalized vertical eccentric load is carried by each pile group varies with Young’s modulus of dry sand. Figure 11.7 shows such variation of 4 × 4 pile group. From the below figure, it is noticed that load which is carried by pile decreases with increase of e/B ratio, and with increase in soil’s Young’s modulus, the load carried by the pile increases. Stiffness of soil increases with Young’s modulus, so the same pile can take higher load in the soil as the pile–soil interface becomes stiffer with higher value of soil’s Young’s modulus.

Effect of the s/d Ratio on Ultimate Load Carrying Capacity

For modeling of the foundation, different pile spacing in group pile to diameter ratio, i.e., 3, 4, 5 is used in this modeling, and the effect of the s/d ratio on ultimate load carrying capacity with eccentricity $e/B = 0.25$ is shown in Fig. 11.8. From the analysis, it is noticed that with lower s/d ratio, the stress field generated around each pile overlaps each other, and as s/d ratio increases, overlap stress field zone reduces. So, the load carrying capacity increases with increase in s/d ratio.

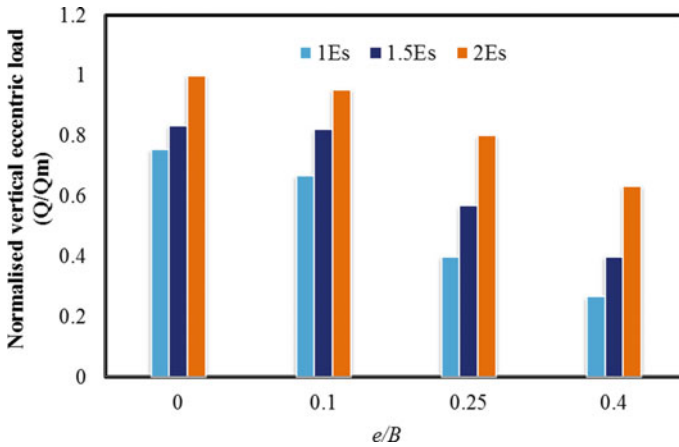


Fig. 11.7 Variation of normalized vertical eccentric load carried by 4 × 4 pile group with different E_s values

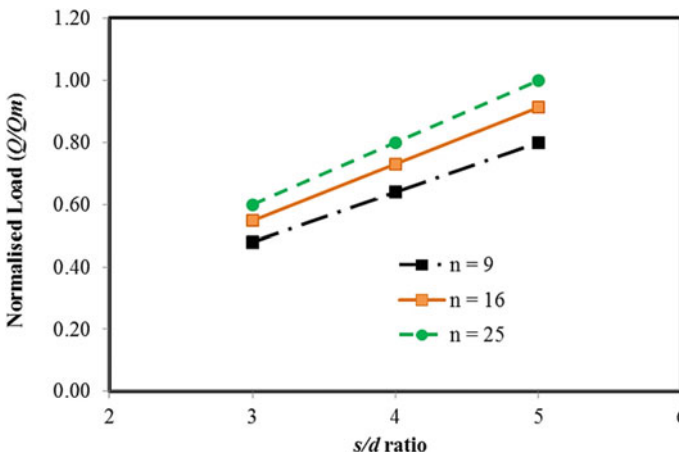


Fig. 11.8 Normalized eccentric load carried by the piled-raft with different values of s/d ratio

Stress in Soil and Piled-Raft

Stress in soil due to vertical eccentric load is represented in Fig. 11.9. In vertical load test, all the piles mobilized together, whereas under eccentric loading, the nearby piles of eccentric loading are mobilized first as the stress concentration occurs around those piles and the adjacent piles are mobilized later. The stress which is developed in piled-raft is analyzed for vertical loading and eccentric loading. Figure 11.10 is showing the stress which is developed in piled-raft foundation under the vertical load and vertical eccentric loading situation. The maximum amount of stress developed

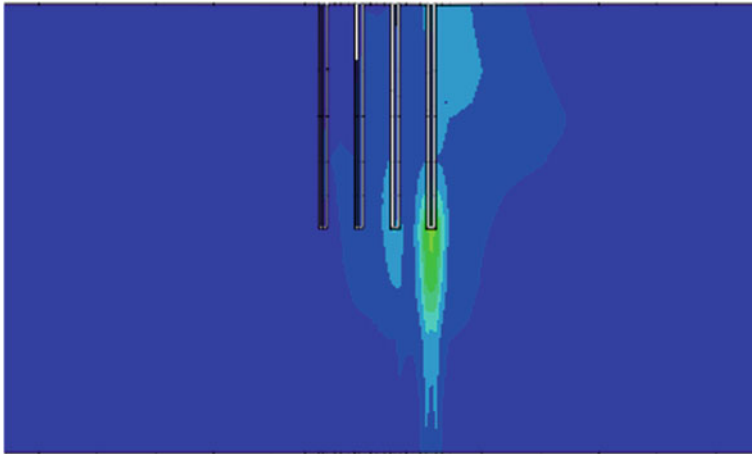


Fig. 11.9 Stress in soil due to vertical eccentric load

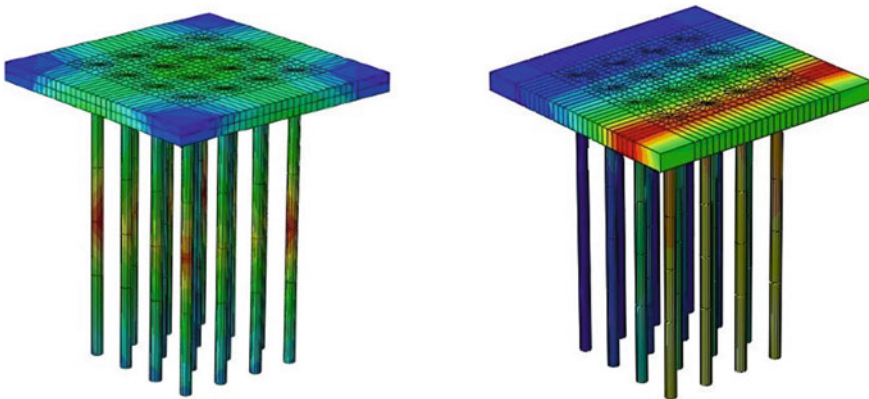


Fig. 11.10 Stress in piled-raft system under the vertical and eccentric loading situation

in piles and the raft experiences a very little amount of stress, and under eccentric loading, the maximum stress is developed in nearby pile row where the eccentricity occurs.

Conclusion

A series numerical model has been made and analyzed in this study. Based on numerical investigations, the conclusions are as follows:

1. In eccentric loading, the maximum amount of eccentric load is carried by the nearby row of group of pile where the eccentric load applied and this eccentric load is gradually decreases in successive rows.
2. The load carrying capacity of the piled-raft foundation increases about 3–4% when the value of Young's modulus increases from E_S to $2E_S$.
3. When the value of e/B ratio changes from 0 to 0.4, the load carrying capacity of the piled-raft foundation decreases up to 46%.
4. In vertical loading, the stress is developed almost equally in all the piles, whereas in vertical eccentric loading, the maximum stress develops in the nearby piles where eccentricity develops.

References

1. Fukumura K, Matsumoto T, Ohno A, Hashizume Y (2003) Experimental study on behaviour of model piled raft foundations in sand using shaking table at 1-g gravitational field. In: BGA international conference on foundations: innovations, observations, design and practice: proceedings of the international conference organised by British Geotechnical Association and held in Dundee, Scotland on 2–5th September 2003. Thomas Telford Publishing, pp 307–320
2. Cao XD, Wong IH, Chang MF (2004) Behavior of model rafts resting on pile-reinforced sand. *J Geotech Geoenviron Eng* 130(2):129–138
3. Bajad SP, Sahu RB (2008) An experimental study on the behavior of vertically loaded piled raft on soft clay. In: The 12th international conference of international association for computer methods and advances in geomechanics (IACMAG), pp 1–6
4. El Sawwaf M (2010) Experimental study of eccentrically loaded raft with connected and unconnected short piles. *J Geotech Geoenviron Eng* 136(10):1394–1402
5. Bajad SP, Sahu RB (2009) Time dependent settlement of piled raft foundation. *Darmstadt Geotech* 18:187–199
6. Shukla SJ, Desai AK, Solanki CH (2011) Behavioural study of piled raft foundation in layered soil deposits. *Int J Adv Eng Technol (IJAET)*. ISSN 0976-3945
7. Elwakil AZ, Azzam WR (2016) Experimental and numerical study of piled raft system. *Alex Eng J* 55(1):547–560
8. Park D, Kyung D, Choi K, Lee J (2013) Analysis of pile raft interaction in sand with centrifuge tests. In: International conference on case histories in geotechnical engineering
9. El-Garhy B, Galil AA, Youssef AF, Raia MA (2013) Behavior of raft on settlement reducing piles: experimental model study. *J Rock Mech Geotech Eng* 5(5):389–399
10. Patil J, Vasanwala SA, Solanki CH (2016) An experimental study of eccentrically loaded piled raft. *Int J Geotech Eng* 10(1):40–45
11. Dezfouli MG, Dehghani M, Asakereh A, Kalantari B (2019) Behavior of geogrid reinforced and unreinforced non-connected pile raft foundation. *Int J Civ Eng* 17(6):709–722
12. Deb P, Pal SK (2019) Numerical analysis of piled raft foundation under combined vertical and lateral loading. *Ocean Eng* 190:106431
13. Deb P, Pal SK (2020) Nonlinear analysis of lateral load sharing response of piled raft subjected to combined V-L loading. *Mar Georesour Geotech* 1–21
14. Deb P, Pal SK (2019) Analysis of load sharing response and prediction of interaction behaviour in piled raft foundation. *Arab J Sci Eng* 44(10):8527–8543

Chapter 12

Shape Optimization of Onshore Wind Turbine Foundations



**M. Deva Kumar, Rajesh Katyal, Anil Kumar Sharma,
and M. K. Haridharan**

Introduction

The foundation is an integral part of a wind turbine to withstand loads coming from the top of the tower. Normally wind turbine foundations are either gravity-based slab foundations or pile-supported foundations depending upon site-specific soil conditions. Gravity-based slab-supported onshore foundations are preferred when the quality of soil is good enough to withstand loads from the tower top. Pile-supported foundations are generally preferred when the quality of soil is loose or is composed of black cotton soil. A literature review reveals that conical raft foundations have higher load-bearing capacity resulting in the reduction of steel weight and concrete volume than flat rafts [1]. Wind turbine foundation designs can be optimized by considering cyclic degradation of soils which lead to reduced foundation cost [2]. The optimized results of a piled-raft foundation created by Pareto Front using knee point concept gives a clear relationship between the cost and differential settlement of a foundation with guidelines to choose the design for a given condition [3]. Optimization using Energy Payback Time (EPT) showed that square-shaped foundation for large-scale

M. Deva Kumar
Department of Civil Engineering, Amrita School of Engineering, Coimbatore, India

R. Katyal
Wind Resource Assessment and Offshore, National Institute of Wind Energy, Chennai, India
e-mail: katyal.niwe@nic.in

A. K. Sharma
Department of Civil Engineering, National Institute of Technology Patna, Patna, Bihar, India
e-mail: aks.ce@nitp.ac.in

M. K. Haridharan (✉)
Department of Civil Engineering, National Institute of Technology, Arunachal Pradesh, Papum
Pare District, Jote, Arunachal Pradesh, India
e-mail: harai411@gmail.com; haridharan@nitap.ac.in

wind turbine (onshore) has the lowest EPT than octagon and circle shapes as they require more reinforcement [4]. Numerical analysis is a valid tool for a seismic analysis of wind turbine foundations, and soil can be modeled as k -model which reduces time and design complexity [5]. Design optimization of many wind turbines considering Soil Structure Interaction (SSI) in different villages in Alaska showed that if foundation flexibility was considered, SSI provided a realistic value of natural frequency [6]. Nonlinear analysis and design procedures can be used to optimize foundations in terms of reduction in cost and time involved in foundation work [7]. The height and type of wind turbine are related to foundation behavior as the seismic forces in concrete and hybrid wind turbines increase dimensions of the foundation compared to a non-seismic condition [8–10]. This paper deals with various shapes of onshore wind turbine foundations with to arrive at the least/optimal weight keeping the other design parameters constant.

Design Data

Gravity-based foundations used in the wind industry are normally square in nature, but the present trend is to use hexagonal, octagonal and circular shapes too considering site-specific conditions. Accordingly four differently shaped configurations have been considered for a 1.8 MW horizontal axis three-bladed wind turbine installed in Theni district, Tamil Nadu, India. The generic configuration of the turbine considered for the analysis is shown in Table 12.1.

Tower top loads obtained from wind turbine manufacturer are shown in Figs. 12.1 and 12.2. The loads were transferred to the bottom of the tower/top of the foundation

Table 12.1 Configuration of the wind turbine

Tower details	
Type of tower	Tubular (space)
Base diameter	6.5 m
Top diameter	1.2 m
Height of the tower	100 m
Tower top moment	59,740 kNm
Vertical static load (comprising 3 FRP blades, drive train assembly, generator, etc.)	3770 kN
Wind shear force (acting at wind turbine hub)	630 kN
Foundation details	
Square	Side length = 15 m
Circle	Side length = 16.7 m
Hexagon	Side length = 9 m
Octagon	Side length = 6.7 m

as tower and foundation are a composite system. Materials used in the design are M40 grade concrete and Fe500 grade steel. The safe bearing capacity (SBC) of the soil for Theni district was considered as 25 T/m^2 . But however, the dimensions of the footings were selected in such a way that the SBC of all shapes fall in a range of $18.5 \text{ T/m}^2 \pm 0.25 \text{ T/m}^2$. The plan and sectional view indicating the dimensions for all the four shapes namely square, circle, hexagonal and octagonal is shown in Fig. 12.3a, b, c and d.

The entire foundation design and code checks were done based on Indian Standard Codal Provisions 456:2000. The designed foundations were further analyzed in PLAXIS 3D to assess soil response.

Fig. 12.1 Wind

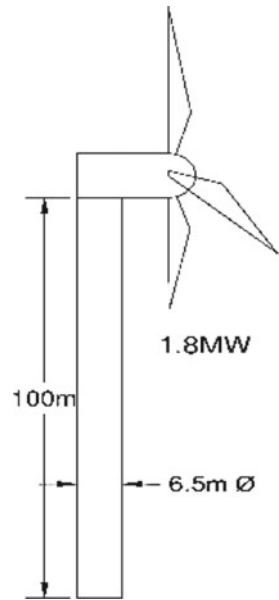
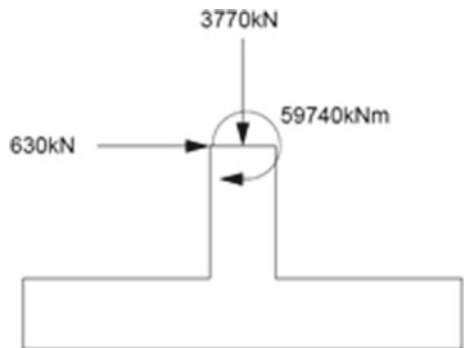


Fig. 12.2 Loads acting at the pedestal top



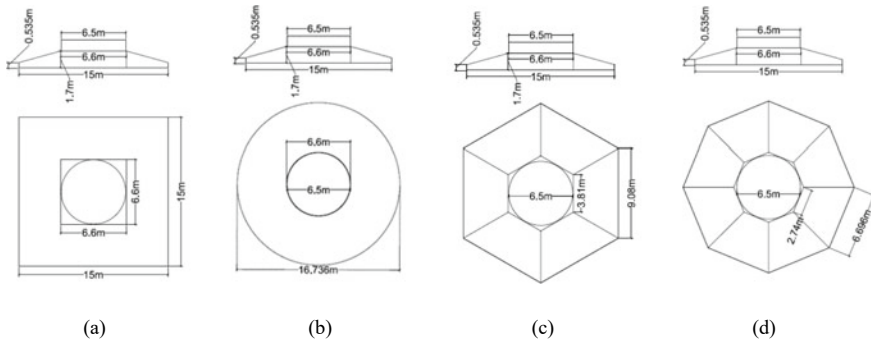


Fig. 12.3 Dimensions of the foundations. a Square. b Circle. c Hexagon. d Octagon

Modeling of the Foundation

All four shapes of foundations were modeled in STAAD Pro using 4-noded plate elements. A sloped footing was generally preferred as the quantity of concrete required was less. As STAAD Pro had no option for a sloped surface, the foundations were modeled as stepped from bottom to the top with different levels to match the configuration of sloped foundation approximately. Loads from the pedestal top were transferred to the foundation top by means of dummy beam elements without impacting the STAAD model analysis as shown in Fig. 12.4. The modulus of subgrade reaction was assumed to be 15 MN/m³, as this value produced a realistic maximum soil deformation of about 1.5 cm. The modulus of subgrade reaction is given as input for the boundary condition in the STAAD analysis.

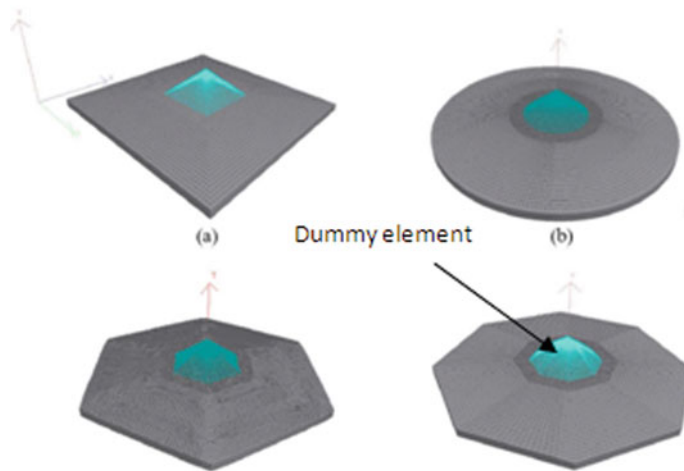


Fig. 12.4 3D view of modeled foundation in STAAD Pro

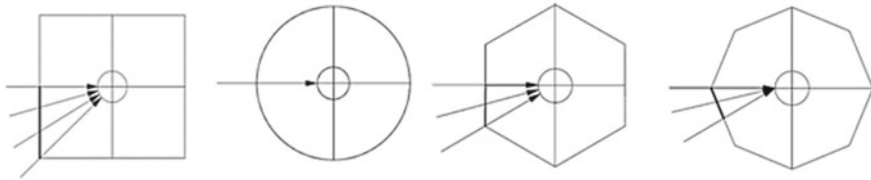


Fig. 12.5 Different angles of wind load considered

As wind load changes its direction from place to place and from time to time, different angles of wind loads were considered to find the worst case of wind loading for each shape as shown in Fig. 12.5. As the different configurations of foundations considered for the design are symmetrical in nature, a total of three different angles of wind loads was considered for square shape which was 15° , 30° and 45° with respect to the X -axis. For the circular shape, only single angle of wind load was considered due to its axis asymmetric property. Two different angles of wind loads were considered for the hexagonal shape which were at 15° and 30° with respect to X -axis, and two different angles for the octagonal shape which were at 11.25° and 22.5° with respect to X -axis were considered. From the linear static analyses in STAAD, two parameters, base pressure and moment, were obtained and used in the manual design calculation.

Each foundation was designed manually according to the Indian Standard Codal Provisions 456:2000 using moment values obtained from STAAD Pro, and reinforcements for both directions were calculated. Also one-way, two-way shear checks and sliding and overturning checks were done manually to ensure the foundations stability and safety.

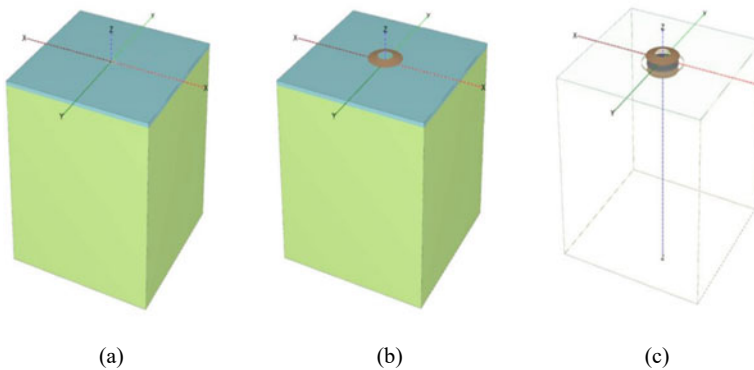
Regarding soil structure response, all foundations were modeled in AutoCAD 3D and imported to PLAXIS 3D. It was clear from the soil report that there were two layers of soil, top gravel sand followed by soft rock. The properties of both soil layers and foundation defined in PLAXIS 3D are detailed in Table 12.2. The model representation of the soil contour, foundation and interference for circular foundation modeled in PLAXIS 3D is similar to all other shapes shown in Fig. 12.6. Soil behavior was assessed in PLAXIS 3D using staged construction which is a step-by-step increment of the structure and load.

In the study, five stages of staged construction were involved. They details are as below:

Stage 1: an initial phase with only soil and without the structure, **Stage 2:** foundation installed on the soil, **Stage 3:** tower self-weight being included, **Stage 4:** combined loading, **Stage 5:** safety factor analysis.

Table 12.2 Properties of soil and footing given in PLAXIS 3D

Properties	Foundation	Top layer sand	Bottom layer soft rock
Material model	Linear elastic	Mohr–Coulomb	Mohr–Coulomb
Drainage type	Non-porous	Drained	Drained
γ_{unsat} (kN/m ³)	25	18.66	22.00
γ_{sat} (kN/m ³)	–	19.78	22.50
E (kN/m ²)	32.00×10^6	61.25×10^3	70.00×10^6
ν (nu)	0.1500	0.2800	0.2000
φ (phi) (°)	–	31.40	34.00
ψ (psi) (°)	–	1.400	4.000
c_{ref} (kN/m ²)	–	0.6630	0.01000×10^{-6}
R_{inter}	1.000	1.000	1.000

**Fig. 12.6** Soil and structure model in PLAXIS 3D. **a** Soil contour. **b** Foundation installed. **c** Interface (+ve) creation

Results and Discussions

The base pressure distribution of each shape's worst case w.r.t the angle of loading of wind is shown in Fig. 12.7. Variation in pressures for all shapes was similar but had different areas occupied for each segment in every shape. The moment acting on the face of the pedestal and at a distance 2 m from the face of the pedestal (steel requirement reduces at distance 'd' roughly equal to the depth of foundation) is shown in Table 12.3. It can be inferred that when sagging and hogging moment acted in the X or radial direction and Y-direction or tangential direction, the circular shape had the least moment compared to the highest moment produced by other shapes. Total reinforcement required by different shapes at the face of the pedestal and at a 2 m distance from the face of the pedestal is shown in Table 12.4. It is inferred that circular foundation had the least reinforcement compared to other shapes of footing

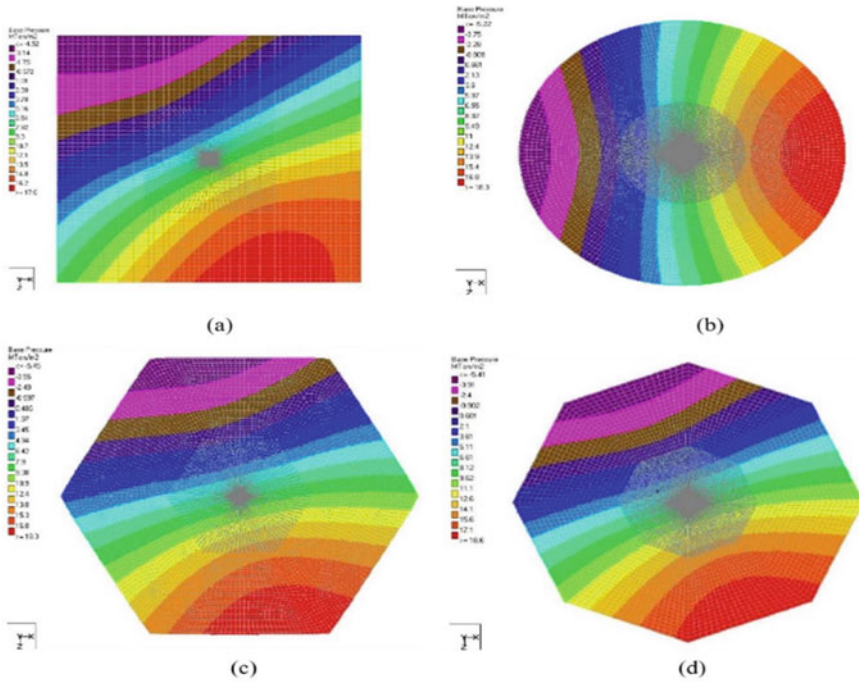


Fig. 12.7 Base pressure distributions of all shapes

which reveal that sectional forces and moments are reduced from the pedestal face toward the edge of the footing.

The load settlement curve obtained from PLAXIS 3D is shown in Fig. 12.8i. Initial settlement in the curve was due to the self-weight of the tower which was considered before the loading stage. It is inferred from Fig. 12.8 that (i) square shape had the least settlement followed by a circular shape due to wind load consideration. As wind load w.r.t to X -axis was only considered for the analysis, the square shape had less settlement than the circular shape or else the circular shape would have the least settlement due to its axisymmetric property, if the wind load's worst angle was considered for other shapes. It is inferred from Fig. 12.8 that (ii) that when the settlement on the other side of the foundation, i.e., in the direction of wind load where uplift of foundation occurred due to negative pressure was considered, the circular shape had less uplift than the square shape which describes the stability of the circular-shaped foundation.

The vertical displacement of soil due to combined loading at the center of the foundation is shown in Fig. 12.9. It is inferred that each shape had a different range of settlement indicating the importance of the shapes geometry. The horizontal displacement of soil in X -direction, i.e., in the direction of wind load and moment is due to combined loading at 0.5 m below the foundation as shown in Fig. 12.10. It shows that each shape had a variation in soil displacement due to combined loading.

Table 12.3 Moment at the face and at 2 m distance from the face of the pedestal

Shape	Angle w.r.t X-axis	Moment acting at the face of the pedestal (kNm/m)				Moment acting at 2 m distance from pedestal face (kNm/m)			
		Radial or X-direction		Tangential or Y-direction		Radial or X-direction		Tangential or Y-direction	
		Bottom	Top	Bottom	Top	Bottom	Top	Bottom	Top
Square	0°	2203.4	1524.4	2910.1	2150.1	672.1	447.0	812.7	379.8
	15°	3199.6	2385.8	2504.5	1760.1	920.1	692.1	812.0	584.3
	30°	3280.8	2518.0	2911.6	2154	969.5	748.7	919.8	690.3
	45°	3191.1	2429.5	3191.1	2429.5	972.7	747.9	972.7	747.9
Circular	0°	3087.1	2092.9	2577.7	1665.9	964.0	670.7	799.3	484.4
Hexagon	0°	2880.0	2089.3	2791.3	1984.0	950.0	685.1	869.5	660.8
	15°	3008.6	2246.5	2758.2	1957.0	873.2	607.6	833.6	603.6
	30°	2879.5	2090.2	2809.6	1975.5	945.2	229.8	865.3	656.6
Octagon	0°	2935.4	2046.3	2711.1	1909.4	949.4	708.7	2711.1	1909.4
	11.25°	2486.2	1984.9	2822.9	1994.4	901.5	660.8	821.8	532.9
	22.5°	2900.4	2096.4	2788.6	1935.9	850.9	610.0	772.0	481.7

Table 12.4 Total A_{st} at the face and at 2 m distance from the face of the pedestal

Shape	Angle w.r.t X-axis	Total A_{st} at the face of the pedestal (mm^2/m)	Total A_{st} at 2 m distance from pedestal face (mm^2/m)
Square	0°	14,682.3	2134.0
	15°	16,251.9	2684.0
	30°	16,873.2	3080.0
	45°	16,350.0	3300.0
Circular	0°	13,619.6	3048.7
Hexagon	0°	14,110.0	3260.6
	15°	14,437.1	2998.8
	30°	14,126.4	2808.4
Octagon	0°	13,897.5	3240.6
	11.25°	13,962.9	2981.4
	22.5°	14,077.4	2757.5

It can be inferred from Fig. 12.11 that (iii) the square foundation had least total displacement followed by the hexagonal, circular and octagonal shapes due to the angle of wind load considered in the analysis. But if the worst case of each shape was considered, then the circular would have the least displacement of all. The Cartesian total stress of the octagonal shape was less than that of the hexagonal, circular and square shapes in the vertical direction as shown in Fig. 12.11i. But the total Cartesian strain of the circular shape is least followed by the square, hexagonal and octagonal

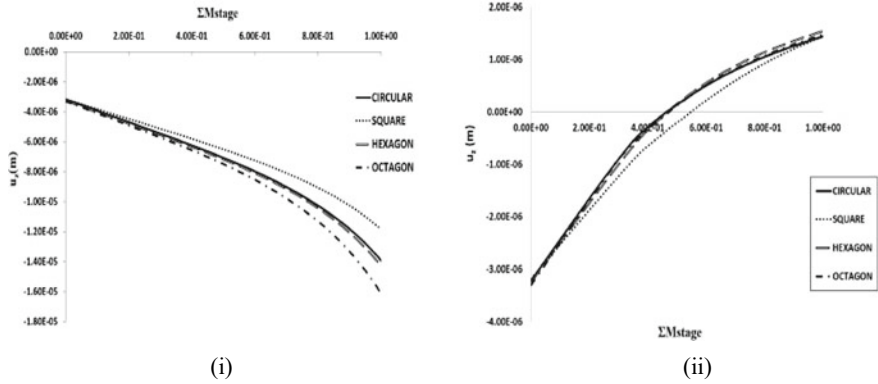


Fig. 12.8 Combined loading (ΣM_{STAGE}) versus vertical settlement (u_z) in m at. **i** Right side of the foundation. **ii** Left side of the foundation

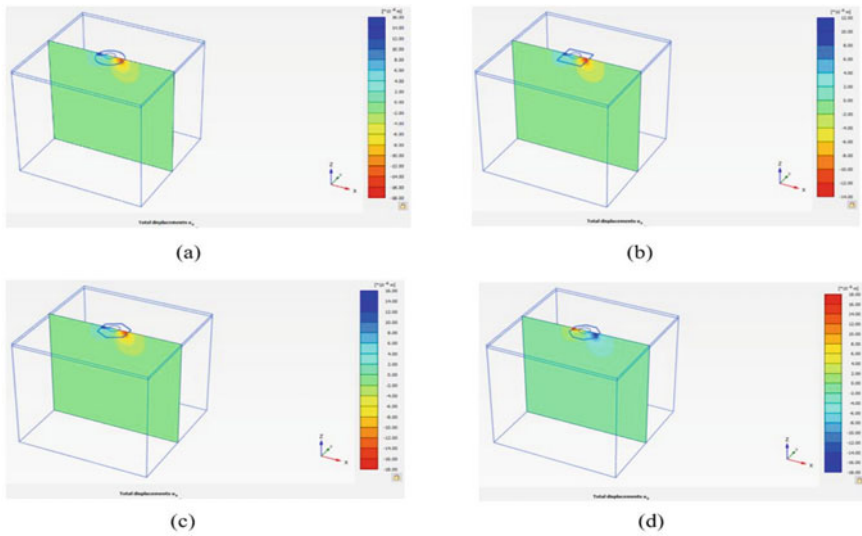


Fig. 12.9 Vertical section of total displacement u_z of the soil after loading at the center of the footing of **a** square **b** circular **c** hexagonal **d** octagon

shapes in the vertical direction as shown in Fig. 12.11ii. From the safety factor analysis, it can be inferred from Table 12.5 that circular-shaped foundations had the highest safety factor followed by the octagonal, square and hexagonal shapes.

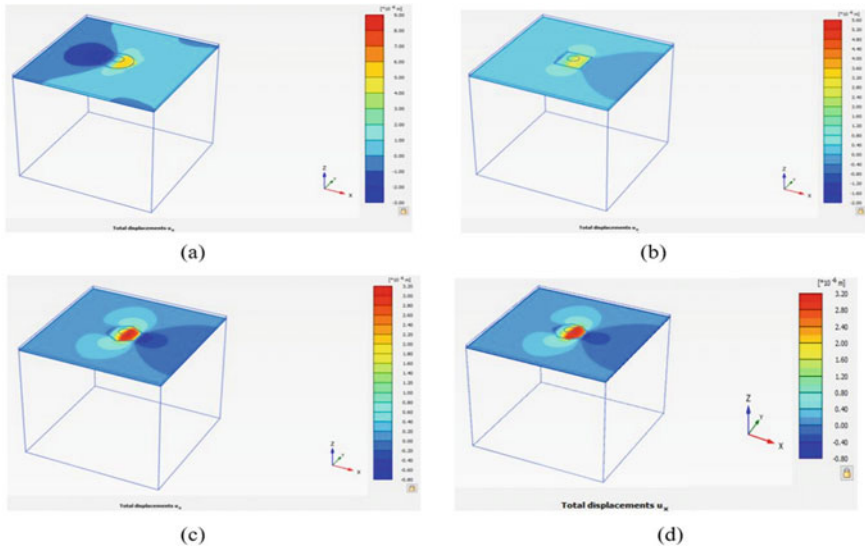


Fig. 12.10 Horizontal section of total displacement u_x of the soil at 0.5 m depth after combined loading of **a** square **b** circular **c** hexagon **d** octagon

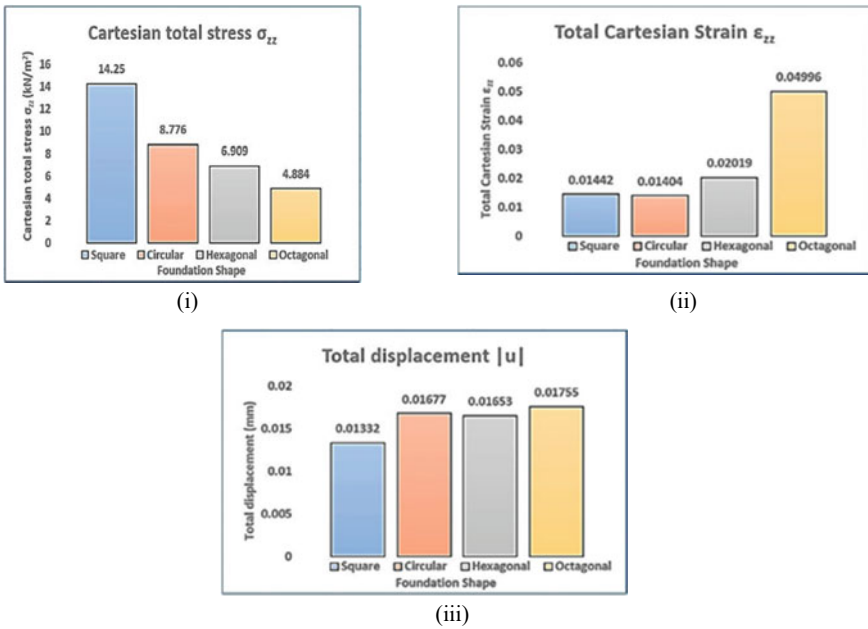


Fig. 12.11 Model output from PLAXIS. **i** Cartesian total stress σ_{zz} in soil. **ii** Cartesian total strain ϵ_{zz} in soil. **iii** Total displacement of all foundation shapes in soil

Table 12.5 Factor of safety for all shapes

Shape of footing	Factor of safety
Circular	1.82
Octagon	1.76
Square	1.55
Hexagon	1.23

Conclusion

It is concluded that in the process, the circular shape had the least moment, least reinforcement, least strain and lesser uplift compared to all other shapes. As the area of steel and the volume of concrete contribute to the major cost of the foundation, it considered a prominent factor to decide the optimum shape. Also the circular shape had the highest factor of safety followed by the octagonal shape. A salient conclusion drawn from the paper is that circular shape is the optimum shape when wind load acts on any direction due to its axisymmetric property. However, due to form work constraints for circular shapes, circle-inscribed octagon-shaped foundation can be preferred for a 1.8 MW onshore wind turbine foundation as an octagonal shape had the highest safety factor next to the circular shape.

References

1. Mohamed W, Austrell P-E (2009) A comparative study of three onshore wind turbine foundation solutions. *Comput Geotech* 36:577–588. <https://doi.org/10.1016/j.compgeo.2017.08.022>
2. Yu H, Guzman C, Ntambakwa E (2016) Consideration of the cyclic degradation of cohesive soils in pile foundation design for onshore wind turbines. *Geo-Chicago 2016*:185–194. <https://doi.org/10.1061/9780784480137.020>
3. Shrestha S, Ravichandran N, Rahbari P (2018) Geotechnical design and design optimization of a pile-raft foundation for tall onshore wind turbines in multilayered clay. *Int J Geomech* 2018(18):1–12. [https://doi.org/10.1061/\(ASCE\)GM.1943-5622.0001061](https://doi.org/10.1061/(ASCE)GM.1943-5622.0001061)
4. Horgan C (2013) Using energy payback time to optimise onshore and offshore wind turbine foundations. *Renewable Energy* 53:287–298. <https://doi.org/10.1016/j.renene.2012.10.044>
5. Austin S, Jerath S (2017) Effect of soil-foundation-structure interaction on the seismic response of wind turbines. *Ain Shams Eng J* 8:323–331. <https://doi.org/10.1016/j.asej.2017.05.007>
6. Alhamaydeh M, Hussain S (2011) Optimized frequency-based foundation design for wind turbine towers utilizing soilstructure interaction. *J Franklin Inst* 348:1470–1487. <https://doi.org/10.1016/j.jfranklin.2010.04.013>
7. Loubser PB, Jacobs AR (2016) Optimised design of wind turbine gravity foundations. In: *Insights and innovations in structural engineering, mechanics and computation, sixth international conference on structural engineering, mechanics and computation*, pp 953–958

8. Rebelo C, Moura A, Gervásio H, Veljkovic M, Simões da Silva L (2014) Comparative life cycle assessment of tubular wind towers and foundations—part 1: structural design. *Eng Struct* 74:283–291. <https://doi.org/10.1016/j.engstruct.2014.02.040>
9. PLAXIS 3D manuals. <https://www.plaxis.com/support/manuals/plaxis-3d-manuals/>. Accessed 21 Sept 2018
10. Global Wind Energy Council. Global statistics. <http://gwec.net/global-figures/graphs/>. Accessed 20 Sept 2018

Chapter 13

Analysis of Load Distribution Coefficient of Piled Raft System: A Numerical Approach



Plaban Deb and Sujit Kumar Pal

Introduction

The composite piled raft system is composed of a general pile foundation and the raft foundation and hence shows composite load transfer behavior as well as some interaction properties among the piled raft components. The idea behind the design of a piled raft system is that pile would carry the major portion of the superstructure load and after the mobilization of pile capacity, the remaining load would be taken by the raft. Therefore, the focus had been given to the development of analytical and numerical solutions for designing the piled raft foundation [1–4]. However, if the raft will not provide sufficient bearing capacity, then further application of piles below the raft will enhance the factor of safety of system against the failure and if raft will offer sufficient bearing capacity, then addition of piles below the raft will act as a settlement reducer. Several researchers have used this concept on piled raft foundation [5–9]. However, very few researchers have focused on the piled raft bearing capacity on soft soil [10, 11] and due to the presence of interaction between the structural elements; some researchers have presented a load distribution coefficient. The prime goal of this study is to evaluate this load distribution coefficient for the piled raft through numerical modeling and to predict a simplified equation of the load distribution coefficient considering various interaction factors.

P. Deb (✉)

Department of Civil Engineering, Chandigarh University, Mohali 140413, Punjab, India
e-mail: plaban930@gmail.com

S. K. Pal

Department of Civil Engineering, National Institute of Technology, Agartala 799046, India

Theoretical Background

According to Liu et al. [12] and Poulos [13], the total superstructure load is divided among the structural elements between piled raft system, i.e., piles and raft, and the load distribution of piled raft at ultimate stage can be given as

$$Q_{PR} = Q_R + Q_P \quad (13.1)$$

Or,

$$Q_{PR} = Q_{UR} + Q_{GP} \quad (13.2)$$

where Q_{PR} , Q_R and Q_P are the load-bearing capacities of the piled raft, raft and pile present in the piled raft, respectively, and Q_{UR} and Q_{GP} are the load-bearing capacities of single raft and pile group, respectively. In this conception, the various interactions such as pile–raft, raft–pile and pile–pile interaction are not incorporated. Therefore, for piled raft system, a load distribution coefficient (ξ_{PR}) was introduced by de Sanctis and Mandolini [10] to incorporate this interaction effect and this load distribution coefficient is expressed as

$$\xi_{PR} = \frac{Q_{PR}}{Q_{UR} + Q_{GP}} = \frac{Q_{PR,ult}}{Q_{UR,ult} + Q_{GP,ult}} \quad (13.3)$$

where $Q_{PR,ult}$, $Q_{UR,ult}$ and $Q_{GP,ult}$ are the ultimate load-bearing capacity of the piled raft, unpiled raft and pile group, respectively.

Numerical Simulation

In this study, three-dimensional finite element method (FEM) is performed using ABAQUS software to comprehend the load distribution coefficient of vertically loaded piled raft foundation. Due to the geometrical symmetry, only one-fourth of the soil continuum is considered for the analysis. The model geometry and the meshing pattern of soil and whole piled raft system are presented in Fig. 13.1. In this analysis, the raft and soil are modelled using the brick element (C3D20R) while the pile is modelled as a triangular prism element. To assign the material properties, piles and raft are considered as elastic material and soil is considered as an elasto-plastic material. To incorporate this elasto-plastic behavior of soil, the modified Drucker–Prager (MDP) method is considered for soil modeling. For the simulation of pile and raft connectivity, a rigid connection is chosen without considering any slippage at the interface and to simulate the interaction behavior, master–slave concept is utilized among the soil, piles and raft interfaces. The general properties of soil and piled raft elements are summarized in Table 13.1. For providing the boundary condition, all

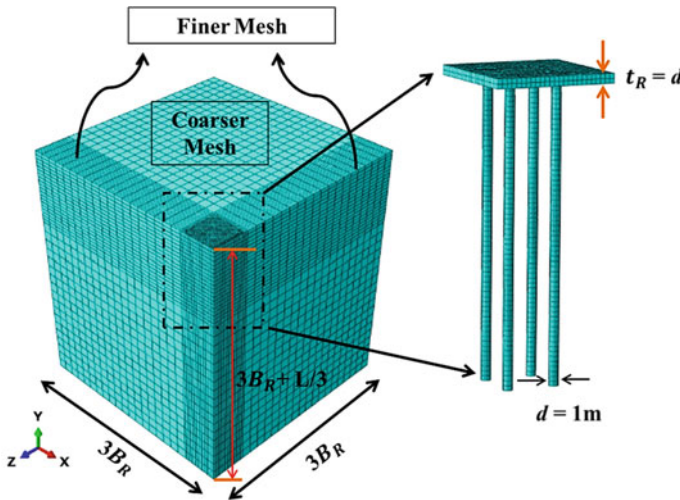


Fig. 13.1 Model geometry, meshing pattern of soil and piled raft system

Table 13.1 Physical properties of soil and piled raft elements

Particulars	Clay	Sand	Pile	Raft
Density (kg/m ³)	1750	1580	2700	7800
Young's modulus (kPa)	6000	25,000	24×10^6	34×10^6
Poisson's ratio	0.45	0.3	0.2	0.2
Failure model	MDP	MDP	LE	LE

Note MDP = Modified Drucker-Prager, LE = linear elastic

kinds of translation and rotation are restricted in the case of bottom nodes, whereas for corner nodes only translations in the direction of x and z are restricted. For face boundary, due to the symmetry, XSYMM and ZSYMM are considered [14]. The detail of boundary condition is shown in Fig. 13.2, and the steps involved to simulate the loading conditions are displayed in Table 13.2.

Numerical Model Configuration

In the present study, two types of soils such as clay and sand are considered as subsoil material; i.e., the top layer is considered as clayey soil and the bottom layer is considered as sand. For assessing the influence of clayey soil, the thickness of clay layer to the pile length ratio (t/L) is altered as t/L ratio of 0.5, 1 and 1.5. Different design variables such as raft width (B_R), number of pile (n), spacing between piles to the pile diameter ratio (s/d) are also varied in order to understand their impacts on

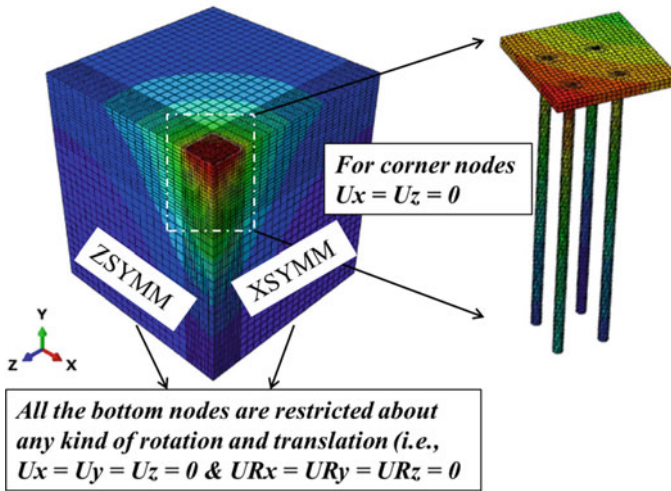


Fig. 13.2 Details of boundary condition

Table 13.2 Loading steps involve in numerical modeling

Loading step	Details
Step-I	Here, geostatic stress condition is simulated in soil block to bring the soil continuum to an equilibrium state
Step-II	Self-weight of whole piled raft system is induced to mimic the field condition
Step-II	This is the final step in which the total supper structure load is provided on the raft

the load distribution coefficient. Further, modeling of the unpiled raft and pile group is also performed to simulate the interaction effect on load distribution coefficient. For all the model configurations, the maximum vertical load is obtained at a load equivalent to a settlement value of 10% of raft width. All the numerical model configurations are revealed in Table 13.3.

Table 13.3 Model configurations

Design variables	Foundation type		
	Unpiled raft	Pile group	Piled raft
Raft width (B_R)	20d, 25d, 30d	–	20d, 25d, 30d
Pile number (n)	–	9, 16, 25	9, 16, 25
Pile spacing (s)	–	3d, 5d, 7d	3d, 5d, 7d

Note d = pile diameter, n = pile number, s = pile spacing and B_R = width of raft

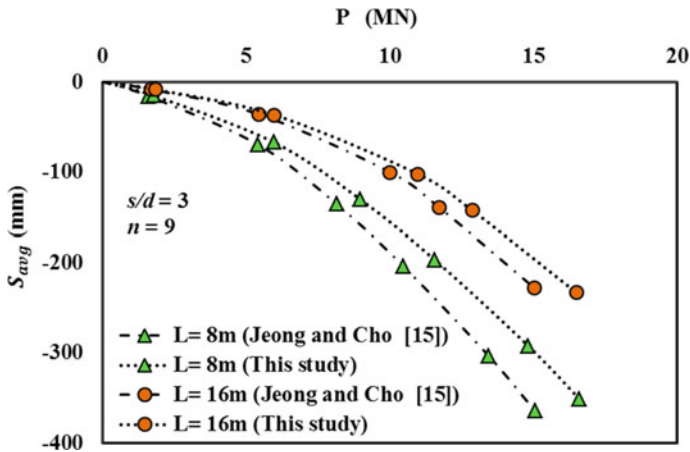


Fig. 13.3 Validation of developed numerical model

Validation of Developed Model

The idea of performing this validation is to check the compatibility of any developed numerical model with other reference numerical models for ensuring the accuracy of the prepared model. The finite element (FE) models developed here is compared with another FE model developed by Jeong and Cho [15]. Two different pile lengths of 8 and 16 m having 9 number of piles and s/d ratio of 3 are chosen for validation purposes. Figure 13.3 represents the comparison of load–settlement response for another numerical model [15] and the developed numerical model. It is observed that the developed numerical model in this study shows very close results with the reference numerical model.

Results

Analysis of Load Distribution Coefficient

The load distribution coefficient (ξ_{PR}) is evaluated by using Eq. (13.3) for different piled raft configurations. The profiles of ξ_{PR} for different design variables are plotted in Fig. 13.4a–d, and it can be found that the load distribution coefficient maintains a nonlinear profile with the normalized settlement. A similar type of variation is observed for the load distribution coefficient in all the configurations, where ξ_{PR} increases with the enhancement of the normalized settlement by following a power law. Considering the effect of number of piles (n), t/L ratio, B_R/d ratio and s/d ratio; it is found that ξ_{PR} increases with the improvement in the pile numbers under

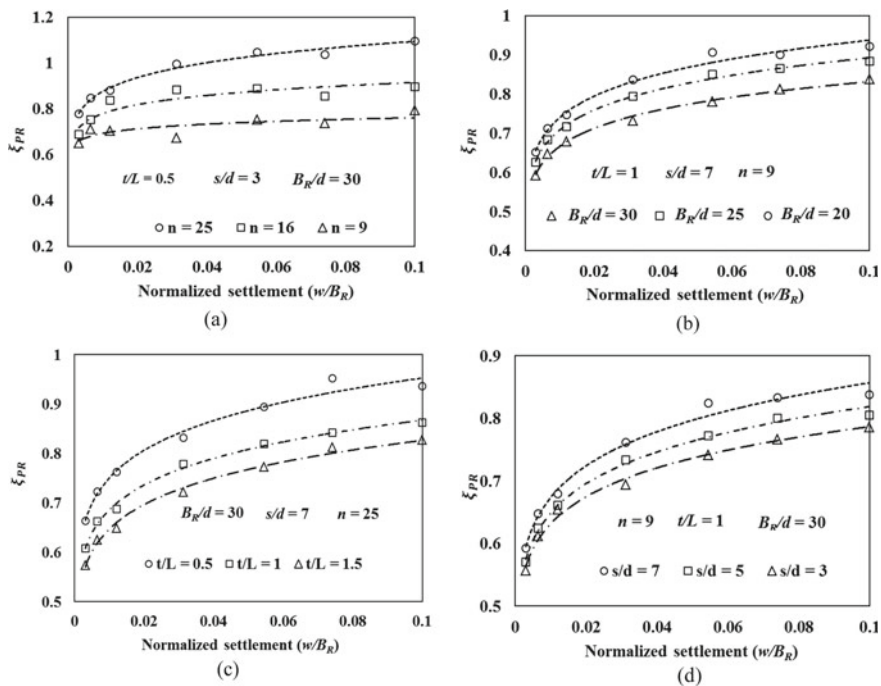


Fig. 13.4 a–d Variations of load distribution coefficient with the normalized settlement

the raft. Similarly, ξ_{PR} also improves with the increase in t/L ratio and s/d ratio; however, it significantly reduces with B_R/d ratio. These trends of variations of ξ_{PR} for all the configurations are almost similar, though there exist some exceptions also. Considering all the model configurations, it is observed that the value of ξ_{PR} at ultimate settlement (i.e., at $w = 0.1B_R$) in maximum cases is coming less than 1, and the range of ξ_{PR} varies between 0.75 and 1.11. This phenomenon indicates that the value of ξ_{PR} mostly provides an opposite effect on the piled raft system, and the final load taken by the piled raft is relatively lower than the sum of individual load withstood by a single raft and group pile. This negative influence of the load distribution coefficient on this load-bearing behavior of the piled raft system suggests an appropriate evaluation of the value of ξ_{PR} is very important before designing any piled raft system.

Prediction Model of Load Distribution Coefficient

The load distribution coefficient (ξ_{PR}) in the previous context is obtained from the general equation provided by other researchers as mentioned in Eq. (13.3). However, ξ_{PR} can also be obtained by using the ‘load sharing’ and the ‘interaction factors’.

According to Deb and Pal [16], the load sharing ratio, load carrying capacity ratio and the various interactions between pile and raft can be defined as

$$\alpha_{PR} = \frac{Q_P}{Q_{PR}} \quad (13.4)$$

$$\eta = \frac{Q_{UR}}{Q_{GP}} \quad (13.5)$$

$$\lambda_{p-r} = \frac{Q_P}{Q_{GP}} \quad (13.6)$$

$$\lambda_{r-p} = \frac{Q_R}{Q_{UR}} \quad (13.7)$$

where α_{PR} is the load sharing ratio, η is load carrying capacity ratio, λ_{p-r} is the pile–raft interaction and λ_{r-p} is the raft–pile interaction. Using Eqs. (13.4), (13.5) and (13.6), the raft–pile interaction can be modified and is conveyed as

$$\lambda_{r-p} = \frac{1}{1 - \alpha_{PR}} - \frac{\lambda_{p-r}}{\eta} \quad (13.8)$$

Now, ξ_{PR} can be predicted by using the above equations and can be expressed as

$$\xi_{PR} = \frac{\eta\lambda_{r-p} + \lambda_{p-r}}{1 + \eta} \quad (13.9)$$

This equation combines the effect of pile–raft and the raft–pile interaction factor together. Equation (13.3) is mainly based on the load endured by the whole piled raft, group pile, and unpiled raft, but it does not consider the sharing of load between the pile and raft. Moreover, the loads endured by the piles and the single raft present in composite piled rafts are not accounted for here. However, Eq. (13.9) includes the interaction factors and thus the effect of the piles and the raft of the piled raft systems are also accounted for, which may give a better understanding of load–settlement response. The percent difference in the values obtained from Eqs. (13.3) and (13.9) is presented in Fig. 13.5, and the figure shows that the predicted values [using Eq. (13.9)] almost match with the calculated results [using Eq. (13.3)], showing a maximum difference of -10 to $+10\%$.

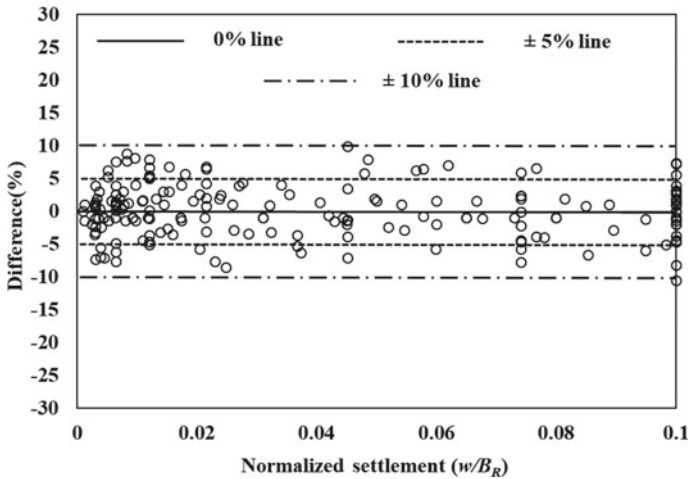


Fig. 13.5 Percent difference in the values of load distribution coefficient obtained from Eqs. (13.3) and (13.9)

Conclusion

The widespread finite element analysis gives the following conclusions:

- The load distribution coefficient maintains a nonlinear profile with the normalized settlement of the piled raft system and the value of the load distribution coefficient increases with the increase in the normalized settlement following a power law.
- Considering all the model configurations, it is observed that the value of ξ_{PR} at ultimate settlement (i.e., at $w = 0.1 B_R$) in maximum cases is coming less than 1, and the range of ξ_{PR} varies between 0.75 and 1.11. This phenomenon indicates that the value of ξ_{PR} mostly provides a negative effect on this combined piled raft system, and the critical load taken by the piled raft is relatively lower than the sum of individual load carried by the existing raft and group pile.
- Finally, with the help of various interaction factors, a predictive model is developed for the load distribution coefficient.

References

1. Clancy P, Randolph MF (1993) An approximate analysis procedure for piled raft foundations. *Int J Numer Anal Methods Geomech* 17:849–869
2. Poulos HG (1994) An approximate numerical analysis of pile–raft interaction. *Int J Phys Model Geotech* 18:73–92
3. Franke E, Lutz B, El-Mossallamy Y (1994) Measurements and numerical modelling of high rise building foundations on Frankfurt Clay. In: *Vertical and horizontal deformations of foundations and embankments*, pp 1325–1336

4. Ta LD, Small JC (1996) Analysis of piled raft systems in layered soils. *Int J Numer Anal Methods Geomech* 20:57–72
5. Burland JB, Kalra JC (1986) Queen Elizabeth II conference centre: geotechnical aspects. *Proc Inst Civ Eng* 80:1479–1503
6. Randolph MF (1994) Design methods for pile groups and piled rafts. In: *International conference on soil mechanics and foundation engineering*, pp 61–82
7. Russo G (1998) Numerical analysis of piled rafts. *Int J Numer Anal Meth Geomech* 22:477–493
8. Poulos HG (2001) Piled raft foundations: design and applications. *Geotechnique* 51:95–113
9. de Sanctis L, Mandolini A, Russo G, Viggiani C (2002) Some remarks on the optimum design of piled rafts. In: *Deep foundations 2002: an international perspective on theory, design, construction, and performance*, pp 405–425
10. de Sanctis L, Mandolini A (2006) Bearing capacity of piled rafts on soft clay soils. *J Geotech Geoenviron* 132:1600–1610
11. Reul O, Randolph MF (2004) Design strategies for piled rafts subjected to nonuniform vertical loading. *J Geotech Geoenviron* 130:1–13
12. Liu JL, Yuan ZL, Shang KP (1985) Cap-pile-soil interaction of bored pile groups. In: *International conference on soil mechanics and foundation engineering*, vol 11, pp 1433–1436
13. Poulos HG (2000) Pile-raft interaction—alternative methods of analysis. *Dev Theor Geomech* 445–463
14. Deb P, Pal SK (2021) Structural and geotechnical aspects of piled raft foundation through numerical analysis. *Mar Georesour Geotech* 1–25
15. Jeong SS, Cho JY (2012) Three dimensional analysis of piled raft foundation in clay soils. *Int J Geo-Eng* 4:11–22
16. Deb P, Pal SK (2019) Analysis of load sharing response and prediction of interaction behaviour in piled raft foundation. *Arab J Sci Eng* 44:8527–8543

Chapter 14

Effect of Slope Inclination on $V-H$ and $V-M$ Capacity Envelope of Strip Foundation on Undrained Clay Slope



Ayushi Goyal, Aarushi Maurya, Dhiraj Raj , and M. Bharathi 

Introduction

The shallow foundations are generally subjected to a combined action of gravity (axial) and wind or earthquake or tidal wave (lateral) loads, depending upon the construction environment. A complex interdependency between these loads, vertical load, V , horizontal shear force, H , and moment, M , make the bearing capacity estimation even more complex. Current code of practice and standards [1–4] recommend traditional method for the bearing capacity estimation of shallow foundations and to incorporate the effect of shear force and bending moment along with vertical force; different correction factors ‘load inclination factor’ and ‘eccentricity’ are used, respectively [5].

To deal with the shallow foundation under complex interactive loads, the capacity envelope method has been generally preferred to check the stability of foundation located on flat ground [6]. Initially, Ukritchon et al. [7] estimated the undrained capacity and failure patterns of shallow strip footing placed on flat ground which consists of cohesive soil using finite element limit analysis (FELA). Later on, the capacity envelope of a shallow foundation on flat ground was estimated by several researchers [6, 8–12]. In reality, the shallow foundations are frequently placed on or near the slope to support the connecting structure like buildings, bridges, etc., and are subjected to complex planar interactive loads. In the past, Georgiadis [13] has performed a numerical study using finite element (FE), upper-bound plasticity and stress field methods to develop $V-H$ capacity envelope of foundations located on top

A. Goyal · A. Maurya · D. Raj (✉)
Department of Civil Engineering, MNIT Jaipur, Jaipur, Rajasthan 302017, India
e-mail: dhiraj.ce@mnit.ac.in

M. Bharathi
Department of Civil Engineering, SKIT Jaipur, Jaipur, Rajasthan 302017, India

of cohesive soil slopes. Recently, Raj et al. [14] have developed the $V-H$ and $V-M$ capacity envelopes using FELA for the strip foundation located on the top and face of homogeneous $c-\phi$ soil slopes.

In this study, an effort is made to develop the $V-H$ and $V-M$ capacity envelopes of strip foundation located on top of slopes consisting of homogenous cohesive soils. 2D plane-strain FE models of slopes with different geometry and soil properties and foundations on the edge with fixed width are developed using OptumG2 finite element limit analysis (FELA) software. The results from this study have been presented in the form of normalized $V-H$ and $V-M$ capacity envelopes. A comparison of capacity envelopes of foundation on slopes to its corresponding envelope on flat ground is also presented to highlight the effect of slope.

Problem Statement, FE Modeling and Analysis

In this study, the capacity envelopes of strip foundations (rigid and rough with width, $B = 1$ m and zero edge distance) placed on top (ground surface without any embedment) of different slopes consisting of cohesive soil have been estimated by performing FELA. Four homogeneous slopes, having same slope height, $H = 40$ m, with different slope inclination, β varying from 10° to 40° at the interval of 10° (i.e., $\beta = 10^\circ, 20^\circ, 30^\circ$ and 40°) have been considered in this study. The same material properties, $c/\gamma H = 0.25$ (here, cohesion, $c = 200$ kPa and unit weight of soil, $\gamma = 20$ kN/m³), Young's modulus = 20 MPa and Poisson's ratio = 0.40 have been considered for all the slopes. For the purpose of comparison, the same foundations have also been considered to be located on the surface of flat ground with alike soil properties. The sign convention for applied loads and moment, used in the study, follows the inward right-hand rule [15].

In the present study, all the analyses have been carried out using OptumG2 [16] software, in which FELA combines the strength of both the finite element discretization and plastic bound theorems of limit analysis to bracket the limit load. In past, FELA has been used successfully in solving various geotechnical stability problems. The details of numerical formulation of FELA in OptumG2 [16] can be found in Krabbenhoft et al. [17].

2D plane-strain FE models of the slopes with strip foundation have been developed using OptumG2 as shown in Fig. 14.1 to generate capacity envelope in $V-H$ and $V-M$ space. The supporting soil mass has been modeled using Mohr–Coulomb failure criterion following associated flow rule and without tension cut-off [18, 19]. The soil mass has been discretized with 3-noded and 6-noded triangular elements for lower- and upper-bound analysis, respectively. A two-noded elastic 'plate' element has been used to model the foundation [20]. Rigid elastic material properties (with very high Young's modulus $\cong 10^5$ times Young's modulus of surrounding soil and Poisson's ratio = 0.3) have been assigned to the foundation. Further, interface element has been used between the foundation and soil to simulate soil–foundation interaction (rough foundation without gap and uplift).

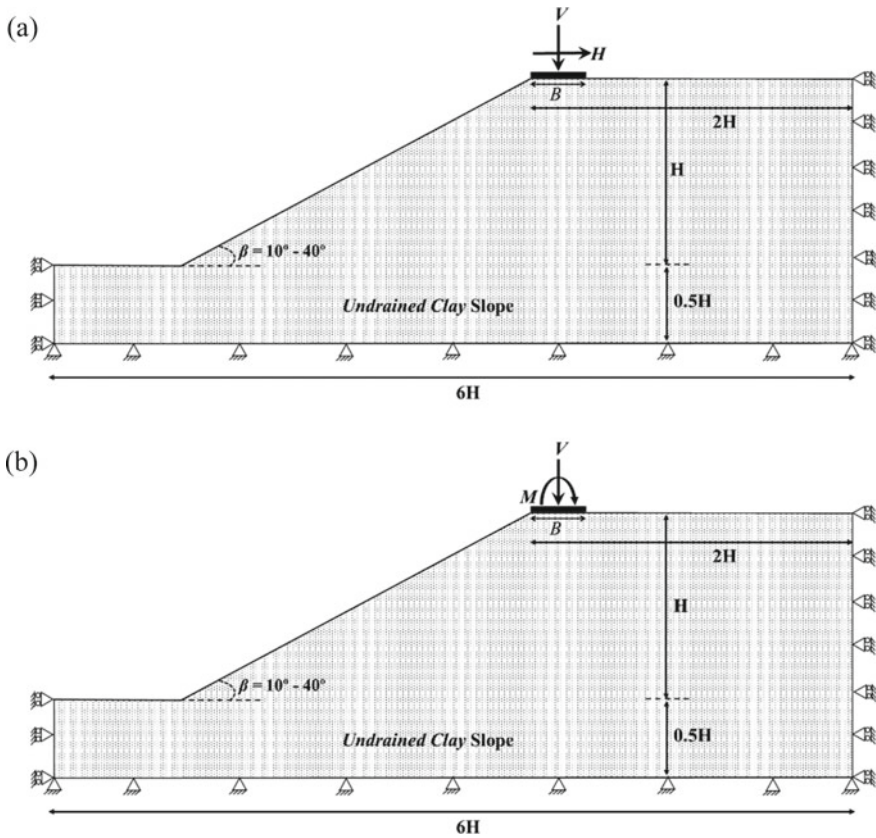


Fig. 14.1 Typical finite element model (developed in OptumG2 [16]) showing strip foundation located on top of slope with zero edge distance, under: **a** V - H load and **b** V - M load

At the base of the FE model, movements in both translational directions have been restrained, whereas only vertical movement has been allowed on the left and right lateral boundaries. To obtain the limit load close to exact load, an adaptive meshing with four iterations and number of elements varying from 8,000 to 10,000 has been used in all the analyses. To develop the V - H and V - M capacity envelopes, force-based ‘Probe’ method has been adopted [14], where a series of FELA has been performed to estimate the limit load in V - H and V - M space. The analyses have been conducted considering two stages of loading. In the first stage, the in-situ stresses in the soil due to self-weight have been generated for the free slope (without foundation). In the second stage, FELA considering both lower- and upper-bound analysis has been conducted for the coupled foundation-slope system to develop capacity envelope. To develop V - H capacity envelope, a successively increasing horizontal force, H , at different value of the (constant) vertical load, V , has been applied at the midpoint of the foundation, whereas a subsequently increasing moment, M , at different value of

the (constant) vertical load, V , has been applied at the midpoint of the foundation to develop V - M capacity envelope [14].

In all analyses, the different values of the vertical load, V , have been selected as fraction (0, 1/6, 1/3, 1/2, 2/3, 5/6, 1) of the maximum load carrying capacity of the foundation under pure vertical loading. The capacity envelopes have been plotted in V - H and V - M planes individually. The forces (vertical load and horizontal load) and moment, for the strip foundation placed on the slope with inclination angle, β , have been normalized by V_0 and BV_0 , respectively, where V_0 is the pure vertical load capacity (i.e., for $H = M = 0$) of the strip foundation placed on flat ground. The validation of adopted methodology and FE model for development of capacity envelope can be found elsewhere in Raj et al. [14].

Results and Discussion

A detailed investigation has been conducted to understand the influence of the governing parameter β on the V - H and V - M capacity envelope under different combinations of V , H and M , as discussed in subsequent section.

V-H Capacity Envelope

Figure 14.2 shows the normalized V - H capacity envelopes for strip foundations placed on top of considered slopes, described earlier, and on the corresponding flat surface. Using Probe method, the maximum value of horizontal force, H , has been obtained at different values of vertical load, V , selected as fraction multiples (0, 1/6, 1/3, 1/2, 2/3, 5/6, 1) of the maximum capacity of the foundation. By following the process described in earlier section, the normalized vertical load and horizontal load have been obtained. It can be observed from the figure that with the increase in β the vertical capacity decreases continuously and a maximum reduction of 15% has been observed in case of $\beta = 40^\circ$. Also, the shape of the V - H capacity envelope for the foundation on slope is asymmetric, whereas the envelope is symmetric for the foundation on flat ground. The asymmetry observed in the capacity envelope further increased with the increase in β .

V-M Capacity Envelope

Figure 14.3 shows the normalized V - M capacity envelopes for strip foundations placed on top of clay slopes, described earlier, and on the flat surface of the corresponding soil. Similar to V - H capacity envelope, V - M capacity envelope has also been obtained using the Probe method, where maximum moment capacity has been

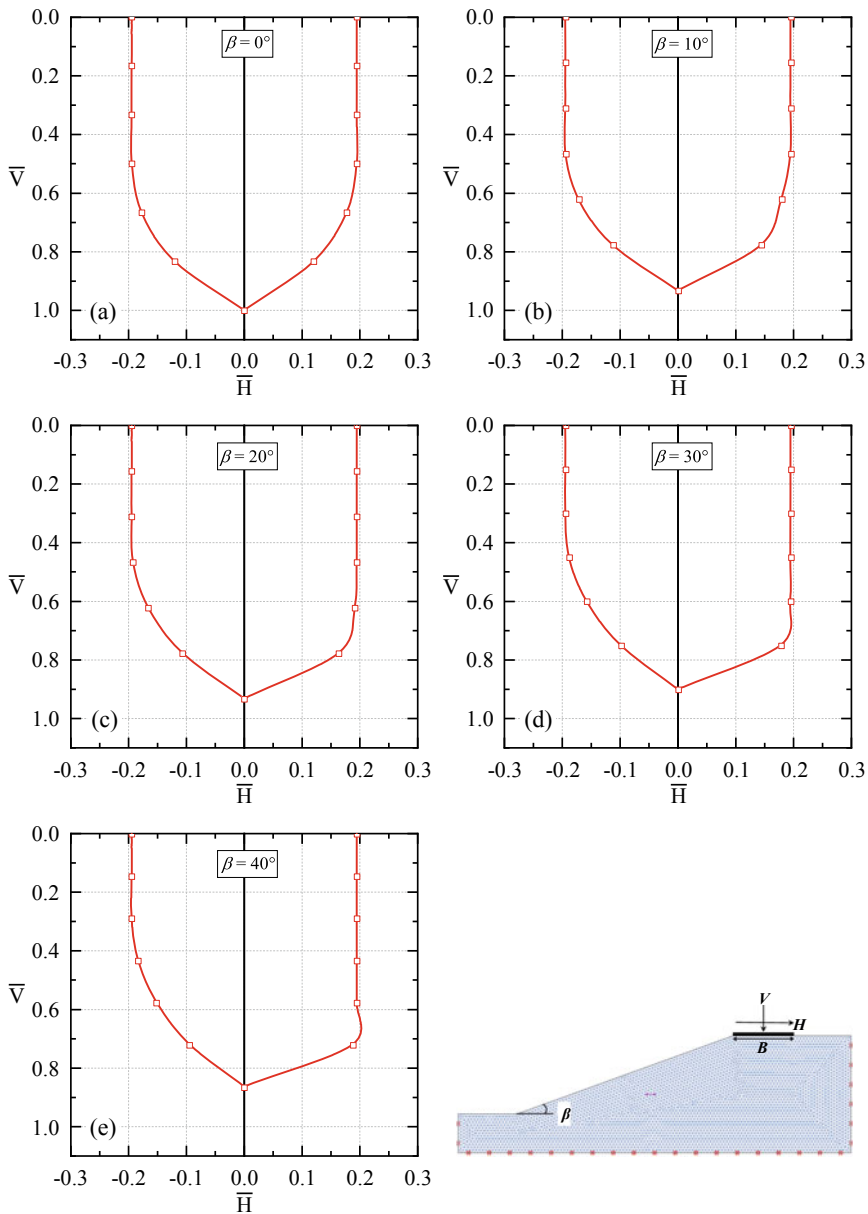


Fig. 14.2 V - H capacity envelope for: **a** $\beta = 0^\circ$; **b** $\beta = 10^\circ$; **c** $\beta = 20^\circ$; **d** $\beta = 30^\circ$; and **e** $\beta = 40^\circ$

estimated at different value of V and the normalized vertical load and moment have been obtained by following the process described in earlier section. It is interesting to note that the shape of the V - M capacity envelope for the foundation on slope is slightly asymmetric when compared to foundation on flat ground.

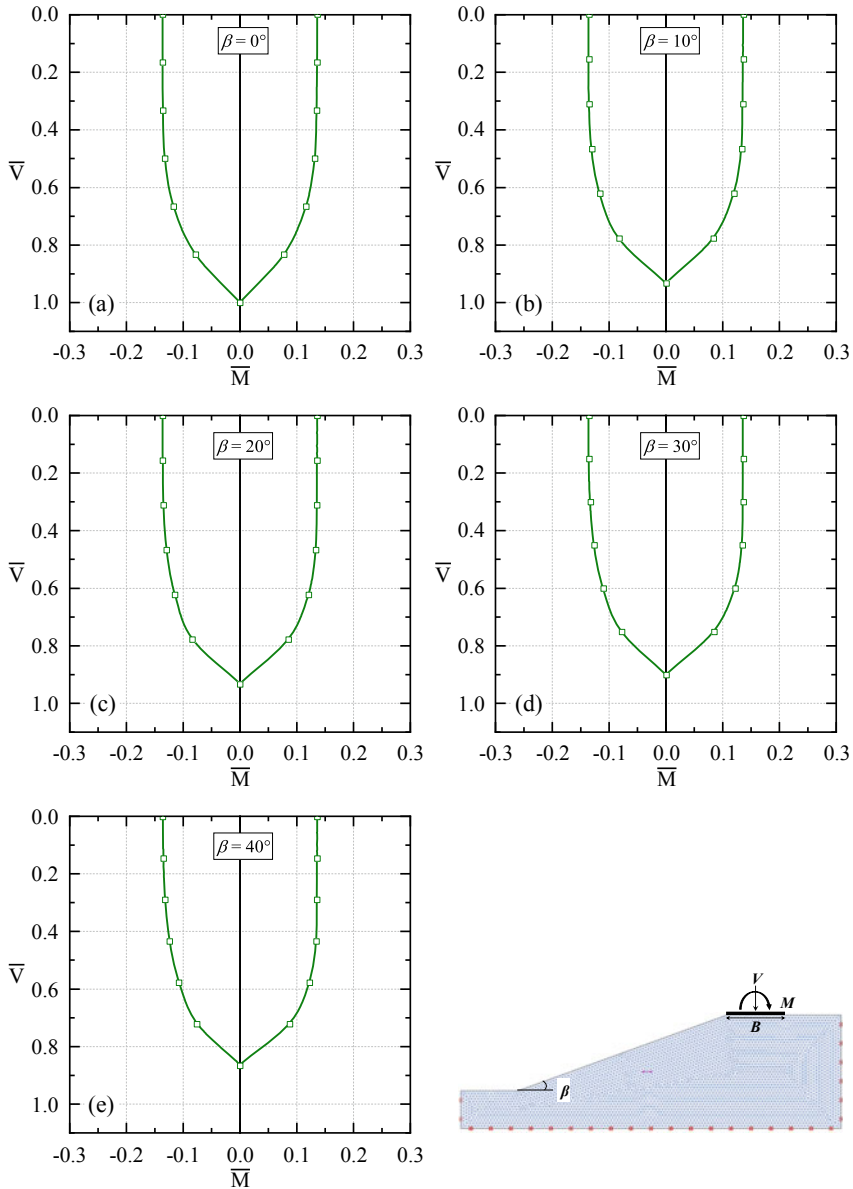


Fig. 14.3 V - M capacity envelope for: **a** $\beta = 0^\circ$; **b** $\beta = 10^\circ$; **c** $\beta = 20^\circ$; **d** $\beta = 30^\circ$; and **e** $\beta = 40^\circ$

Conclusion and Limitation

To understand the behavior and capacity envelopes of strip foundations placed on slopes under V - H and V - M load combinations, two-dimensional finite element limit analyses have been conducted in detail using OptumG2. The behavior and capacity envelopes of foundation-slope systems have been compared with foundation on flat ground.

Interestingly, in all the cases, it has been observed that the peak horizontal load capacity (at $M = 0$) and the peak moment capacity (at $H = 0$) of the foundation remain practically constant for the vertical load approximately equal to half of the maximum vertical load capacity. A maximum reduction of 15% in vertical capacity of foundation slope was observed in case of $\beta = 40^\circ$ when compared to foundation on flat ground.

The present study is limited to 2D FE simulation of homogenous undrained clay slope-foundation system under V - H and V - M loading combinations. A more detailed study using 3D FE simulation considering a wider range of slope geometries and material properties, material heterogeneity, V - H - M loading combinations and water table level is recommended for a broader understanding of the foundation-slope system.

Acknowledgements The authors are thankful to Optum CE for providing the academic license to use OptumG2 software.

References

1. IS6403 (2002) Code of practice for determination of bearing capacity of shallow foundations. Bureau of Indian Standards, New Delhi
2. EN1998-5 (2004) Eurocode 8: design of structures for earthquake resistance—part 5: foundations, retaining structures and geotechnical aspects. Sixth revision edn. British Standards Institution, London
3. ASCE (2017) Seismic evaluation and retrofit of existing buildings. ASCE/SEI 41–17. American Society of Civil Engineers, Reston, Virginia
4. NCHRP (2010) Report 651: LRFD design and construction of shallow foundations for highway bridge structures. National cooperative highway research program, Transportation Research Board, Washington, D.C.
5. Terzaghi K (1943) Theoretical soil mechanics. Wiley, New York, USA
6. Gourvenec S, Randolph M (2003) Effect of strength non-homogeneity on the shape of failure envelopes for combined loading of strip and circular foundations on clay. *Géotechnique* 53(6):575–586
7. Ukritchon B, Whittle AJ, Sloan SW (1998) Undrained limit analyses for combined loading of strip footings on clay. *J Geotech Geoenviron Eng* 124(3):265–276
8. Taiebat HA, Carter JP (2000) Numerical studies of the bearing capacity of shallow foundations on cohesive soil subjected to combined loading. *Géotechnique* 50(4):409–418
9. Yun G, Bransby MF (2007) The horizontal-moment capacity of embedded foundations in undrained soil. *Can Geotech J* 44(4):409–424

10. Gourvenec S (2008) Effect of embedment on the undrained capacity of shallow foundations under general loading. *Géotechnique* 58(3):177–185
11. Taiebat HA, Carter JP (2010) A failure surface for circular footings on cohesive soils. *Géotechnique* 60(4):265–273
12. Vulpe C, Gourvenec S, Power M (2014) A generalised failure envelope for undrained capacity of circular shallow foundations under general loading. *Géotech Lett* 4(3):187–196
13. Georgiadis K (2010) The influence of load inclination on the undrained bearing capacity of strip footings on slopes. *Comput Geotech* 37(3):311–322
14. Raj D, Singh Y, Kaynia AM (2019a) Behavior and critical failure modes of strip foundations on slopes under seismic and structural loading. *Int J Geomech* 19 (6):04019047–04019041/04019018
15. Butterfield R, Houlsby GT, Gottardi G (1997) Standardized sign conventions and notation for generally loaded foundations. *Géotechnique* 47(5):1051–1054
16. OptumG2 (2020) v2.0.15.0_2020.04.08, Optum computational engineering. Copenhagen NV, Denmark
17. Krabbenhoft K, Lyamin A, Krabbenhoft J (2016) OptumG2: theory. Optum Computat Eng. Available on: <https://optumce.com/wp-content/uploads/2016/05/Theory.pdf>
18. Krabbenhoft K (2018) Static and seismic earth pressure coefficients for vertical walls with horizontal backfill. *Soil Dyn Earthq Eng* 104:403–407
19. Raj D (2018) Seismic behaviour of foundations and buildings on slope. Ph.D. thesis, Indian Institute of Technology Roorkee, India
20. Raj D, Singh Y, Kaynia AM (2019) V-H-M seismic capacity envelopes of strip foundations on slopes for capacity design of structure-foundation system. *Bull Earthq Eng* 17(6):2963–2987

Chapter 15

Wind Turbine Foundation Using PHC Piles in Problematic Soil



Shirlin Charles, Sunil Ranjan Mohapatra, and Sudhansu Bhusan Prusty

Introduction

The study aims to propose a suitable foundation system for 4.5 MW wind turbine structure having a hub height of 130 m and rotor diameter of 155 m for 40 MW wind power project in Southeast Asia. The WTG tower is analyzed, and the foundation is designed based on the tower bottom loads provided by the tower design team [1]. This paper presents the analysis and calculations carried out for the design of the foundation system. The foundation system consists of standard circular foundation resting on the piles. The piles are pretensioned spun high-strength concrete pile (PHC), which are found to be economical compared to conventional solid pile and can effectively resist the applied load combination during the service life of the structure [2].

From the soil investigation report, it is observed that the top 20 m of the foundation soil is very soft clay having SPT N value of ≈ 1 followed by stiff to very stiff clay soil as shown in Fig. 15.1. Groundwater table is observed near the ground surface. Considering the soil conditions and the load coming from the wind turbine, it is proposed to use standard circular foundation supported on PHC piles as the foundation system [3, 4].

S. Charles (✉) · S. R. Mohapatra · S. B. Prusty
NeXHS Renewables Pvt Ltd., IITM Research Park, Chennai 600113, India
e-mail: shirlin.charles@nexhs.com

© The Author(s), under exclusive license to Springer Nature Singapore Pte Ltd. 2023
K. Muthukkumaran et al. (eds.), *Foundation and Forensic Geotechnical Engineering*, Lecture Notes in Civil Engineering 295,
https://doi.org/10.1007/978-981-19-6359-9_15

147

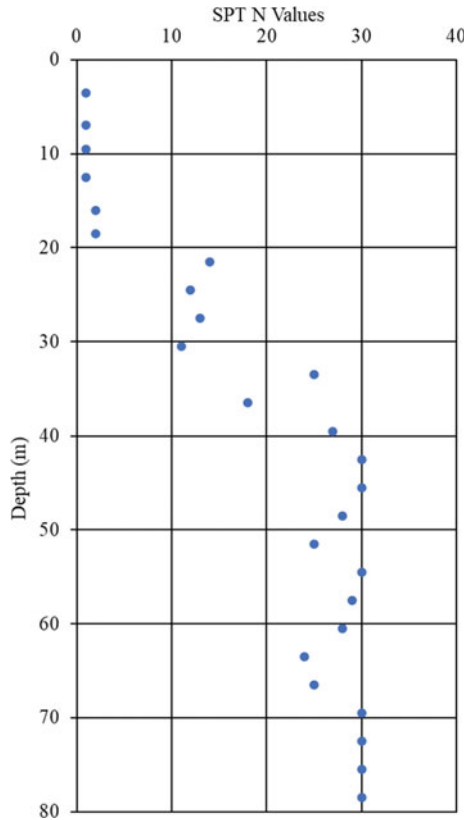


Fig. 15.1 Variation of SPT N along the depth of bore hole

Background of the Study

Installation of wind turbines in poor soils is usually challenging. Soil stabilization methods are commonly adopted prior to the construction of foundation system in poor soils. Soil stabilization techniques such as compaction methods, soil improvement by introduction of lime/cement are usually adopted [5]. This soil stabilization causes a time delay in the initiation of the construction of foundation. The foundation system is expected to undergo considerable fatigue loading during its service life. Considering above factors, the foundation system with slab resting on a PHC pile group is proposed.

Pretensioned Spun High-Strength Concrete Piles (PHC)

Pretensioned spun high-strength concrete (PHC) piles are an economical deep foundation system with higher quality and consistency compared to conventional cast in-situ/precast concrete piles. These piles have a hollow section with an outer diameter ranging from 300 to 1200 mm. The piles can be easily fixed to any combination of lengths as per the design requirements. A conventional hammer can be used to drive the PHC piles. PHC piles have lesser volume and lower cost of manufacturing due to their hollow section.

These piles are factory made having good quality control resulting in better concrete strength. Higher strength of concrete enables pile driving through hard strata and has high flexural strength and resistance against corrosion in the marine environment. Higher production rate of the piles ensures reduction in project lead time. The complete manufacturing process is carried out inside a factory eliminating the need for a casting yard at the site. Due to steam curing, the piles can achieve high early strength compared to 28 days curing period of conventional precast piles [6].

The Foundation System

The foundation system consists of a 21.6 m standard circular foundation supported on 36 PHC piles having 50 m length as shown in Fig. 15.2.

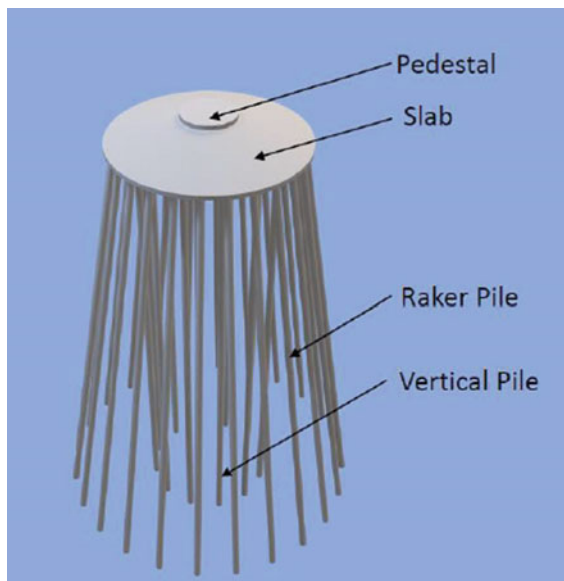


Fig. 15.2 3D model of the foundation

The raker piles (inclined piles) are provided close to the perimeter of the slab, and vertical piles are provided at 2.4 m from raker pile (center to center spacing) as shown in Fig. 15.2. The raker piles are expected to mobilize higher lateral resistance to counter the lateral load coming from the tower. Then, 18 numbers of vertical piles and 18 number of raker piles at 10° angle [7, 8] having 50 m length are provided below the standard foundation. The dimensions of the foundation are finalized such that all piles are in compression under quasi-permanent loading condition [9].

Pile–Soil–Structure Interaction

The length of the pile below the ground level at which all the degree of freedom can be arrested to reduce the computational times is known as the fixity point which is basically arrived based on the soil spring values. Sufficient length of pile penetration is necessary to achieve the compression and tension (pull-out) capacities required to support the wind turbine.

The soil around the pile must resist lateral and axial loads. As the nature of the soil is complicated to predict, finding a closed-form solution to such a problem is extremely difficult. So, the soil behavior is predicted as a series of independent springs, in which the lateral stiffness at one point was affected by the lateral stiffness at other points along the length of the pile.

Design Procedure

The design is carried out based on the respective European standard.

Material Properties

Tables 15.1 and 15.2 show the properties of concrete and steel used for the foundation design [10, 11], respectively.

Finite Element Analysis

The finite element (FE) analysis was performed using Abaqus 6.18 software to understand the soil structure interaction of the foundation system subjected to given loading condition [12]. Both quasi- and extreme loading conditions were analyzed using the FE model. About 18 numbers of raker pile and 18 numbers of vertical piles were

Table 15.1 Properties of concrete used in the design

Properties	Value	Unit
Density of reinforced concrete	2500	kg/m ³
Standard foundation concrete strength	45	MPa
Pedestal top concrete strength	50	MPa
Pile concrete strength	80	MPa
Aggregate max. size	20	mm
Elastic modulus of standard foundation	36,283	MPa
Elastic modulus of pile	42,244	MPa
Poisson ratio	0.17	–

Table 15.2 Reinforcement steel properties used in the design

Properties	Value	Unit
Elastic modulus	200,000	MPa
Density	7850	Kg/m ³
Yield stress	500	MPa
Cover	50	mm

modeled as shown in Fig. 15.3. The sectional view of the foundation system with the respective dimensions is shown in Fig. 15.4.

The mesh of the model (Fig. 15.5) consists of shell elements of S4R which is assigned to the pedestal and slab portion of the foundation, and the pile is modeled by 1D beam element B31. The size of the element was 0.35 m which was obtained using grid independency study.

**Fig. 15.3** FE model of the foundation

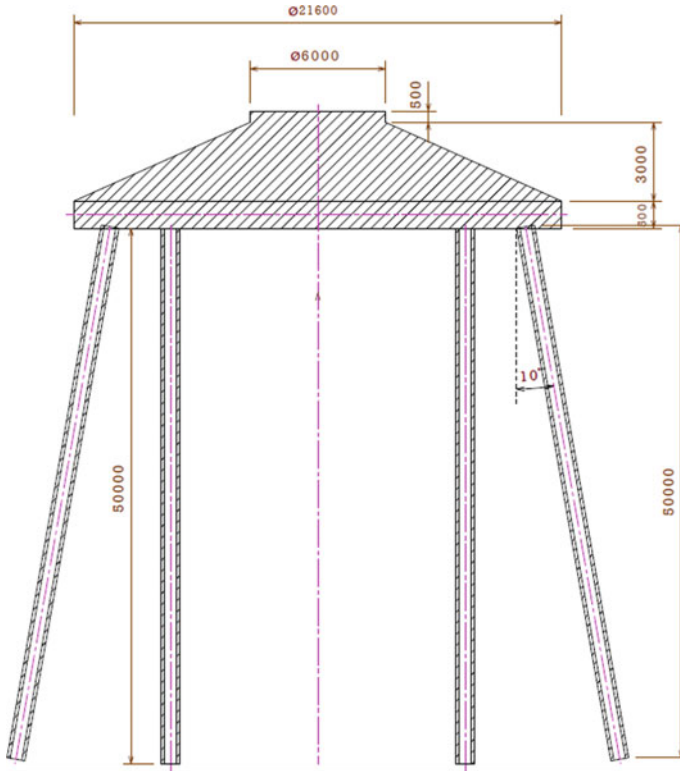


Fig. 15.4 Sectional view of the foundation system (*Dimensions in mm*)

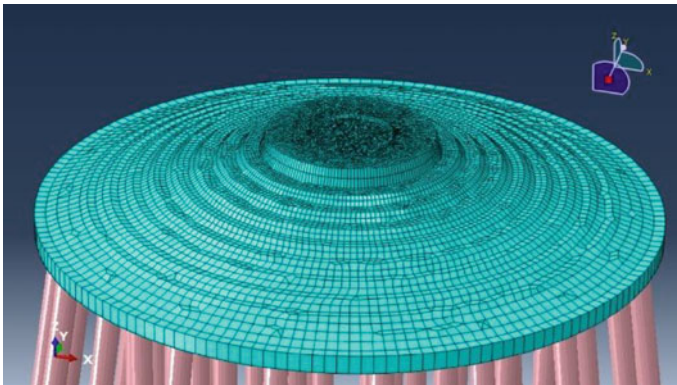


Fig. 15.5 Meshing of the model

Boundary Conditions

To simulate the confinement from the soil, subgrade modulus of the foundation soil is calculated based on the variation of its Young’s modulus along the depth of the pile. In the FE model, horizontal spring values were applied on the pile surface and pinned support is applied at the pile tip. The spring values are calculated using the following formula as mentioned in Eq. 15.1.

$$k'_s = 1.3 \left[\frac{E_s B^4}{E_p I_p} \times \frac{1}{12} \times \frac{E_s}{1 - \mu^2} \right] \tag{15.1}$$

where

- μ Poisson’s ratio of soil
- E_s Compressibility modulus of the soil
- E_p Young’s modulus of concrete
- I_p Moment of inertia of the pile.

Loads

The load components are applied on top of the foundation by a reference point. This node transfers the load rigidly to other nodes in the pedestal that simulate the tower joint to foundation as shown in Fig. 15.6. These load components are applied in the direction defined in the following figure to obtain the most unfavorable load case.

For extreme condition, the value of resultant force and moment is 1335.46 kN and 155,817 kN, respectively. For quasi-condition, the value of resultant force and moment is 744 kN and 88,350 kN, respectively. These values were supplied by the tower design team.

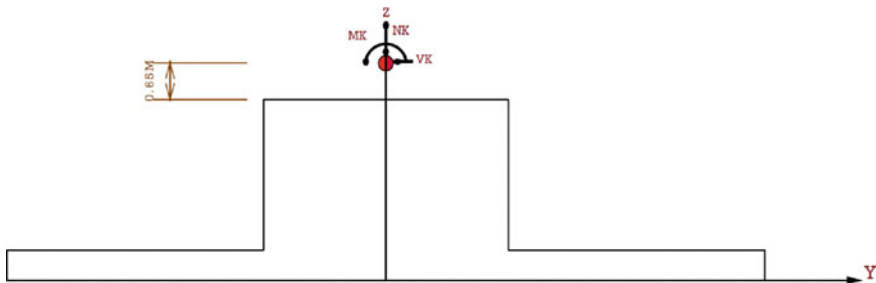


Fig. 15.6 Applied loads, FEM global coordinate system and loaded nodes

Results and Discussion

The quasi-permanent and governing extreme loads were applied to the foundation, and a static structural analysis was performed considering appropriate partial load factors. Under quasi-permanent loading condition, the piles should be in compression, and no tension is allowed in the piles. Pile can be subjected to tension under extreme loads. Proper checks are carried out for rotational stiffness under different load combination.

The foundation designed dimension is found to be acceptable considering the loads under quasi-permanent and governing extreme loads. It has been verified that under quasi-permanent loads, no piles are in tension. Calculation of the reinforcement is carried out based on the results obtained from FE analysis.

The FEM analysis was performed considering extreme loads, self-weight of the foundation and weight of backfill, without safety factors, for calculating the settlement. The difference between the maximum and minimum vertical displacements of the pedestal upper line and slab base line per meter was found to be within acceptable limits, i.e., $\text{Diff}_{\text{pedestal}}/\text{Diff}_{\text{slab}} \leq 3 \text{ mm/m}$ (Fig. 15.7).

The admissible stresses in the concrete are found to be within $0.6f_{ck}$ as shown in Fig. 15.8.

Vertical Capacity of Pile

The pile capacity was calculated based on European code [3, 13] design approach 2.

$$F_{cd} \leq R_{cd} \quad (15.2)$$

where

F_{cd} Design axial compression load on pile

R_{cd} Pile compressive design resistance

For extreme condition

$$R_{cd} = 0.719 \times R_{bk} + 0.719 \times R_{sk} = 3927.69 \text{ kN}$$

For quasi-condition

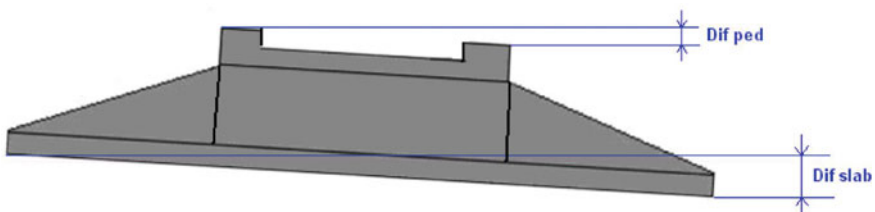


Fig. 15.7 Schematic view of settlement of the foundation

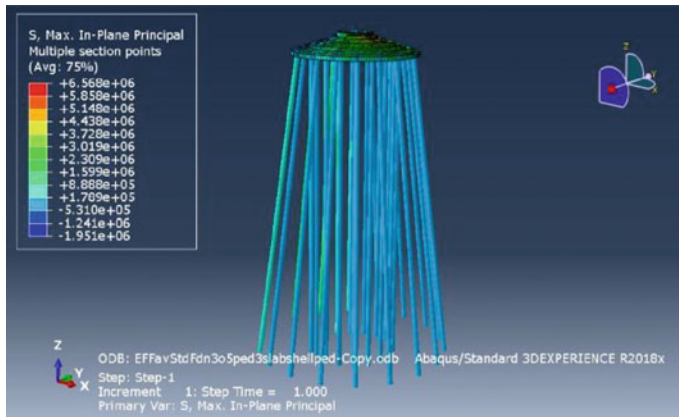


Fig. 15.8 Maximum permissible stresses

Table 15.3 Pile capacity as per EN 1997-1, Eurocode 7

Combination	F_{max} (kN)	Comment
Extreme	3927 > 1992	ok
Quasi	2747 > 1354	ok

$$R_{cd} = 0.503 \times R_{bk} + 0.503 \times R_{sk} = 2747.75 \text{ kN}$$

where

R_{bk} Characteristic base resistance

R_{sk} Characteristic shaft resistance

F_{cd} under extreme loading case from the FE analysis was 1922 kN < 3927 kN. Hence, the capacity of the pile was safe under extreme condition, and the same trend was obtained for quasi-condition as shown in Table 15.3.

Comparison of maximum pile load with characteristic pile resistance is shown in Table 15.3.

Conclusions

A FE analysis is carried out to design the foundation system for a 4.5 MW wind turbine constructed in very soft foundation soil. From the study, the following points are concluded.

- The 21.6 m standard circular foundation having a pedestal height of 3.5m supported on 36 PHC piles (18 vertical + 18 raker) is suitable to support the horizontal loads and moments acting at the base of the wind turbine.

- PHC piles are used in this study as they have better quality control and minimize the lead time of the project. The cost of the foundation is also minimized.
- FE analysis helped to optimize the foundation system and satisfy all the design criteria as per the codal provisions.
- PHC piles have higher section modulus and higher strength compared to similar volume of precast concrete piles. Hence, it satisfies the requirements of drivability and erection stresses.
- Use of PHC pile helps to reduce the usage of passive reinforcement.

References

1. DNV/RISØ (2002) Guidelines for design of wind turbines, 2nd edn. Jydsk Centraltrykkeri, Denmark
2. TCVN 7888 (2014) Pretensioned spun concrete pile
3. EN 1997-1 (2004) Geotechnical design-general rules (EC-7)
4. EN 1997-2 (2007) Geotechnical design-ground investigation and testing (EC-7)
5. Moseley MP, Kirsch K (2004) Ground improvements, 2nd edn. Spon press, Abingdon UK
6. TCXD 205 (1998) Construction standard on pile foundations-design standards
7. Giannakou A, Gerolymos N, Gazetas G, Tazoh T, Anastasopoulos I (2010) Seismic behaviour of batter piles: elastic response. *J Geotech Geo-Environ Eng* 1187–1199. ASCE
8. Poulos HG (2006) Raked piles-virtues and drawbacks. *J Geotech Geo-Environ Eng* 795–803. ASCE
9. EN 61400-1 (2005) Wind turbine generator systems-Safety requirements
10. EN 1992-1-1 (2004) Design of concrete structures. General rules and rules for buildings
11. SP-16 (1980) Design aid to reinforced concrete to IS 456
12. Abaqus user's manual Version 6.14 (2007)
13. Geotechnical design worked examples (2013) 13–14 June, Dublin (EC-7)

Chapter 16

Effect of Super Structural Symmetry on Pile Foundations Under Pseudo-static Loading



Aniket Chanda, Saumitro Mandal, and Arghadeep Biswas 

Introduction

The geotechnical engineers face difficulties to predict the behavior of piles while an earthquake wave hits the system. The responses of pile foundation in dynamic loading are one of the most complex soil–structure interactions when superstructures are having irregular and/or complex geometries. Piles may be heavily damaged during and/or immediately after the earthquake occurs. Therefore, a proper design is of immense importance to avoid the adverse effects of dynamic loading on pile foundations.

Analyzing the pile responses under earthquake load, finite element and boundary element methods are extremely efficient. Using finite element methods for analyzing the pile behavior is having a very rich history [1, 2]. Considering earthquake as the pseudo-static loading has been very popular and effective compared to the convergence, simplicity, and time consumption. Abghari and Chai [3] had also analyzed the pile behavior for the pseudo-static method and dynamic finite element analysis. Tabesh and Poulos [4–6] presented the results obtained by using pseudo-static and dynamic analysis for different piles and soil properties. A good agreement in results is received for both the cases which confirmed the advantage of using the pseudo-static method. Ishihara and Cubrinovski [7] analyzed the pile responses for soil deposits subjected to lateral spreading in a pseudo-static approach based on the Kobe earthquake that occurred in 1995. Further investigation, in a similar context, was also

A. Chanda · S. Mandal
Department of Civil Engineering, Jalpaiguri Government Engineering College, Jalpaiguri, West Bengal 735102, India

A. Biswas (✉)
Department of Civil Engineering, Jadavpur University, Kolkata, West Bengal 700032, India
e-mail: arghadeep.biswas@gmail.com

Table 16.1 Material properties

Parameters	Sand	Concrete
Material model	Mohr–Coulomb	Linear elastic
Drain condition	Drained	Non-porous
Angle of internal friction (°)	33	–
Poisson's ratio	0.35	0.2
Saturated unit weight of soil (kN/m ²)	18	25
Modulus of elasticity (kN/m ²)	3×10^4	3×10^7

performed by Liyanapathirana and Poulos [8]. In the reported article, the pseudo-static approach was adopted in liquefying soil. They concluded that pile responses calculated from the pseudo-static approach are consistent with the observed pile behavior. Phanikanth et al. [9] have reported a study of the laterally loaded pile in cohesionless soil. Further, Chatterjee et al. [10] presented a study on seismic analysis of laterally loaded piles under the influence of vertical loading using the finite element method.

Based on the literature, this present study is envisaged to analyze the pile behavior supporting high-rise building of different symmetrical and asymmetrical shapes. For this purpose, finite element software, PLAXIS 3D, has been used. The PLAXIS 3D can afford both dynamic (time history analysis) and pseudo-static methods; however, the pseudo-static method of analysis is considered due to simplicity and time limitations. At present, variables such as pile length and diameter ratio and the pseudo-static accelerations are considered for this study.

Materials and Modeling

Medium dense sand is considered as foundation soil for the study; while, reinforced concrete is adopted as the material for the piles to transfer the superstructural load deeper into the soil. In the finite element program, the Mohr–Coulomb material model is considered for the sandy soil, whereas the reinforced concrete is modeled as a linear-elastic material. The material properties are summarized in Table 16.1.

Finite Element Modeling

In general, earthquake load can be analyzed as time-domain analysis and pseudo-static loading. In the case of force-based pseudo-static analysis, the effects of dynamic loading are represented by equivalent inertia forces. These are approximately constant body forces with magnitude proportional to the horizontal and/or vertical accelerations imposed by the dynamic loading as $F_i = k_i W$, where, 'i' denotes

the force direction in X , Y , and Z directions, respectively. Hence, the F_i represents the body forces and k_i is the pseudo-static acceleration in the corresponding directions; while ‘ W ’ represents the corresponding mass. In analysis, these forces are going to be applied to the whole mesh.

Seven-story symmetrical and unsymmetrical buildings are modeled using PLAXIS 3D. A square building, having a symmetrical configuration about both the axes, is considered to compare the asymmetrical responses corresponding to ‘T’ ‘E’ and ‘L’ shaped buildings. The plan view of different building configurations is presented in Fig. 16.1. In this regard, it should be mentioned here that the ‘T’ and ‘E’ shaped buildings are symmetrical about one axis and unsymmetrical about the other, whereas the ‘L’ shaped building is asymmetrical about both of its axes. In all the cases, the soil properties, the number of columns, and building-structural properties are kept constant. Buildings are constructed using beam, column and floor slabs.

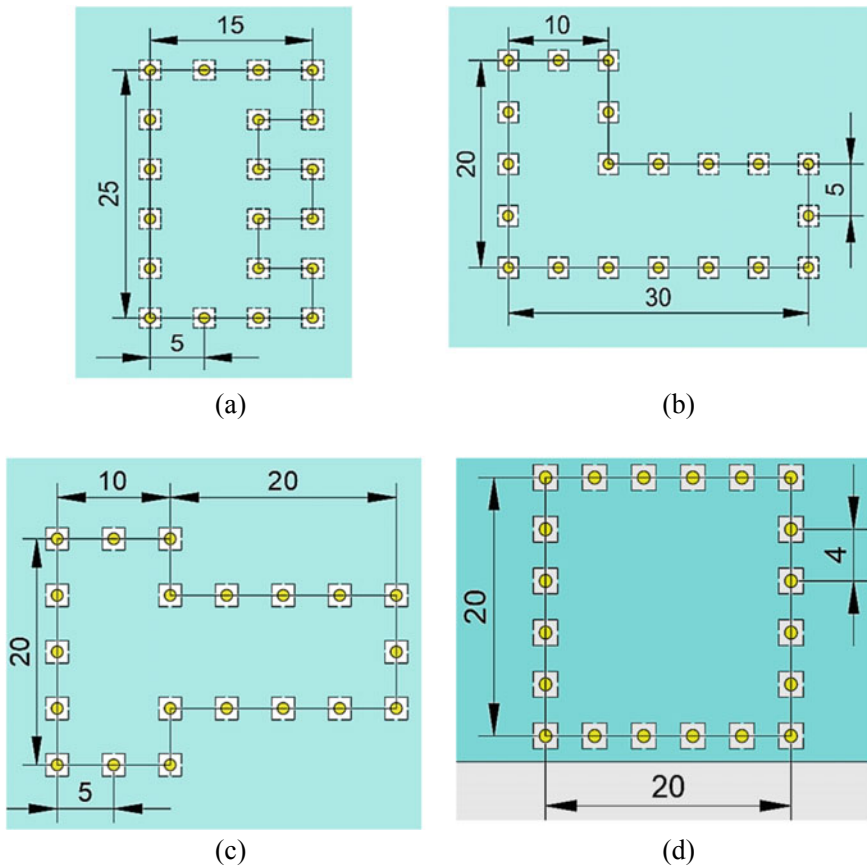


Fig. 16.1 a ‘E’ shaped, b ‘L’ shaped, c ‘T’ shaped and d square shaped building

The present study is performed by keeping pile diameter constant at 1 m while varying the pile length from 10 to 40 m, for different pseudo-static accelerations. A soil stratum is considered in such a way that the pressure bulb should not extend the outside of the modeled dimension. In the finite element models, the X and Y boundaries are made normally fixed, while the Z_{\min} and Z_{\max} are modeled as fully fixed and free, respectively.

Results and Discussions

The present study has investigated the performance of piles supporting superstructures of different shapes, viz. square, 'T' 'E' and 'L' shapes. The pile performance is analyzed based on displacements concerning parametric variations such as L/D ratio (10 to 40) and horizontal accelerations ranging between 0.1–0.5 g.

Figure 16.2 is showing a comparative performance of corner piles, in terms of horizontal displacements under different pseudo-static accelerations (0.2 g and 0 g) for the pile with $L = 10$ m. It may be noticed that piles associated with the square shaped building have undergone higher displacements compared to the rest.

Figures 16.3, 16.4 and 16.5 are depicting comparative performances of corner piles, in terms of horizontal displacements under different pseudo-static accelerations (from 0.1 g to 0.5 g) at various observation points along pile length for $L/D = 20$. In general, it is found that displacements of a pile of various buildings are increased with an increase in horizontal acceleration ranging from 0.1 g to 0.5 g. The displacements are found to be maximum at the pile cap and gradually decrease along with the depth of the pile. Figure 16.2 is showing the displacement behavior of the pile cap for the parametric variations as mentioned above ($L/D = 20$). It may be noticed that piles associated with the square shaped building have undergone higher displacements compared to the rest. Further, it is noticed that the piles with 'E' and 'T' buildings have almost the same displacement for different accelerations within the range considered.

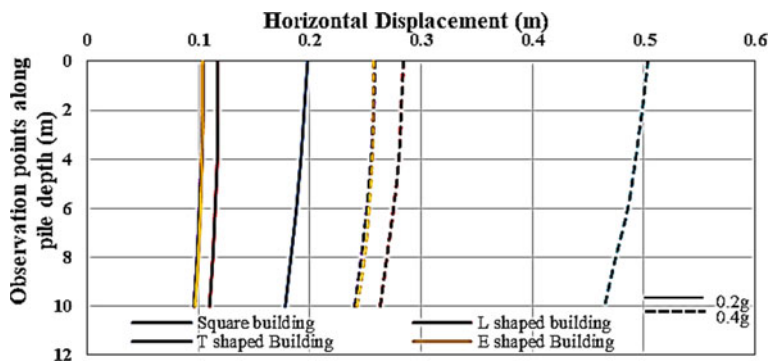


Fig. 16.2 Displacement profiles of corner pile ($L = 10$ m) for different horizontal accelerations

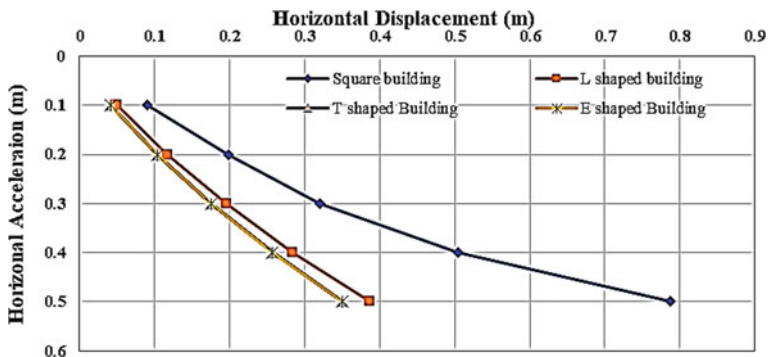


Fig. 16.3 Displacement profiles of pile cap of a corner pile ($L = 20$ m) for varying accelerations

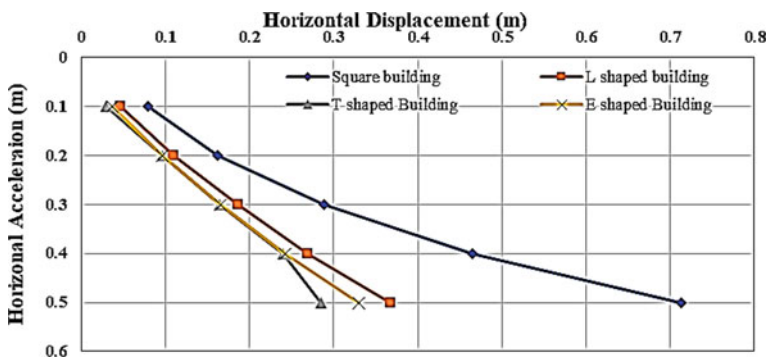


Fig. 16.4 Displacement profiles of pile at 10 m depth ($L = 20$ m) for varying accelerations

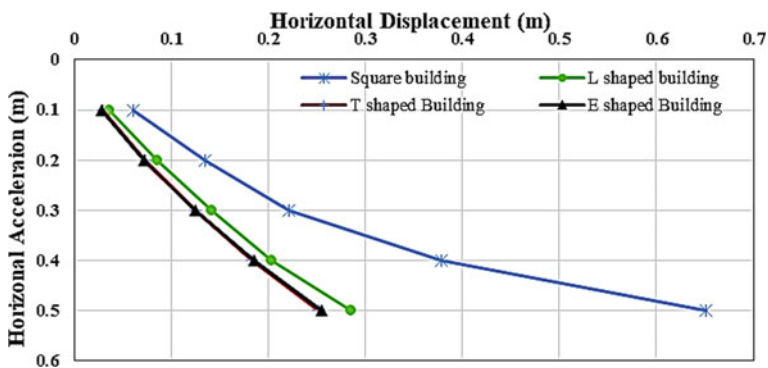


Fig. 16.5 Displacement profiles of pile at 20 m depth ($L = 20$ m) for varying accelerations

Table 16.2 Summary of horizontal displacements of piles ($L/D = 40$) for different conditions

Building shape	Observation point depths (m)	Pseudo-static acceleration				
		0.1 g	0.2 g	0.3 g	0.4 g	0.5 g
		Horizontal displacement of piles (m)				
Square	Pile cap	0.042	0.114	0.194	0.284	0.393
	20	0.042	0.119	0.214	0.316	0.426
	40	0.033	0.082	0.154	0.235	0.321
T	Pile cap	0.045	0.117	0.199	0.295	0.41
	20	0.04	0.109	0.192	0.284	0.383
	40	0.027	0.059	0.105	0.157	0.213
L	Pile cap	0.054	0.14	0.236	0.348	0.489
	20	0.057	0.156	0.268	0.339	0.529
	40	0.051	0.127	0.226	0.329	0.441
E	Pile cap	0.044	0.116	0.196	0.293	–
	20	0.039	0.109	0.194	0.288	–
	40	0.023	0.056	0.102	0.155	–

In Table 16.2, a typical performance, in terms of displacement of piles, for the pile with length 40 m (i.e., $L/D = 40$) supporting superstructures of various shapes, for different pseudo-static accelerations is briefly summarized. In general, it may be concluded that pile displacements are proportional to horizontal acceleration. The horizontal deformation of piles increases with higher pseudo-static accelerations. It is observed that the displacements are maximum at pile cap, while it has gradually reduced down with depth. It is also found that the pile displacements are not following any trend, but their variation lies within a narrow range. It could be the shape of the building and the direction of pseudo-static acceleration for concern building inertia about the axis which plays an extremely important role in resisting the load and thus the displacement concern.

Performance of comparatively longer piles, $L/D = 40$ is different compared to earlier cases of 10 and 20 m. The asymmetric 'L' shaped building pile has depicted higher deformation compared to others. In general, a steep change in deformation profile is seen for greater depths (>20 m). Such behavior can be associated with the slenderness of the pile. In addition, the soil–pile adhesion and the lateral confinement provided by the highly overburdened soil could be the reason behind anchoring the bottom part of the piles from getting displaced.

Conclusions

The study is intended to investigate the responses of piles supporting superstructures of different structural configurations under different parametric variations. The

variations included the pile length (keeping the diameter constant) and horizontal acceleration. As per the observation, the following conclusions can be drawn.

Under similar horizontal accelerations, the magnitudes of displacements decrease with an increase in pile length.

A gradual decrease in displacement along the pile length is found irrespective of acceleration intensity.

Displacement of the piles in symmetrical building (e.g., square building) for all pseudo-static load is higher than asymmetrical building (e.g., 'L' shaped building, 'T' shaped building, 'E' shaped building) when the L/D ratio is within 20.

Although, the study has assumed the earthquake load as pseudo-static forces, which itself has some limitations such as the mass and inertia were not considered, and model verification could not be performed; however, the outcome could be a good lead-in configuring the piles for buildings of different shapes as per feasibility.

References

1. Blaney GW, Kausel E, Roesset JM (1976) Dynamic stiffness of piles. In: 2nd international conference on numerical methods in geomechanics. ASCE, Reston, VA, pp 1001–1012
2. Dowrick DJ (1977) Earthquake resistant design, 2nd edn. Wiley, New York
3. Abghari A, Chai J (1995) Modeling of soil-pile superstructure interaction for bridge foundations. In: Turner JP (ed) Proceedings of performance of deep foundations under seismic loading. ASCE Geotechnical Special Publication No.51, New York, pp 45–59
4. Tabesh A, Poulos HG (2000) A simple method for the seismic analysis of piles and its comparison with the results of centrifuge tests. In: 12th World conference on earthquake engineering, Paper no.1203 Auckland, New Zealand
5. Tabesh A, Poulos HG (2001) The effect of soil yielding on seismic analysis of single piles. *Soils Found* 41(3):1–16
6. Tabesh A, Poulos HG (2001) Pseudostatic approach for seismic analysis of single piles. *J Geotech Geoenviron Eng* 127(9):757–765
7. Ishihara K, Cubrinovski M (1998) Performance of large-diameter piles subjected to lateral spreading of liquefied deposits. In: 13th Southeast Asian geotechnical conference, Taipei, Taiwan, ROC
8. Liyanapathirana DS, Poulos HG (2005) Pseudostatic approach for seismic analysis of piles in liquefying soil. *J Geotech Geoenviron Eng* 131(12):1480–1487
9. Phanikanth VS, Choudhury D, Reddy GR (2010) Response of single pile under lateral loads in cohesionless soil. *Electron J Geotech Eng* 15(H):813–30
10. Chatterjee K, Choudhury D, Poulos HG (2015) Seismic analysis of the laterally loaded pile under influence of vertical loading using finite element method. *Comput Geotech* 67:172–186

Chapter 17

Behavior of Pile in Sloped Grounds Under the Influence of Surcharge Loads



Jegatheeswaran Boompani, K. Muthukkumaran, and R. Manjula

Introduction

The pile is an important substructural element to transfer the superstructure loads to the soil. The pile can able to transfer both axial and transverse loads from the superstructures or different situations. Wind, earthquake, soil movements, surcharge load nearer to structures, etc., influence lateral force to pile. Many research works are going on in the field of study on lateral responses of the pile [1]. The effect of vertical load on lateral response of the long pile in sandy soil is significant, and it is not valid in clayey soil if the pile length is beyond 15 times its width. Muthukkumaran et al. [2] modify the API method to construct the P-Y curves for the lateral responses of a piles in a sloped ground [3]. Until a spacing of a pile is 8d, the spacing between [4]. In the case of long piles, the soil's subgrade reactions can increase by reducing the thickness of the weaker soil layer. In short pile, the pile subgrade reaction increases by increasing the compactness of the soil and slenderness ratio of the pile [5]. The effects of embankment slopes are invalid if the pile has been placed 15 times the pile diameter from the slope crest [6]. Reduction of the adhesiveness between soil and the pile will significantly reduce the P-Y curve's ultimate load. Chandrasekaran et al. [7] the lateral capacity of pile in 3×3 pile group with 3d times spacing is 40% less than a single pile with [8, 9] developed a finite element model and determined the influences of slope and relative density of soil [10]. The combined loads increase the

J. Boompani (✉)

Department of Civil Engineering, AAACET, Sivakasi, Tamil Nadu, India
e-mail: jegatheesb@gmail.com

K. Muthukkumaran · R. Manjula

Department of Civil Engineering, NIT, Trichy, Tamil Nadu, India
e-mail: kmk@nitt.edu

R. Manjula

e-mail: manju@nitt.edu

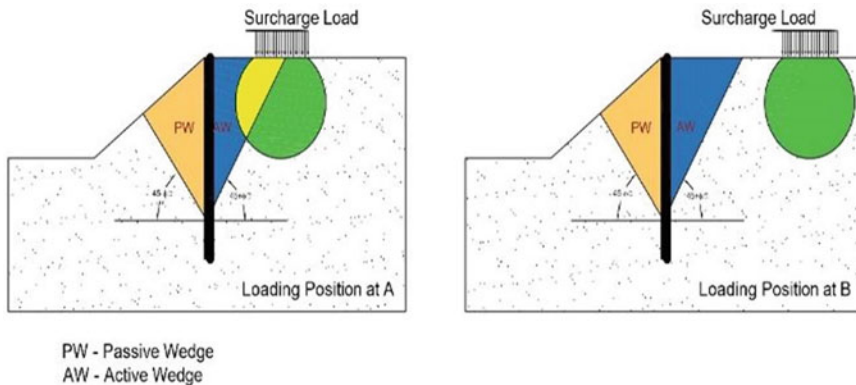


Fig. 17.1 Schematic diagram of surcharge loads at loading positions A and B

lateral load-carrying capacity of a pile in homogenous sandy soil, and it is not valid in the pile with combined loading in clayey soil. Rathod et al. [11] study influences of ground sloping on P-Y curves for lateral piles. Jayasree et al. [12] compare the comparative study between Indian standard and theoretical (using Vesic's equation) approaches [13]. Three-dimensional study on the pile group at sloped surfaces. The influences of the slope angle on the pile and pile spacing are discussed. The literature shows the importance of the studies on the lateral responses of the pile under the effects of lateral soil movements. This present study is about the lateral responses of a free head pile in homogenous sandy soil medium at slope crest, under the influences of varying surcharge loads, ground slopes and relative densities of soil. For the effects of different surcharge loads (50–200 kN/m) with a 5 m span, consider it at two locations (A and B). The loading position A starts immediately from the end of the active wedge, and the loading position B starts from 10 m away from the end of the active wedge. Both the surcharge loading positions will ensure with and without interactions between the pressure bulb of surcharge loads and active wedge. This study considers the varying ground slope as (1V:1.5H, 1V:2H and 1V:2.5H) and relative densities of soil as 70%. Develop the two-dimensional finite element models with standard fixities boundary conditions in PLAXIS 2D and calculating the lateral responses of the pile at slope crest (lateral deflections) by considering various lateral forces (surcharges load and ground slopes) on it. The schematic diagram of the surcharge loading positions in the model is shown in Fig. 17.1.

Model Features and Validation

The lateral responses of a free-headed single pile at slope crest loads in homogenous sandy soil profiles under the influences of varying surcharges loads are determining

Table 17.1 Input parameters

Soil details		Pile details	
C_u (kN/m ²)	0.1	E.A. (kN)	2.83×10^7
φ	38°	E.I. (kNm ²)	2.54×10^6
ψ	8°	Diameter	1.2 m
E_s (MPa)	78	Length	18 m
μ_s	0.3	Material	Concrete
γ_s (kN/m ³)	17.6	Grade of concrete	M25
R.D (%)	70%	μ_c	0.15

Table 17.2 Active wedge calculation as per IS 2911

S. No.	Soil type	Relative density (R.D.) (%)	Width of active wedge (m)
1	Loose sand	30	1.89
2	Medium sand	45	1.46
3	dense sand	70	1.05

by developing two-dimensional finite element models under the plane-strain condition with standard fixities boundary conditions in PLAXIS 2D. Generate a pile model using five-nodded plate elements (Beam element), and a soil model uses 15 noded triangular Mohr–Coulomb model for soil.

Considering 15 nodes triangular elements for soil medium generate five pairs of nodes with zero thickness interface. The standard fixities boundary condition confirms the fixed condition at the bottom and roller at the vertical direction of the model. Table 17.1 shows the input parameters of the model. Calculate the active wedge width from IS2911, and Table 17.2 shows it. Figure 17.2 shows the surcharge loading positions at A and B in the present finite element models in PLAXIS 2D. The dimensions of the finite element models are dimensions from Karthigeyan et al. [1].

Two different published studies [1, 14] are using for the validation of this present finite element model in PLAXIS 2D. Figure 17.3 shows that the current two-dimensional finite element PLAXIS models match the lateral responses of pile in homogenous and multilayered soil models.

Results and Discussion

This present study evaluates the lateral responses of a pile at slope crest by considering varying ground slopes (1V:1.5H, 1V:2H and 1V:2.5H) surcharge loads (50–200 kN/m) at two different loading positions A and B. The soil profile is entirely homogenous sandy soil with a relative density of 70%. The results and discussions of this paper are based on the developed two-dimensional finite element model in

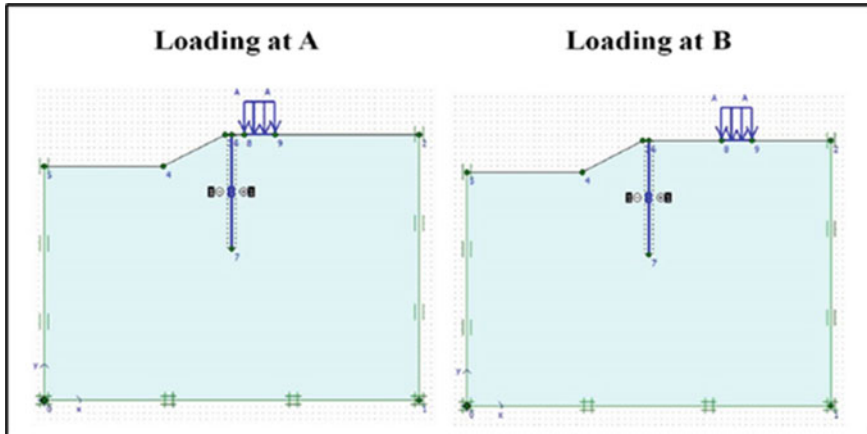


Fig. 17.2 Present finite element model

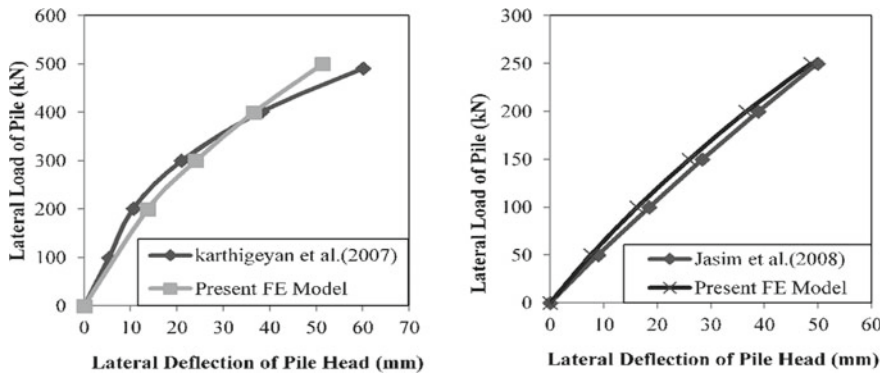


Fig. 17.3 Validation of the present finite element model

PLAXIS 2D. The varying surcharge loads and ground slopes are the significant factors for the magnitude of passive loads on a pile at slope crest. When the surcharge load is at loading position A, the passive loads (surcharge loads and soil movements due to sloping effect) dominate at the pile head zone. Due to soil confinement, the overburdened pressure is dominant at the pile base portion. It will work against the pile displacements. The pressure distribution of the surcharge load at loading position B will affect the pile base. It will create the base displacement of the pile in the direction of the passive loads, and the pile head will displace the opposite to the pile base displacement. Both the opposite directions of displacements will create rotation in the pile. Nearer to the pile head, the overburden pressure is very minimum. So, the pile head displacement in the opposite direction is possible. The magnitude of the surcharge load at the loading position at B is directly proportional to the magnitude of bottom displacement of a pile (along with the direction of passive load).

Figures 17.4, 17.5, 17.6, 17.7, 17.8, 17.9, 17.10 and 17.11 represent the lateral displacements of a pile at slope crest due to the varying surcharge loads (50–200 kN/m) at loading positions A and B with different ground slopes (1V:1.5H, 1V:2H and 1V:2.5H).

Fig. 17.4 Lateral displacement of pile at sloped ground 1V:1.5H, surcharge load at A

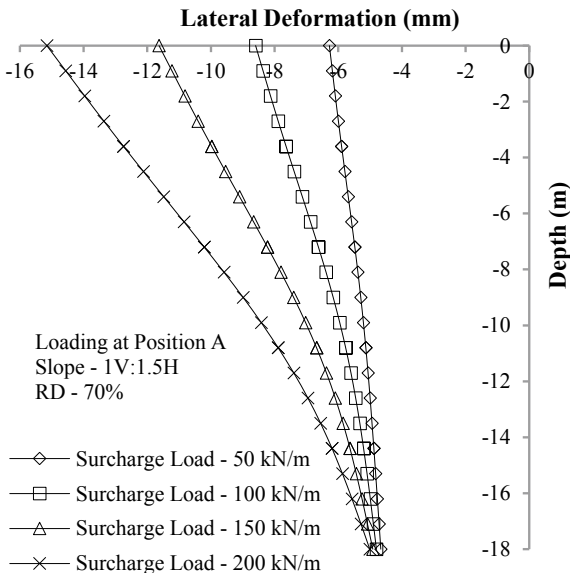


Fig. 17.5 Lateral displacement of pile at sloped ground 1V:1.5H, surcharge load at B

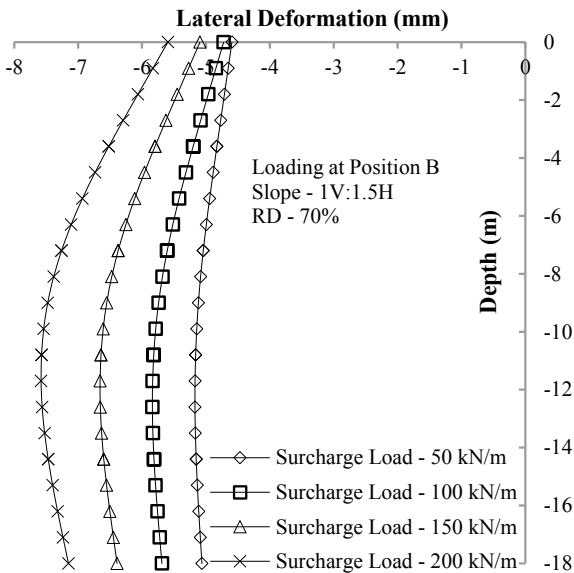


Fig. 17.6 Lateral displacement of pile at sloped ground 1V:2H, surcharge load at A

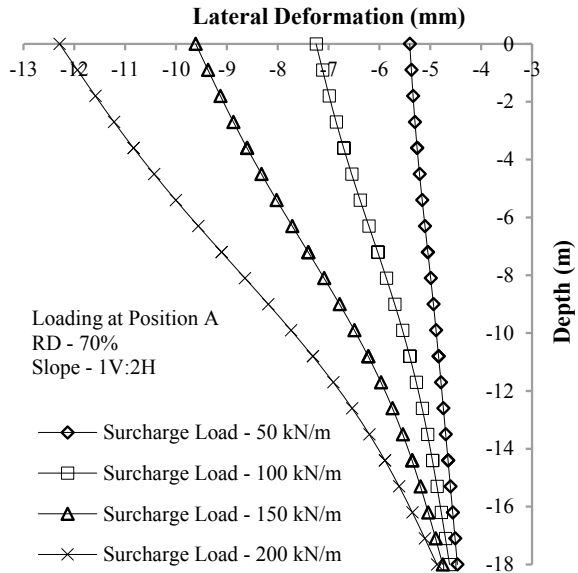
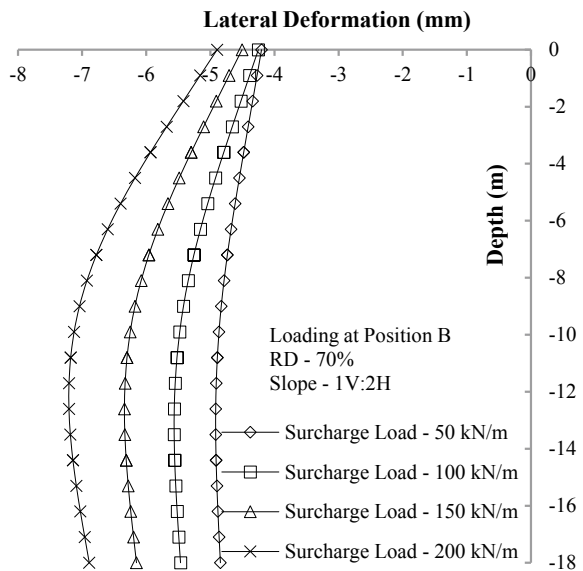


Fig. 17.7 Lateral displacement of pile at sloped ground 1V:2H, surcharge load at B



Figures 17.4 and 17.5 show the varying surcharge loading at positions A and B in the homogenous sandy soil of 70% relative density at sloping ground 1V:1.5H. The varying surcharge load at loading position A will create both pile head and bottom displacements in a pile at slope crest. Comparing the pile head displacements with pile base for the corresponding surcharge loads 50, 100, 150 and 200 kN/m, the pile

Fig. 17.8 Lateral displacement of pile at sloped ground 1V:2.5H, surcharge load at A

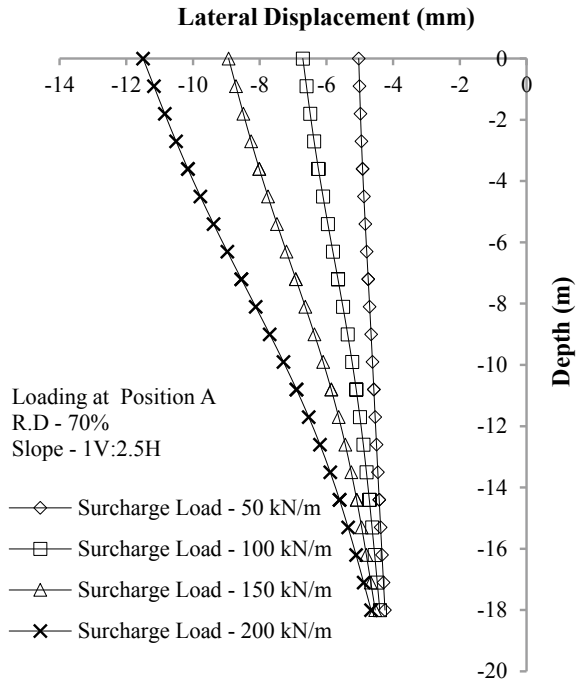
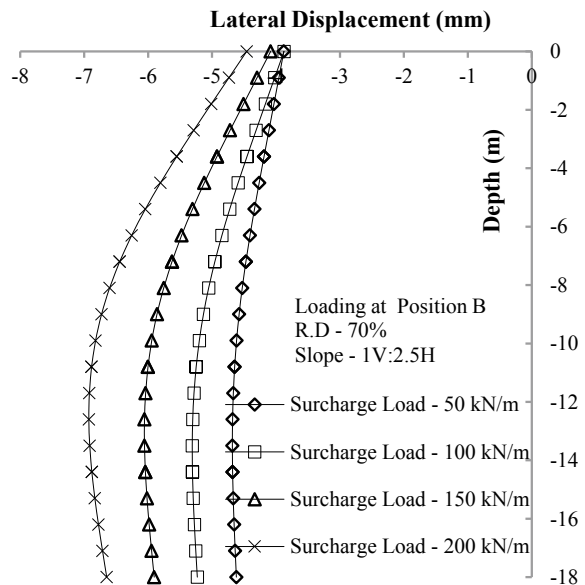


Fig. 17.9 Lateral displacement of pile at sloped ground 1V:2.5H, surcharge load at B



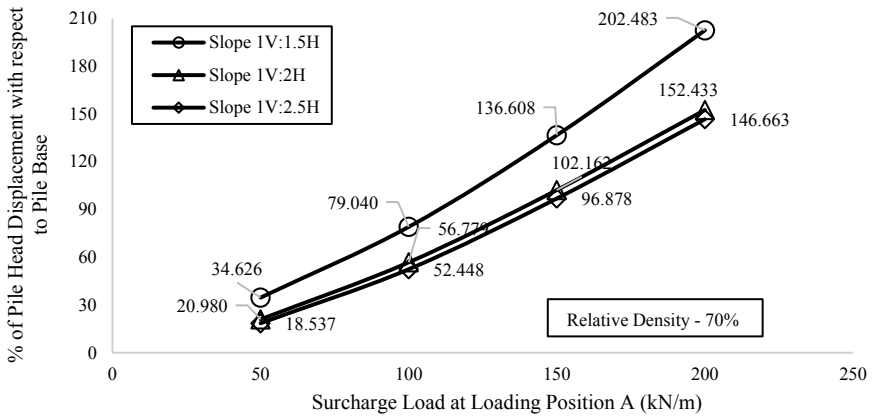


Fig. 17.10 Percentage of pile head displacement, surcharge load at position A

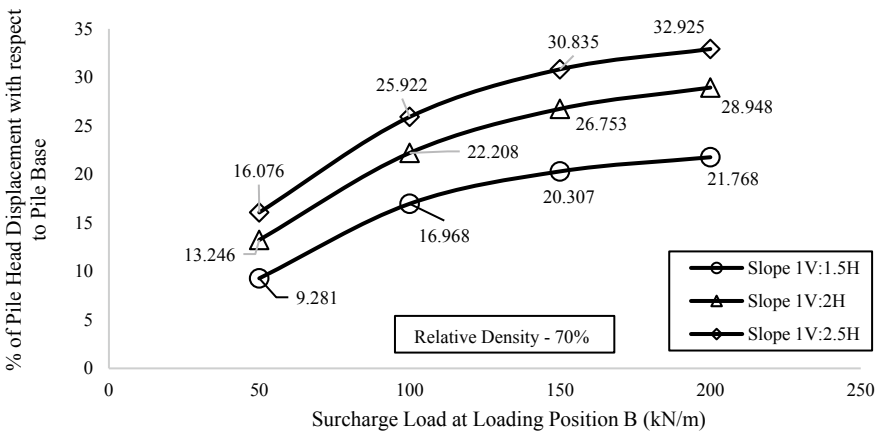


Fig. 17.11 Percentage of pile head displacement, surcharge load at position B

head displacements are 34.626, 79.040, 136.608 and 202.483% high. The varying surcharge loading at position B in the sandy soil of 70% relative density at sloping ground 1V:1.5H will create both pile head and bottom displacements in a pile at slope crest. Comparing pile head displacements with pile base for the corresponding surcharge loads 50, 100, 150 and 200 kN/m, the pile head displacements are 9.281, 16.968, 20.307 and 21.768% low.

Figures 17.6 and 17.7 show the varying surcharge loading at positions A and B in the homogenous sandy soil of 70% relative density at sloping ground 1V:2H. Comparing pile head displacements with pile base displacements when the varying surcharge loads at loading positions A, for the corresponding surcharge loads 50, 100, 150 and 200 kN/m, the pile head displacements are 20.980, 56.779, 102.162

and 152.433% high. Comparing pile head displacements with pile base when the varying surcharge loads at loading positions B for the corresponding surcharge loads 50, 100, 150 and 200 kN/m, the pile head displacements are 13.246, 22.208, 26.753 and 28.948% low.

Figures 17.8 and 17.9 show the varying surcharge loading at positions A and B in the sandy soil of 70% relative density at sloping ground 1V:2.5H. Comparing pile head displacements with pile base displacements for the corresponding surcharge loads 50, 100, 150 and 200 kN/m, the pile head displacements are 18.537, 52.448, 96.878 and 146.663% high. Comparing pile head displacements with pile base displacements for the corresponding surcharge loads 50, 100, 150 and 200 kN/m, the pile head displacements are 16.076, 25.922, 30.835 and 32.925% low. Figures 17.10 and 17.11 show the percentages of the pile head displacements with pile base displacements in both surcharge loading positions A and B.

Figure 17.10 shows that the percentage of pile head displacement increases with increasing surcharge loads (50–200 kN/m) at loading position A and rising ground slopes (1V:1.5H, 1V:2H and 1V:2.5H). The percentage of pile head displacement is high in steeper ground slope 1V:1.5H and low in flatter ground slope 1V:2.5H. The surcharging loading at position A highly dominates the pile head displacements. Under this loading condition, with the effects of ground slope, both pile head and base are displacing toward the same direction (direction of passive load). The pile head displacement is higher than its base displacement, and the difference between pile head and base displacement is more significant. It will make higher bending curvature in the pile.

Figure 17.11 shows that the percentage of pile head displacement increases with increasing surcharge loads (50–200 kN/m) at loading position B and rising ground slopes (1V:1.5H, 1V:2H and 1V:2.5H). Figure 17.11 shows that increasing surcharge load at loading position B will increase the pile head displacements, and it is valid for surcharge load at both loading positions.

In the surcharge loading position A, increasing ground slope angle increases the pile head displacements. Still, it is invalid in the surcharge load at location B. Because the surcharging loading at position B highly dominates the pile base displacements. Due to this, the pile base will move along the direction of passive load, and the pile head will move in the opposite direction of passive load. But in the sloping ground, the lateral soil movement is very high at surface level and acts as a passive load on the pile. The lateral soil movement in the sloping ground will work against the pile head displacement. As a result, in the case of surcharge loads at loading position B, the slope steepness of the grounds reduces the bending curvature of the pile by decreasing the difference between pile head and base displacements. So in the case of surcharge loads at loading position B, the pile bending moment is high in flat slope (1V:2.5H). But it is not valid for the surcharge load at loading position A. The maximum bending curvature due to the surcharge loading at position A is directly proportional to the ground steepness. It is inversely proportional to the surcharge loading at position B.

Conclusion

This present study is discussing the behavior of a single pile due to the passive loading conditions. By considering the varying surcharge load at different locations and ground slopes, we can derive the passive load conditions to the pile at the slope crest. Under these conditions, developed a finite element two-dimensional model in PLAXIS 2D. Based on the finite element model, the following results are made.

1. Due to the varying surcharge load at loading position A, both the pile head and pile base move along the same directions (direction of passive load).
2. Due to the varying surcharge load at loading position B, both the pile head and pile base will move along in the opposite directions (pile base will move along the direction of passive load, and pile head will move opposite to it.).
3. Surcharge loading at position A, comparing the pile head displacements with pile base for the corresponding surcharge loads 50, 100, 150 and 200 kN/m. The pile head displacements are 34.626, 79.040, 136.608 and 202.483% high in a sloped ground 1V:1.5H.
4. Surcharge loading at position B, comparing pile head displacements with pile base for the corresponding surcharge loads 50, 100, 150 and 200 kN/m. The pile head displacements are 9.281, 16.968, 20.307 and 21.768% low in a sloped ground 1V:1.5H.
5. Surcharge loading at position A, comparing pile head displacements with pile base displacements when the varying surcharge loads at loading positions A, for the corresponding surcharge loads 50, 100, 150 and 200 kN/m, the pile head displacements are 20.980, 56.779, 102.162 and 152.433% high in a sloped ground 1V:2H.
6. Surcharge loading at position B, comparing pile head displacements with pile base when the varying surcharge loads at loading positions B for the corresponding surcharge loads 50, 100, 150 and 200 kN/m, the pile head displacements are 13.246, 22.208, 26.753 and 28.948% low in a sloped ground 1V:1.5H.
7. Surcharge loading at position A, comparing pile head displacements with pile base displacements for the corresponding surcharge loads 50, 100, 150 and 200 kN/m. The pile head displacements are 18.537, 52.448, 96.878 and 146.663% high in a sloped ground 1V:2.5H.
8. Surcharge loading at position B, comparing pile head displacements with pile base displacements for the corresponding surcharge loads 50, 100, 150 and 200 kN/m. The pile head displacements are 16.076, 25.922, 30.835 and 32.925% low in a sloped ground 1V:2.5H.
9. In the case of surcharge loading at position A, by comparing pile head displacements with pile base displacements, the pile head displacements are higher than the pile base displacements and directly proportional to the magnitude of surcharge load and ground slope steepness.

10. In the case of surcharge loading at position B, by comparing pile head displacements with pile base displacements, the pile head displacements are lower than the pile base displacements and directly proportional to the magnitude of surcharge load and indirectly proportional to the ground slope steepness.

References

1. Karthigeyan S, Ramakrishna VVGST, Rajagopal K (2007) Numerical investigation of the effect of vertical load on the lateral response of piles. *J Geotech Geoenviron Eng* 133(5):512–521
2. Muthukkumaran K, Sundaravadivelu R, Gandh SR (2008) Effect of slope on P-Y curves due to surcharge load. *Soils Found* 48(3):353–361
3. Rifat Kahyaoglu M, Gökhan Imancli A, Ozturk U, Kayalar AS (2009) Computational 3D finite element analyses of model passive piles. *Comput Mater Sci* 46(1):193–202. <https://doi.org/10.1016/j.commatsci.2009.02.022>
4. Biswas SK, Mukherjee S, Chakrabarti S, De M (2015) Experimental investigation of free head model piles under lateral load in homogenous and layered sand. *Int J Geotech Eng* 9(4):363–378
5. Muthukkumaran K, Sundaravadivelu R (2007) Numerical modeling of dredging effect on berthing structure. *Acta Geotech* 2(4):249–259
6. Georgiadis K, Georgiadis M (2010) Undrained lateral pile response in sloping ground. *J Geotech Geoenviron Eng* 136(11):1489–1500
7. Chandrasekaran S, Boominathan A, Dodagoudar GR (2010) Group interaction effects on laterally loaded piles in clay. *J Geotech Geoenviron Eng* 136(4):573–582
8. Muthukkumaran K, Almas Begum N (2011) Technical note finite element analysis of laterally loaded piles on sloping ground 41(3):155–161
9. Muthukkumaran K (2014) Effect of slope and loading direction on laterally loaded piles in cohesionless soil. *Int J Geomech* 14(1):1–7
10. Jegatheeswaran B, Muthukkumaran K (2016) Behavior of pile due to combined loading with lateral soil movement. *Int J Geo-Eng* 7(1)
11. Rathod D, Muthukkumaran K, Sitharam TG (2017) Effect of slope on P-y curves for laterally loaded piles in soft clay. *Geotech Geol Eng* 36(3):1509–1524
12. Jayasree PK, Arun KV, Oormila R, Sreelakshmi H (2018) Lateral load capacity of piles: a comparative study between indian standards and theoretical approach. *J Inst Eng (India): Series A* 99(3):587–593. <https://doi.org/10.1007/s40030-018-0306-7>
13. Deendayal R, Muthukkumaran K, Sitharam TG (2020) Analysis of laterally loaded group of piles located on sloping ground. *Int J Geotech Eng* 14(5):580–588. <https://doi.org/10.1080/19386362.2018.1448521>
14. Abbas JM, Hj Chik Z, Taha MR (2008) Single pile simulation and analysis subjected to lateral load. *Electr J Geotech Eng* 13 E
15. Ramakrishna VVGST, Karthigeyan S, Rajagopal K (2006) Response of piles under passive lateral loads-a numerical approach, pp 14–16

Chapter 18

Influence of Flexural Rigidity of Footing and Shear Strength of Supporting Soil on Internal Stresses in Foundation



Aleena Sam, A. Arunima Anil, Smitha Anna Kurian, Sujina Kabeer, J. Jayamohan, and Swathy Pushpan

Introduction

In geotechnical terms, soil–structure interaction is a complicated study that focuses on the impact of the soil on structural movement and vice versa. Soil is an essential component of every construction project, and its shear strength has an impact on a loaded member’s structural performance. Shear strength of soil is a critical parameter which influences the load–settlement behavior and contact pressure distribution and structural deformations of the footing. The distribution of internal stresses developed within the footing is dependent of its deformation pattern.

Many researches have been conducted to study the load–deformation behavior of footings resting on various types of soil. The structural deterioration of a footing considerably impacts the service lifespan of a structure, thereby resulting in massive destructions [1]. Analysis of deformation pattern of a loaded footing based on flexural stiffness (K) is an integral parameter to formulate the structure’s resistance to bending. Lower values of K indicate a higher concentration of contact stress beneath the footing center, which causes tensile stresses at the footing edges due to linear-elastic soil [2]. The nature of soil movement beneath the footing during loading is a significant factor contributing to the load–settlement behavior. By adjusting the number of stiffeners in the footing, it would be able to improve the structural characteristics by better confining the underlying soil. By applying a centrally focused force to a flexible footing placed above cohesionless soil, a maximum contact pressure occurs underneath the point of load application, thus producing maximum settlement in the center and minimum settlement at the edges. The distribution of contact

A. Sam · A. Arunima Anil · S. A. Kurian · S. Kabeer · J. Jayamohan (✉) · S. Pushpan
Civil Engineering Department, LBS Institute of Technology for Women, Thiruvananthapuram,
Kerala 695012, India
e-mail: jayamohanj@lbsitw.ac.in

© The Author(s), under exclusive license to Springer Nature Singapore Pte Ltd. 2023
K. Muthukkumaran et al. (eds.), *Foundation and Forensic Geotechnical Engineering*, Lecture Notes in Civil Engineering 295,
https://doi.org/10.1007/978-981-19-6359-9_18

177

stress beneath the footing is determined by the stiffness of the footing, which varies according to the coefficient of rigidity [3].

The additional settlement of a footing due to loads acting on an adjacent footing has been investigated [4]. They outlined that the additional settlement of an existing loaded footing because of loads acting on a new adjacent footing is influenced by the distance and the relative elevation between them. The improvement in load–settlement behavior attained by altering the shape of cross section of footings has been investigated [5]. They have reported that rectangular footing with flanges increases the confinement of the underlying soil, thereby improving the load–settlement behavior.

Stabilization using fly ash inhibits particle mobility by cementing soil grains together, thereby improving the structural characteristics of the soil mass [6]. This hypothesis is extensively studied in different applications such as foundation stability analysis, seismic activity, structural displacement, ground displacement and so on [7].

Modeling the soil and structure set (soil–structure interaction) is one of the most important issues in geotechnical and structural field [8]. Numerical simulation develops simpler and feasible approaches for various structures with a complicated geometrical analysis or complex loading conditions, thus providing accurate insight to tackle one of the most important issues in geotechnical and structural field.

In this paper, the influence of flexural rigidity of the footing and shear strength of the underlying soil on internal stresses developed in the foundation is investigated. Laboratory scale load tests are carried out on a model flexible footing fabricated with GI sheet. The flexural rigidity of the flexible model footing is altered, for various cases, by adding stiffeners. The shear strength of the underlying soil is altered by stabilizing the soil in the footing's influence zone with varying percentages of fly ash.

Laboratory Scale Load Tests

Materials Used

The materials used for the research are sand, fly ash (stabilizing material), GI sheet and stiffeners. The model flexible footing of dimension 100×50 mm is fabricated using GI sheet with a thickness of 2 mm. To adjust the flexural rigidity, steel rods with a thickness of 2 mm and a length of 100 mm are employed as stiffeners. The properties of the sand used for the project are presented in Table 18.1.

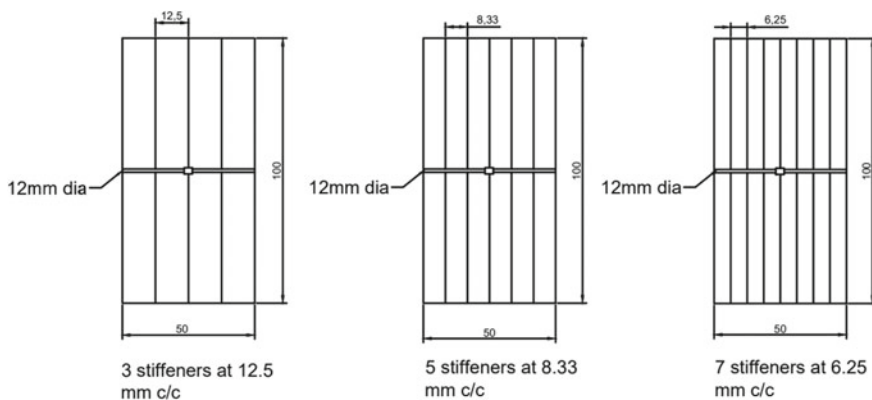
Table 18.1 Properties of sand

Properties	Values
Specific gravity	2.65
Permeability (m/s)	2.86×10^{-4}
Percentage of gravel (%)	8.2
Percentage of sand (%)	91.8
Percentage of clay (%)	0
Cohesion (kg/cm ²)	0
Angle of internal friction	27.12°
Coefficient of uniformity	4.25
Coefficient of curvature	1.00
Grade of sand	(SP)

Experimental Setup

Fabrication of Footing. A model rectangular flexible footing with dimensions of $100 \times 50 \times 2$ mm is fabricated with 2 mm thick GI sheet. As illustrated in Fig. 18.1, model footings of four different flexural rigidities are used: flexible footing (without stiffeners) and footing with varying flexural rigidity (with 3, 5, and 7 stiffeners). To evenly distribute the centrally imposed load, a steel rod with a thickness of 12 mm is welded centrally perpendicular to the stiffeners.

Laboratory Scale Load Tests. Laboratory scale load tests are carried out in order to investigate the load–settlement behavior of the model rectangular footings of varying flexural rigidities. The shear strength of supporting soil is varied by stabilizing with fly ash (after curing for 3 days as per optimum moisture content of sand, i.e., 8%) in varying proportions of 1:3, 1:5, 1:7 and 1:10, respectively. The load tests are carried

**Fig. 18.1** Model rectangular footing

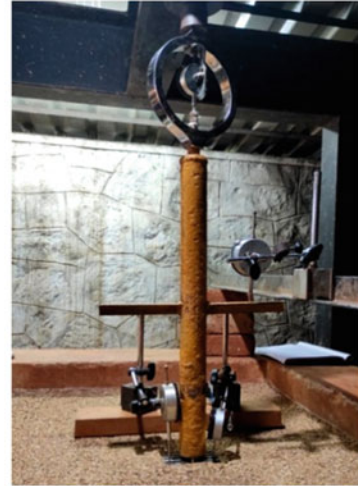
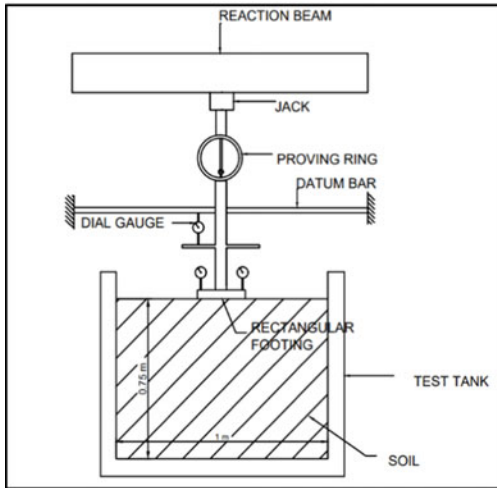


Fig. 18.2 Test setup

out in a combined test bed and loading frame assembly with the test beds prepared in a tank of internal dimensions 1000 mm length \times 750 mm width \times 750 mm depth. The soil surface is prepared and compacted after which the model footings are placed for testing. A hand-operated mechanical jack of capacity 50 kN is used to apply the load to the fabricated footing. The settlement of the model footing is measured using three dial gauges, two of which are placed diametrically opposite to each other on the footing to determine the upward deflections at the edges and the third dial gauge being placed on the loading arm to determine the central settlement as shown in Fig. 18.2. In all the tests, model footing is kept at the soil surface. The model rectangular footing is placed exactly beneath the center of the loading jack to avoid eccentric loading.

Finite Element Analyses

Finite element analyses are carried out on the rectangular flexible footing with the software PLAXIS 3D. The Mohr–Coulomb criteria are used to simulate the cohesionless soil characteristics in this analysis. The basic soil properties such as angle of shearing resistance and cohesion intercept, which may be acquired through direct shear testing, are primarily used in this nonlinear model. Since rectangular flexible footing is being analyzed, a plane-strain model is used in the computations. The bottom boundary's displacement is limited in all directions, whereas displacement on the vertical sides is restricted only in the horizontal direction. 15-noded triangular elements are used to create the soil model. In all analyses, the dimensions of the model strip footing are 10 \times 5 \times 0.2 cm and the dimensions of the soil mass are 100

$\times 75 \times 75$ cm. The rectangular footing is placed at the center of the model soil, and the linear-elastic model is used to create the rectangular foundation. An interface element is added to the footing's bottom surface to represent the interaction between the footing and the underlying soil. Variations in the amount of fly ash incorporated into the soil and the number of stiffeners on the footing are considered as the variable parameters. As the soil property is altered in different mix proportions, Poisson's ratio of the soil fluctuates.

Finite element analysis is composed of three programs: input, output and curves. Firstly, a prototype rectangular footing is developed, with the load prescribed in increments and iterative failure analysis. For the computation and presentation of the findings, the output program is used. Curves are also utilized to represent graphical elements of the failure mechanism.

Results and Discussions

The results obtained from laboratory scale load tests on model rectangular footings of various flexural rigidities are presented below.

Influence of Flexural Rigidity of Footing

The influence on the load–settlement characteristics at varying flexural rigidity is determined by providing 3, 5 and 7 stiffeners, respectively, at constant shear strength of underlying soil, and the results obtained are presented below.

Variation in Load–Settlement Behavior. For a flexible footing placed on cohesionless soil, settlement characteristics are maximum at the mid-span of footing and minimum at the edges as shown in Fig. 18.3. For analysis, the cumulative settlement is considered by taking the sum total of the mid-span settlement and the average upward deflection at the edges.

Figure 18.4 represents vertical stress versus normalized settlement curves for model footings with varying flexural rigidity resting on untreated soil. It is observed that the load–settlement behavior improves with an increase in flexural rigidity due to a considerable reduction in the structural deformation. The equations based on the geometry of various curves are also presented. A similar variation in trend is discerned for different shear strength of the supporting soil mass in mix proportions of 1:3, 1:5, 1:7 and 1:10, respectively.

Variation in Curvature Characteristics. The variation in radius of curvature with increasing applied stress at constant shear strength and varying flexural rigidity is analyzed using Eqs. (18.1), (18.2) and (18.3).



Fig. 18.3 Deformation of footing during application of load

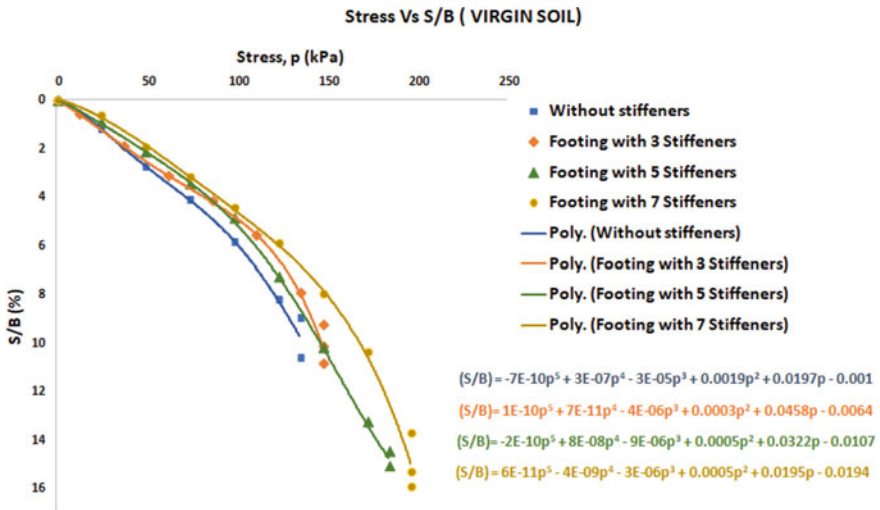


Fig. 18.4 Stress versus normalized settlement curves for footings of various flexural rigidity resting on untreated soil

$$\text{Length of Curve } (L) = \frac{\pi R \Delta}{180} \tag{18.1}$$

$$\text{Mid - ordinate } (O_o) = R \left[1 - \cos\left(\frac{\Delta}{2}\right) \right] \tag{18.2}$$

Thus,

$$\frac{L}{O_o} = \frac{\frac{\pi \Delta}{180}}{1 - \cos\left(\frac{\Delta}{2}\right)} \tag{18.3}$$

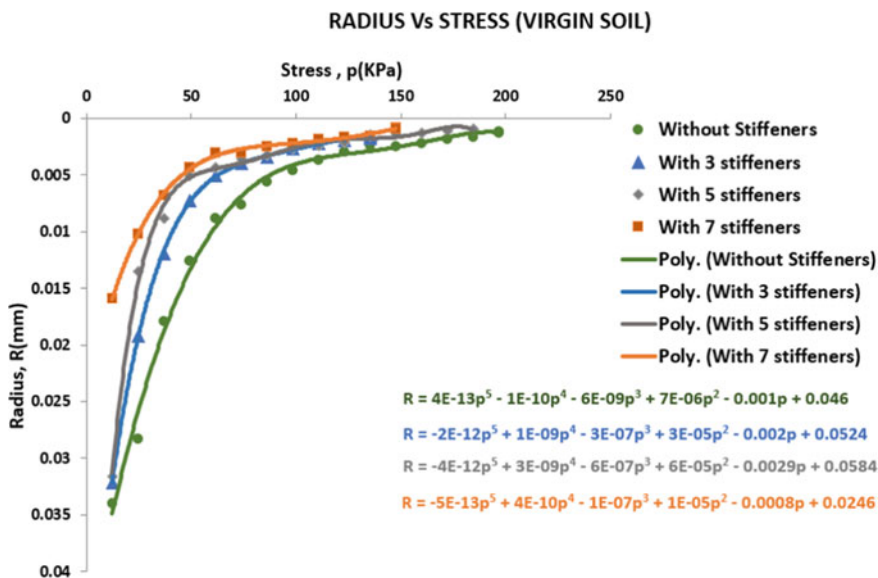


Fig. 18.5 Relation between applied stress and curvature of footing resting on untreated soil at varying flexural rigidity

For experimental analysis at varying conditions, the mid-ordinate of the curved shape of loaded footing, which is the sum of downward deflection at mid-span and average upward deflection at edges, is used to determine the radius of curvature of footing at various stages of loading. The degree of curvature is observed to increase considerably with a decrease in radius of curvature on increasing the applied stress in all cases. The stress versus radius of curvature for footings of various flexural rigidity resting on untreated soil is presented in Fig. 18.5. The utmost reduction in curvature was obtained in the case of footing having 7 stiffeners inferring an inverse proportionality between flexural rigidity and radius of curvature at constant shear strength of underlying soil. The equations based on the geometry of various curves are also presented.

Influence of Shear Strength of Underlying Soil

The shear strength of the soil in the influence area of the footing is varied by stabilizing with fly ash at varying proportions (1:3, 1:5, 1:7 and 1:10). The results of laboratory scale load tests carried out on stabilized soil are presented below.

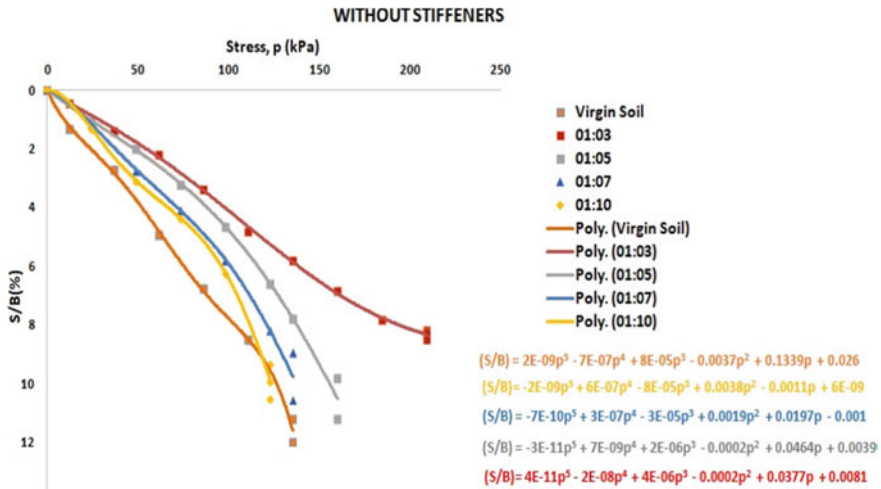


Fig. 18.6 Load–settlement behavior of footing without stiffeners with varying shear strength

Variation in Load–Settlement Behavior. The load–settlement behavior improves with fly ash content of underlying soil at constant flexural rigidity due to an increase in shear strength and is presented in Fig. 18.6. The equations based on the geometry of various curves are also presented.

Variation in Curvature Characteristics. The stress versus radius of curvature curves for footings resting on soil stabilized with various percentages of fly ash is presented in Fig. 18.7. The graphical representations denoting the stress–curvature characteristics indicate that the curvature of the loaded footing is considerably influenced by the shear strength of the supporting soil. The maximum reduction in curvature was obtained in the case of stabilized soil with mix proportion 1:3. The equations based on the geometry of various curves are also presented.

Relation Between Applied Stress and Bending Stress

The bending stress equation is adopted in order to determine the influence of external applied stress on bending stress of the rectangular footing to formulate the load-carrying capacity of the flexible footing at constant shear strength and increasing flexural rigidity. The variation is analyzed with respect to Eq. (18.4).

$$\text{Bending Stress, } \sigma = \frac{M_y}{I} \tag{18.4}$$

where

M calculated bending moment

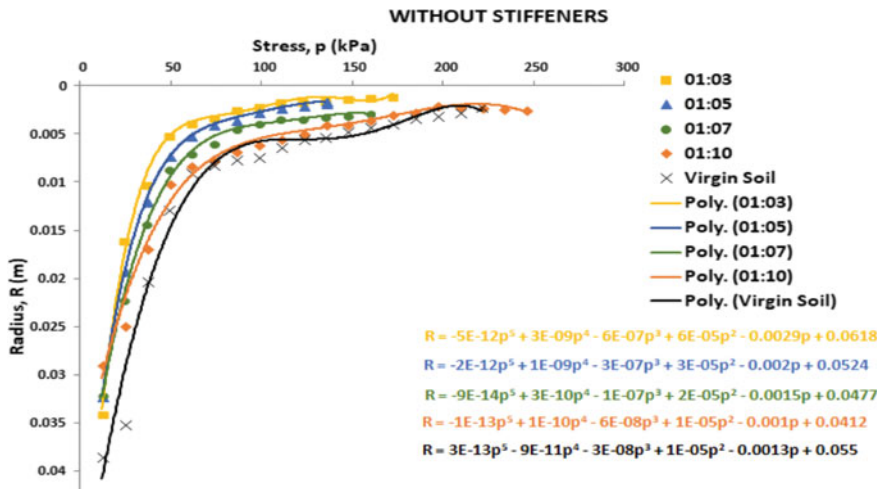


Fig. 18.7 Stress versus radius of curvature in footing without stiffeners at varying shear strength

- y distance away from neutral axis
- I moment of inertia about neutral axis.

The graphical plots of bending stress versus applied stress indicate a proportional variation in bending stress with increasing applied load in all experimental conditions. An inverse relation in bending stress with increasing flexural rigidity is also observed at constant shear strength of supporting soil. The maximum reduction in bending stress is obtained in the case of footing having 7 stiffeners in all cases. The comparative plot of variation in bending stress with increasing applied stress is analyzed with respect to the approach observed in untreated soil as shown in Fig. 18.8.

Comparison of Laboratory and Finite Element Analysis Results

The results obtained from laboratory scale load tests are compared with those obtained from finite element analyses and are presented below.

Constant Flexural Rigidity Varying Shear Strength

Figures 18.9 and 18.10 present the influence of vertical applied stress on normalized settlement and radius of curvature, respectively. The dotted lines represent the results obtained from FEA, while the solid lines illustrate the experimental results. The

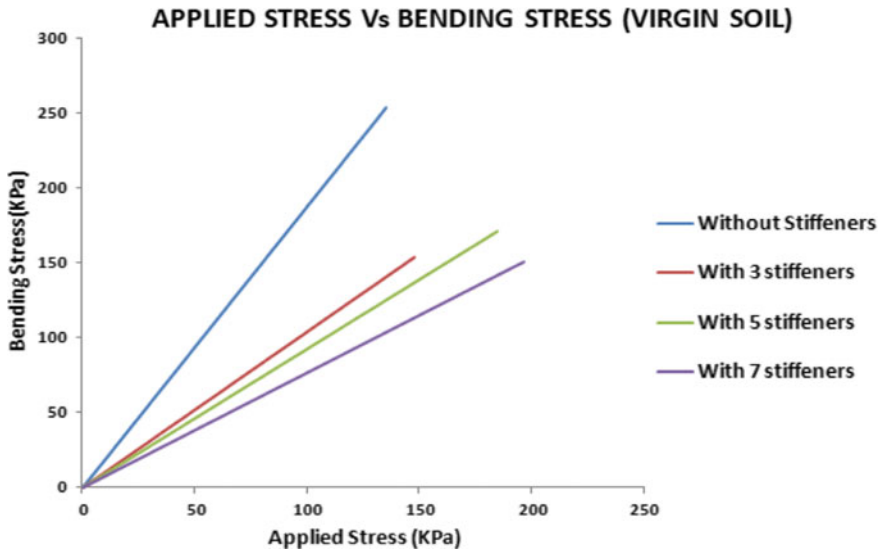


Fig. 18.8 Applied stress versus bending stress for untreated soil

reduction in settlement and radius of curvature with increasing shear strength at constant flexural rigidity can be extrapolated from these graphs, indicating good agreement between laboratory and FEA results.

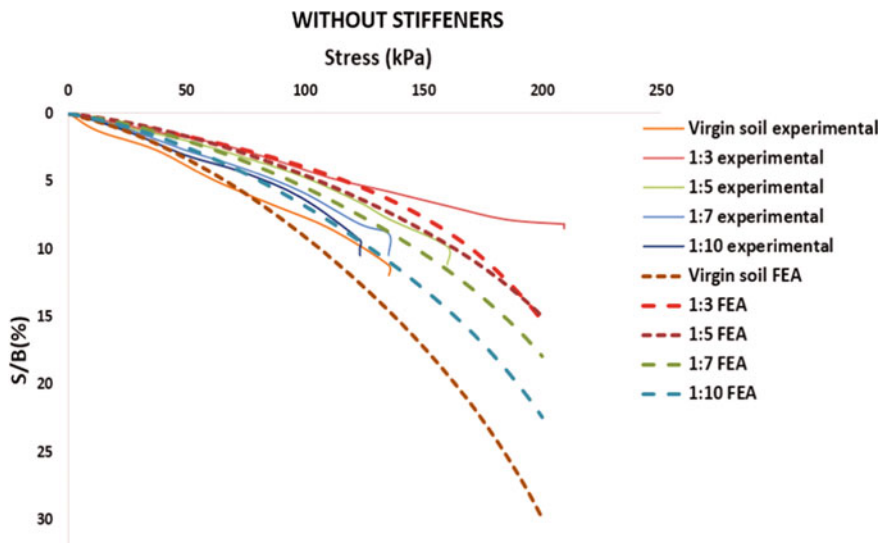


Fig. 18.9 Load–settlement behavior on footing without stiffeners (experimental and FEA)

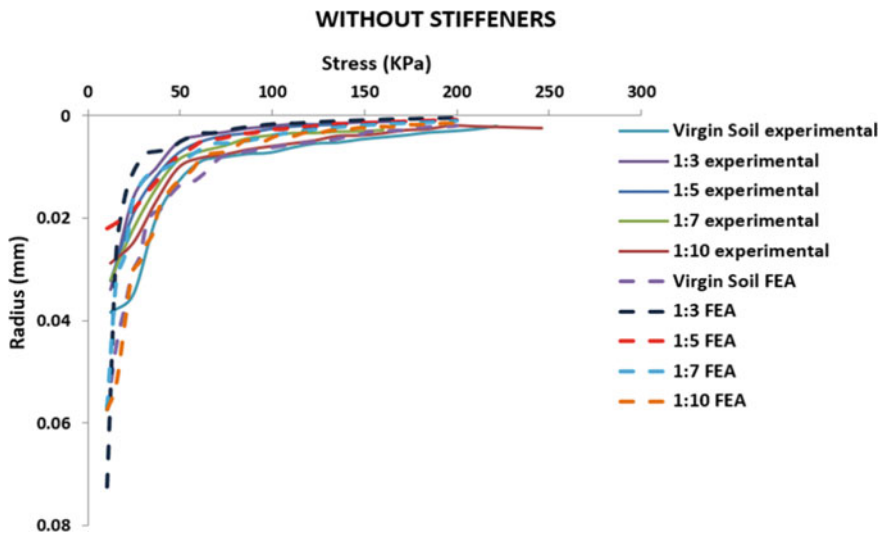


Fig. 18.10 Stress versus radius of curvature in footing without stiffeners (experimental and FEA)

Influence of Flexural Rigidity of Footing

Figure 18.11 shows that increasing flexural rigidity improves load–settlement behavior, and Fig. 18.12 indicates that for constant shear strength, an inverse proportionality between flexural rigidity and radius of curvature can be deduced. There is a reasonably good agreement between experimental and FEA results.

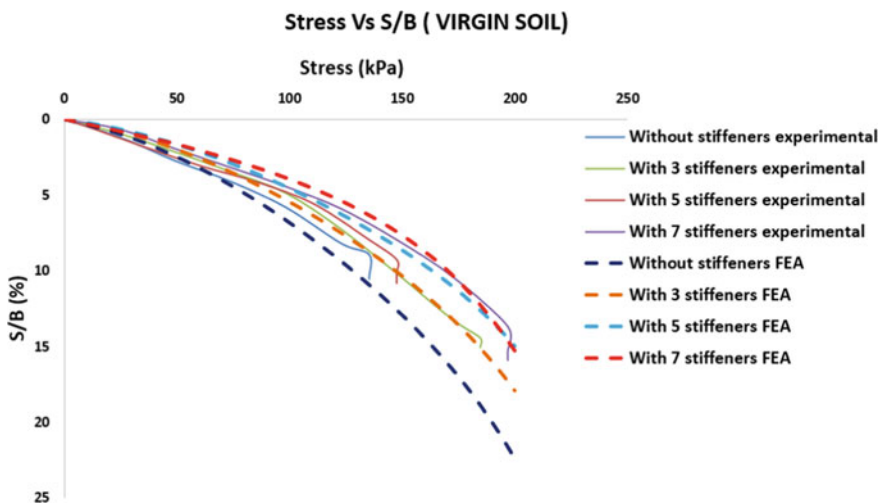


Fig. 18.11 Load–settlement behavior in virgin soil (experimental and FEA)

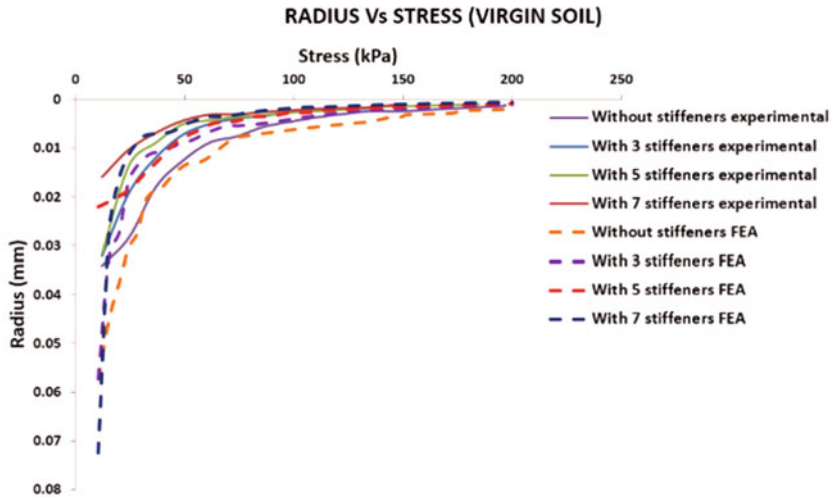


Fig. 18.12 Stress versus radius of curvature in virgin soil (experimental and FEA)

Conclusions

With reference to the results obtained, the following conclusions are drawn.

- With the increasing shear strength of supporting soil and flexural rigidity of footing, the settlement and radius of curvature of the footing decrease.
- The maximum reduction in settlement and curvature is obtained in the case of footing having 7 stiffeners placed on soil stabilized using fly ash having 1:3 mix proportion.
- The bending stress increases with increase in load applied.
- Bending stress decreases with increase in flexural rigidity.
- There is a reasonably good agreement between the results of laboratory scale load tests and finite element analyses.

References

1. Fu F (2018) Design and analysis of tall and complex structures. Butterworth-Heinemann, Elsevier. ISBN: 978-0-08-101121-8. <https://doi.org/10.1016/c2015-0-06071-3>
2. Farouk H, Farouk M (2014) Effect of soil type on contact stress. Geo-Hubei 2014 international conference on sustainable civil infrastructure, pp 57–66
3. Sam A, Arunima Anil A, Jayamohan J, Kurian SA, Kabeer S, Pushpan S (2021) Influence of shear strength of soil on stresses in footing-a review. In: Proceedings of international web conference in civil engineering for a sustainable planet ICCESP 2021, AIJR proceedings, pp 94–10

4. Jayamohan J, Aishwarya S, Soorya SR, Balan K (2020) Additional settlement of footing due to loads acting on adjacent foundation. In: Duc Long P, Dung N (eds) Geotechnics for sustainable infrastructure development. Lecture notes in civil engineering, vol 62. Springer, Singapore. https://doi.org/10.1007/978-981-15-2184-3_149
5. Jayamohan J, Sajith P, Vijayan S, Nair A, Chandni S, Vijaya A (2020) Influence of shape of cross section on the load–settlement behaviour of strip footings. Advances in computer methods and geomechanics. Lecture notes in civil engineering, vol 56
6. Indraratna et al (1991) Engineering behaviour of a low carbon, pozzolanic fly ash and its potential as a construction fill. Can Geotech J 28
7. Chang Q, Peng DU, Fan J, Fu L, Liu X (2019) Numerical simulation of soil-structure interface mechanical behaviour. In: Iop conference series: journal of physics: conference series 1168, p 032095. <https://doi.org/10.1088/1742-6596/1168/3/032095>
8. Gabar M, Lasefir WA, Tleish SA (2019) Study the effect of soil and bedrock conditions below the footing on the footing behaviour. Tobruk Univ J Eng Sci 1(1)

Chapter 19

Influence of Oil Spill on the Load–Settlement Behavior of Footings of Adjacent Structures



S. B. Ardra, H. A. Athira, J. P. Janu, S. Parvathy, J. Jayamohan,
and Shruthi Johnson

Introduction

In the present world, soil contamination is one of the most common and controversial environmental issues which is caused by the industrial activities, agricultural chemicals, leakage of petroleum hydrocarbon, etc. The exploration, production and consumption of oil and petroleum products are increasing worldwide. Accidents can happen during any of these exploration, production, transportation and storage stages. Soil contaminated by petroleum hydrocarbons can cause adverse effect on ecosystem as well as human health. Also, it causes significant variations in the physical, chemical, mechanical and geotechnical characteristics of soil. Alterations in the soil engineering properties should be given greater importance since the stability of structures is dependent on it.

Research on the geotechnical properties of oil contaminated soil has shown that the oil makes the soil weaker and is detrimental to the buildings and structures resting on it. Changes in the engineering properties and behavior of soil strata may lead to a loss in the bearing capacity and increase in the settlement of the footing of structures. These ultimately result in the failure of the structure. Therefore, there is a greater significance in determining the effect of contaminants on soil properties before recommending the contaminated soil as a supporting medium for the constructions.

Various studies were conducted to determine the geotechnical properties of oil contaminated soil and the effect of footing resting on oil contaminated soil. But very few studies deal with the effect of oil spillage on the behavior of nearby footings. Al-Sanad et al. [1] carried out various laboratory tests to determine the effect of oil

S. B. Ardra · H. A. Athira · J. P. Janu · S. Parvathy · J. Jayamohan (✉) · S. Johnson
Department of Civil Engineering, LBS Institute of Technology for Women, Thiruvananthapuram,
Kerala 695012, India
e-mail: jayamohanj@lbsitw.ac.in

contamination on the properties of Kuwaiti sands. Compaction characteristics and CBR values of sand improved with the presence of oil up to 4% by weight. The reduction in angle of friction was 2% for specimens prepared at a relative density of 60% and mixed with 6% of heavy oil. Ostovar et al. [2] examined the effects of crude oil on geotechnical properties of sandy soils and reported that increasing crude oil in all soil samples resulted in decreasing friction angle for all sandy soils, increasing cohesion for all non-clayey sandy soils up to about 15 kPa and decreasing cohesion for clayey sand down to about 14 kPa.

Investigations by Nasehi et al. [3] considered the influence of gas oil contamination on geotechnical properties of fine- and coarse-grained soils. The soil samples were artificially contaminated with 3, 6 and 9% of gas oil in relative to its dry weight. Results thus obtained indicate a decrease in the friction angle, an increase in the cohesion, liquid limit and plastic limit of the soils with the increase in gas oil content.

Shin et al. [4] conducted a study to analyze the bearing capacity of footing resting on crude oil contaminated sand. He observed that when the crude oil content increased from 0 to 1.3%, the peak friction angle reduced by about 25%. With the decrease in soil friction angle with contamination, the ultimate bearing capacity also reduced. Abtahi and Boushehrian [5] studied the behavior of circular foundation on oil contaminated sand, and their results showed that the increase in contamination depth is influential in decreasing bearing capacity of footing.

Fadhil et al. [6] carried out investigations on bearing capacity of isolated square footing resting on contaminated sandy soil with crude oil and concluded that the bearing capacity of footing decreases considerably when the underlying sand is contaminated with crude oil. Pousti and Marnani [7] carried out a numerical and analytical evaluation of crude oil contamination effect on strip foundation's bearing capacity and reported that the crude oil contamination causes a reduction in bearing capacity, and it depends on embedment depth, soil type and contamination content.

The aim of this research is to determine the influence of oil spill on the bearing capacity and settlement behavior of footings of nearby structures. The influence of eccentricity of the point of spill, quantity of oil spill on the load–settlement behavior and tilt of footing are investigated through a series of laboratory scale load tests.

Materials Used

Soil

Locally available sand is used as foundation soil. Laboratory tests were performed to determine the properties of and are presented in Table 19.1.

Table 19.1 Properties of sand

Sl. No.	Properties	Values
1	Dry unit weight	17 kN/m ³
2	Specific gravity	2.65
3	Uniformity coefficient, Cu	5
4	Coefficient of curvature, Cc	0.8
5	Effective grain size D10 (mm)	0.2
6	D30 (mm)	0.4
7	D60 (mm)	1
8	Coefficient of permeability (m/sec)	2.18×10^{-4}
9	Soil classification	SP

Table 19.2 Properties of oil [8]

SAE grade	40
Kin.Vis.cSt @ 100 °C	13–15
Viscosity index, Min	90
Flash point (COC), °C Min	220
Pour point, °C Max	(–) 6
TBN mg KOH/gm	9.5–12.5

Oil

Heavy motor oil (Servo Pride 40) is used as the contaminant. Its properties (Table 19.2) are obtained from the official website of the Indian oil corporation.

Square Model Footing

A steel square plate with side dimensions of 10 cm and thickness of 1.6 cm is used as the model footing in all tests.

Experimental Setup

The laboratory scale plate load tests are performed in a combined test bed and loading frame assembly. The test beds are set up in a tank with an internal dimension of 1000 mm length \times 750 mm width \times 750 mm depth. A steel square plate of dimensions 100 \times 100 \times 16 mm is used as a model footing in all the tests. The vertical load

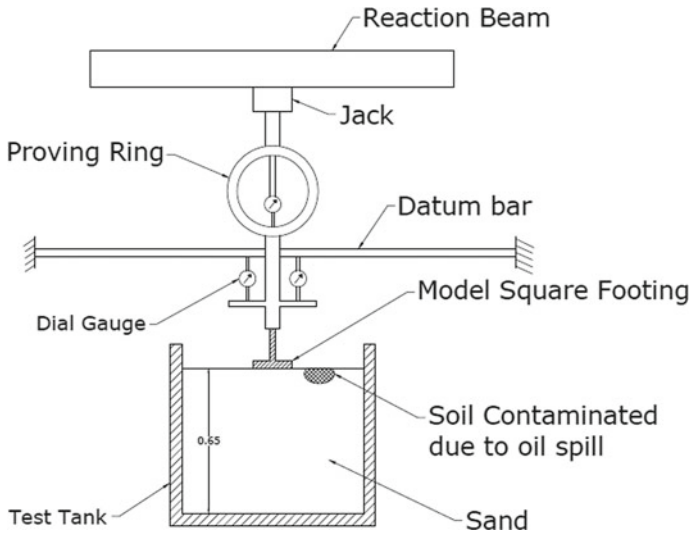


Fig. 19.1 Laboratory setup

is applied using a hand-operated mechanical jack of capacity 50 kN. The applied vertical load is measured using a proving ring of capacity of 50 kN. Two dial gauges are provided directly to the footing to measure settlement and tilt. The schematic diagram of the laboratory setup is shown in Fig. 19.1.

Testing Procedure

The sand is filled in the test tank to the required level with compaction done in layers of 10 cm thickness. The sand is compacted using a plate vibrator. The model footing is placed exactly beneath the center of the loading jack to avoid eccentric loading. The vertical load is applied in equal increments by the hand-operated mechanical jack fabricated on the loading frame. The vertical settlement of the model footing is measured using two dial gauges of 0.01 mm sensitivity kept diagonally opposite to each other. The tests are conducted up to failure. The test tank is emptied and refilled for each test to ensure that controlled conditions are maintained throughout the investigation. The experimental setup is shown in Fig. 19.1. The laboratory scale plate load test is then carried out after spilling oil at varying eccentricities ($0.5B$, $1B$, $1.5B$, $2B$ where B is the width of model footing) by keeping the quantity of oil constant at 25 ml. The plate load test is repeated by varying the oil quantity by 25, 50, 75 and 100 ml while keeping the eccentricity of contamination constant at $1.5B$.

Modified Direct Shear Test

Direct shear tests are performed on both uncontaminated and contaminated samples in order to determine the shear parameters. The tests are carried out in a large shear box having dimensions 30 cm × 30 cm × 20 cm. The effect of oil contamination on cohesion intercept and angle of shearing resistance of sand are determined.

Relationship Between Quantity of Contaminant and Extent of Contamination

The relationship between quantity of contaminant and the extent of contamination is determined by exhuming the soil after contamination. The depth of collection of sample, corresponding horizontal extent of contamination and the oil content of collected samples are presented in Table 19.3.

Table 19.3 Relationship between quantity of contaminant and extent of contamination

Sl. No.	Quantity of oil (ml)	Depth of sample collection (cm)	Horizontal extent of contamination (cm)	Oil content (%)
1	25	0	7.2	3.5
		1	10	2.7
		2	3	1.5
		3	Negligible	0.8
2	50	0	10	5.2
		1	12	4.1
		2	4	3.3
		3	1	1.9
3	75	0	19	9.7
		1	21	7.4
		2	5	5.6
		3	1.3	2.5
4	100	0	21	12.4
		1	23	9
		2	6	6.7
		3	1.6	3.8

Results and Discussion

Influence of Oil Content on Shear Parameters

The Angle of Shearing Resistance. Figure 19.2 presents the variation of angle of shearing resistance with oil content in sand. It is observed that an increase in oil content causes a reduction in angle of shearing resistance. The behavior is observed to be linear. The equation obtained from the geometry of the curve also is presented in the figure.

Cohesion Intercept. The influence of oil content on the cohesion intercept is presented in Fig. 19.3. Initially, cohesion intercept increases rapidly with increase in oil content and later it reduces. The behavior is observed to be nonlinear. The equation obtained from the geometry of the curve also is presented in the figure.

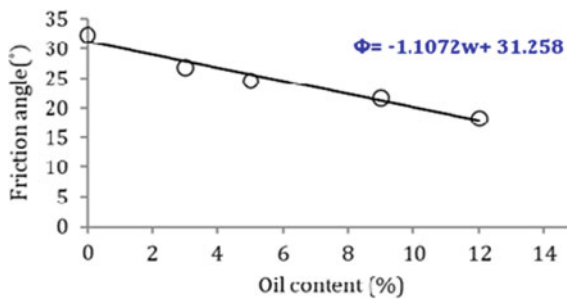


Fig. 19.2 Variation of the angle of shearing resistance with oil content

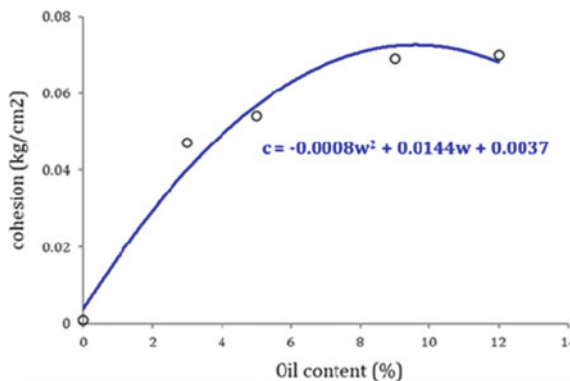


Fig. 19.3 Variation of cohesion intercept with oil content

Influence of Eccentricity of Contamination on Load Settlement Behavior of Footing

Vertical stress versus normalized settlement curves for various eccentricities of contamination is presented in Fig. 19.4. The quantity of oil contaminant is 25 ml for all the tests. It is observed that a decrease in the eccentricity of contamination adversely affects the load–settlement behavior.

The influence of eccentricity ratio (e/B) and of contamination on normalized settlement (S/B) of footing is presented in Fig. 19.5. It shows that settlement increases with decrease in eccentricity of contamination.

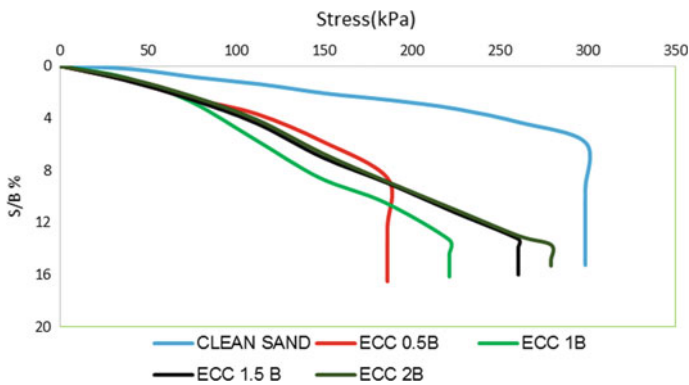


Fig. 19.4 Vertical stress versus normalized settlement curves for various eccentricities of contamination

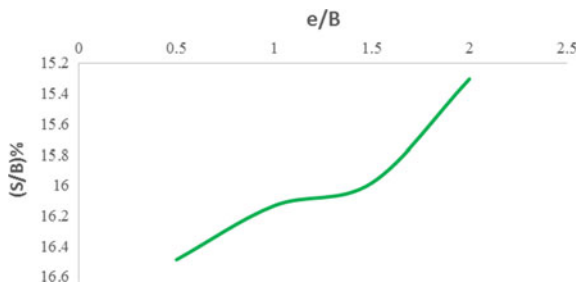


Fig. 19.5 Variation of settlement with eccentricity of contamination

Influence of Quantity of Contaminant on Load–Settlement Behavior of Footing

Figure 19.6 presents vertical stress versus normalized settlement curves for various quantities of contamination at a constant eccentricity of $1.5B$ from the center of footing. It is observed that an increase of contaminant adversely affects the load–settlement behavior.

The influence of quantity of contaminant (Q/A) on the normalized settlement (S/B) of footing is presented in Fig. 19.7. Q is the quantity of contaminant in cm^3 and A is the plan area of footing in cm^2 . It is observed that settlement increases with the quantity of contaminant.

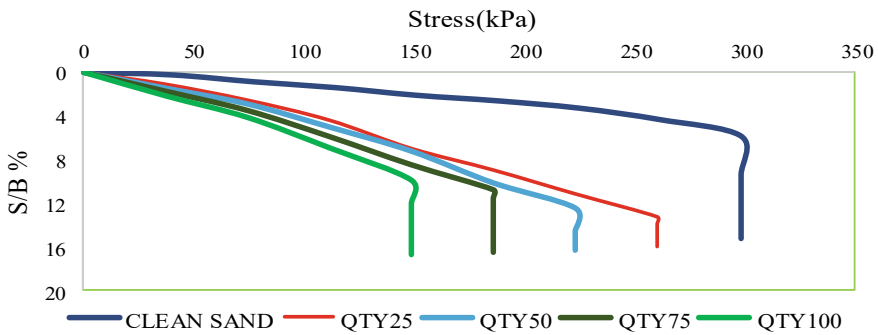


Fig. 19.6 Vertical stress versus normalized settlement curves for various quantities of contamination

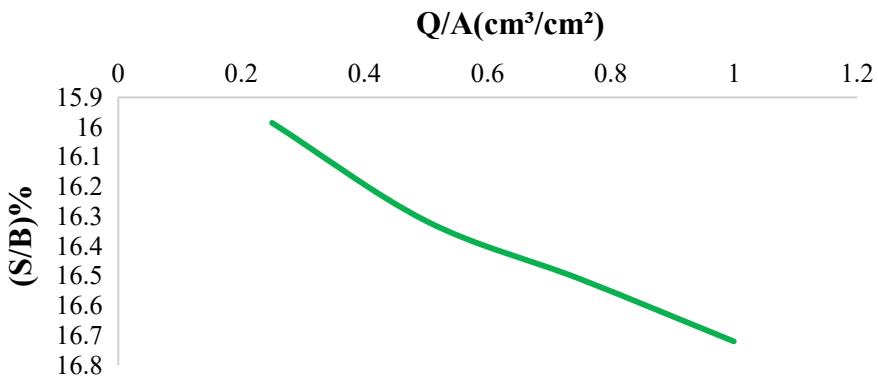


Fig. 19.7 Variation of settlement with quantity of contaminant

Influence of Eccentricity of Contamination on the Tilt of Footing

It can be seen from Fig. 19.8 that with the decrease in the eccentricity of contamination tilt of footing increases. It is observed that a maximum tilt of $0^{\circ}44'1''$ is obtained upon the spillage of oil at the edge of footing.

Influence of eccentricity ratio (e/B) of contamination on tilt of footing, at a stress of 100 kPa is presented in Fig. 19.9. It is observed that the tilt of footing increases as the eccentricity of contamination decreases.

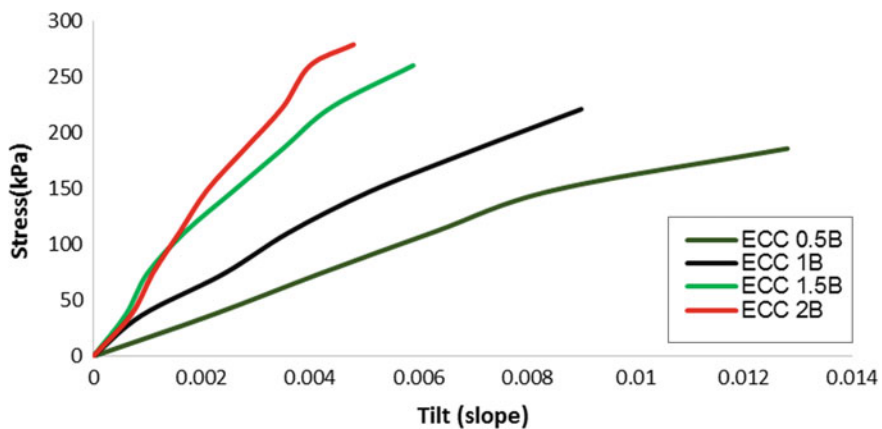


Fig. 19.8 Tilt versus stress curve (varying eccentricity of contamination)

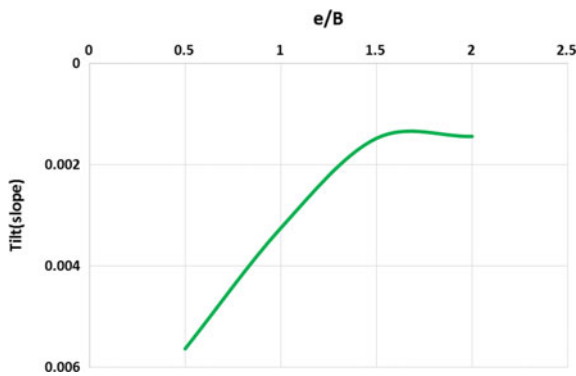


Fig. 19.9 Variation of tilt with eccentricity of contamination

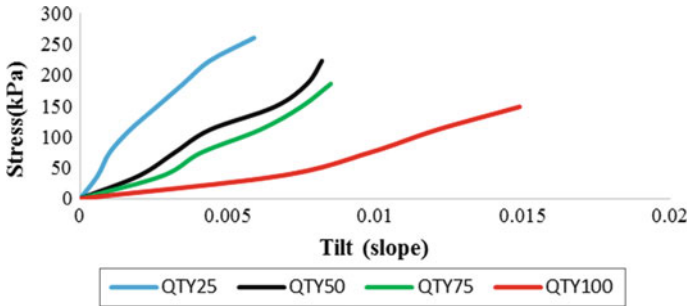


Fig. 19.10 Tilt versus stress curve (varying quantity of contaminant)

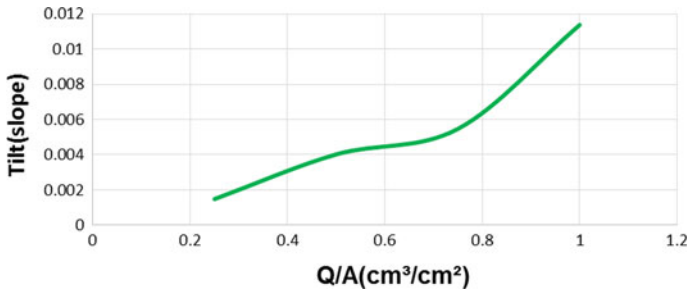


Fig. 19.11 Variation of tilt with quantity of contaminant

Influence of Quantity of Contaminant on the Tilt of Footing

Influence of quantity of contaminant on tilt of footing is presented in Fig. 19.10. It is seen that with increase in quantity of contaminant the tilt increases. A maximum tilt of 0°51'13" is observed upon the spillage of 100 ml oil at a distance of 1*B* from the edge of the footing.

Influence of quantity of contaminant (*Q/A*) on the tilt of footing at a stress of 100 kPa is presented in Fig. 19.11. It is observed that the tilt increases with the quantity of contaminant.

Reduction Factor

To quantify the influence of various parameters, a reduction factor is defined as given below. The stress corresponding to a normalized settlement of 5% is used for the calculation of the reduction factor in all cases.

$$\text{Reduction factor} = \frac{\text{stress}(\text{uncontaminated}) - \text{stress}(\text{contaminated})}{\text{stress}(\text{uncontaminated})}$$

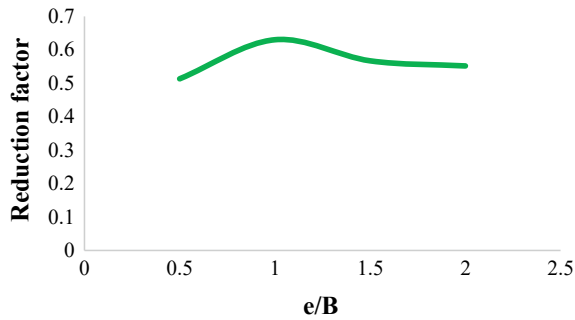


Fig. 19.12 Variation of reduction factor with e/B

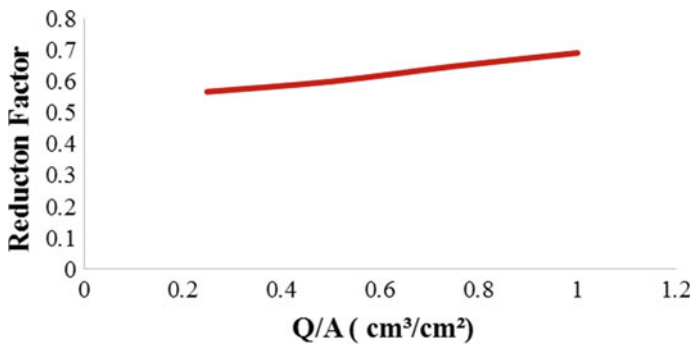


Fig. 19.13 Variation of reduction factor with Q/A

Figure 19.12 presents the relation between e/B and the reduction factor, where ‘ e ’ is the eccentricity of contamination from the center of footing and ‘ B ’ is the width of model footing. Up to an e/B ratio of 1, the reduction factor increases and thereafter shows a slight decrease.

Figure 19.13 presents the relation between Q/A and reduction factor where ‘ Q ’ is the quantity of oil contaminant and ‘ A ’ is the area of footing. It is observed that with the increase in the quantity of contaminant, the reduction factor increases.

Conclusions

Based on the test results, the following conclusions can be drawn:

- Oil contamination reduces the angle of shearing resistance and increases the cohesion intercept.
- Increase in quantity of contaminant and decrease in the eccentricity of contamination increases the settlement.

- For varying eccentricity of contamination, the maximum reduction in bearing capacity is obtained as 37.6% at an eccentricity of contamination of $0.5B$.
- For varying quantity of contaminant, the maximum reduction in bearing capacity is 50.17% which is obtained at $Q/A = 1$.
- The percentage reduction in stress is 62.99 for e/B ratio of 1 and 69.07 for Q/A ratio of 1 at a normalized settlement of 5%.
- It is also observed that the tilt of footing increased with the increase in quantity of contaminant and decrease in eccentricity of contamination.
- With the increase in quantity of contaminant and decrease in eccentricity of contamination, the oil content in the influence zone of footing increases which causes a reduction in shear strength of sand and as a result the bearing capacity decreases.

References

1. Al-Sanad HA, Eid WK, Ismael NF (1995) Geotechnical properties of oil contaminated Kuwait sand. *J Geotech Eng* 121:407–412
2. Ostovar M, Ghiassi R, Mehdizadeh MJ, Shariatmadari N (2020) Effects of crude oil on geotechnical specification of sandy soils. *Soil Sediment Contam* 30(4):1–16
3. Nasehi SA, Uromeihy A, Nikudel MR, Morsali A (2016) Influence of gas oil contamination on geotechnical properties of fine and coarse grained soils. *Geotech Geol Eng* 34:333–345
4. Shin EC, Lee JB, Das BM (1999) Bearing capacity of a model scale footing on crude oil contaminated sand. *Geotech Geol Eng* 17:123–132
5. Abtahi SA, Boushehrian H (2018) A experimental behaviour of circular foundation on oil contaminated sand. *J Geotech Geo Environ Eng* 27(1):80–87
6. Fadhil AI, Fadhil AI, Fattah MY (2018) Bearing capacity of isolated square footing resting on contaminated sandy soil with crude oil. *Egypt J Petrol* 28(3):281–288
7. Pousti S, Marnani AJ (2014) Numerical and analytical evaluation of crude oil contamination effect on strip foundation's bearing capacity. *Int J Sci Res* 3(4)
8. IOCL Homepage, <http://iocl.com>. Last accessed 2021/7/16

Chapter 20

Behavior of Vertical and Battered Piles Under Combined Axial and Lateral Load



Poulami Ghosh , Shilak Bhaumik, and Sibapriya Mukherjee 

Introduction

Piles are normally required when subsoil at shallow depth is very weak and where shallow foundations are unable to sustain the superstructure load. Some structures like high-rise buildings, transmission towers, offshore structures, and the like are generally supported by pile foundations. Pile foundations of such structures are often subjected to large lateral loads as well as axial loads. Especially, for offshore structures, the lateral loads are notably high of the order 10–20% of the vertical loads. Therefore, in such cases, the study of interaction effects and the safe design of vertical piles and battered piles under combined loading (lateral and axial) have become essential for geotechnical engineers.

There are many well-established theoretical methods to evaluate the pile behavior under individual axial and lateral loadings. There are, however, limited numerical studies which reported pile behavior under combined effect of lateral–axial loading [1, 2]. Whereas, quite a few researchers have attempted to study the behavior of battered piles subjected to pure lateral loads. It has been commonly observed that the negative battered piles develop greater resistance than that by vertical and positive battered piles in sandy soils, as noted from full-scale lateral load tests [3] and model scale tests [4–6]. Most recently, Hazzar et al. [7] utilized finite difference software FLAC–3D to study the behavior of battered piles in sandy soil and observed that the vertical load, pile batter angle and the soil relative density significantly influence the lateral response of battered piles. Based on the literature mentioned above, it has been observed that the study of the battered pile behavior under combined lateral–axial

P. Ghosh (✉) · S. Bhaumik · S. Mukherjee
Department of Civil Engineering, Jadavpur University, Kolkata 700032, India
e-mail: poulamig04@gmail.com

loading is not well addressed. Therefore, an attempt has been made in the present research paper to examine the combined effect of axial and lateral loading on vertical and battered piles using finite element software PLAXIS 3D.

Motivation and Objective

Since, piles are not often structurally designed to resist lateral loads, the consideration of lateral response of piles becomes more critical in case of structures supported on battered piles intended to resist very large lateral loads in combination with axial loads. Also, as discussed in the previous section, it may be inferred that even though many theoretical and numerical studies have been undertaken by researchers to study the pile behavior under individual axial and lateral loadings, only a few reported the battered pile behavior under combined lateral–axial loading leading to a research gap that requires further probing. Therefore, the objective of this study is to investigate the behavior of single piles, both vertical and battered, embedded in non-cohesive soil of homogeneous deposits of varying angle of internal friction (ϕ) when subjected to combined axial and lateral loading for different pile diameters.

Numerical Study

Description of the Numerical Model Adopted in Present Study

A finite element model has been developed using PLAXIS 3D software to examine the effect of combined axial and lateral loading on vertical and battered piles. The pile has been modeled as a linear-elastic embedded beam element following Hooke's law. On the other hand, Mohr–Coulomb failure criterion has been used to model the nonlinear behavior of surrounding soil. The overall dimensions of the pile–soil continuum (Fig. 20.1) have been taken as 60.0 m (L) \times 30.0 m (B) \times 30.0 m (D). The domain so chosen has been fixed by carrying out trial analyses to eradicate the boundary effects on the performance of pile. The soil continuum has been discretized using 15-noded wedge elements and adopting medium coarse mesh element size with global scale factor of 1.2. The soil–pile interface has been discretized using 12-noded interface elements. An embedded pile consists of a beam element with embedded interface element to describe the interaction with the surrounding soil at the pile skin and at the pile toe with no relative slip condition. The side boundaries of the pile–soil model have been constrained against horizontal direction and the bottom boundaries have been constrained against both horizontal and vertical directions. Then, the model has been analyzed for various pile and soil parameters with appropriate boundary conditions subjected to various combinations of lateral–axial load.

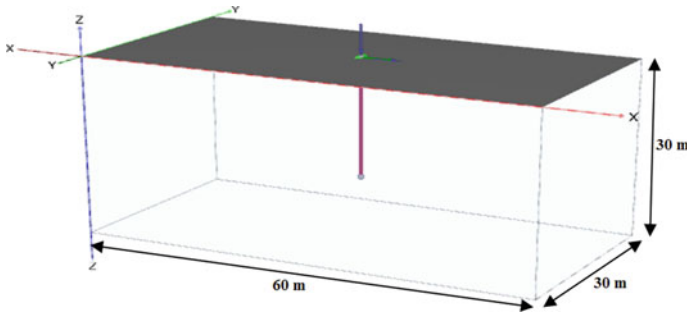


Fig. 20.1 Typical pile–soil model dimensions

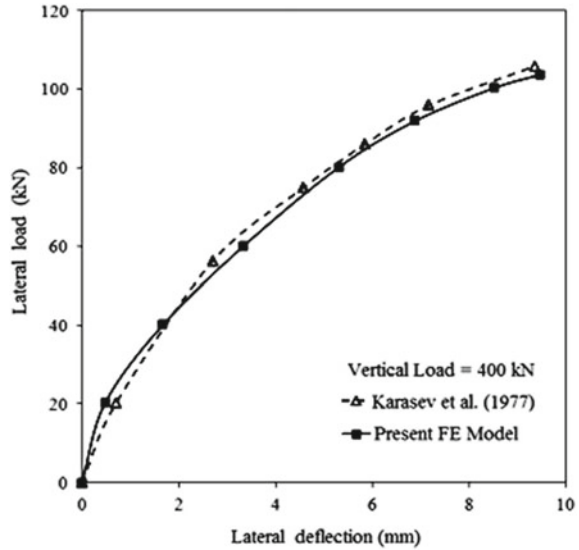
Validation of the Developed Numerical Model

The validity of the numerical model employed in the present study has been verified by back predicting the pile response based on pile loading test data of two published research papers. The first case corresponds to field load tests carried out on a single vertical pile installed in sandy soil subjected to both vertical and horizontal loading, while, the second case corresponds to centrifuge model tests conducted on laterally loaded single battered piles. The second case has been so chosen to validate the adopted numerical model as no real-time field, model or centrifuge test data were available for a single batter pile subjected to combined lateral–axial loading. The details of these two cases have been presented in the following subsections.

Field load tests. Karasev et al. [8] conducted several field load tests on a single vertical concrete pile, with a diameter of 0.6 m and a length of 3.0 m, embedded in a 6.0-m-thick sandy loam soil having a cohesion (c) of 18 kN/m², a friction angle (ϕ) of 18°, a shear modulus (G) of 9.3×10^3 kN/m², and a Poisson’s ratio (μ) of 0.35. The pile behaved as a short/rigid pile and field tests was conducted by first loading the pile in the vertical direction in increments of 50–100 kN upto 400 kN, maintaining each load increment until a vertical settlement rate of 0.1 mm/h was attained. After stabilization of vertical settlement at a load of 400 kN and keeping the vertical load constant, a horizontal load was then applied to the pile head at a height of 20 cm from the ground surface in increments of 5–10 kN upto 80 kN, withholding at each load increment until the horizontal and vertical displacements were stabilized.

The adopted numerical model in the present study (developed using PLAXIS 3D software) has been utilized to recreate the aforementioned pile–soil continuum, and the same sequence of load application has been followed to obtain the subsequent pile response. Then, the pile responses predicted by the adopted numerical model have been compared with the reported data [8] as shown in Fig. 20.2, from which it can be inferred that the numerical results are in accordance with the reported test data.

Fig. 20.2 Comparison of the present numerical analysis results with test data of Karasev et al. [8]



Centrifuge pile model tests. Zhang et al. [9] carried out a series of centrifuge model tests on laterally loaded single battered piles, with batter angles (β) of $\pm 14^\circ$ and $\pm 7^\circ$, in dry medium-dense sand bed having a relative density (D_r) of 55.0%, dry unit weight (γ_d) of 14.50 kN/m^3 , and internal friction angle (ϕ) of 33.3° . The model was tested at 45 g. The square aluminum model piles used were 304.0 mm long and 9.5 mm wide. In prototype scale, the width, and total length of each square pile were 0.43 m, and 13.7 m respectively. The elastic modulus (E) of a single model aluminum pile was $73.1 \times 10^3 \text{ kN/m}^2$ and the flexural stiffness (EI) of a single prototype pile was 206 MN-m^2 . The piles behaved as a long/flexible pile as the embedded length of pile–soil system was computed to be greater than 4.0 times the stiffness factor, assuming the value of coefficient of subgrade reaction (η_h) to be 2.71 MN/m^3 for medium-dense sand [10]. The point of application of lateral load was 2.14 m above the sand bed.

The adopted PLAXIS 3D model in the present study has been used to replicate the above described pile–soil continuum and analyze the subsequent pile response to lateral load. The comparison between the lateral load–pile head deflection responses of the prototype scale of the centrifuge tests and the proposed numerical model has been depicted in Figs. 20.3 and 20.4 for $\beta = \pm 7^\circ$ and $\pm 14^\circ$ respectively. In general, a good agreement has been observed between the measured and predicted lateral load responses for both positive and negative battered piles.

Based on the comparative results shown in Figs. 20.3 and 20.4, it may be concluded that the proposed numerical model can be satisfactorily used in the present study to replicate the soil–pile interaction under combined lateral–axial loads.

Fig. 20.3 Comparison of the present numerical analysis results with centrifuge test data of Zhang et al. [9] for $\beta = \pm 7^\circ$

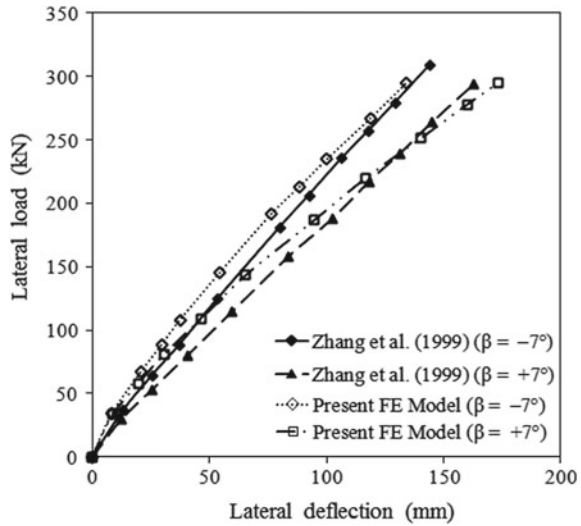
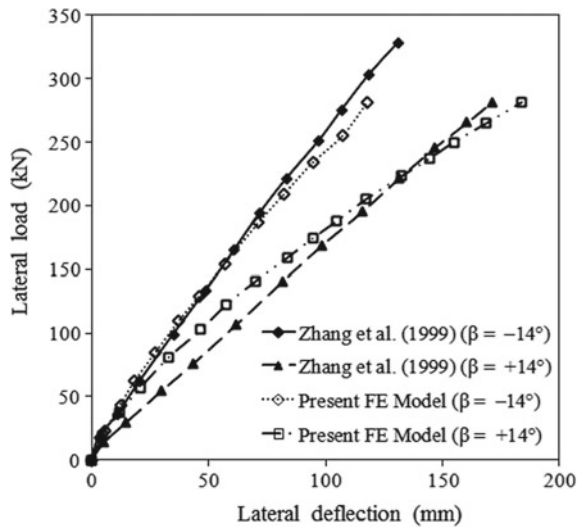


Fig. 20.4 Comparison of the present numerical analysis results with centrifuge test data of Zhang et al. [9] for $\beta = \pm 14^\circ$



Present Study

An attempt has been made in the present study to perform a rigorous numerical study by adopting the finite element model described in Sect. 3.1, to study the effect of combined axial and lateral loading on vertical ($\beta = 0^\circ$) and battered ($\beta = \pm 10^\circ$ and $\pm 20^\circ$) piles embedded in homogeneous sand deposits. The engineering properties of the homogeneous sand deposits have been suitably assumed as per Bowles [11] and presented in Table 20.1. Reinforced concrete (RC) piles of M25 grade having a

Table 20.1 Engineering properties of sand deposits (Bowles [11])

Material	ϕ (°)	E (kN/m ²)	μ	γ_{sat} (kN/m ³)	γ_d (kN/m ³)
Sand 1	30°	15,000	0.25	19.0	17.0
Sand 2	40°	58,000	0.35	22.5	21.0

ϕ angle of internal friction, E elasticity modulus, μ Poisson's ratio, γ_{sat} saturated unit weight, γ_d dry unit weight

Table 20.2 Pile parameters

Material	Section	E (kN/m ²)	μ	γ (kN/m ³)
RC	Circular	27×10^6	0.20	25.0

E elasticity modulus, μ Poisson's ratio, γ unit weight

length of 20.0 m and diameters of 500, 650 and 800 mm, have been considered in this study. The various pile parameters have been presented in Table 20.2.

First, the numerical analyses have been carried out using PLAXIS 3D software to determine the ultimate axial load (P_u) of a single pile embedded in sand for different diameters and batter angles of pile. Then, a certain percentage of the ultimate axial load, P ($=0, 0.2 P_u, 0.4 P_u, P_u$ being ultimate axial load) has been applied on the pile head alongside a lateral load acting simultaneously on the pile head. The pile response under the influence of combined loading, so obtained, has been recorded and the ultimate lateral capacity (H) of piles has been reported from the lateral load–pile head displacement curve as the load corresponding to the horizontal deflection of 5 mm. A total of 90 analyses have been performed with PLAXIS 3D considering different parameters according to Table 20.3.

From the output of the numerical analyses, the variation of lateral load with pile head deflection with and without different values of axial load has been obtained for various diameters of pile and batter angles.

Results and Discussion

Pile Behavior Under Lateral Load

The variation of the lateral load with pile head deflection, for vertical and battered piles embedded in homogenous sand deposits, has been found to be nonlinear under no axial load condition ($P = 0$). The lateral response of a typical pile, having a diameter of 500 mm, embedded in medium sand ($\phi = 30^\circ$) and dense sand ($\phi = 40^\circ$) beds, has been shown in Figs. 20.5 and 20.6, respectively. It may be observed that the lateral response of positive battered piles does not change appreciably with respect to vertical piles ($\beta = 0^\circ$). In case of medium sand ($\phi = 30^\circ$), the lateral load has been found to be slightly higher for $\beta = 20^\circ$ but does not significantly change for $\beta = 10^\circ$.

Table 20.3 Details for numerical analysis

ϕ (°)	Diameter of pile (mm)	P/P_u	β (°)			No. of numerical cases
30°	500	0	0°	±10°	±20°	Total 18 × 5 = 90
		0.2	0°	±10°	±20°	
		0.4	0°	±10°	±20°	
	650	0	0°	±10°	±20°	
		0.2	0°	±10°	±20°	
		0.4	0°	±10°	±20°	
	800	0	0°	±10°	±20°	
		0.2	0°	±10°	±20°	
		0.4	0°	±10°	±20°	
40°	500	0	0°	±10°	±20°	
		0.2	0°	±10°	±20°	
		0.4	0°	±10°	±20°	
	650	0	0°	±10°	±20°	
		0.2	0°	±10°	±20°	
		0.4	0°	±10°	±20°	
	800	0	0°	±10°	±20°	
		0.2	0°	±10°	±20°	
		0.4	0°	±10°	±20°	

While, in case of dense sand ($\phi = 40^\circ$), the lateral load decreases significantly for all positive batter angles. However, the lateral response of negatively battered piles increases quite considerably for all batter angles in both medium and dense sand deposits.

Also, the variation of the ratio of lateral capacity of battered piles to that of vertical piles ($H_{batter}/H_{vertical}$) with the batter angle (Fig. 20.7) has been plotted for different angles of internal friction (ϕ) to study the influence of batter angles on lateral response of piles under no axial load condition ($P = 0$). It may be noted that the lateral capacity (i.e., the lateral load corresponding to a pile head deflection of 5 mm, as obtained from the lateral load–pile head displacement curve) decreases by almost 17% for positive battered piles embedded in dense sands, whereas, in medium sands, it increases by 13% and 35% for batter angles of 10° and 20° , respectively. For negative battered piles, the effect of pile batter angles on the lateral response of piles becomes more significant. The lateral capacity of battered piles has been found to increase by 26% and 74% for batter angles of -10° and -20° , respectively, in medium sands. But, for dense sands, the same increases by 8% and 26% for batter angles of -10° and -20° , respectively. This may possibly happen due to the fact that considerable increase and decrease in the confining pressure occurs in the soil in the vicinity of the negative battered and positive battered pile respectively, which, then, increases or decreases

Fig. 20.5 Typical lateral response of vertical and battered pile (diameter, $d = 500$ mm) in medium sand ($\phi = 30^\circ$)

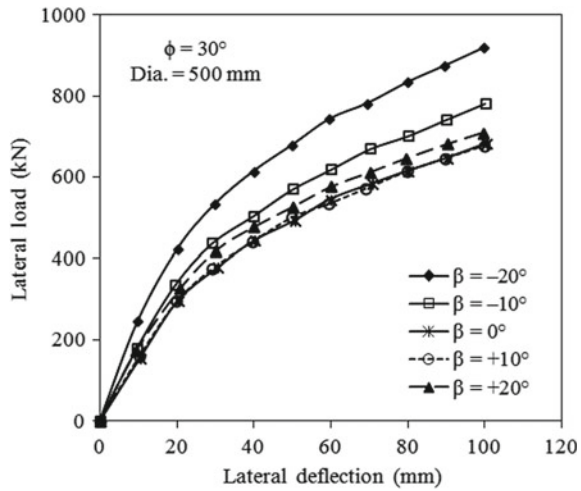
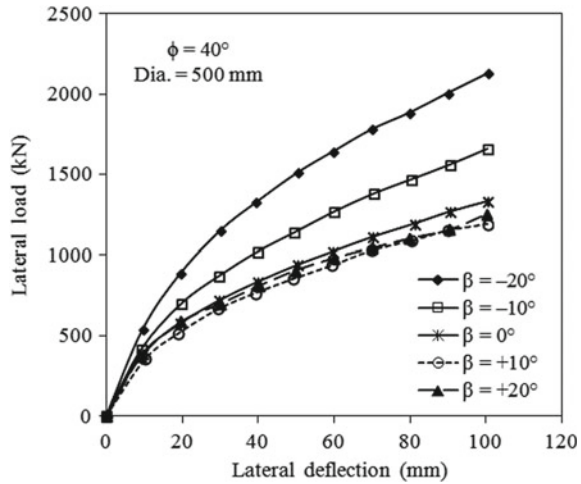


Fig. 20.6 Typical lateral response of vertical and battered pile (diameter, $d = 500$ mm) in dense sand ($\phi = 40^\circ$)

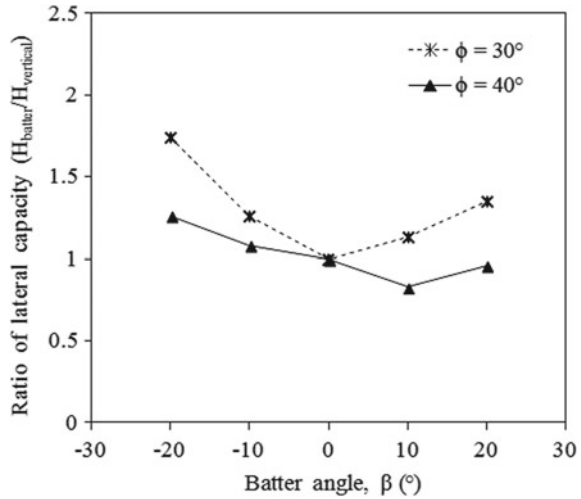


the soil–pile resistance depending upon the sand packing. Further, similar behavior has been observed for all pile diameters.

Pile Behavior Under Combined Axial and Lateral Load

The lateral response of vertical and battered piles under constant axial load has been also found to be nonlinear. The effect of axial loads on the lateral response of vertical ($\beta = 0^\circ$) and battered ($\beta = \pm 10^\circ$) piles has been shown in Figs. 20.8 and 20.9, respectively, for a typical case of piles of diameter 500 mm embedded in

Fig. 20.7 Effect of pile batter angle on lateral resistance of pile (diameter, $d = 500$ mm) embedded in sand under no axial load condition ($P = 0$)



medium sand ($\phi = 30^\circ$) and dense sand ($\phi = 40^\circ$) beds. It may be noted that under the combined effect of axial and lateral loads, the lateral capacities developed at all deflections are less and more than that of the corresponding case under pure lateral loading, for negative battered piles and positive battered piles respectively. Similar behavior has been observed for all pile diameters and batter angles.

An improvement factor (I_H), defined by Eq. (20.1), has been utilized to measure the percentage improvement in lateral capacity in order to study the influence of axial loads on the lateral response of vertical and battered piles.

Fig. 20.8 Typical lateral response of vertical and battered pile (diameter, $d = 500$ mm) in medium sand ($\phi = 30^\circ$) subjected to combined load

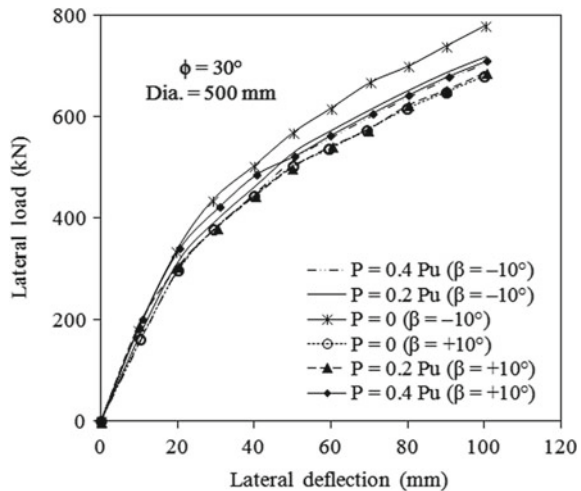
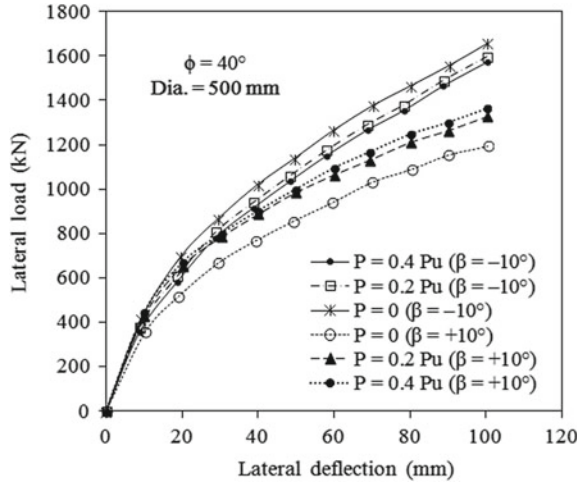


Fig. 20.9 Typical lateral response of vertical and battered pile (diameter, $d = 500$ mm) in dense sand ($\phi = 40^\circ$) subjected to combined load



$$I_H = \left(\frac{H_{P>0} - H_{P=0}}{H_{P=0}} \right) \times 100 \tag{20.1}$$

where $H_{P>0}$ is the lateral capacity of piles under combined loads, and $H_{P=0}$ is the lateral capacity of piles under pure lateral load (without axial load). A typical plot showing the variation of the I_H values with β for different angles of friction and combined load has been depicted in Figs. 20.10 and 20.11 for a pile, having a diameter of 500 mm.

It may be noted from Figs. 20.10 and 20.11 that the I_H values increase with the increase in values of batter angle, β . For negative battered piles, I_H values are almost

Fig. 20.10 I_H versus β for vertical and battered pile (diameter, $d = 500$ mm) subjected to 20% of the ultimate axial load along with lateral load

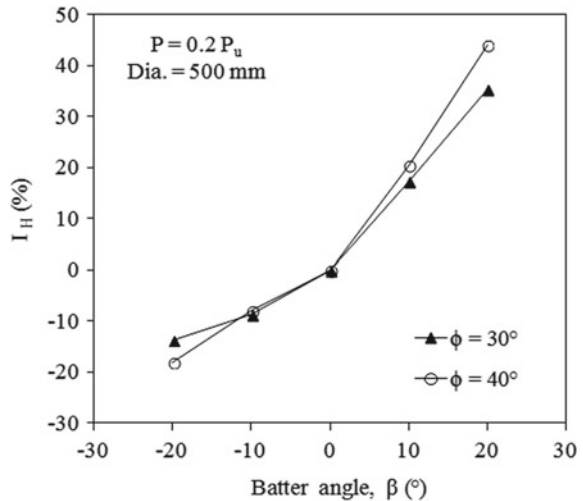
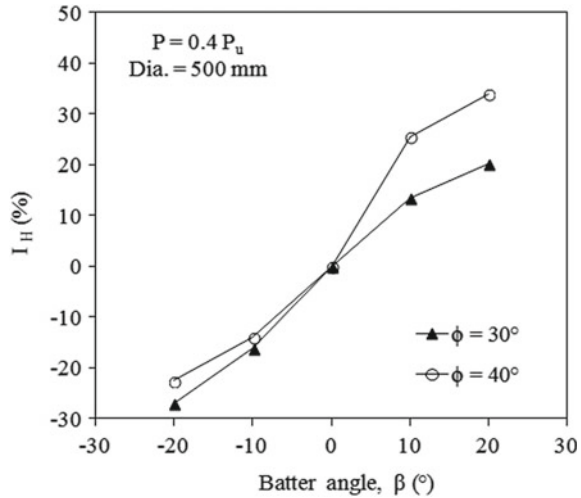


Fig. 20.11 I_H versus β for vertical and battered pile (diameter, $d = 500$ mm) subjected to 40% of the ultimate axial load along with lateral load



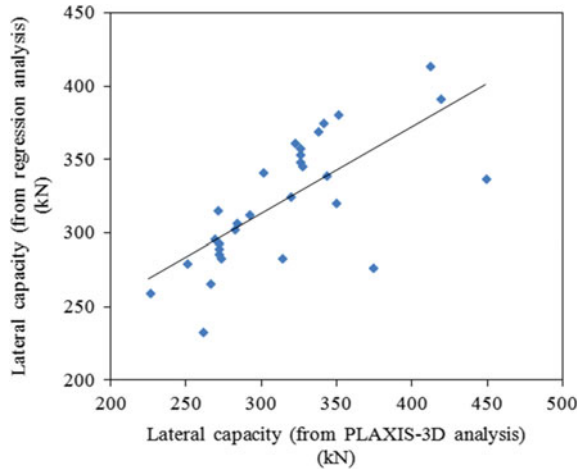
same for both medium and dense sands. An I_H value of -27% has been observed for a negative battered pile ($\beta = -20^\circ$) of 500 mm diameter embedded in medium sand ($\phi = 30^\circ$) when subjected to 40% of the ultimate axial load along with lateral load. While for positive battered piles, in case of dense sands, I_H varies considerably with friction angles of sand, reaching a value of 34% for $\beta = 20^\circ$. Further, similar behavior has been observed for all pile diameters.

Regression Analysis

From the results of numerical analysis, an attempt has been made to obtain a multiple linear regression model using MS-Excel with lateral capacity (H) as response and angle of internal friction of sand bed, ϕ ($=a$), diameter of pile ($=b$), % constant axial load in terms of ultimate axial load, P/P_u ($=c$) and batter angle, β ($=d$) as predictors. From the range of above parameters adopted in the present study, the values from first 60 numerical cases as described in Table 20.3 have been used to obtain the equation, whereas the values from rest of the numerical cases have been used to validate the equation. From the multiple linear regressions, Eq. (20.2), as shown, has been formed with R^2 value = 0.921.

$$\begin{aligned}
 H(kN) = & 15.983 - (0.6122 \times b) + (0.0257 \times ab) - (0.2946 \times ac) \\
 & - (0.0014 \times ad) - (0.1425 \times bc) + (0.004 \times bd) \\
 & + (0.0047 \times abc) - (0.0002 \times abd) + (0.0055 \times acd) \\
 & - (0.0249 \times bcd) + (0.001 \times abcd)
 \end{aligned} \tag{20.2}$$

Fig. 20.12 Comparison curve for lateral capacity predicted by regression analysis and that obtained from numerical model



Further, a considerable correlation between the lateral capacity values obtained from PLAXIS 3D analysis and that obtained from regression analysis may be seen from Fig. 20.12. The variation of results predicted by the above equation and that computed from the numerical model are found to be within 25%

Conclusions

Based on the results obtained from the numerical analysis, the following conclusions have been drawn:

- Under no axial load condition ($P = 0$), the lateral capacity decreases by almost 17% for positive battered piles embedded in dense sands, whereas, in medium sands, it increases by 13% and 35% for batter angles of 10° and 20° , respectively. For negative battered piles, the effect of pile batter angles on the lateral response of piles becomes more significant. The lateral capacity of battered piles has been found to increase by 26% and 74% for batter angles of -10° and -20° , respectively, in medium sands. But, for dense sands, the same increases by 8% and 26% for batter angles of -10° and -20° , respectively.
- Under the combined influence of axial load, P ($=0.2 P_u, 0.4 P_u$) and lateral load, the percentage increase in lateral capacity (I_H) increases with the increase in values of batter angle, β . For a negative battered pile, I_H values are almost same for both medium and dense sands. An I_H value of -27% has been observed for a negative battered pile ($\beta = -20^\circ$) of 500 mm diameter embedded in medium sand ($\phi = 30^\circ$) when subjected to 40% of the ultimate axial load along with lateral load. While for positive battered piles, in case of dense sands, I_H varies

considerably with friction angles of sand, reaching a value of 34% for $\beta = 20^\circ$. Similar behavior has been noted for all pile diameters.

- The following multiple linear regression equation, with R^2 value = 0.921, has been developed using MS-Excel with lateral capacity (H) as response and angle of internal friction of sand bed, ϕ ($=a$), diameter of pile ($=b$), % constant axial load in terms of ultimate axial load, P/P_u ($=c$) and batter angle, β ($=d$) as predictors.

$$\begin{aligned} H(kN) = & 15.983 - (0.6122 \times b) + (0.0257 \times ab) - (0.2946 \times ac) \\ & - (0.0014 \times ad) - (0.1425 \times bc) + (0.004 \times bd) \\ & + (0.0047 \times abc) - (0.0002 \times abd) + (0.0055 \times acd) \\ & - (0.0249 \times bcd) + (0.001 \times abcd) \end{aligned}$$

The variation of results predicted by the above equation and that computed from the numerical model are found to be within 25%.

However, it is to be noted that the above conclusions may not be applicable for soil–pile systems having parameters substantially different from those adopted in this study. The present paper has largely focused on examining the influence of batter angle and axial loads on the lateral capacity of piles. However, further parametric studies may be undertaken to investigate the influence of the pile parameters, namely, pile diameter, slenderness ratio, and pile head fixity on the lateral response of piles subjected to combined loading. The study may also be extended for other soil types and non-homogenous soil deposits and pile parameters, supported by experimental investigations, to develop a generalized formulation to predict the lateral response of battered piles subjected to combined lateral–axial load.

References

1. Karthigeyan S, Ramakrishna VVGST, Rajagopal K (2007) Numerical investigation of the effect of vertical load on the lateral response of piles. *J Geotech Geoenviron Eng* 133(5):512–521
2. Liang F, Yu F, Jie H (2013) A simplified analytical method for response of an axially loaded pile group subjected to lateral soil movement. *J Civ Eng* 17(2):368–376
3. Alizadeh M, Davisson MT (1970) Lateral load tests on piles-Arkansas River project. *J Soil Mech Found Div* 96(5):1583–1604
4. Meyerhof GG, Ranjan G (1973) The bearing capacity of rigid piles under inclined loads in sand II: batter piles. *Can Geotech J* 10(1):71–85
5. Meyerhof GG, Yalcin AS (1994) Behavior of flexible batter piles under inclined loads in layered soil. *Can Geotech J* 30(2):247–256
6. Juvekar MS, Pise PJ (2008) Behavior of rigid batter piles and pile groups subjected to horizontal load in sand. *Indian Geotech J* 38(2):221–242
7. Hazzar L, Hussien MN, Karray M (2016) Numerical investigation of the lateral response of battered pile foundations. *Int J Geotech Eng* 11(4):376–392
8. Karasev OV, Talanov GP, Benda SF (1977) Investigation of the work of single situ-cast piles under different load combinations. *Soil Mech Found Eng* 14(3):173–177
9. Zhang L, McVay MC, Lai PW (1999) Centrifuge modeling of laterally loaded single battered piles in sands. *Can Geotech J* 36(6):1074–1084

10. IS 2911 (Part I/Sec II) (2010) Design and construction of pile foundations—code of practice, Bureau of Indian Standards, New Delhi
11. Bowles JE (2001) Foundation analysis and design, 5th edn. McGraw-Hill, New York

Chapter 21

Footings Resting on Clayey Slopes



Rajesh P. Shukla and Ravi S. Jakka

Introduction

The bearing capacity of a footing located close to a slope possesses a relatively lower bearing capacity than level ground [1]. Footings located close to the slope crest show the minimum bearing capacity. Meyerhof [1] assumed uniform strength mobilization below the footing. Later, studies reveal that strength mobilization is not uniform in the sloping ground [2–8]. The strength mobilized along the sloping side of the footing axis earlier than soil located on the other side of the footing.

Most of the earlier studies were carried out for cohesionless soils [7]. Some of the studies studied the footing on clayey slopes also. A study by Kusakabe et al. [9] shows that the failure mechanism and bearing capacity also depend significantly on soil shear strength ($c_u/\gamma B$). Georgiadis [10] investigated clayey soil slope using upper-bound analysis and found the critical edge distance to be $2B$ without considering the height of the slope. Georgiadis and Chrysouli [11] found that bearing capacity decreases linearly with horizontal seismic acceleration. Farzaneh et al. [12] analyzed footing located close to slope crest under seismic loading. Mirzababaei et al. [13]

R. P. Shukla (✉)
National Institute of Technology Srinagar, Srinagar 190006, India
e-mail: rpshukla.2013@iitkalumni.org

R. S. Jakka
Indian Institute of Technology Roorkee, Roorkee 208016, India

also constrained the edge distance to $3B$. Baazouzi et al. [14] studied footing resting on an undrained slope. Aminpour et al. [15] determined the effect of surcharge loading slope behavior. Some studies considered footing resting on $c-\phi$ soils [6, 8, 16, 17]. Acharyya and Dey [17] developed an interaction mechanism for multiple footings on a slope based on a displacement pattern. Shukla and Jakka [3] proposed the slope factors and failure mechanism for a strip footing located on clayey soil slopes using limit analysis. Finally, regression equations were presented to predict the bearing capacity ratio, bearing capacity and critical setback. However, most of the results were expressed in non-dimensional form, which reduces the application of study. Zhao and Wei [18] recognized that the bearing capacity increases even up to a setback of 10 times footing width in clayey soil. This value is almost twice of setback suggested by some of the previous studies [3, 10–15].

It is observed from the literature study that most of the studies have used limit equilibrium. A few studies have also used limit analysis but used either upper or lower bound. This study used both upper and lower bound to analyze the problem. Previous studies presented results either in terms of bearing capacity factor or in terms of slope factor. The results are presented in the form of bearing capacity factor and slope factor as well. It will enhance the current understanding of footing on cohesive soil slopes. The slope factor shows the slope effect on bearing capacity directly.

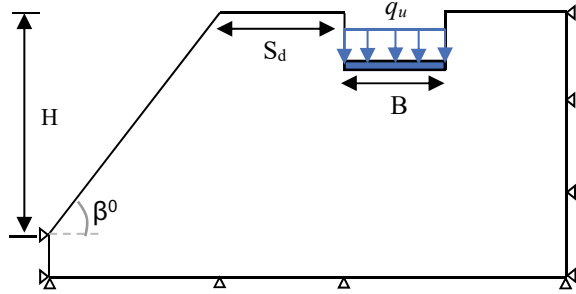
In the study, a 2D finite element analysis, an association with limit analysis, has been performed to determine the effect of various factors, such as slope inclination, soil strength and footing depth on bearing capacity, and slopes factor for a strip footing resting on clayey soil slopes is determined. The change in failure mechanism with slope inclination is also discussed briefly.

The Material Used and Experimental Testing Methodology

The strip footings located close to the slope can be modeled as a plane strain problem [19]. OptumG2 program was used to perform the 2D finite element analysis. A 2D model used in the analysis is shown in Fig. 21.1. The slope gradient is maintained unvarying along the slope. The domain area is assumed to have a width of $18B$ and a height of $8B$. The vertical displacement was allowed, and horizontal displacements were retained along the vertical boundary. Along the bottom boundary, all displacements were constrained.

The strip footing has been modeled as a perfectly ‘rigid plate’ element. The stiffness of rigid footing has been assumed to be infinite. The soil has been modeled as 15-node mixed Gauss elements. The clayey soil has been supposed to be an elastic-perfectly plastic material, which follows the modified Mohr–Coulomb failure criteria. The soil strength was assumed to be independent of the depth of soil strata, which is

Fig. 21.1 Problem geometry and boundary conditions



true in cohesive soil. The undrained strength (S_u) has been varied from 20 to 320 kPa (20, 40, 80, 160 and 320 kPa). The corresponding ($S_u/\gamma B$) varied from 0.7 to 10.6 (0.7, 1.4, 2.8, 5.6 and 10.6). This range is adequate to reproduce the all possible soil consistency. The unit weights of soil varied from 14 to 17 kN/m³. The soil stiffness is varied from 2500 to 14,000 kN/m² with undrained strength.

The number of elements has been increased from 5000 in the initial iteration to 7000 in the final iteration. The mesh is refined at the critical area of the domain by means of iterations. The shear dissipation has been used to refine the mesh. The load multiplier acting on footing was increased continuously till the failure. The stable slopes are considered in the present study. The present study considers only shear failure criteria and does not consider the settlement. However, the previous studies concluded that the bearing capacity failure prevails in footing resting on slopes [2–8]. Therefore, the results may remain independent of settlement. The setback (S_d) and footing depth (D_f) normalized with respect to footing width. The details of modeling, elements and soil properties and boundary conditions are discussed in a detailed manner in earlier study [3]. The details of OptumG2 can be found in the program manual [20].

Results and Discussions

The bearing capacity factor variation with slope inclination, setback and footing depth and soil strength is studied and presented separately herein in this section. The effect of slope height has not been considered in the study as very high slope has been considered in the study. These slopes represent the critical condition as decreasing the slope height has a positive impact on slope stability. The slope factor is defined as bearing on the slope to the level ground. The slope factor (S_{fc}) is identical to those of Shukla and Jakka [3]. The results are also compared with the earlier studies

Table 21.1 Comparison of results with earlier studies

$S_u/(\gamma B)$	Present study	UB, Kusakabe et al. [9]	LB, Kusakabe et al. [9]	Bishop [21]	Kotter solution	Fellenius solution
0.5	11.3	10.3	3.84	7	11	7
1	17	18.3	6.86	17	17	12
5	70	81	32.11	88	81.2	58

to validate the developed model in Table 21.1. The results are reasonably closed to earlier studies.

Figure 21.2. demonstrates the typical variation in bearing capacity factor (N_{cq}) and slope factor (S_{fc}) with slope angle for three footing depths ($D_f/B = 0, 0.5$ and 1). The bearing capacity factor (N_{cq}) represents the combined effect of cohesion and surcharge. Bearing capacity, as well as slope factor, declines nonlinearly with slope inclination. The adverse effect of the slope is found to be a function of footing depth and setback. The slope effect becomes more in footing placed near slope crest, which becomes more noticeable with an increase in footing depth (Figs. 21.2a–c). The results show the effect of slope for the short term only as steep slope may not be stable considering long-term stability. The plots show that for safe slopes, the slope factor is 0.45, which indicates a 55% reduction in bearing capacity. The bearing capacity reduction on clayey soil is relatively smaller than those were reported in cohesionless soil slope [1, 2, 4–8].

The effect of slope inclination on the failure mechanism for a footing resting at a setback of $3B$ is shown in Fig. 21.3. The red color shows the maximum relative displacement of soil with respect to footing, and the blue color shows no relative movement in all failure mechanism plots. It shows that the failure mechanism is symmetrical and independent of slope inclination at gentle slopes. However, the interaction between slope and footing increases with slope steepness, which reduces the bearing capacity. Previous studies made comparable observations for clayey and cohesionless soils [3–7, 20]. At gentle slopes, the failure is bearing capacity failure (Fig. 21.3a–c). The failure is slope failure at a very steep slope, not the bearing capacity failure (Fig. 21.3e–f). A combined failure mechanism coexists in moderate to steep slopes (i.e., slope failure and bearing capacity failure occur together) (Fig. 21.3d). Even a footing on a steep slope can be stable if resting at a significant edge distance as it remains intact and unaffected from the slope. However, soil near the slope edge and along the slope surface may fail. In this case, either the slope geometry needs to be modified, or a soil reinforcement option can be adopted to avoid the failure of the slope face.

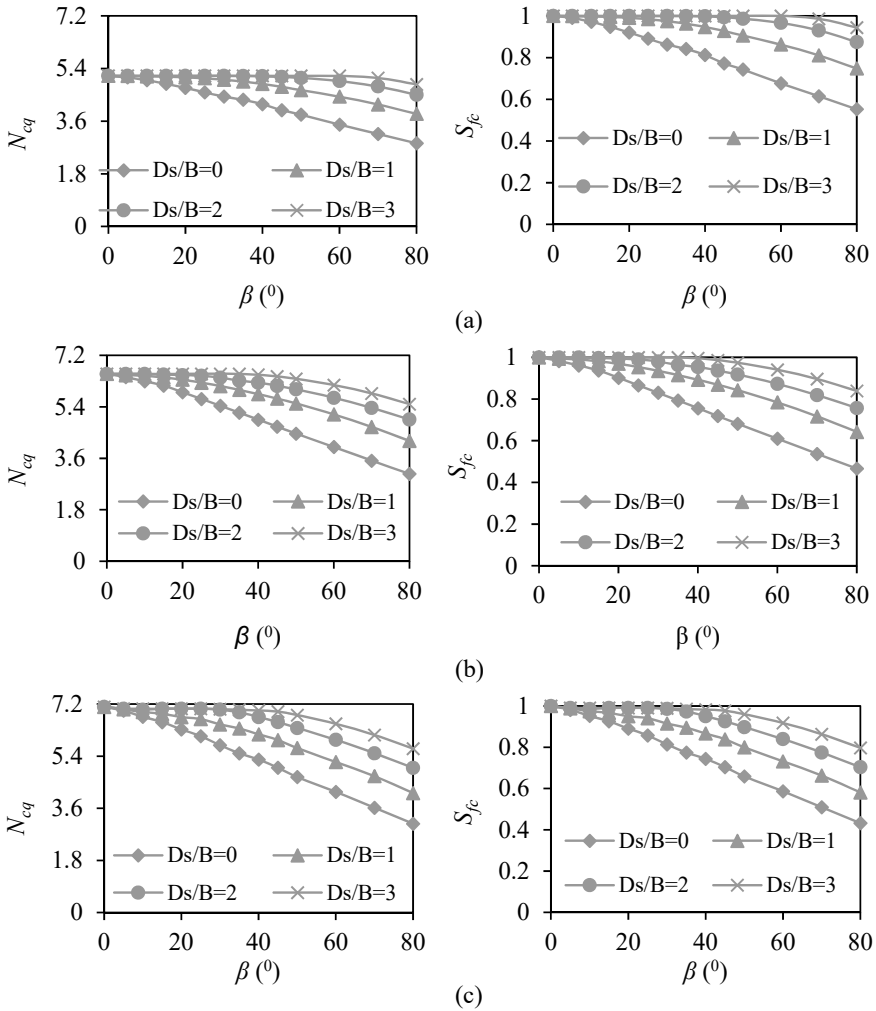


Fig. 21.2 Effect of slope inclination: **a** $D_f/B = 0$, **b** $D_f/B = 0.5$, **c** $D_f/B = 1$

Figure 21.4 shows that the bearing capacity factor increases and the slope factor decreases with the footing depth. The surcharge increases with footing depth, which improves the bearing capacity. At D_f/B of 0, the bearing capacity factor is almost identical for all setbacks. However, at the D_f/B of 1, the effect of setback is more visible. It means, bearing capacity enhancement with a setback can further improve with footing depth. The bearing capacity increase with footing depth is more noticeable in soil with relatively gentle slopes or level ground than steep slopes. Earlier studies also made a similar observation in cohesionless soil slopes [3–5, 22, 23]. Contrary to this, the variation in slope factor is more noticeable in footing placed

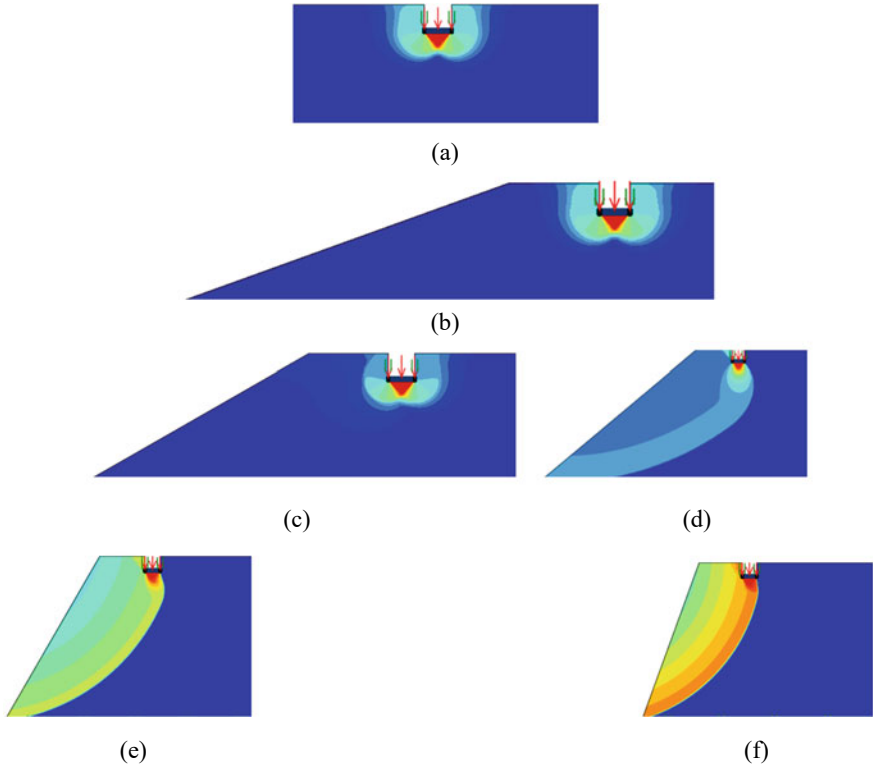


Fig. 21.3 Effect of slope inclination on failure mechanism: **a** $\beta = 0^\circ$, **b** $\beta = 20^\circ$, **c** $\beta = 30^\circ$, **d** $\beta = 40^\circ$, **e** $\beta = 50^\circ$, **f** $\beta = 70^\circ$

at greater depth (Fig. 21.4a–c). This indicates that not only bearing capacity but the slope effect also enhances with footing depth.

The effect of embedment depth on the failure mechanism is presented in Fig. 21.5. The footing resting on ground level possesses a small load carrying capacity. A very small area of foundation soil involves and contributes to bearing capacity (Fig. 21.5a). Therefore, even at lower edge distances, the footing is independent of the slope effect. While, in the case of greater embedment depth, the large soil area contributes to bearing capacity, a large edge distance is required to cover that much area to mobilize the soil strength optimally (Fig. 21.5b, c). Therefore, S_f reduces with the increase in embedment depth of footing, as depicted in Fig. 21.4.

Figure 21.6 shows that the slope and bearing capacity factors increase with the setback, indicating the reduction in slope effect. The bearing capacity factor on the slope reaches equal to level ground at small setbacks in gentle slopes. Compared

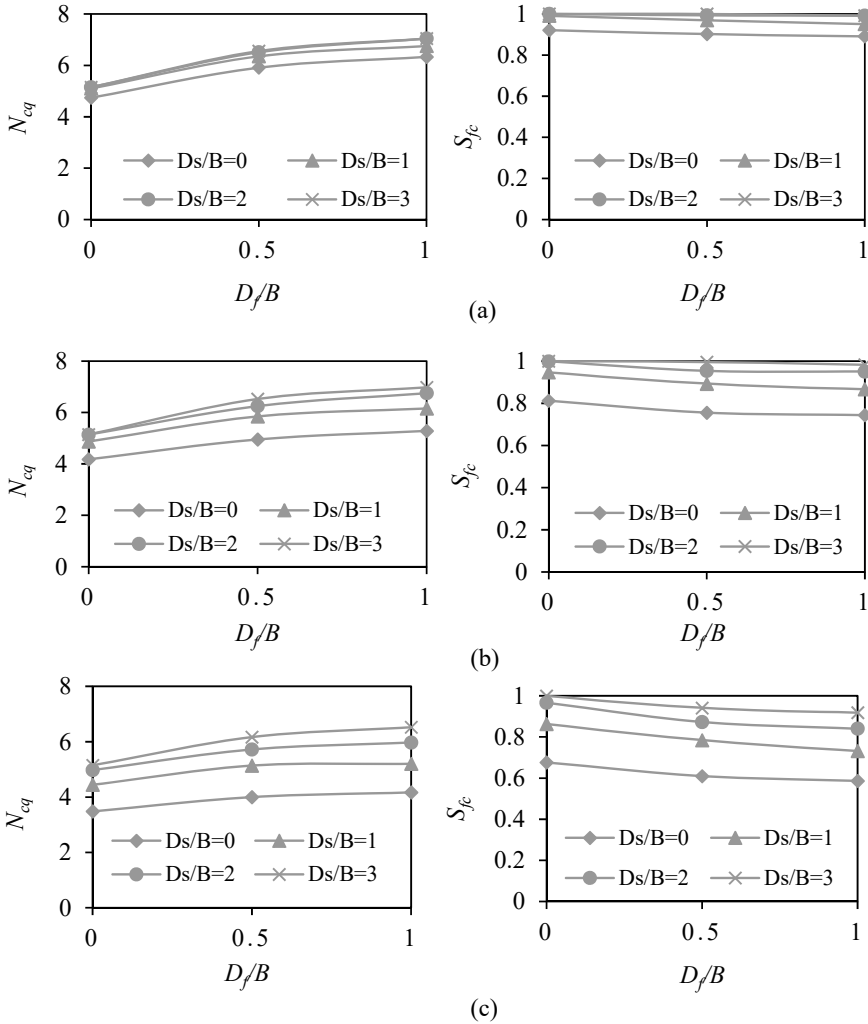


Fig. 21.4 Effect of footing depth for different slope inclination: **a** $\beta = 20^\circ$, **b** $\beta = 40^\circ$, **c** $\beta = 60^\circ$

to the footing on the ground surface, the footing placed at a deeper depth becomes independent of slope at a relatively large setback (Fig. 21.6a–c). The effect of steep slopes remains present even at the large setback. Therefore, the footing behavior on a steep slope becomes independent of slope at large setbacks than those placed on gentle slopes.

The effect of edge distance on failure mechanism and soil deformation for a footing of embedment ratio of 1 resting over the soil having $c_u/(\gamma B)$ equal to 2.85 is presented in Fig. 21.7. It is observed that the shearing starts from the footing edge and propagating toward the slope surface. At a small edge distance, failure is

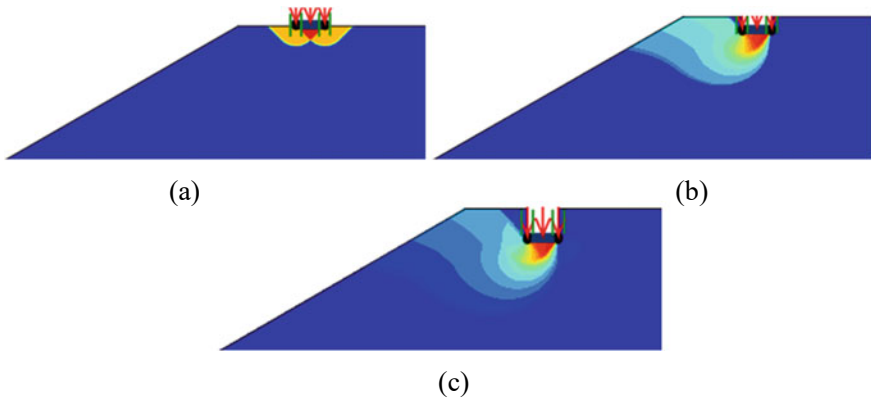


Fig. 21.5 Effect of embedment depth of footing on failure surface **a** $D_f/B = 0.0$, **b** $D_f/B = 0.5$, **c** $D_f/B = 1.0$

one sided (slope side only), and the soil on the side of level ground does not fully contribute to bearing capacity (Fig. 21.7a–c). Therefore, the S_f is small for footings resting precisely on the slope crest or near the slope crest. The degree of strength mobilization on level side soil increases with the increase in edge distance, and at a particular edge distance, both sides of soil contribute to an equal amount. At this edge distance, footing behavior and bearing capacity turn into the independence of slope, and failure pattern becomes symmetrical about footing axis (Fig. 21.7d, e).

Conclusions

The bearing capacity factor, as well as slope factor, is presented together for comparison purposes. The adverse effect of the slope depends on slope steepness, soil characteristics, footing depth and setback. The presence of a slope adjacent to footings decreases the bearing capacity. The bearing even reduces by 50–60% in the case of stable steep slopes. The failure mechanism was modified from the bearing capacity to slope failure with an increase in slope steepness. The bearing capacity and slope factor increase with setback and reduce with slope angle. However, interestingly, the bearing capacity increases, and the slope factor reduces with footing depth. Similar to the cases of level ground, the bearing capacity is a function of the undrained soil strength, but the bearing capacity factor is independent.

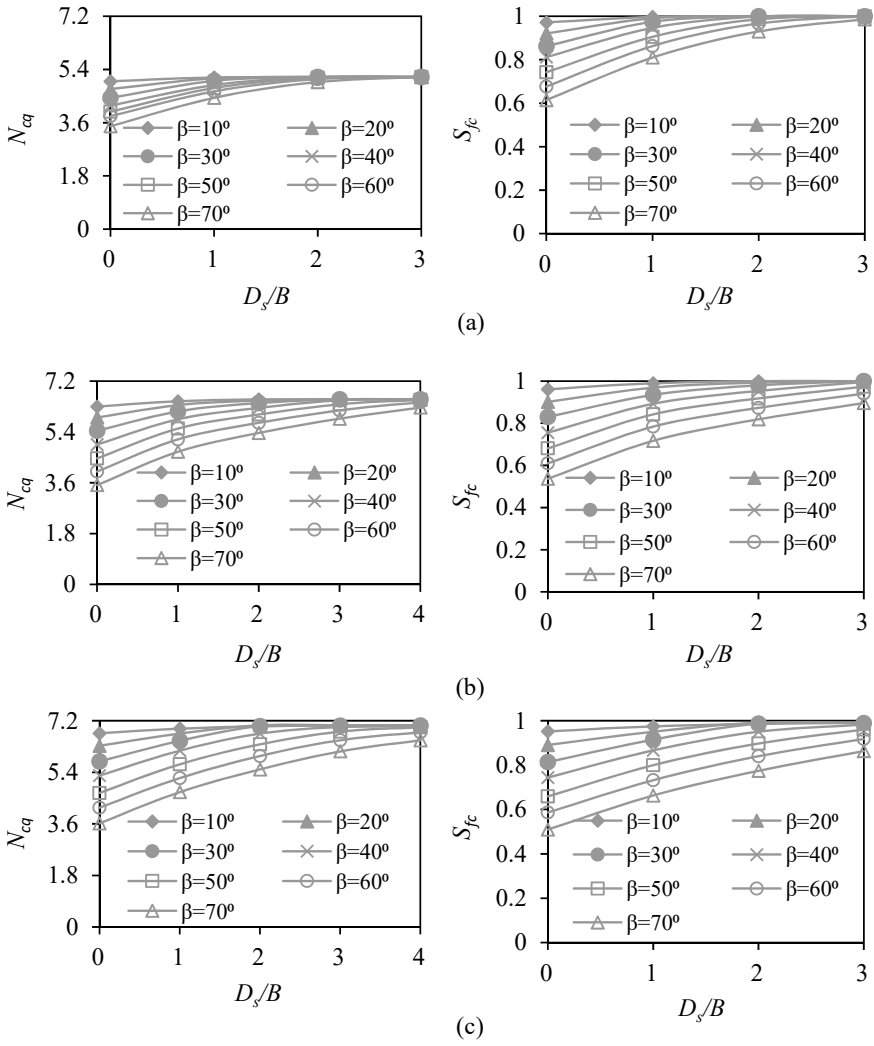


Fig. 21.6 Effect of setback on bearing capacity and slope factor: **a** $D_f/B = 0$, **b** $D_f/B = 0.5$, **c** $D_f/B = 1.0$

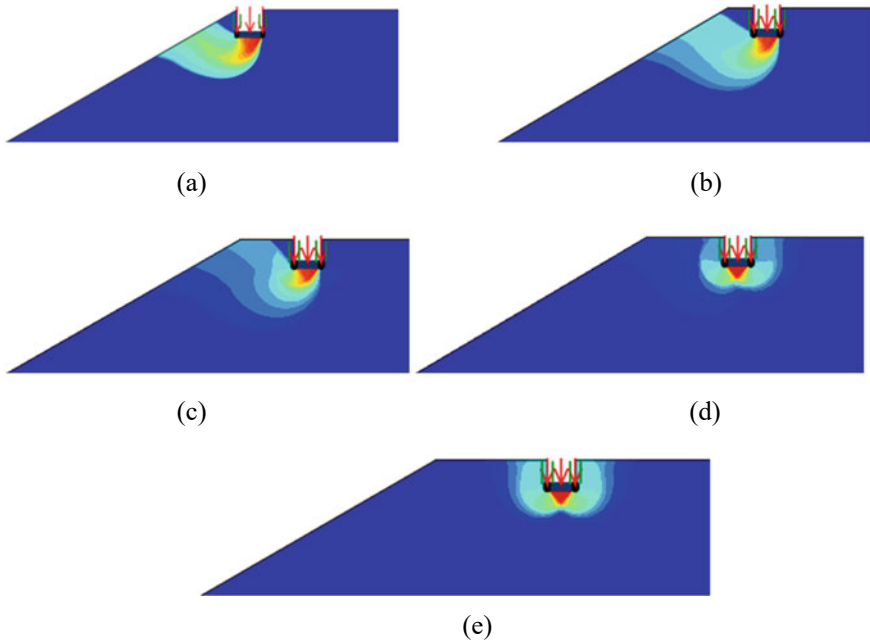


Fig. 21.7 Effect of edge distance on failure pattern: **a** $D_s/B = 0$, **b** $D_s/B = 1$, **c** $D_s/B = 2$, **d** $D_s/B = 3$, **e** $D_s/B = 4$

References

1. Meyerhof GG (1957) The ultimate bearing capacity of foundation on slopes. In: 4th international conference on soil mechanics and foundation engineering, vol 3, pp 384–386
2. Saran S, Sud V, Handa S (1989) Bearing capacity of footings adjacent to slopes. *J Geotech Engg ASCE* 115(4):553–573
3. Shukla RP, Jakka RS (2019) Determination and prediction of bearing capacity on clayey slopes. *Acta Geotechnica Slovenica* 16(2):50–65. <https://doi.org/10.18690/actageotechslov.16.2.50-65.2019>
4. Shukla RP, Jakka RS (2018) Critical setback distance for a footing resting on slopes under seismic loading. *Geomech Eng* 15(6):1193–1205. <https://doi.org/10.12989/gae.2018.15.6.1193>
5. Shukla RP, Jakka RS (2017) Critical setback distance for a footing resting on slopes. *Acta Geotechnica Slovenica* 14(2):19–31
6. Acharyya R, Dey A, Kumar B (2018) Finite element and ANN-based prediction of bearing capacity of square footing resting on the crest of c - ϕ soil slope. *Int J Geotech Eng* 1–12. <https://doi.org/10.1080/19386362.2018.1435022>
7. Shukla RP, Jakka RS (2021) Failure mechanism and slope factors for a footing resting on slopes. *Mag Civil Eng* 104(4):1–15. <https://doi.org/10.34910/MCE.104.1>
8. Dey A, Acharyya R, Alammyan A (2019) Bearing capacity and failure mechanism of shallow footings on unreinforced slopes: a state-of-the-art review. *Int J Geotech Eng*
9. Kusakabe O, Kimura T, Yamaguchi H (1981) Bearing capacity of slopes under strip loads on the top surfaces. *Soils Found* 21(4):29–40. https://doi.org/10.3208/sandf1972.21.4_29
10. Georgiadis K (2010) Undrained bearing capacity of strip footings on slopes. *J Geotech Geoenviron Eng* 136(5):677–685. [https://doi.org/10.1061/\(ASCE\)GT.1943-5606.0000269](https://doi.org/10.1061/(ASCE)GT.1943-5606.0000269)

11. Georgiadis K, Chryssouli E (2011) Seismic bearing capacity of strip footings on clay slopes. In: 15th European conference on soil mechanics and geotechnical engineering, pp 723–728
12. Farzaneh O, Mofidi J, Askari F (2013) Seismic bearing capacity of strip footings near cohesive slopes using lower bound limit analysis. In: 18th international conference on soil mechanics and geotechnical engineering, Paris
13. Mirzababaei M, Mohamed M, MirafTAB M (2016) Analysis of strip footings on fiber-reinforced slopes with the aid of particle image velocimetry. *J Mater Civ Eng* 29(4):04016243. [https://doi.org/10.1061/\(ASCE\)MT.1943-5533.0001758](https://doi.org/10.1061/(ASCE)MT.1943-5533.0001758)
14. Baazouzi M, Mellas M, Mabrouki A, Benmeddour D (2017) Effect of the slope on the undrained bearing capacity of shallow foundation. *Int J Eng Res Africa* 28:32–44. <https://doi.org/10.4028/www.scientific.net/JERA.28.32>
15. Aminpour MM, Maleki M, Ghanbari A (2017) Investigation of the effect of surcharge on behavior of soil slopes. *Geomech Eng An Int'l J* 13(4):653–669. <https://doi.org/10.12989/gae.2017.13.4.653>
16. Leshchinsky B, Xie Y (2016) Bearing capacity for spread footings placed near $c'-\phi'$ slopes. *J Geotech Geoenviron Eng* 143(1):06016020. [https://doi.org/10.1061/\(ASCE\)GT.1943-5606.0001578](https://doi.org/10.1061/(ASCE)GT.1943-5606.0001578)
17. Acharyya R, Dey A (2018) Assessment of bearing capacity and failure mechanism of isolated and interfering strip footings on sloping ground. *Int J Geotech Eng*. <https://doi.org/10.1080/19386362.2018.1540099>
18. Zhao Z, Wei Z (2017) Study on the safety distance of strip footing on cohesive soil slope. *J For Eng* 2(1):130–134. <https://doi.org/10.13360/j.issn.2096-1359.2017.01.023>
19. Shukla RP, Jakka RS (2017) Discussion of “experimental and numerical studies of circular footing resting on confined granular subgrade adjacent to slope.” *Int J Geomech ASCE* 17(2):1–3. [https://doi.org/10.1061/\(ASCE\)GM.1943-5622.0000704,0701600](https://doi.org/10.1061/(ASCE)GM.1943-5622.0000704,0701600)
20. Optum G2 [Computer software]. OptumCE, Copenhagen, Denmark
21. Bishop AW (1955) The use of the slip circle in the stability analysis of slopes. *Géotechnique* 5(1):7–17. <https://doi.org/10.1680/geot.1955.5.1.7>
22. Narita K, Yamaguchi H (1990) Bearing capacity analysis of foundations on slopes by use of log-spiral sliding surfaces. *Soil Found* 30(3):144–152. https://doi.org/10.3208/sandf1972.30.3_144
23. Cure E, Sadoglu E, Turker E, Uzuner BA (2014) Decrease trends of ultimate loads of eccentrically loaded model strip footings close to a slope. *Geomech Geoeng* 6(5):469–485. <https://doi.org/10.12989/gae.2014.6.5.469>

Chapter 22

A Comparison of Solutions of Laterally Loaded Long Piles Using Subgrade Modulus Approach



Rupam Mahanta

Introduction

Lateral loading of pile is essentially a pile–soil interaction problem where the stress–displacement relation of soil is practically nonlinear except at very low stress in soil. Analysis of piles subjected to lateral load involves a lot of uncertainties mainly due to the uncertainties associated with the analysis methods and soil parameters used for analysis. Among the existing methods of analysis, no particular method is considered as perfect. The methods based on subgrade modulus of soil are practically convenient and popularly used although there are a few other approaches for analysis of the problem [1]. The subgrade approach for the analysis is based on Winkler’s (1867) ‘beam of elastic subgrade’ model, where the soil is represented by discrete springs supporting a beam. The springs are independent of each other, and the reaction at any point in the beam is influenced only by the displacement at that point. The same principle is applied for analysis of lateral loading of a pile embedded in soil where the springs are supposed to resist the lateral movement of pile and the spring constant is represented by the horizontal subgrade modulus of the soil.

Earlier, the solution of laterally loaded piles was based on certain simple assumptions. For example, subgrade modulus was assumed to be constant and/or soil behavior was considered linear. Subsequently, solutions incorporating nonlinear soil behavior and variation of subgrade modulus with depth were incorporated. Currently, finite difference solution of the differential equation governing the lateral loading of piles is generally used for important structure–foundation systems using nonlinear ‘ p - y ’ curves. It practically accommodates the arbitrary variation of subgrade modulus with depth.

R. Mahanta (✉)
Civil Engineering Department, ONGC, Assam, India
e-mail: rupam.mahanta@gmail.com

However, a detailed analysis using nonlinear ' p - y ' data requires the use of computer application. Relatively simplified solutions based on the 'subgrade approach' are also prevalent and still recommended by some codes of practice. It is felt that the most uncertain part regarding analysis with the simplified approaches in normally consolidated (NC) clay is the selection of appropriate value of the subgrade parameter η_h . Since the soil modulus varies with many aspects such as load level, pile properties and soil condition, it makes the selection of appropriate subgrade parameter difficult. The paper presents the results of a study for piles in NC clay in offshore. The value of η_h to be used in simplified solutions (for NC clays of increasing shear strength with depth) was back-calculated for application with relatively simplified subgrade approaches. The analytical study was carried out for long piles of steel in tubular shape, commonly used for offshore structures. Data of ' p - y ' used in the analysis were generated assuming equilibrium under static loading.

It was also of interest to examine the degradation of η_h value with increasing lateral loads on a pile. Finally, the range of η_h values of applicable for use in simplified subgrade methods was determined.

Description of Methods

It is well known that soil's stress-strain behavior is nonlinear for most of the practical applications and the value of subgrade modulus is actually not constant; it may arbitrarily vary at various depths along the pile length.

A comprehensive non-dimensional solution method [2] was proposed by Reese and Matlock [2] for linearly increasing E_s with respect to depth, and generalized solution [3] was proposed by [3] for cases with different variations of E_s with depth. Analysis was carried out in the study using the solution method [2] for further comparisons with detailed analysis using ' p - y ' data.

The ' p - y ' data at any depth below the surface are defined as the stress-displacement relation of soil subjected to lateral pressure. Formulations for generating ' p - y ' curves or data are well established and recommended by current international codes of practice. One of these methods of obtaining ' p - y ' data was given by [4] for soft clay for both static and cyclic loading based on full-scale test data of instrumented pile. Detailed analysis using nonlinear ' p - y ' data and actual pile geometry can avoid unrealistic and simplifying assumptions. Currently recommended practice adopted by the offshore industry recommends application of nonlinear ' p - y ' data which are used for solutions of lateral loading of piles. Such solutions incorporate the arbitrary nature of the subgrade modulus, varying geometry of the pile and layered soil conditions. However, such a detailed solution requires computer application and also generation of appropriate ' p - y ' data for various soil types and loading conditions. Therefore, it was of interest to find out appropriate values of η_h relevant for pile solution for NC clays which can be used in simplified or closed form solutions for quick estimates of pile results with reasonable accuracy. Analysis was carried out for comparing the

relatively simplified solutions with the detailed analysis using nonlinear ‘ p - y ’ data along the length of the pile.

For laterally loaded long piles, the results of analysis such as displacement, moment, shear, slope and soil pressure can be found by solving the 4th-order differential Eq. (22.1).

$$EI \frac{d^4 y}{dx^4} + E_s y = 0 \quad (22.1)$$

where E Young’s modulus of pile material; I moment of inertia of pile; x depth below the pile top; E_s modulus of subgrade reaction or soil modulus and y lateral displacement of pile. For linearly increasing E_s , it is related with depth as under:

$$E_s = \eta_h x \quad (22.2)$$

where η_h coefficient of variation of the modulus of horizontal subgrade reaction or constant of horizontal subgrade reaction; x depth of a point below the pile top.

For cases where the E_s is not constant, Eq. (22.1) is conveniently solved numerically by finite difference method. The parameter E_s is given by corresponding ‘ p - y ’ data at various depths along the pile length. Thus, input of ‘ p - y ’ data corresponding to soil properties along the length of a pile is required for a detailed solution. The study presented in this paper was carried out for piles embedded in NC clays. The ‘ p - y ’ data were derived by applying the API RP 2GEO [5] method for soft clay [5]. Corresponding method for generating ‘ p - y ’ data is based on [4]. As mentioned already, static loading was considered for the ‘ p - y ’ data generation at every meter depth along the pile length below the seafloor (or submerged ground).

Analysis using non-dimensional method presented by Reese and Matlock [2] to find out bending moment and displacement of piles was carried out by using the moment and displacement coefficients prescribed for the method. Details of the non-dimensional solution are referred to publication by Reese and Matlock [2]. The bending moment (BM), displacement, rotation, slope, etc., for a laterally loaded pile may be found at any depth along the pile by using formulations and relevant coefficients prescribed in the method. Assuming linear variation of E_s with depth, the formulations from the method to calculate displacement and bending moments of pile at any depth are mentioned below.

Displacement of pile is given by

$$y = A_y \frac{P_t T^3}{EI} + B_y \frac{M_t T^2}{EI} \quad (22.3)$$

Pile bending moment is given by

$$M = P_t T A_m + M_t B_m \quad (22.4)$$

where P_t and M_t are the lateral force and moment applied at the pile top; A_y and B_y are the non-dimensional coefficients for displacement due to shear and moment; A_m and B_m are the non-dimensional coefficients for bending moment; and T is defined as the relative stiffness factor. For linear variation of soil modulus with depth

$$T = \sqrt[5]{EI/n_h} \tag{22.5}$$

Expressions are also given for slope, shear, etc. The results of solution can be found at any depth along the pile using the equations and applying appropriate coefficients A and B depending on a depth coefficient Z (given as $Z = x/T$).

Some analysis was also carried out to examine the cantilever method prescribed in the Indian standard code of practice [6] using same pile geometry and material. In this method, in case of piles in NC clay, the pile needs to be first verified whether it falls in the category of long or short pile. It is carried out by calculating the relative stiffness factor (T) using Eq. (22.5). When pile penetration in soil is more than $4T$, the pile is considered as a long pile. Prescribed charts are to be used to calculate the appropriate factors to determine the maximum BM and displacement of piles.

Pile and Soil Data

Open ended steel tubular pile of 1 m and 2 m diameters was used in the analysis. Wall thickness of 25 mm and 50 mm was considered for the 1 m and 2 m diameters, respectively. Further, sensitivity of pile wall thickness on the analytical results was also examined with respect to applicable equivalent values of η_h .

Clays with undrained shear strength (s_u) of 2 kPa at the seafloor and increasing s_u at the rate of 1 and 2 kPa per meter increase of depth were considered. Table 22.1 shows the details of soil parameters. Accordingly, the ‘ p - y ’ data for the piles were generated for the soil profiles. ‘ p - y ’ data were generated for pile diameters 1 m and 2 m. Data of ‘ p - y ’ were generated at one meter depth interval along the pile.

Derived ‘ p - y ’ data at some depths are shown in Fig. 22.1 for the pile of 1 m diameter embedded in NC clay with s_u gradient of 1 kPa/m.

Table 22.1 Soil parameters type-1

Soil profile	Depth (m)	s_u (kPa)	Effective unit weight (kN/m ³)	ϵ_{50} (%)	s_u gradient (kN/m ² per m depth)
1	0–50	2–52	4.0–6.5	1.5	1
2	0–25	2–52	4.0–6.5	1.5	2
2	25–50	52–102	6.5–7.5	1.0	2

Note ϵ_{50} = strain at one-half the maximum deviator stress in laboratory undrained compression tests of undisturbed soil samples

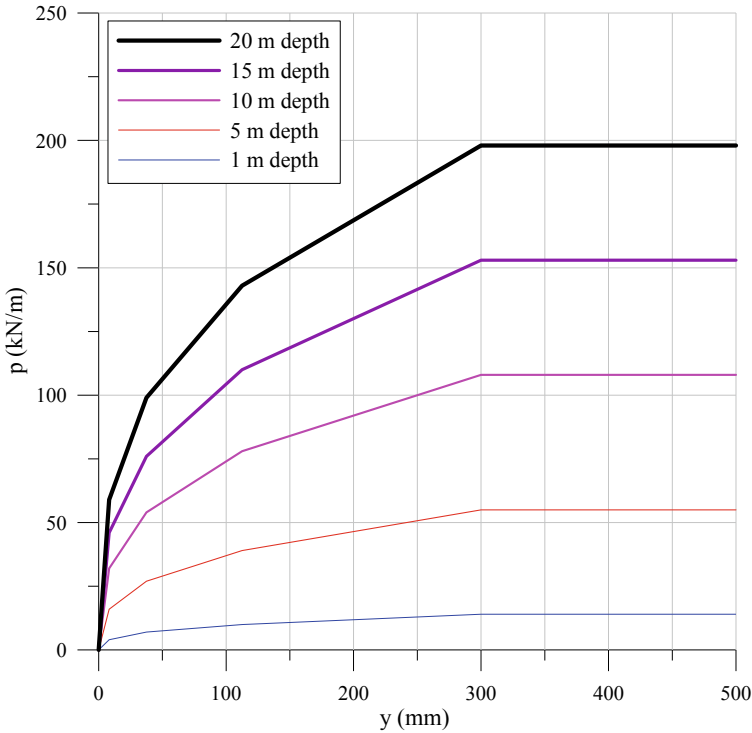


Fig. 22.1 Static ‘p-y’ curves for pile diameter of 1 m for soil profile 1

Analysis

The value of η_h for increasing shear strength profile was calibrated with respect to the ‘p-y’ method prescribed by API RP2GEO [5]. Applicable values for both ‘free-headed’ and ‘fixed-headed’ piles were investigated.

As mentioned already, non-dimensional solution given by Reese and Matlock [2] was applied to compare the results of analysis using detailed ‘p-y’ data. The non-dimensional solution was applied to calculate bending moment, displacement, shear, etc., using the coefficients given by the developers of the solution. Appropriate η_h values which matched the non-dimensional solution with the detailed solution were determined. Initially, the BM and displacement curves for piles were checked to validate the results.

There are also other simplified methods where pile analysis results can be estimated by using ‘subgrade approach’ with the help of recommended formulas and curves. However, it also requires the input of η_h value to derive the results of analysis. Indian standard codes [6] also recommend ‘subgrade approach’ for analysis of lateral loading of piles. Although the code is for analysis of concrete piles, some

results of this approach were checked on steel tubular piles by using the actual values of flexural rigidity corresponding to the steel tubular piles.

Results and Discussion

From the analysis, the range of equivalent values of η_h was determined for piles embedded in two s_u profiles of normally consolidated clays which are found to exist below seafloor in many offshore areas. The values were calibrated with respect to the recommended ‘ p - y ’ method of API RP 2GEO [5] generally followed for analysis of offshore piles.

Initially, the matching of pile solution results was achieved for a long pile of 1 m diameter pile with pile wall thickness of 25 mm. Subsequently, the range of the value of η_h was examined for the practical range of pile diameter, pile displacement and NC clay profiles generally applicable at many offshore sites.

Figure 22.2 shows the load–displacement patterns of a long pile of 1 m diameter with wall thickness of 25 mm. Curves for both ‘fixed-headed’ and ‘free-headed’ piles derived by using the detailed ‘ p - y ’ data are presented.

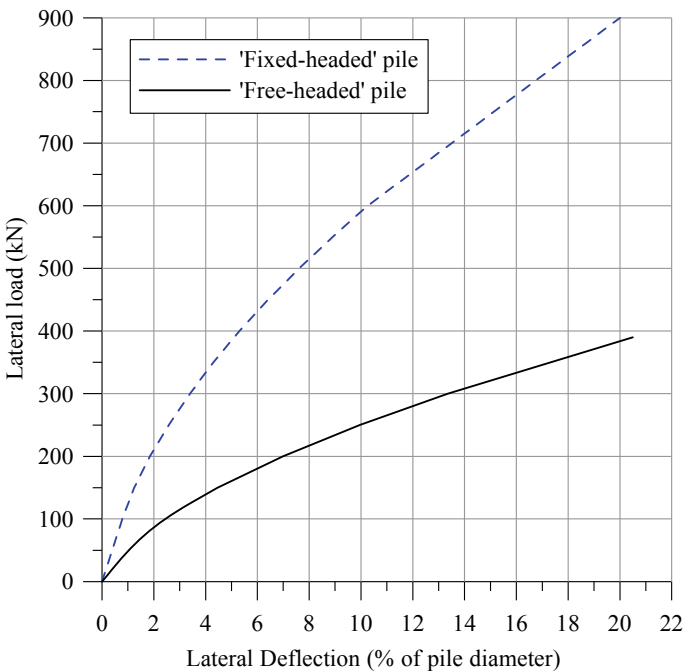


Fig. 22.2 Load–displacement curves for a long tubular pile of steel having diameter 1 m and wall thickness 25 mm in NC soil with 1 kPa/m strength gradient

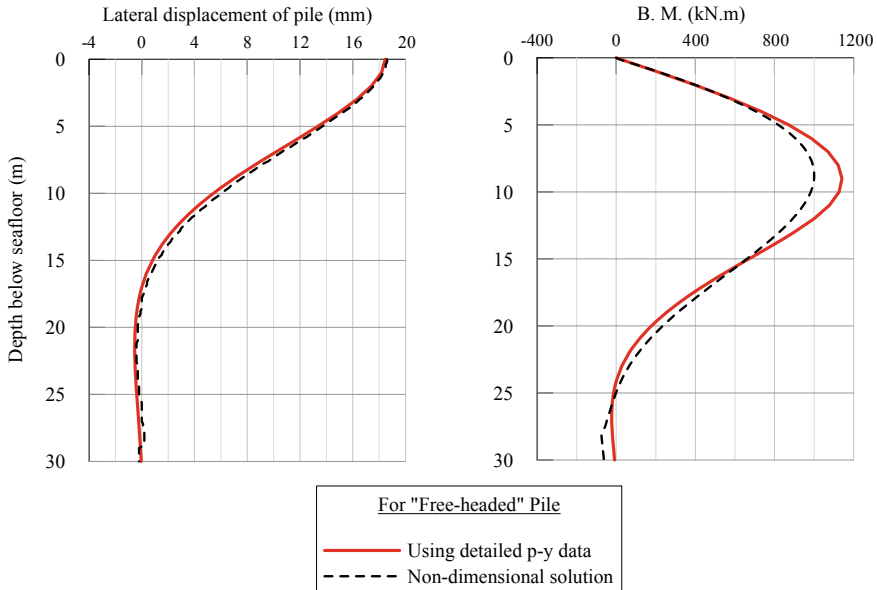


Fig. 22.3 Matching lateral displacement and bending moment for a ‘free-headed’, long, tubular pile of steel having outer diameter 1 m and wall thickness 25 mm, embedded in NC soil with s_u increasing with depth at the rate of 1 kPa/m

Matching of pile bending moments and displacements is shown in Figs. 22.3 and 22.4 for pile head restraint conditions ‘free’ and ‘fixed’, respectively. It is observed that depth-wise results from detailed ‘ p - y ’ analysis and analysis using an equivalent value of η_h match quite well for the soil and pile conditions considered in this study.

Analysis was also carried out for a pile of 2 m diameter with 50 mm wall thickness to examine the change in applicable equivalent value of η_h .

It was also of interest to examine the change in applicable value of η_h with respect to the change in strength gradient of the NC clay. Therefore, analytical results for soil profiles with s_u gradient at the rate of 1 and 2 kPa per meter depth were verified. It is observed that the equivalent maximum value of η_h increases with increasing shear strength profiles for the same pile properties. The results are presented in Table 22.2 subsequently.

It is known that the value of η_h for a particular pile–soil condition changes with the pile displacement. In other words, the value of η_h degrades (for the same soil profile) with increasing lateral load in piles. This aspect is shown in Fig. 22.5 with the analysis of a pile of 1 m diameter in NC clay with increasing s_u gradient of 1 kPa/m depth.

Similar trends are observed from analysis of piles of different diameters embedded in NC soil profiles. It is observed that for relatively small displacement of piles, the value of η_h remains almost the same for a small range of the pile displacements. As the load is increased, the degradation of the value of η_h starts and finally, at

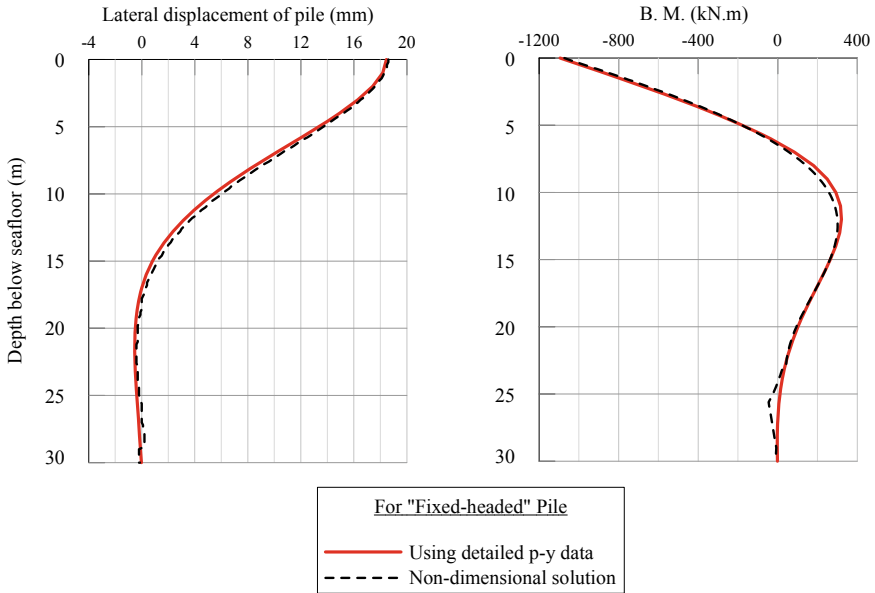


Fig. 22.4 Matching lateral displacement and bending moment for a ‘fixed-headed’, long, tubular pile of steel of diameter 1 m and wall thickness 25 mm, embedded in NC soil with s_u increasing with depth at the rate of 1 kPa/m

Table 22.2 Results of analysis

Pile dia. (m)	Pile wall thickness (mm)	Pile head restraint condition	s_u gradient (kN/m ² per m depth)	Maximum η_h value (MN/m ³)	Minimum η_h value (MN/m ³)
1.0	25	Free	1	0.42	0.09
1.0	25	Fixed	1	0.40	0.07
1.0	25	Free	2	0.57	0.13
1.0	25	Fixed	2	0.59	0.12
2.0	50	Free	1	0.37	0.08
2.0	50	Fixed	1	0.36	0.07
2.0	50	Free	2	0.56	0.12
2.0	50	Fixed	2	0.59	0.11

significantly higher lateral displacement, the applicable η_h value is much smaller. Some important results of analysis are presented in Table 22.2.

It may be noted that the minimum equivalent value of η_h in Table 22.2 was determined for a pile displacement of approximately 20% of the pile diameter. It was also found that the value of η_h does not change insignificantly with changes in pile wall thickness. Thus, it was observed that the value of η_h was mainly dependent on

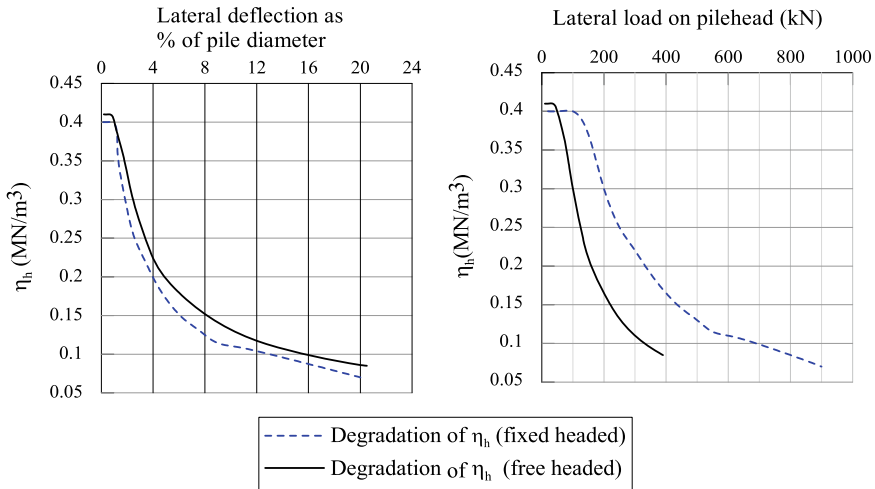


Fig. 22.5 Degradation of η_h value with increasing lateral loads for a pile of diameter 1 m embedded in NC clay with increasing s_u gradient of 1 kPa per meter depth

pile diameter, load level and the soil profiles. Values of η_h increase with increasing s_u gradient.

Results of analysis for maximum BM and displacement using the method recommended by Indian standard code [6] were also verified for some cases. Results match quite well when calibrated values of η_h are used. This is demonstrated with an example for the steel pipe pile of 1 m diameter with 25 mm wall thickness which is embedded in NC clay with increasing s_u gradient of 1 kPa per meter depth. Calculation is first carried out for 20 kN lateral load for a fixed-headed pile. For this case, analysis using detailed ‘ p - y ’ analysis shows that the maximum BM at pile head is 100 kN m where the lateral displacement is 1.56 mm. Now, using the method as given in Indian standard code [6], stiffness factor is found to be 5.4 when using calibrated value of η_h as 420 kN/m³. The pile’s moment of inertia of the cross section is 0.009105403 m⁴. Therefore, the calculated displacement using the method recommended by the code is found to be 1.5 mm and the maximum BM at pile head is 99.6 kN m. Compared with corresponding values calculated by carrying out detailed analysis using ‘ p - y ’ curves, the match is almost exact. Similarly, for quick calculation of displacement and BM for other loads, appropriate value of η_h should be considered using degradation curves as shown in Fig. 22.5. For example, when the pile mentioned above is subjected to a lateral load of 200 kN, stiffness factor is 5.8 for the calibrated value of η_h as 300 kN/m³. Maximum displacement and BM are calculated as 17.8 mm and 1066 kN m. Corresponding values of lateral displacement and BM, when calculated by carrying out detailed analysis using ‘ p - y ’ curves, are found to be 18.5 mm and 1094 kN m showing quite reasonable match.

Conclusion and Recommendation

An attempt was made to compare the results of detailed analysis of laterally loaded steel tubular piles embedded in normally consolidated clay using nonlinear ' p - y ' data with analyses using single (equivalent) values of η_h . The purpose of the study was to make it possible for reliable assessment of lateral displacement and bending moment of piles relatively quickly, using simplified approaches using appropriate values of η_h . The recommended values of η_h were calibrated with the ' p - y ' data for static loading generated by using API RP2GEO [5] method for soft clay. The results are summarized below:

1. Results of analysis using subgrade approaches for laterally loaded piles, where an equivalent value of η_h is to be used, are highly sensitive to the input value of η_h .
2. The appropriate η_h values for steel tubular piles of diameter 1–2 m embedded in NC clay profiles near seafloor with s_u gradient in the range of 1–2 kPa/m depth are found to be in the range of 0.59–0.07 MN/m³ corresponding to lateral displacement of pile starting from very small value up to 20% of pile diameter.
3. Apart from soil profile, the value of η_h is also dependent on pile diameter. However, it is found that the equivalent value of η_h is not significantly dependent on the pile wall thickness.
4. The maximum value of η_h is applicable for lateral displacement of pile in the elastic range, typically, where lateral displacement is within about 1% of pile diameter. It is also observed that for small displacement of pile, maximum applicable value of η_h is higher for piles with smaller diameter compared to piles with higher diameter.
5. Value of η_h degrades rapidly when pile lateral displacement exceeds about 1% of diameter and degrades at a slow rate at relatively large displacement of pile.

The study shows that for piles embedded in NC clays, relatively simplified solutions using the 'subgrade approach' match quite well with the results obtained by using detailed ' p - y ' data if appropriate equivalent values of η_h are used. Nevertheless, the detailed analysis using nonlinear ' p - y ' curves (appropriate for pile, soil and loading condition) is a more reliable choice, especially, when dealing with non-uniform pile properties and non-uniform variation of soil properties along the pile length.

Results presented in the paper are based on analyses carried out using static ' p - y ' data. Similar analysis may be carried out using cyclic ' p - y ' data to derive 'ready to use' equivalent value of η_h appropriate for soil, pile and load combinations.

Acknowledgements The author is grateful to ONGC for permission to publish the paper. Views expressed in the paper are author's own and not necessarily those of ONGC.

References

1. Poulos HG, Davis EH (1980) *Pile foundation analysis and design*. Wiley, New York
2. Reese LC, Matlock H (1956) Non-dimensional solution for laterally loaded piles with soil modulus assumed proportional to depth. In: *Proceedings of eighth Texas conference on soil mechanics and foundation engineering*, University of Texas, Austin
3. Matlock H, Reese LC (1960) Generalized solutions for laterally loaded piles. In: *Journal of the soil mechanics and foundations division, ASCE*, vol 86, SM5, pp 63–91
4. Matlock H (1970) Correlations for design of laterally loaded piles in soft clay. In: *Proceedings of the offshore technology conference*. OTC Paper No. 124, pp 577–594
5. American Petroleum Institute: *Geotechnical and Foundation design Considerations*, ANSI/API RP 2GEO. 1st edn. API, Washington, DC (2011, Addendum 1, 2014)
6. IS 2911 (Part 1/Sec 3) (2010) *Design and construction of pile foundations—code of practice, part 1, concrete piles, section 1 driven cast in-situ concrete piles, second revision*, Bureau of Indian Standards, New Delhi

Chapter 23

An Overview of Large Capacity Pile Load Test: A Case Study



B. Vani and Madan Kumar Annam

Introduction

In recent years, large capacity piles (bigger diameter and deeper length) are widely used in infrastructure projects to support heavily loaded structures such as expressway, railway bridges, long-span viaducts, high-rise buildings, large infrastructure projects and offshore structures. Large diameter piles have its advantages of high-load transferring ability with smaller deformation and convenient in construction practices. Large capacity piles usually preferred in offshore structures due to its high vertical and lateral load carrying capacity.

Initial load tests have to be carried out for such large capacity piles to validate design assumptions. Application of load using kentledge with concrete blocks or with reaction piles is usual practice for conducting initial pile load tests on land [1]. However, conducting initial pile load tests in marine environment is highly challenging. It is hence piles used for marine structures usually tested nearshore by simulating marine conditions as required in project design requirements. The test pile was installed through already inserted large-diameter casing (i.e., external casing). Large-diameter casing is retrievable, and it was terminated at design scour level [2]. Further, test pile was installed through the already installed external casing, and this simulates marine condition on land. Hydraulic rig having suitable drilling tools was used to install external and internal casings. Annual space created between external and internal casing forms marine conditions. Reaction piles with a connecting frame setup were used to conduct the initial pile load test. Objective of this paper is to illustrate the executional challenges and brief illustration on the observed results.

B. Vani (✉) · M. K. Annam
Keller Ground Engineering India Pvt Ltd., Kodambakkam, Chennai, India
e-mail: vani@kellerindia.com

M. K. Annam
e-mail: madankumar@kellerindia.com

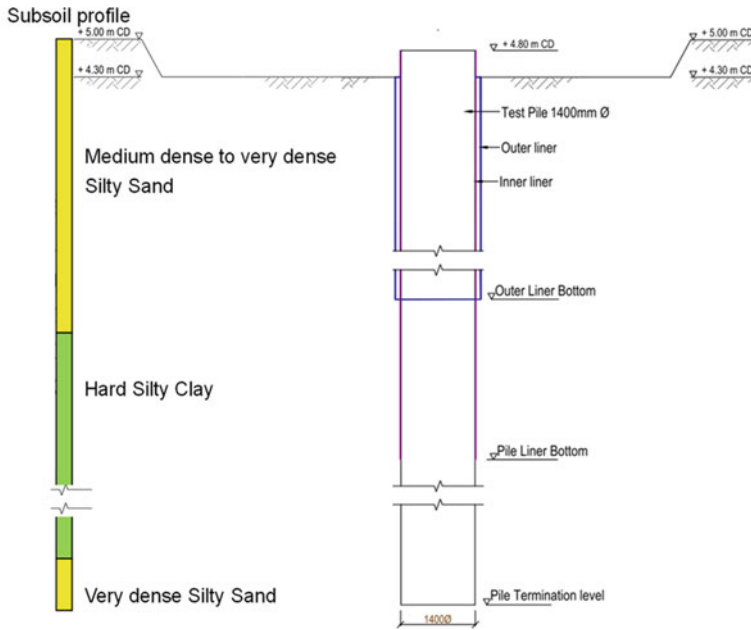


Fig. 23.1 Simulation of marine condition using large-diameter steel liner

Load Test Arrangements

Simulation of Marine Conditions

Logic to simulate marine conditions on land is to create annular space around the test pile to a depth of design scour level. Actual diameter of test pile is usually smaller than the outer casing. The test pile having sacrificial casing shall be inserted through already installed large-diameter casing. This will ensure no skin friction is mobilized for the test pile till the design scour level. This arrangement replicates freestanding length of working pile of marine structure on land (i.e., at test location). In the present case, diameter of test pile is 1.4 m, whereas diameter of outer casing is 1.6 m. The external and internal casings were installed in such a way that there is no skin friction mobilized to a depth of 24 m below the existing ground level. Figure 23.1 shows simulation of marine condition of test pile with external casing and subsoil profile.

Reaction Piles and Frame

A reaction frame capacity of 3600 T was supported by four large-diameter reaction piles of each 1500 mm diameter with uplift capacity of 900 T. The reaction frame

setup was arranged in such a way that the secondary beams will pull up the reaction piles which in turn exert reactions on the primary beam and then to test pile. Thus, the required compression load will be applied on the test pile. Layout plan of reaction pile load test is shown in Figs. 23.2 and 23.3.

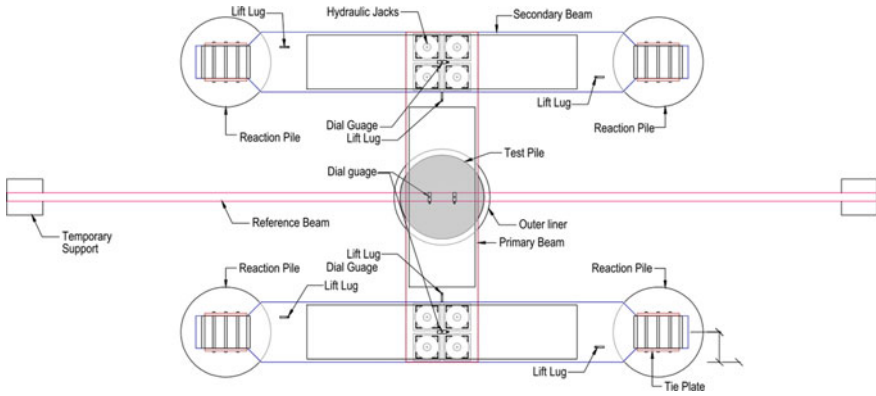


Fig. 23.2 Test pile, reaction pile and load test setup



Fig. 23.3 Actual load test setup at site



Fig. 23.4 Bentonite tank setup

Best Practices

Borehole Stabilization

Borehole stability is the major challenge of pile installation activity through thick sand layers. In addition, stabilizing large-diameter pile bores in presence of high groundwater table especially in the permeable strata is another challenge. Piles were installed using hydraulically operated rotary machines where augers and cutting buckets were suitably selected, for installation of external and internal casings. A good-quality bentonite slurry circulating system is required to address borehole stability. Key parameters like specific gravity, viscosity, sand content and saturation time are to be ensured. The established bentonite tank setup is presented in Fig. 23.4.

Adequately matured bentonite mud prepared in potable water was used for stabilizing the borehole. The mud was supplied at top of the casing during the boring process, and borehole was topped up cautiously while lifting the cutting tool. Additional hydrostatic pressure was created by creating bentonite pond contained around the pile. Refilling of fresh bentonite slurry is continuously supplied to the pond while lifting of the cutting tool as illustrated in Fig. 23.5. Positive hydrostatic pressure was maintained always in the pile bore to avoid bore collapse.

Rate of Drilling

Rate of drilling plays important role in avoiding borehole collapse. This is one of the major reasons for borehole collapse. Rate of drilling was regulated while pile boring (up to 75% in normal soil and up to 50% in sandy strata) in this project. Slow drilling rate was adopted to minimize borehole collapse. Simultaneously, lifting and driving speed of Kelley is also controlled in order to reduce borehole stability. Drilling progress using hydraulic rig with bentonite containment bund is shown in Fig. 23.6.



Fig. 23.5 Ponding of drilling mud



Fig. 23.6 Drilling of boreholes using hydraulic rig

Base Cleaning

The boring process normally allows mixing of loosened sand and silt fractions which mixes with bentonite. This mixing is relatively lesser while progressing of bore with auger rather cutting bucket. Since fresh bentonite slurry was supplied from top of

the casing, certain amount of loosening of soil below the groundwater table will happen and hence contamination of soil with stabilizing fluid is expected. The soil particles are expected to settle at the bottom pile bore from the contaminated fluid. In addition, intrusion of saline water reduces the thixotropic property of bentonite slurry which in turn affects the viscosity of the fluid. The quality of stabilizing fluid gradually decreases due to all these factors, while advancing to deeper depths. Base cleaning was appropriately carried out after deploying cleaning buckets once drilling is reached to its termination level. Borehole cleaning was taken place after lowering of reinforcement and tremmie pipes. Flushing operation was also carried out till the slurry parameters satisfies technical specifications.

Pile Load Test

Pile load test was conducted in accordance with the stipulations suggested in IS 2911 Part 4-2013 [1]. About 20 mm settlement was observed at a load of about 2000 T, and pile was not loaded up to the failure due to technical snatches occurred in hydraulic loading jack. Leakage was observed in one of the hydraulic jack hoses at 200% load increment, and test could not be continued. Differential ram lifts were observed at both ends, and attempt was made to place steel plates. Reaction piles were intact, and an uplift movement less than 5 mm was recorded. It is evident from the observations that the pile behaved well up to 200% load and rate of settlement was relatively significant (Fig. 23.7).

Hyperbolic curve fitting as suggested by Chin [3] is used to extrapolate load carrying capacity of the test pile. A linear trend line equation has been arrived for the extrapolation of pile load–settlement response toward the final loading increment, but limited to lower-bound load of about 2250 T. Hyperbolic method of estimation of pile capacity is presented in Fig. 23.8.

Summary and Conclusions

Maintaining high quality of installation of large diameter pile is discussed. It is essential to concentrate on important aspects such as quality of drilling fluid, hydration time of bentonite slurry, maintaining positive bentonite fluid head, slow drilling rate in sand, slow lifting and driving speed of Kelley and appropriate base cleaning. Operational excellence with best practices delivers the high quality, while ensuring good quality of pile is built. Successful installation and testing of large diameter pile are discussed by simulating marine condition. It is seen from the pile load test result that the installed pile performed well. Chin method suggested reasonable pile capacity.

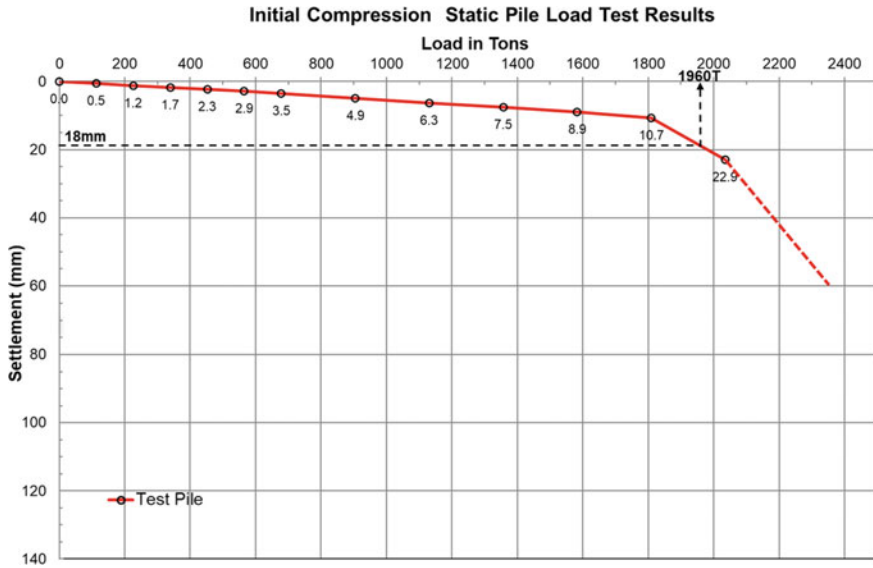


Fig. 23.7 Graph showing load versus settlement

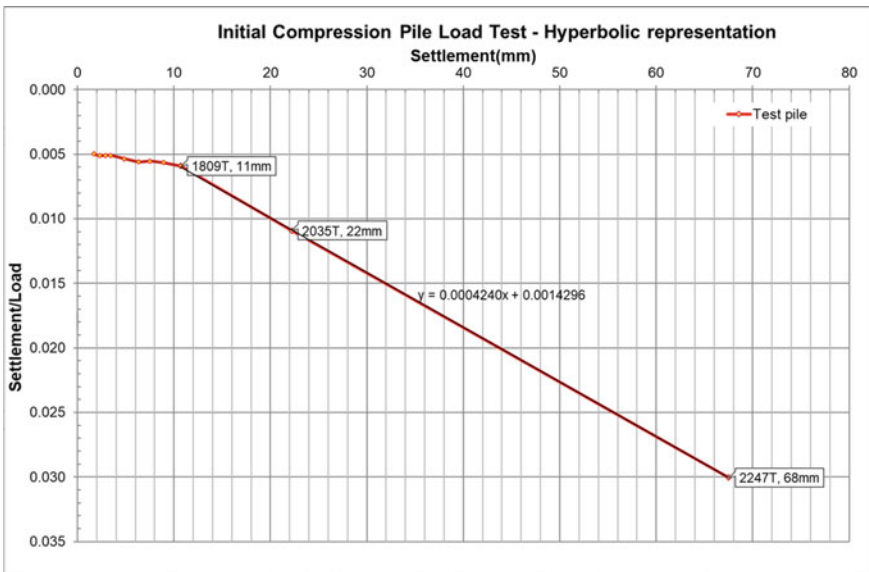


Fig. 23.8 Hyperbolic extrapolation for the initial static load test

Acknowledgements The authors acknowledge with gratitude to Keller management for their continuous support and encouragement in finalization of theme of this paper. Appreciations to other colleagues who have helped the authors in compilation of the paper. Thanks also to Keller India site management for providing photographs, execution and monitoring data.

References

1. IS: 2911 (Part 4)-2013, Code of practice for design and construction of pile foundations—load tests on piles
2. IS: 2911 (Part 1-sec 2)-2010, Bored cast—in-situ concrete piles (second revision)
3. Chin FK (1972) The inverse slope as a prediction of ultimate bearing capacity of piles. In: Proceeding's 3rd Southeast Asian conference on soil engineering, pp 83–91

Chapter 24

Influence of Soil Cover on Lateral Response of Rock-Socketed Piles



C. R. Neeraj , K. T. Saikumar , and Sudheesh Thiyyakandi 

Introduction

Large diameter bored piles or drilled shafts socketed into the bedrock, also known as rock-socketed shafts/piles, are widely adopted to resist both axial and lateral loads from structures like high-rise building, bridges, industrial buildings, transmission lines, etc. [1–8]. The analytical methods, such as p - y method [9, 10] and elasto-plastic solutions [11, 12], are generally used for the lateral analysis of rock-socketed piles. Apart from the analytical solutions, the finite element method (FEM) is used as an efficient tool to simulate the behavior of laterally loaded rock-socketed piles. Even though several researchers have studied the lateral response of drilled shafts embedded in soil through FE modeling by considering different soil models such as elastic continuum [13], elasto-plastic [14], and Mohr–Coulomb [15] models, such FEM studies on laterally loaded rock-socketed pile are rather limited.

A 3D FEM study on the load transfer mechanism of rock-socketed pile subjected to lateral load by assuming rock as modified Drucker–Prager material was reported by Yang and Liang [16]. Singh et al. [7] investigated the combined axial and lateral load response of rock-socketed piles by performing FE analyses. However, the past studies have not addressed the influence of various important parameters such as socket length, embedment depth in soil, and total pile depth, and especially their combined effect. Very recently, Prakash and Muthukkumaran [4] presented a comprehensive

C. R. Neeraj (✉) · K. T. Saikumar (✉) · S. Thiyyakandi (✉)
Department of Civil Engineering, Indian Institute of Technology Palakkad, Palakkad,
Kerala 678623, India
e-mail: 102004006@smail.iitpkd.ac.in

K. T. Saikumar
e-mail: 101902012@smail.iitpkd.ac.in

S. Thiyyakandi
e-mail: sudheesh@iitpkd.ac.in

lab-scale experimental study using instrumented model piles installed in a layered soil-rock profile. Their study focused on the influence of the length of socket and the diameter of pile on the lateral response of rock-socketed piles. It is often intuitively assumed that the socket length plays a major role in load resistance. Ideally, when the hard stratum is available at a shallow depth, the piles are socketed into the hard rock up to a minimum depth of 1 to 3 times the diameter (D) of pile. However, if the depth of availability of hard rock is high, socketing pile into the rock stratum may lead to uneconomical design. In such commonly encountered field scenario, the contribution of lateral resistance from the soil layer(s) above the hard rock becomes significant [4]. Therefore, the length of embedment of pile in the soil layer(s), termed as ‘soil cover’ plays a key role in design of rock-socketed pile.

A detailed literature survey revealed that the influence of depth and shear strength parameters of the soil cover on the lateral load response of rock-socketed piles is not extensively studied in the past. In this work, a finite element (FE) model of rock-socketed pile was created in ABAQUS to specifically study the influence of soil cover on the lateral load response. The model was initially validated using an experimental study found in literature. The detailed description of the FE model and the parametric study is presented in subsequent sections.

Model Validation

A full-scale lateral load testing of drilled shafts fully socketed in rock reported by Yang et al. [17] was used to validate the 3D FE model in ABAQUS. The test was conducted in Dayton, Ohio, USA, where the subsurface condition was characterized as gray shale inter-bedded with limestone. The schematic diagram of experimental model and the rock properties used for the validation are presented in Fig. 24.1 and Table 24.1, respectively. The cohesion and friction angle of the rock masses were obtained from the unconfined compression test results using the correlations given by Yang and Liang [16].

The rock mass was modeled as Mohr–Coulomb material and the pile (diameter, $D = 1.83$ m and socket length, $L_s = 5.5$ m) as linearly elastic material with a Young’s modulus of 26.4 GPa and Poisson’s ratio of 0.15. The interface between the rock mass and the pile was modeled using constitutive relation based on surface-based contact. The pile and the rock surfaces are treated as master and slave surfaces, respectively. A

Fig. 24.1 Schematic representation of experimental model [16]

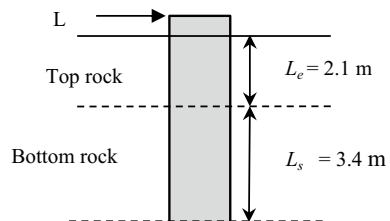


Table 24.1 Rock properties used for validation [17]

Parameter	Top rock layer	Bottom rock layer
Cohesion (KPa)	1062	1731
Friction Angle (°)	20	27
Young’s modulus (MPa)	1662	4068
Poisson’s ratio	0.3	0.3
Effective unit weight (kN/m ³)	19	19
Rock type	Soft gray shale, slightly weathered to decomposed, laminated with limestone	Medium gray shale, slightly weathered, laminated with hard limestone

frictional coefficient of 0.5 was adopted in the tangential direction along the interface based on a ϕ value of 27° for the bottom rock layer [16]. In the normal direction, the surfaces do not transmit contact pressure until the nodes of slave surface comes in contact with the master surface. When the surfaces are in contact, there is no limit set to the contact pressure transmitted in the normal direction [18]. The bottom face of the rock mass was fixed in all directions while the normal fixity was assigned to the vertical faces. The rock mass was meshed using eight-noded brick elements, C3D8R, adopting structure mesh control with a global mesh size of 0.25 m. Finer mesh using biased seeding option was applied up to a lateral distance of $2/3 D$ from the pile face for better results. Pile was discretized by the second order 15-noded triangular prism elements, C3D15. The meshed model of rock mass with socketed pile is shown in Fig. 24.2. First, the gravitational field was applied to entire system, and subsequently, the lateral load was applied in increments up to a maximum load of 2000 kN.

Fig. 24.2 Discretized model

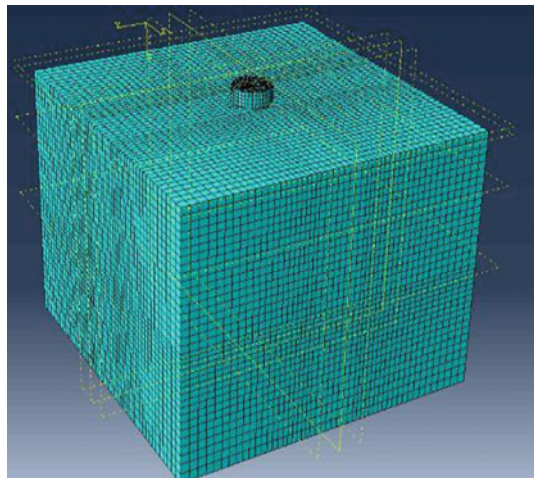


Fig. 24.3 Comparison of FE results with the experimental load–displacement response

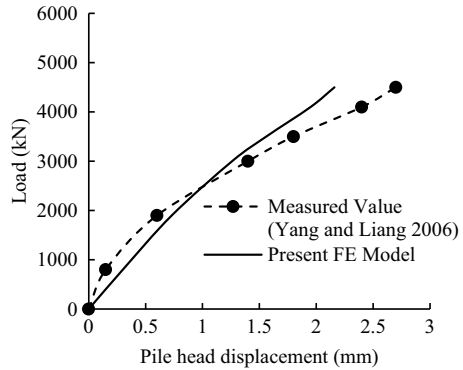


Figure 24.3 compares the lateral load versus displacement response obtained from the present FE analysis with the experimental results reported Yang et al. [17]. It can be observed that the FE result was in reasonable agreement with the measured field response.

Parametric Study

Influence of Soil Cover Length

The influence of the length of embedment in soil on the lateral response of rock-socketed piles was investigated through a parametric analysis of FE model developed in this work. More than 30 FE models were analyzed by varying the geometric parameters like soil cover, socket length, pile length and the shear strength parameters of the soil cover. The results of the parametric study are discussed in this section. Here, L_e , refers to the length of embedment in soil or the soil cover height; L_s refers to the socket length; and L , denotes the length of pile. For the convenience of comparison, L_e and L_s are expressed in terms of the diameter of pile. An overhanging pile length of 0.6 m was considered in all the models. The diameter of piles was kept constant as 1.2 m. Table 24.2 shows the properties used for the parametric study which were taken referring to the past studies [7, 17].

Case 1: Varying Soil Cover; Constant Socket Length

To study the influence of the length of the soil cover (L_e) independently, the socket length of the pile was kept constant as three times the diameter of pile ($L_s = 3D$) and three specific cases of $L_e = 2.5D, 4D,$ and $5D$ were considered for the analysis. Note that the length of pile (L) varies as L_e changes. The schematic representations of the models are shown in Fig. 24.4. All other parameters were kept constant and the load–displacement plots were generated using the FE models.

Table 24.2 Properties adopted for the parametric study

Properties	Rock	Soil
Unit weight (kN/m ³)	19	18
Cohesion (kPa)	1062	5
Friction angle	20	30
Poisson's ratio	0.3	0.3
Young's modulus (MPa)	1662	30

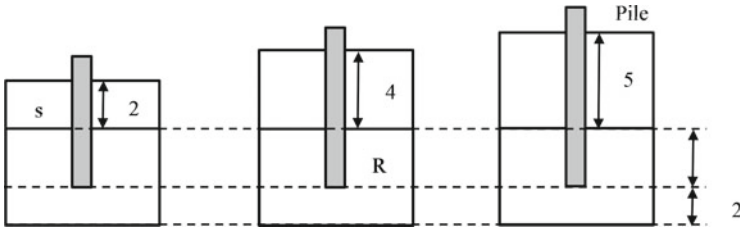


Fig. 24.4 Schematic representation of the models with varying soil cover and constant socket length

The lateral load versus displacement response for different L_e is depicted in Fig. 24.5a. It can be observed that for a constant socket length (L_s), the lateral deflection increases with the increase in soil cover length (L_e). This can also be attributed to the increase in the total pile length (L). Figure 24.5b shows the lateral displacement along the pile length for each case. The pile deflection along the socket length, i.e., lower $3D$ of the pile, was found to be negligible. In case of $L_e = 2.5D$, more than half of the embedment was within rock and the socketing was effectively arresting the lateral deflection of the pile. Even though the pile was short ($L = 5.5D$), it was exhibiting a flexural behavior (bending) due to the restraining effect from the socketed portion in contrast to a rigid body rotation in case of pile fully embedded in soil. As the thickness of soil cover increases, the depth of fixity increases and most of the lateral load has to be resisted by the portion of pile embedded in the soil. It is clearly evident that the allowable lateral load for a given serviceable displacement was significantly influenced by the thickness of soil cover although socket length was the same.

Case 2: Constant Soil Cover; Varying Socket Length

To investigate how the influence of soil cover varies when the socket length changes, analyses were carried out with different socket lengths ($1D$, $2D$, $3D$, and $5D$). The material properties used for modeling were the same as that given in Table 24.2. The lateral load versus displacement responses corresponding to different L_s for $L_e = 2.5D$ and $4D$ are presented in Fig. 24.6a, b, respectively. It is evident from the figures that for a constant soil cover height, lateral resistance under a given lateral deflection increases substantially as L_s increases from 1 to $2D$ and then marginally

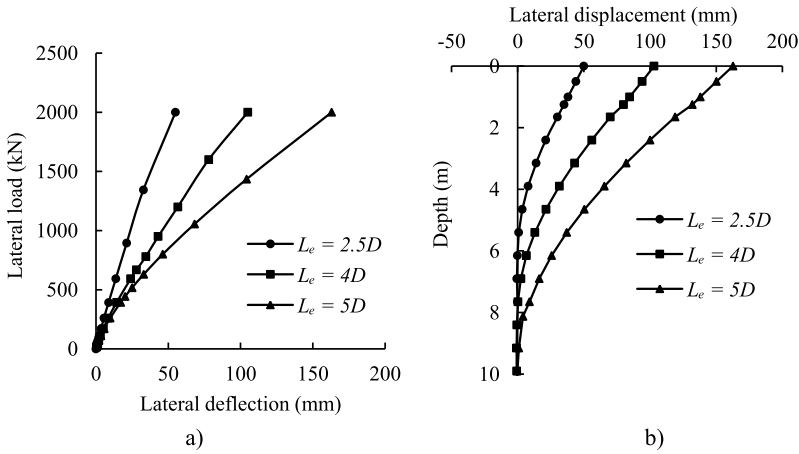


Fig. 24.5 a Lateral load–displacement responses; b lateral displacement profile for varying L_e and constant $L_s = 3D$

up to $L_s = 3D$. However, the increase in lateral resistance was negligible with the further increase in socket length ($>3D$). The rate of increase was found to be relatively higher at smaller soil cover thickness (L_e). It can be inferred that the thickness of soil cover plays a determining role rather than the socket length.

Case 3: Constant Pile Length, Varying L_e/L_s Ratio

In all the previous analyses, the total length of pile was a varying parameter. To eliminate the influence of varying pile length (L) and to study the effect of the ratio of soil cover thickness to the socket length (L_e/L_s) on the lateral response, additional analyses with constant L and varying L_e/L_s ratio have been performed (Fig. 24.7).

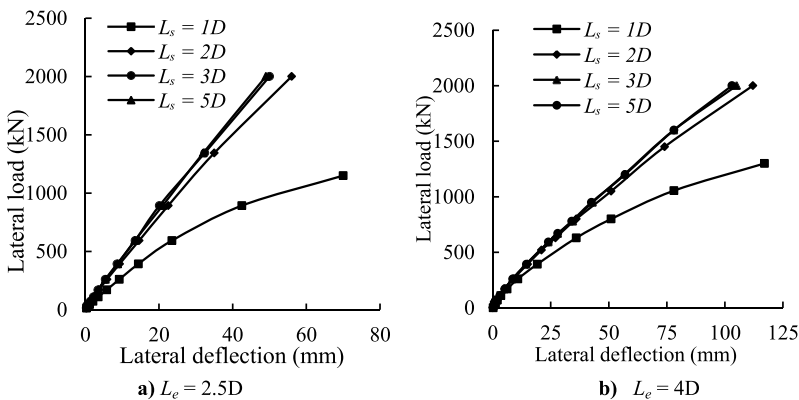


Fig. 24.6 Lateral load–displacement responses for different L_s cases

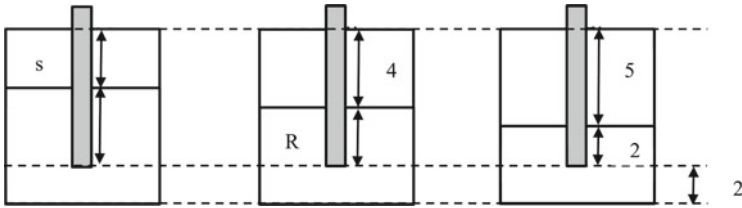
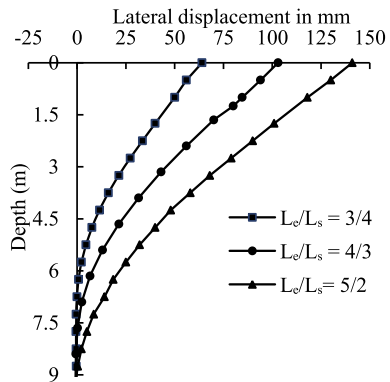


Fig. 24.7 Schematic representation of models with constant pile length and varying L_e/L_s ratio

Note that in these cases, an increase in soil cover brings a corresponding reduction in the socket length as L is constant.

The lateral deflection profile of piles with different L_e/L_s ratios is presented in Fig. 24.8. For a given pile length, the pile deflection was found to increase with an increase in L_e/L_s ratio. For lower L_e/L_s ratio ($3/4$), the pile displacement ceases to zero at the soil-rock interface due to the restraining effect of the socketed portion of pile. As the L_e/L_s ratio increases, a tendency for the piles to rotate (short pile behavior) instead of bending was observed. In such cases (e.g., $L_e/L_s = 5/2$), portion of pile socketed in rock was seen to rotate opposite to the direction of loading. The same can also be observed from Fig. 24.9, which presents the cross-sectional view of the models during the loading for the above mentioned cases. This reinstates the previous observations from Case 1 and Case 2 that when the height of soil cover is high (usually encountered in the field), the effect of socket length is less significant and the embedment length in soil becomes the prominent factor.

Fig. 24.8 Lateral displacement profiles for constant pile length cases



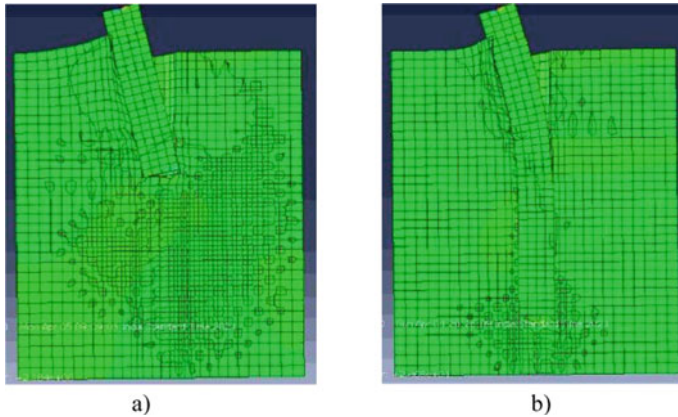


Fig. 24.9 Lateral deformation of pile **a** $L_e/L_s = 5/2$ and **b** $L_e/L_s = 3/4$

Sensitivity of Shear Strength Parameters on the Influence of Soil Cover

The sensitivity of shear strength parameters on the observed influence of soil cover on the lateral load response was also investigated. Additional analyses have been carried out by varying the strength parameters (cohesion and angle of internal friction) and keeping all other parameters including geometry identical. In all the analyses, unit weight, Young's modulus and Poisson's ratio of the soil cover were taken as 18 kN/m^3 , 45 MPa , and 0.2 , respectively. The bottom rock layer properties given in Table 24.1 [16] were adopted for the rock mass. The analyses by varying the shear strength parameters were carried out for the following two sets of geometric scenarios: (i) $L = 8D$; $L_e = 3D$; $L_s = 5D$ and (ii) $L = 5D$; $L_e = 3D$; $L_s = 2D$. It should be noted that the height of soil cover ($L_e = 3D$) was the same in both scenarios.

Figure 24.10 presents the lateral deformation profiles obtained from the analyses with varying soil shear strength parameters. As expected, lateral displacement decreases with the increase of cohesion and friction angle of soil cover. However, the rate of reduction in displacement decreases with the increase of the shear strength parameters. It can be seen that the variation in pile head displacement with cohesion or friction angle was nearly the same for both geometric scenarios owing to the same soil cover height. In other words, the influence of soil cover thickness on the lateral response of pile was found to be independent of the shear strength parameters.

Summary and Conclusions

A finite element model of rock-socketed pile was developed in this work to study the influence of soil cover on the lateral response. The FE model was validated using an

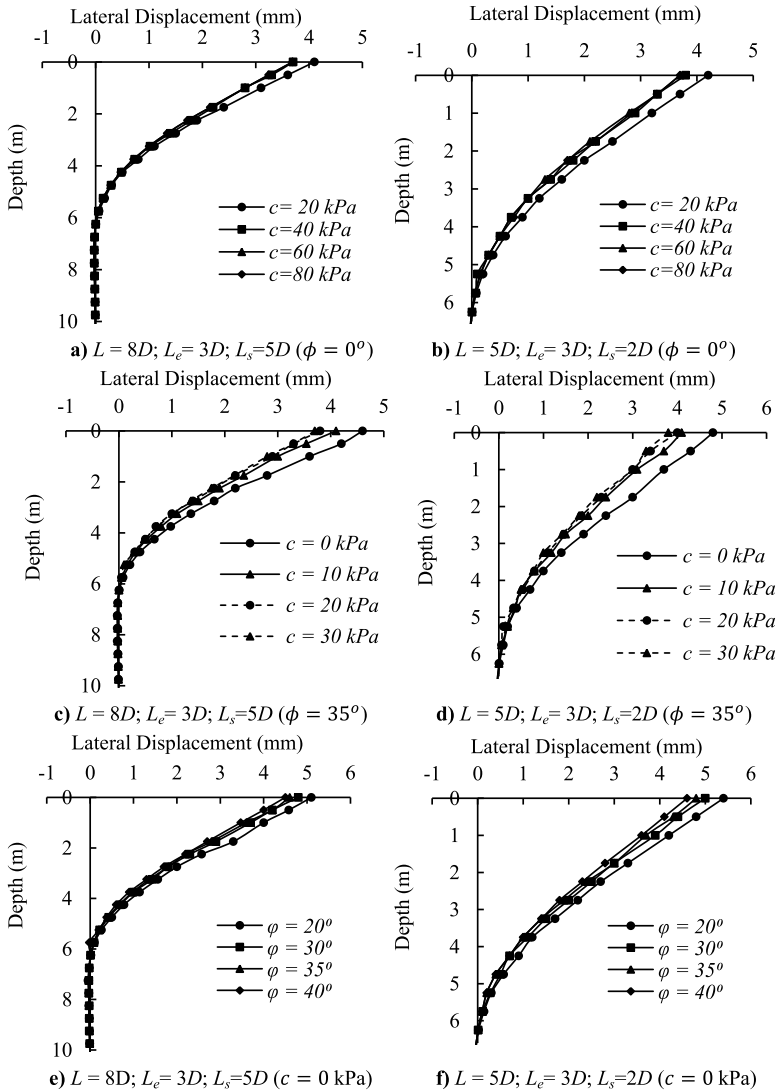


Fig. 24.10 Variation of lateral displacement with shear strength parameters of soil cover and pile length

experimental study found in literature. A detailed parametric study was conducted and the following specific inferences were made.

- The length of embedment of pile in soil (L_e) is found to have significant effect on the lateral response of rock-socketed piles. For a constant socket length, the allowable lateral load at a given displacement decreases with increase in the height of soil cover.

- The socket length is observed to have considerable influence up to a limiting value ($\approx 3D$ in the present study) and beyond that the effect is practically negligible. The influence of socket length is more pronounced at smaller soil cover thickness (L_e). Therefore, merely increasing the socket length does not guaranty an increase in the lateral resistance.
- When a minimum socket length of $3D$ is provided, all the piles, irrespective of the length, are displaying a flexural response due to the bottom restraining effect offered by the socketed portion. However, with the decrease in socket length (or increase in L_e/L_s ratio), the piles are found to exhibit a rotational mode of movement.
- The influence of soil cover depth on the lateral load response is observed to be insensitive to the shear strength characteristics of the soil.

In general, the geometric parameters, viz., soil cover depth, socket length and ratio of soil cover to socket length are found to have determining effect on the lateral response of rock-socketed pile.

References

1. Cole KW, Stroud MA (1976) Rock socket piles at coventry point, market way, coventry. *Geotechnique* 26(1):47–62. <https://doi.org/10.1680/geot.1976.26.1.47>
2. McVay MC, Townsend FC, Williams RC (1992) Design of socketed drilled shafts in limestone. *J Geotech Eng* 118(10):1626–1637. [https://doi.org/10.1061/\(ASCE\)0733-9410\(1992\)118:10\(1626\)](https://doi.org/10.1061/(ASCE)0733-9410(1992)118:10(1626))
3. O'Neill MW (2001) Side resistance in piles and drilled shafts. *J Geotech Geoenviron Eng* 127(1):3–16
4. Prakash AR, Muthukkumaran K (2021) Estimation of lateral capacity of rock socketed piles in layered soil-rock profile. *Int J Geo-Eng* 12(1):1–15
5. Radhakrishnan R, Leung CF (1989) Load transfer behavior of rock-socketed piles. *J Geotech Eng* 115(6):755–768. [https://doi.org/10.1061/\(ASCE\)0733-9410\(1989\)115:6\(755\)](https://doi.org/10.1061/(ASCE)0733-9410(1989)115:6(755))
6. Rosenberg P, Journeaux NL (1976) Friction and end bearing tests on bedrock for high capacity socket design. *Can Geotech J* 13(3):324–333. <https://doi.org/10.1139/t77-013>
7. Singh AP, Bhandari T, Ayothiraman R, Rao KS (2017) Numerical analysis of rock-socketed piles under combined vertical-lateral loading. *Procedia Eng* 191:776–784. <https://doi.org/10.1016/j.proeng.2017.05.244>
8. Williams AF, Johnston IW, Donald IB (2002) The design of socketed piles in weak rock. In: *Proceedings of international conference on structural foundations on rock*, Sydney, Australia, pp 327–347. <http://worldcat.org/isbn/9061910730>
9. Gabr M (1993) Analysis of laterally loaded shafts in rock-discussion. *J Geotech Eng-ASCE* 119(12):2015–2018
10. Reese LC (1997) Analysis of laterally loaded piles in weak rock. *J Geotech Geoenviron Eng* 123(11):1010–1017
11. Carter JP, Kulhawy FH (1992) Analysis of laterally loaded shafts in rock. *J Geotech Eng* 118(6):839–855. [https://doi.org/10.1061/\(ASCE\)0733-9410\(1992\)118:6\(839\)](https://doi.org/10.1061/(ASCE)0733-9410(1992)118:6(839))
12. Zhang L, Ernst H, Einstein HH (2000) Nonlinear analysis of laterally loaded rock-socketed shafts. *J Geotech Geoenviron Eng* 126(11):955–968. [https://doi.org/10.1061/\(ASCE\)1090-0241\(2000\)126:11\(955\)](https://doi.org/10.1061/(ASCE)1090-0241(2000)126:11(955))
13. Randolph MF (1981) The response of flexible piles to lateral loading. *Geotechnique* 31(2):247–259

14. Wakai A, Gose S, Ugai K (1999) 3-D elasto-plastic finite element analyses of pile foundations subjected to lateral loading. *Soils Found* 39(1):97–111. <https://doi.org/10.3208/sandf.39.97>
15. Wallace JW, Fox PJ, Stewart JP, Janoyan K, Tong Q, Lermite SP (2002) Cyclic large deflection testing of shaft bridges part II: analytical studies. Report from California Department of Transportation
16. Yang K, Liang R (2006) A 3D FEM model for laterally loaded drilled shafts in rock. In: *GeoCongress 2006: geotechnical engineering in the information technology age*, February, Atlanta, Georgia, USA, pp 1–6. [https://doi.org/10.1061/40803\(187\)174](https://doi.org/10.1061/40803(187)174)
17. Yang Z, Jeremić B, Liang R (2005) Study of soil layering effects on lateral loading behavior of piles. *J Geotech Geoenviron Eng* 131(6):762–770
18. Hibbitt K (1998) ABAQUS standard user's manual, Ver. 5.8 Karlsson and Sorensen, Inc., Pawtucket, RI, USA

Chapter 25

Analysis of Foundation System of the Taj Mahal



Leonardo Souza, Yeshwant Chodnekar, and Purnanand Savoikar 

Introduction

Many ancient monuments and structures are built on river banks using well foundations. The Taj Mahal is the most famous of such monuments. The foundation needs further analysis to check for safety. The science of soil mechanics was hardly known to the builders of India in the seventeenth century, but they relied on a very rich experience of heavy foundation construction based on post-performance experience of earlier foundations.

History of Taj

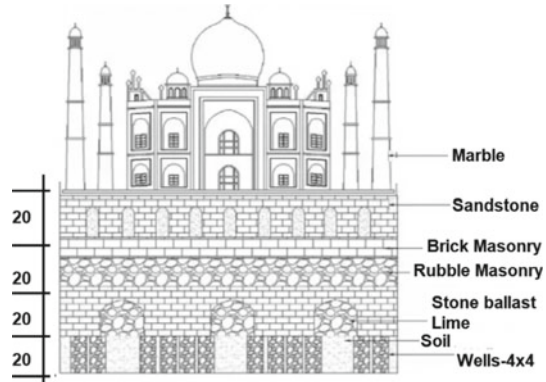
Taj Mahal is the final resting place of Queen Mumtaz-uz-Zamani niece of Emperor Jahangir, wife of Emperor Shah Jahan, and she died on June 28, 1631, while giving birth to her 14th child whither she had accompanied her husband as he marched to punish Khan Lodi the governor of Deccan. The site was purchased from Raja Jai Singh of Jaipur. Ustad Amhad Lahori designed it on the Persian holy poem describing a vision of heaven. She was finally buried here on Jan 8, 1632, at the seat of God as described therein to be joined by her husband on Feb 1, 1666 [1, 2]

L. Souza · Y. Chodnekar · P. Savoikar (✉)
Department of Civil Engineering, Goa Engineering College, Farmagudi, Goa 403401, India
e-mail: psavoikar@gmail.com

© The Author(s), under exclusive license to Springer Nature Singapore Pte Ltd. 2023
K. Muthukkumaran et al. (eds.), *Foundation and Forensic Geotechnical Engineering*, Lecture Notes in Civil Engineering 295,
https://doi.org/10.1007/978-981-19-6359-9_25

261

Fig. 25.1 Structure and foundations [3]



Structure and Foundation

It was built with stone and lime concrete and clad with thick white Macarena marble veneer from Jaipur. The $284.4 \times 98.4 \times 20$ m high plinth is clad with red sandstone from Fatehpur Sikri (Fig. 25.1).

The whole structure rests on firm rubble masonry supported on brick piers sunk at close intervals [1, 4]. FEM structural analysis using superelement structural analysis module (SESAM) of the superstructure gave factor of safety of the order of 4–8 [5]. A 3D seismic analysis of the Taj Mahal structure was done, and it was found that the bending stresses would have been smaller for soft base as compared to fixed base condition [6].

Yet there is constant danger because the structure and foundations have been analyzed not considering their previous damage records.

Repeated Repairs

As it was built in a hurry, there was not enough time given for settlement and the piers acted as stone columns causing rapid consolidation settlement post construction which resulted in damages from the beginning itself as listed below.

1652—Prince Aurangzeb—leaking roof dismantled and redone. Cracks on galleries and water in seven arched underground chambers and mosque observed.

1810—Captain Taylor and Col. Hyde—cleaning and replacing of missing stones with colored chunna.

1864—Dr. Murray—replacing of flowers and marble.

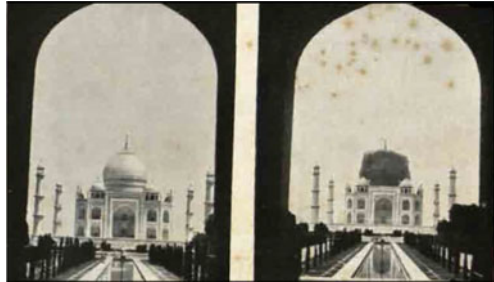
1874—Engr. Alexander—replace broken marble with Portland cement.

1921—Engr. Marshal—repairing of courtyard and surrounding walls (Fig. 25.2) [7] garden repairs.

Fig. 25.2 Repairs to Taj
1921 [8]



Fig. 25.3 Repairs to Taj
1945 [1]



1936—given to Archeological Society of India—government constitutes committee.

1941–45—recommendations received (Fig. 25.3).

1942—repairs started and completed in 1945; lots of lime plaster was used [1].

Recently, the Taj Trapezium Zone (TTZ) was created to conserve all monuments near and including three World Heritage Sites the Taj Mahal, Agra Fort and Fatehpur Sikri based on The Supreme Court of India ruling on December 30, 1996, relocating dangerous industries.

Previous Soil Investigation

The Taj has been subject to numerous studies notably by IIT Roorkee. This paper depends on data they have shared on their papers at various fora for the soil profile and properties only.

Soil Investigation by University of Roorkee [9]

Site investigation of Taj soil has already been done by IIT Roorkee; their results are given in Table 25.1.

They advanced 6 boreholes to 40 m depth in close proximity and used a 100 m borehole from CBRI Roorkee to cross-check for greater depths (Fig. 25.4).

From the data, soil profiles were drawn as shown in Figs. 25.5 and 25.6.

Rock was assumed at 90 m depth (Fig. 25.7). Alternate sand and clay layers were assumed. Maximum scour depth was estimated at 14 m below the top.

The settlement worked out by them for 350 years considering the foundation as one solid raft and ignoring the stone column drainage effect was 99.4% of 141 cm (Fig. 25.7). Hence, only 8.7 mm of settlement is expected in the next 100 years. It is safe from uniform settlement, and as substantial settlement has already taken place, any change in water table will not affect the Taj [9].

Table 25.1 Properties of soil layers [5, 9]

Property	Stratum 1 (CL-CI) clay	Stratum 2 (SP-SM) sand	Stratum 3 (CI) clay
Unit weight, γ	19.8 kN/m ³	20.0 kN/m ³	20.2 kN/m ³
Specific gravity	2.65	2.65	2.67
Undrained shear, c_u	45 kN/m ²		50 kN/m ²
Shear angle, ϕ		42°	
Young's modulus, E_s		55,000 kN/m ²	50,000 kN/m ²
Poisson's ratio, μ		0.25	0.4
Coefficient of permeability, k	2×10^{-4} mm/s	2×10^{-2} mm/s	1.5×10^{-5} mm/s

Fig. 25.4 Borehole locations [9]

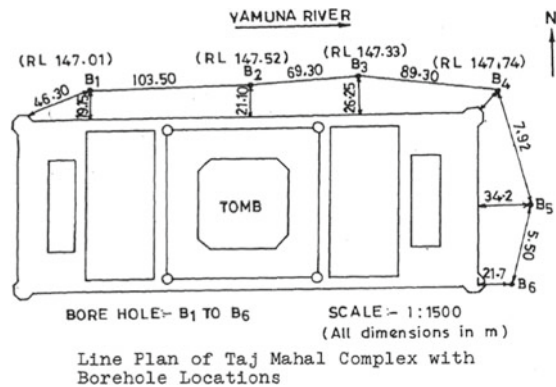


Fig. 25.5 River side profile
[9]

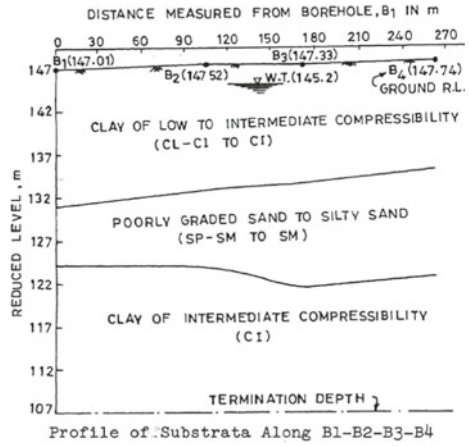


Fig. 25.6 Land side profile
[9]

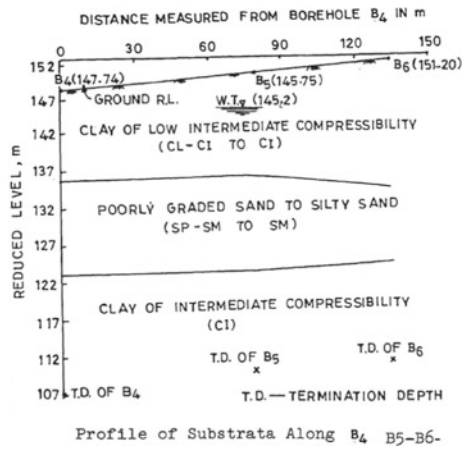
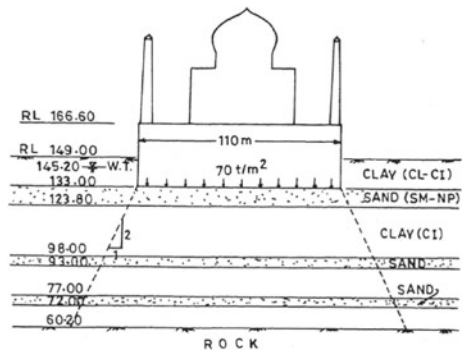


Fig. 25.7 Settlement of Taj
[9]



Previous Soil Investigation by (IIT) Roorkee University

Investigations had also been done by IIT Roorkee, previously called University of Roorkee, under Professor Handa. A tube well was dug to supply water for Taj gardens. The boring up to 441 feet (132.3 m) below ground level indicates absence of rock till this large depth [2] (Figs. 25.8, 25.9 and 25.10).

The bottom of foundations is placed on layers of wooden boxes filled with sand-stone and fine sand starting at 20 m depth and having a thickness of 7 m in between wells (Figs. 25.9 and 25.10). The platform originally meant to project 12 m above ground is today totally exposed. Each well is about 1.2 m wide.

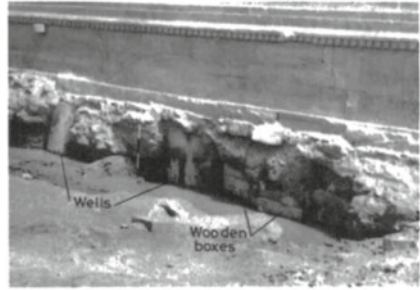
There were tilts in all four minarets: S-E minaret by 114.3 mm, N-E minaret by 48.26 mm, N-W minaret by 35.56 mm and S-W minaret 215.9 mm. In 1947, the above tilts for a height of 40 m were not dangerous. Structural weight was 12,000 tones, and structural stress on foundation was 75 MPa [3].

Fig. 25.8 Bore for tube well [3]

G.L.	Depth below G.L., (m)	Thickness in feet	Strata details
	3.00		Clay
	10.5		Clay with kankar
	15.0	2.5	Kankar
	17.5	0.75	Fine sandy clay with kankar
	20.0	2.25	Kankar
	27.0	7.00	Sand stone with fine sand
	36.0	9.00	Clay with stone
	47.5	12.25	Sand with kankar and sand stone
	64.5	18.75	Clay with kankar with sandwiched layer of sand and stone
	71.5	3	Sand stone with sand
	88.5	18.75	Clay with kankar
	100.5	14.25	Clay
	115.0	15.00	Clay with kankar and sand stone
	116.75	1.75	Fine sand
	128.5	12.00	Clay with kankar and sand stone
	135.0	2.50	Clay

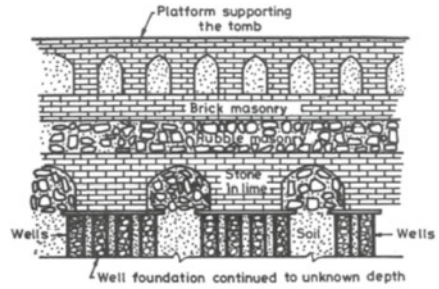
substrata through tube well at nursery near taj

Fig. 25.9 Exposed foundations [3]



Exposed well foundations and wooden boxes under North wall.

Fig. 25.10 Foundation reconstruction [3]



(Note: Drawing not to scale)
Imaginative view of foundations based upon available description

Well Foundation or Pile–Raft Foundation

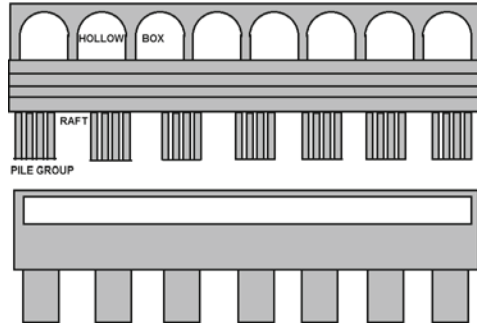
There is a dichotomy in the soil investigations of both the reports; therefore, a fresh analysis is needed and has been proposed in this paper. It can be seen from above that the foundation is exhibited as a well foundation. Each well is filled by stones that have silted over the years, so they act as piles rather than wells. The load is shared by the foundation box and the pile groups, so it is more likely a pile–raft foundation.

Analysis of Capacity of Foundation

The thick upper box foundation acts as a pile cap which is supported by a set of stone-well-piles (of dia. 1.2 m) of 4 × 4 group admeasuring 5 m width and spaced 7 m apart. As the wells are too closely placed, the wells can be designed as a pile group. [10–12] (Fig. 25.11).

$$\text{Skin friction} = (\pi \cdot \text{Avg. Diameter} \cdot \text{Length}) \cdot (\text{Cohesion} \cdot \text{Adhesion reduction factor})$$

Fig. 25.11 Piled raft foundation



$$f_s = K \cdot \sigma'_v \cdot \tan \delta$$

$$\sigma'_v = \gamma' \cdot D$$

$$Q_s = \sum f_s \cdot A_s$$

Values of D for masonry 0.90 m; values of K for sand 0.67 kN/m²; values of K for clay 0.9 kN/m²; and $A_s = \text{perimeter} \cdot \text{height} = 20$ h.

From the data presented in Table 25.2, the balance of upward pressure on masonry foundation is calculated by subtracting the load taken by the piles (of 20 m length) from the total load of the structure and dividing it with area of the raft. The upward pressure on masonry foundation works out to be 4.54 kN/m². Since the compressive strength of stone is 4 kN/m² (assumed) and the flexural strength is even less, the factor of safety for piled raft works out to be 0.88, so the foundation fails.

Table 25.2 Calculations for pile group action

Layer	Height (m)	Type	K (kN/m ²)	f_s (kN/m ²)	Q_s (kN)
1	3.0	Clay	0.90	0.2	10.3
2	10.5	Clay–Gravel	0.80	0.7	143.9
3	2.5	Gravel	0.55	150.2	7510.5
4	0.75	Sand–Gravel	0.65	168.8	2531.8
5	2.25	Gravel	0.55	178.4	8026.8
6	7.00	Sand–Quartz	0.60	241.8	33,858.3

Dangers to Foundation of Taj

Conventional analysis which was done by renowned experts shows no danger to the Taj. Pile–raft concept also shows safety in excess of what is needed. The threat to the foundations of the Taj therefore comes from another source (Figs. 25.12 and 25.13). River quality is deteriorating with pollutants, and river course is shifting [13–15].

Salts in brick masonry may come from the raw material, the subsoil or the surroundings (River Jamuna). Such harmful dissolved salts may be characterized by sodium, potassium, calcium, magnesium and ammonium cations and by anions such as sulfates, chlorides and nitrates. The greatest damage of bricks leading finally to their weathering is caused by the repeated dissolution and recreation of crystals [17–19]. In lime mortar, the lime putty gives an additional pathway for this damage [20]. This can cause brittle-collapse of the wells on the river side and hence differential settlement which can be catastrophic.

Possible ruptures (Fig. 25.14), including overall and local failure modes, could lead to sliding, toppling or overturning of the structure [21]. Already in 1945, a tilt was observed. Recent monitoring of the tilts was also carried out. A survey by ASI and UNESCO in 1985 found the tilt in each minaret had increased by 0.1 inches (0.3 cm) [22]. According to the ASI, tilt of dome center and spike center of north-east minaret in 2011–12 is 0.95 cm, 0.53 cm, respectively, when compared with initial values observed in 1952–53 [23]. River water treatment in the Taj vicinity is of the utmost importance.

Fig. 25.12 River-quality fluctuation [16]

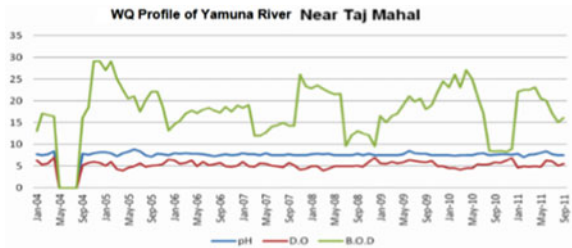


Fig. 25.13 Rarely seen view of the Taj Mahal—air and river pollution



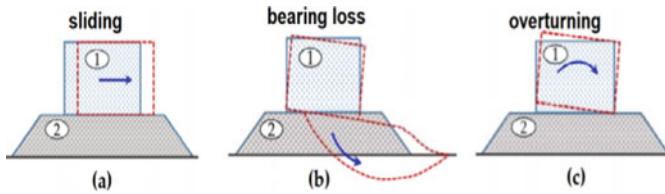


Fig. 25.14 Possible damage due to differential settlement

Remedial Measures

A Subsection Sample

Based on the information presented earlier, it may be concluded that:

- (a) Foundation is apparently safe in settlement though tilting of minarets continue.
- (b) Foundation capacity factor of safety for pile–raft foundation is less than unity.
- (c) Water may be the primary cause of the foundation masonry damage, so reduction of river salt content and providing the masonry surface with silicone-based water repellent coatings are needed [17].

Skirting piles/skirting sheet piles on river side and flanking sides are necessary to arrest local and overall failure. Grout injections and micro-piles may also have to be considered if there is an indication of increase in tilt.

Conclusion

The Taj Mahal is one of the wonders of the world. It has suffered frequent damage and has been repaired several times in the past. All past conventional analysis points to great factor of safety. Present analysis shows that the foundation is inadequate for the structure. There is also a looming danger as shown by the continued tilt of the monument which is luckily within permissible limits as of yet. River and air pollutions are rapidly advancing the deterioration of the foundations. However, steps like grouting and skirting piles may be necessitated as the river water degradation is affecting the foundations of the Taj Mahal.

References


1. Vats MS (1945) Repair to the Taj (Plate IV). Ancient India, Vol 4-Northern Circle, Archaeological Survey of India, vol 1, article 1, asi.nic.in-ancient India
2. Bhat PS, Athawale AL (1985) The question of the Taj Mahal. Itihas Patrika, 5

3. Handa SC (1984) Foundation performance of very old structures. In: Proceedings of the international conference on case histories in geotechnical engineering, vol 23. <https://scholarsmine.mst.edu/icchge/1icchge/1icchge-theme1/23>
4. Balasubramaniam R (2009) New insights on architects of Taj. *Indian J His Sci* 44(3):389–410
5. Viladkar MN, Bhandari NM, Godbole PN, Trikha DN (2006) Three-dimensional finite element analysis of Taj Mahal structure. In: Lourenço PB, Roca P, Modena C, Agrawal S (eds) *Structural analysis of historical constructions*, New Delhi
6. Dubey RN, Thakkar SK, Gupta A (1998) Seismic analysis of safety evaluation for Taj Mahal monument. In: Proceedings of eleventh world conference on earthquake engineering
7. Dhama BL (1929) Annual report, archeological survey of India
8. Marshall J (1921) Annual report, archeological survey of India
9. Rao ASR, Saran S, Handa SC, Ramasamy G, Viladkar MN (1993) Taj Mahal—an appraisal of foundation performance. In: Proceedings of international conference on case histories in geotechnical engineering, vol 57
10. NCHRP_syn_42 (1977) Design of pile foundations, transportation research board, National Research Council Washington, D.C.
11. O'Brien A, Bown A (2010) Pile group design for major structures, Report Mott MacDonald Ltd, Croydon, Surrey, UK. www.geomarc.it
12. EM 1110-2-2906 (1991) Design of pile foundations, 15 Jan 1991, Department of the Army, U.S. Army Corps of Engineers, Washington, DC 20314-1000
13. Misra AK (2010) A river about to die: Yamuna. *J Water Resour Prot* 2:489–500
14. Upadhyay A, Rai RK (2013) Brief overview of the Yamuna river basin and issues. Chapter 2, *Water management and public participation*, Springer Briefs in Earth Sciences
15. Ali AY, Jie D, Khan A, Liaqat NS, Rao AK, Hao C (2019) Channel migration characteristics of the Yamuna River from 1954 to 2015 in the vicinity of Agra, India: a case study using remote sensing and GIS. *Int J River Basin Manag*
16. ADA-Agra Development Authority (2013) Comprehensive Environmental Management Plan (CEMP) for Taj Trapezium Zone (TTZ) Area, Report—CSIR-National Environmental Engineering Research Institute (NEERI), Nehru Marg, Nagpur-440 020, India
17. Rovnaníková P (2007) Environmental pollution effects on other building materials. *WIT transactions on state of the art in science and engineering*, vol 28. www.witpress.com. ISSN 1755-8336 (on-line)
18. Charola AE, Bläuer C (2015) Salts in masonry: an overview of the problem. *Restor Build Monuments* 21(4–6):119–135
19. Delgado JM, Guimarães AS, de Freitas VP, Antepará I, Koli V, Henry R (2016) Salt damage and rising damp treatment in building structures. *Adv Mater Sci Eng* 2016(1280894):13
20. Lubelli B, Van Hees RP, Pei L (2001) The role of the pointing mortar in the damage due to salt crystallization. *Trans Built Environ* 55
21. Doan NS, Huh J, Mac VH, Kim D, Kwak K (2020) Probabilistic risk evaluation for overall stability of composite caisson breakwaters in Korea. *J Mar Sci Eng*
22. Tata P (2004) <https://www.newscientist.com/article/dn6629-concerns-over-tilting-taj-mahal-dismissed/>
23. Rediff: Taj Mahal's minaret tilted 3.57 cm in 30 years: ASI www.rediff.com/news. January 28

Chapter 26

Heritage Impact Assessment of the Subordinate Court Complex Near the David Yale and Joseph Hyner's Tomb



Angel Paul, K. V. Aishwarya, M. Keerthana, T. Satyamurthy,
and Jitesh T. Chavda 

Introduction

Heritage Impact Assessment was carried out for the Public Works Department, Government of Tamil Nadu by REACH Foundation to assess the impact of the proposal of a subordinate court near the David Yale and Joseph Hyner's Tomb, which is under the protection of the Archaeological Survey of India, GOI, located within the current Madras High Court complex. The proposal comprises two parts, firstly the demolition of the old law college building and auditorium located in proximity of the monument and secondly the construction of the subordinate court complex around the monument. The report addresses the concerns of the demolition and proposed new construction and the impact it may have on the value of the heritage site and the structural stability of the monument.

A. Paul (✉)

Department of Civil Engineering, National Centre for Safety of Heritage Structures (NCSHS),
Indian Institute of Technology Madras, Chennai 600036, India
e-mail: angelpaulmaliakkal@gmail.com

K. V. Aishwarya · M. Keerthana
Conservation Mainstream, Chennai, India

T. Satyamurthy
Reach Foundation, Chennai 600020, India

J. T. Chavda
Department of Civil Engineering, Sardar Vallabhbhai National Institute of Technology,
Surat 395007, India
e-mail: jtc@amd.svnit.ac.in

Monument and Site Context

Monument

The obelisk located adjacent to the old law college building in the High Court complex was built during the year 1680 AD, as mentioned in the epitaph. The obelisk marks the death of Joseph Hymers, who was sworn in as an acting governor of Madras in the 1670 s. He died in 1680 AD and was buried in the burial grounds of the 'White Town' which was later developed as a site for High Court and law college building. The monument is located within the present High Court complex. The complex is bounded by the NSC Bose road and George Town in the north, Fort Road and Fort St George in the south, Esplanade road and Pachaiyapas School in the west and the beach road and Chennai port in the east. The site area comprises the monument, old law college building to the north of the monument and auditorium to the south of the monument. The old law college building is an L-shaped building located along the north and east boundary of the site with the closest distance from the monument being 700 mm in the north. The auditorium is located at 8000 mm from the site boundary to the south.

Proposal

The proposed area includes the area around the heritage site consisting of the old law college building, auditorium and the open space to the west of the monument (see Figs. 26.1 and 26.2). It was stated that the land and the buildings around the monument have no utility value and therefore could be demolished so that a multi-story building housing the subordinate courts with maximum permissible floors could be constructed in that place to make optimum use of the site. In the site level, firstly the old law college and the auditorium building would be demolished followed by the leveling of the ground level to the level of the approach road. Consequently, the protected monument would be provided with a green wall which will enhance the visual appeal of the cultural property. The proposed design scheme offers a buffer or setback of 7000 mm from the monument in comparison to 700 mm in the current scenario. A well-designed drainage system to prevent water stagnation in the site, owing to the difference in levels, is also proposed.

Potential Threats Due to the Proposal

The proposal envisages the careful dismantling of the old law college building and auditorium in the site, located 700 mm from the monument and the careful construction of a multi-story new court complex surrounding the monument on all four sides.

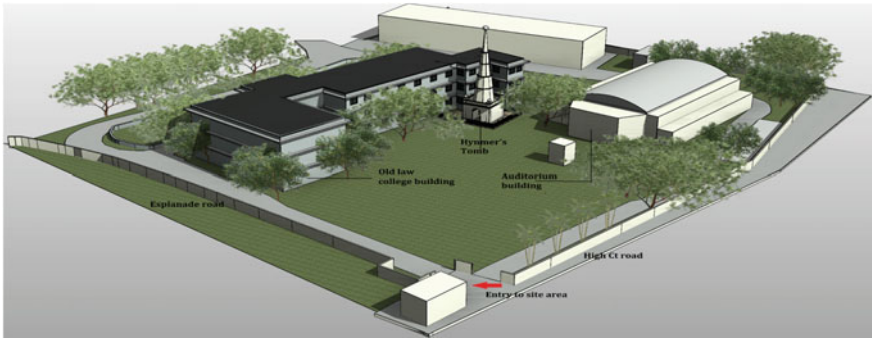


Fig. 26.1 Proposed site of construction with existing buildings

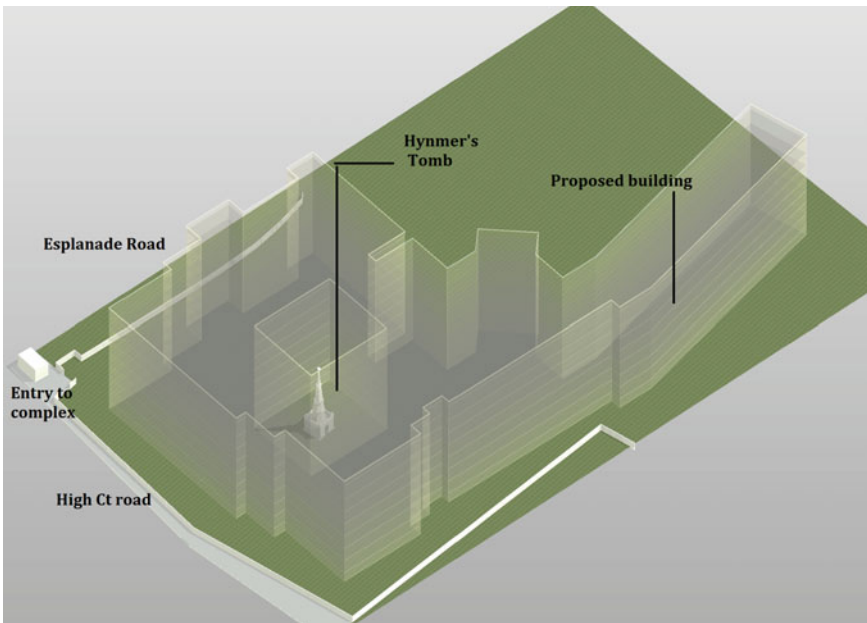


Fig. 26.2 Proposed new constructions around Hynmer's Tomb

From the conditional assessment of the monument and the surrounding buildings in the site, it can be inferred that the monument is in a good state of preservation while the old law college building and the auditorium are in a poor state of preservation and have been reported as being unsafe. Thereby, it can be concluded that since the old law college building is located less than a meter away from the monument, it possesses a potential threat to the monument and therefore should be demolished with care to ensure the safety of the monument. Furthermore, the proposed construction works also located within 7000 mm might result in the settlement of soil or

vibration during the construction may thereby impact and pose a potential threat to the monument. Therefore, necessitating a proper Heritage Impact Assessment before the demolition of the structures and the construction of the new structures.

Methodology

The proposed methodology mainly focuses on four assessments which are value assessment, structural risk assessment, baseline condition assessment and review of the legal framework (refer Fig. 26.3). Value assessment comprises the listing of values and establishing the statement of significance. Structural risk assessment is carried out to assess the structural risk the monument might be subjected due to the various proposed construction activities. The structural risk assessment comprises three sub assessments, namely condition assessment, vibration assessment and assessments for differential settlement of the soil. This is followed by the baseline condition assessment, which is an assessment of the social and cultural setting in which the proposed project is to be located, and where local impacts (both positive and negative) might be expected to occur. Finally, a review of the legal framework is carried out to check the feasibility of the proposal. Based on the impacts arrived at, in assessments suitable mitigative measures to reduce the potential impacts through design discussion and consultation, potential impacts of the proposal, design measures to avoid impacts and further mitigations that need to be discussed with the concerned experts and the appropriate measures needed to be taken were suggested.

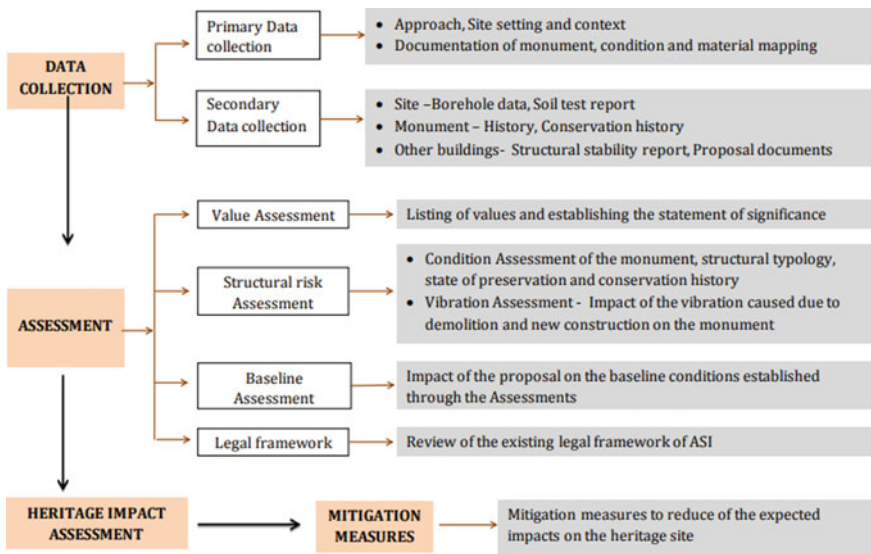


Fig. 26.3 Proposed methodology adopted in the study

Assessment and Evaluation

Baseline Condition Assessment

The baseline condition assessment is an assessment of the social and cultural setting in which the proposed project is to be located, and where local impacts (both positive and negative) might be expected to occur. The baseline conditions including the brief description and assessment are built heritage and landscape which are identified, upon the proposed construction affecting the monument. The monument is built on a plane and is found to be in a good state of preservation. The proposal is to demolish the old law college building, 700 mm away from the monument, and the auditorium to construct a building in its place, for accommodating the needs of judicial democratic system and thereby warranting a detailed value and structural risk assessment to protect the monument from any impacts associated with the proposal.

Value Assessment

The monument has a high historical value as it marks the death of Joseph Hymers, who was the acting governor of Madras in the year 1670s, during the British India period. It is even considered as one of the oldest memorials in South India by Late Historian Muthaiah making it an important example of early memorial architecture, thereby of immense architectural significance.

Structural Risk Assessment

Building Condition

From a primary survey by conservation architects/archaeologists, the monument continues to be in a good state of preservation. Annual maintenance is also carried out by the conservation officer, Chennai subcircle, ASI. From the conditional assessment of the surrounding buildings in the site, it can be inferred that the old law college building and the auditorium are in a poor state of preservation and have been reported as being unsafe. Thereby, it can be concluded that since the old law college building is located less than a meter away from the monument, it possesses a potential threat to the monument and therefore should be demolished with care to ensure the safety of the monument.

Table 26.1 The machineries used for the evaluation of PPV

Description of vibration source	Quantity of equipment	Comments	Proposed action
DEWALT hand breaker	1	Rated energy: 5–25 J	Demolition
Hitachi hand breaker	1	Rated energy: 68 J	Demolition
JCB 3DX xtra backhoe loader	1	–	Demolition
Bosch jackhammer	1	–	Demolition
Bored piling machine	1	–	Construction

Structural Typology

The monument is a complete load-bearing structure with the two tombstones in the walls which act as the base which is then surmounted by a five-floor spire.

Ground Vibration Assessment

The mechanical vibration induced due to demolition of the existing structure, ground leveling or piling activity may cause distress in the heritage buildings near the proposed structure. Ground vibrations due to the machinery used for demolition of the structure can disturb the foundation soil, and the soil may become unstable leading to foundation settlement. Moreover, vibrations during the demolition and construction shall be within permissible limits. Therefore, the ground vibration that can be caused by demolishing operations must be quantified and the safety of nearby heritage structures must be ensured. This was executed using the following steps:

- The permissible limits of ground vibration for heritage structures were established using accepted standards and guidelines.
- Vibration source levels were determined for each proposed vibration-intensive equipment. Ground vibration is measured in terms of Peak Particle Vibration (PPV). The methodology to determine the ground vibration is explained in this section.
- The overall PPV is then calculated for all the vibration-intensive equipment.
- Comparison of the predicted PPV values with the established threshold levels is used to predict the potential risk to the adjacent heritage structures during demolition operations (Table 26.1).

Vibration Inducing Machinery

The vibration inducing equipment used for the demolition of the existing court complex and construction of the foundation of the proposed structure is as follows.

Vibration due to Hydraulic Breakers

Vibration due to hydraulic breakers can be predicted using the following formula obtained from Caltrans guidelines [1]:

$$PPV_{Receiver} = PPV_{Ref} \left(\frac{25}{d} \right)^n \left(\frac{E_{equip}}{E_{ref}} \right)^{0.5}$$

where $PPV_{Receiver}$ = peak particle velocity at the nearest building foundation in inch/s, $PPV_{Ref} = 0.24$ inch/s for a reference hydraulic breaker at 25 ft., d = horizontal distance from the source to the receiver (ft) and $n = 1.3$ (the value related to the attenuation rate through the ground). The value is obtained from Caltrans guidelines [1], $E_{equip} = 5,000$ ft-lbs. (rated energy of reference hydraulic breaker) and E_{ref} = rated energy of hydraulic breaker in ft-lbs.

Vibration due to other Construction Works Equipment

Vibration due to other equipment can be predicted using the following formula obtained from FTA guidelines [2]:

$$PPV_{Receiver} = PPV_{Ref} \left(\frac{d_{ref}}{d} \right)^{1.5}$$

where $PPV_{Receiver}$ = peak particle velocity at the nearest building foundation in mm/s, $PPV_{Equipment Ref}$ = peak particle velocity of the source (construction equipment), measured at the reference distance (7.6 m), d_{ref} = reference distance for the vibration source (7.6 m) and d = horizontal distance from the source to the receiver (m). Source vibration levels used to estimate the vibrations generated due to construction and demolition work equipment are presented in Table 26.2.

The closest edge of the existing building is 0.7 m from the heritage structure. The vibration estimation is done considering this limiting distance and is continued

Table 26.2 Source vibration reference levels obtained from published literature for the identified equipment from the provided list for predicting ground vibrations induced by proposed demolition and construction activities

Description of vibration source	Category of vibration source	PPV at 7.6 m (mm/s)	Reference/comment
JCB 3DX xtra backhoe loader	Large bulldozer	2.2	FTA guidelines [2]
Piling rig (bored)	Piling rig (bored)	1	British standard BS5228 [3]
Bosch jackhammer	Jackhammer	0.9	FTA guidelines [2]

beyond the safe distance (found from analysis) to 10 m for all possible combinations of the machinery proposed for carrying out the demolition of the existing court complex. The closest edge of the proposed foundation is 7 m from the heritage structure. The vibration estimation is done considering this closest distance. The calculations for estimating the ground vibrations for heritage structures near the proposed construction and demolition activities are done using the above methodology and presented in the preceding section. The overall PPV obtained from the above methods can be compared with the guideline targets for structural damage established in Sect. 4.4 of this paper.

Ground Settlement Assessment

Previous studies suggest that net soil displacement is likely to be small when piles are driven into clean granular soils [4–7]. On the other hand, significant soil displacement occurs during pile driving in fine-grained soil deposits [8–10]. A soil characterization and grain size distribution of soil were not available. From the available data, it is assumed that the site consists of predominantly non-cohesive soil for preliminary analysis. Hence, the soil heave and subsequent settlement due to bored piling can be neglected.

Permissible Limits

The permissible limit for the PPV value is given in the following table. This chart also serves as the guideline target for determining the possible structural damage to adjacent heritage structures while estimating ground vibrations during construction and demolition activities adjacent to it.

Results and Recommendations

Figures 26.4 and 26.5 represent the results for the estimated ground vibrations induced due to demolition and construction of the proposed building's foundation. The following conclusion recommendations were arrived at using the results:

- Figure 26.4 represents the complete vibration estimation done using the proposed methodology in Sect. 4.3.3 for the machinery to be used for demolition of existing complex and the construction of the new building.
- Ground vibration of more than 10 PPV is unsafe for heritage structures as per the guideline targets established in Table. 26.3. Hence, any combination of vibration inducing machinery generating more than 10 PPV cannot be permitted, and such scenarios are ruled out.

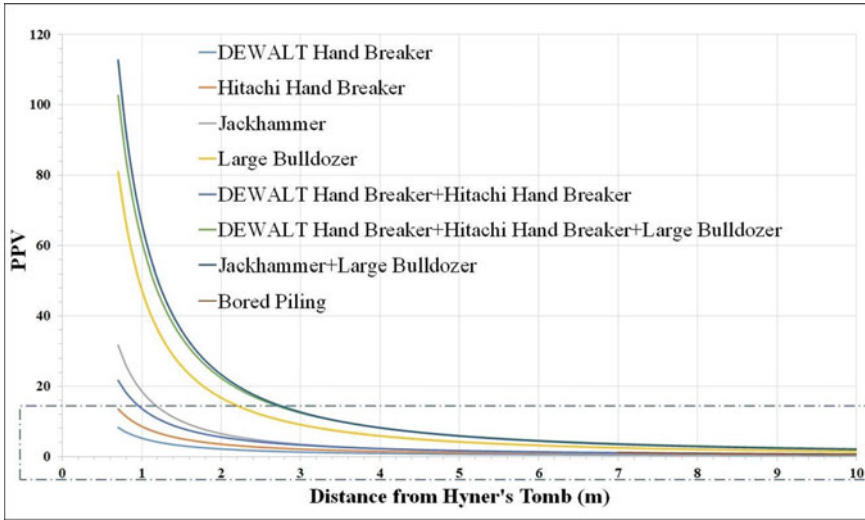


Fig. 26.4 PPV versus distance from Hyner’s Tomb

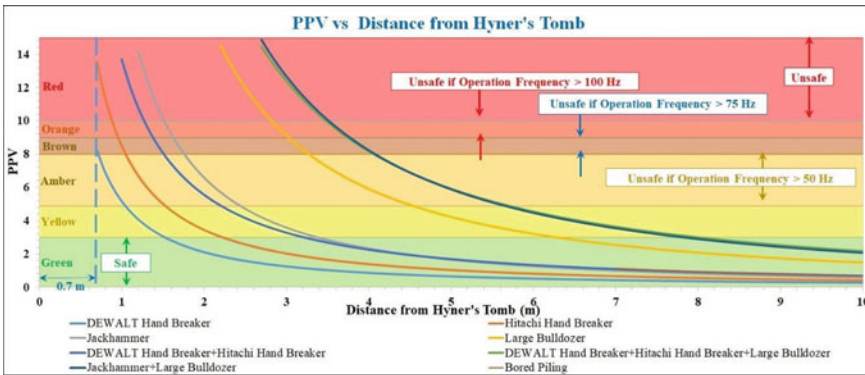


Fig. 26.5 Operation guideline using PPV versus distance from Hyner’s Tomb

- The optimization of machinery needs to be done such that the ground vibration lies within the prescribed limits. This is done using Fig. 26.5 which represents the ground vibration ranging between 0 and 15 PPV and their corresponding distance. Color coding is used to represent limits based on operation of frequency of machinery as prescribed in guideline targets to arrive at safe operation guidelines for the demolition and construction activities [11].
- Eight possible combinations (individual and different combination) of proposed vibration inducing machinery are analyzed separately. It must be noted that at a given time only a single combination out of 8 can be operated considering the operation guidelines developed and laid out below.

Table 26.3 Permissible limit for PPV values

Code	Type of building	PPV suggested (mm/sec)		Remarks
		PPV	Frequency range	
DIN 4150 part 3, 1984 structural vibration	Sensitive buildings under preservation	3	1–10	Measured at the maximum points of amplitude for short-term vibrations
		3–8	10–50	
		8–10	50–100	
		2.5		Measured at the highest floor for long-term vibrations
Directorate General of Mines Safety, India	Objects of historical importance and sensitive structures	2	< 8	
		5	8–25	
		10	> 25	

- The conservative value among the two guideline targets is chosen to develop the operation guidelines to ensure safe operations.

Operation Guidelines/Recommendations

- The ground vibration of 0–3 PPV is safe as per the established guideline targets. This region is highlighted using color code green (Fig. 26.5). The vibration inducing activity can be safely done using either of 8 combinations at distances falling in this region.
- The ground vibration of 4.9–3 PPV is safe if the operation frequency of the machinery is greater than 25 Hz as per the established guideline targets. This region is highlighted using color code yellow (Fig. 26.5). The vibration inducing activity can be safely done using either of 8 combinations at distances falling in this region provided the operation frequency of the machinery used is maintained above 25 Hz.
- The ground vibration of 8–4.9 PPV is safe if the operation frequency of the machinery is greater than 50 Hz as per the established guideline targets. This region is highlighted using color code amber (Fig. 26.5). The vibration inducing activity can be safely done using either of 8 combinations at distances falling in this region provided the operation frequency of the machinery used is maintained above 50 Hz.
- The ground vibration of 9–8 PPV is safe if the operation frequency of the machinery is greater than 75 Hz as per the established guideline targets. This region is highlighted using color code brown (Fig. 26.5). The vibration inducing activity can be safely done using either of 8 combinations at distances falling in this region provided the operation frequency of the machinery used is maintained above 75 Hz.

- The ground vibration of 10–9 PPV is safe if the operation frequency of the machinery is greater than 100 Hz as per the established guideline targets. This region is highlighted using color code orange (Fig. 26.5). The vibration inducing activity can be safely done using either of 8 combinations at distances falling in this region provided the operation frequency of the machinery used is maintained above 100 Hz.
- Ground vibration of more than 10 PPV is unsafe for heritage structures as per the guideline targets established. Hence, any combination of vibration inducing machinery generating more than 10 PPV cannot be permitted, and such operations must be strictly not executed. This region is highlighted using color code red (Fig. 26.5).

Impact Assessment

In the impact assessment, the impact of various parameters on the monument due to the proposed construction activity is assessed. The scale or severity of impacts or changes can be judged considering their direct and indirect effects and whether separate impacts should also be considered. The scale or severity of impact indirect reference to the value of the asset is classified as follows (Table 26.4):

Impact of Location

The proposed demolition is located 700 mm away from the monument, and the proposed new construction is located 7000 mm from the monument David Yale and Joseph Hyner’s Tomb. The proposed construction activities are located within the prohibited boundary of the ASI on all the four sides of the monument, thereby enclosing it. The proposed construction, being of important public work in nature, is in conformation with the regulations and will have a **moderate adverse impact** on the monument.

Table 26.4 Categories of impact on the heritage site

Value of the heritage site	No change	Negligible change	Minor change	Moderate change	Major change
Impact of the heritage site	Neutral	Slight	Moderate	Large	Very large

Impact of Activity

The proposed construction is a subordinate court with multiple courtrooms, record rooms and parking. The functioning of the court would result in the movement of people in the complex in large numbers. At present, the foot fall at the monument is negligible. The monument will have direct access, and visual connectivity which was hidden all these years will be rectified. Therefore, the large number of people visiting the court might bring the monument into the limelight again. Thus, the proposed construction will have a **slight beneficial impact** on the monument.

Visual Impact Assessment

The monument at present is only partially visible from the Esplanade road and the High Ct road due to the obstruction caused by the existing vegetation along the west and south compound wall. The site is approached from the road diverging from the High Ct road which visually appears to be inaccessible to the general public. In the proposal, the design scheme provides a direct access path leading to the monument from the Esplanade road. The solid and high compound wall is also proposed to be replaced with grills which would provide visual connectivity to the monument through the stilt floor from multiple points in the Esplanade road, thereby making the monument more visually approachable and accessible. Thus, the proposal has a **slight beneficial impact** on the monument.

Impact of Parking and Vehicular Movement

Adequate parking shall be provided for the proposed construction if not will lead to the traffic congestion on the existing approach road leading to the building site. Since there is already an existing road which will be used by the users of the subordinate court, there will be a **neutral impact** on the monument.

Impact of Design and Material

The design and building material used for proposed construction shall result in a **slight adverse impact** on the value of the monument since the new construction style would follow the style of the other buildings in the High Court complex and not the monument.

Impact of Construction Activity on Site

The vibration caused by the proposed demolition activity using the types of equipment which were furnished by the PWD will have a **very large adverse impact** on the monument. The vibration caused by the proposed new construction activity using the equipment which was furnished by the PWD will have a **moderate adverse impact** on the monument. The site would also be leveled before the new construction commences which if done improperly can have a **moderate adverse impact** on the monument. On the completion of the impact assessment, it was found that most of the causes of impact have an adverse impact on the monument in exception to a few that were found to be beneficial. In order to reduce the adverse impact, a few mitigative measures have been suggested.

Recommendations and Mitigative Measures

Ambient ground vibration measurements must be at least taken at the closest corner of the heritage structure to the construction activities. The proposed scheme of mitigation measures is only an initial suggestion of possibilities based on the vibration assessment carried out. It is underlined that mitigation interventions ranging from temporary structural stabilization and ground improvement techniques must be designed before starting the project.

- The demolition and construction operations must be done in accordance with the operation guidelines established in Sect. 4.5.
- Temporary structural stabilization of heritage structure must be carried out by adequate propping and bracing, and confinement if required
- Soil: Ground improvement by grouting must be carried out with an appropriately designed grout mix. Trenches can be executed around the monument, and/or ground improvement by grouting can be carried out with an appropriately designed grout mix.
- Vibration measurements must be continuously recorded during the execution of work, and they must not exceed threshold PPV level as identified in the DGMS and DIN 4150-3 standards. A geotechnical engineer must be consulted if values exceed.

If the proposed mitigative measures and recommendations are completely followed, all the causes of adverse impact were found to be neutralized in exception to the impact of demolition which is due to the proximity of the building to the monument. The various causes of impact on the monument due to proposed demolition and construction and the impact assessment after following the proposed mitigation measures have been summarized below (Table 26.5).

Table 26.5 Impact of risk assessment and mitigative measures on the monument

S. No.	Causes of impact	Impact on monument without mitigation	Impact on monument after mitigation
1	Impact of location	Moderate adverse	Neutral
2	Impact of metro operation	Neutral	
3	Impact of activity	Slight beneficial	Slight beneficial
4	Visual impact	Slight beneficial	Slight beneficial
5	Impact of parking	Slight adverse	Neutral
6	Impact of vehicular movement	Moderate adverse	Neutral
7	Impact of design	Moderate beneficial	Moderate beneficial
8	Impact of demolition	Very large adverse	Slight adverse
9	Impact of new construction	Very large adverse	Neutral
10	Impact of leveling	Moderate adverse	Neutral

References

1. California Transportation Department (2013) Transportation and construction vibration guidance manual. CT-HWANP-RT-13-069.25.3
2. Aurecon Jacobs Mott Macdonald and Grimshaw (2016) Melbourne metro rail project, noise and vibration impact assessment
3. BS 5228-2:2009 (2009) Code of practice for noise and vibration control on construction and open sites—part 2: vibration. British Standards Institute
4. Kerisel J (1961) Fondations profondes en milieu sableu. In: Proceedings of the 5th international conference on soil mechanics and foundations engineering, vol 2
5. Meyerhof GG (1959) Compaction of sands and bearing capacity of piles. ASCE Proceedings, 85(SM12):1292–1321
6. Plantema G, Nolet CA (1957) Influence of pile driving on the sounding resistance in a deep sand layer. In: Proceedings of the 4th international conference on soil mechanics and foundations engineering, vol 2
7. Stuedlein AW, Christopher BR (2013) Sound geotechnical research to practice. American Society of Civil Engineers
8. Hagerty D, Peck RB (1971) Heave and lateral movements due to pile driving. J Soil Mech Found Div, ASCE Proceedings, 97(SM11):1513–1532
9. Rajapakse RA (2016) Pile design and construction rules of thumb. Butterworth-Heinemann
10. Bouillon AM (1934) Heaving and distortion of piles. Mil Eng 26(149):373–380
11. FTA predictive methodology from FTA document (2006) Transit noise and vibration impact assessment. FTA-VA90–1003–06, FTA

Chapter 27

Numerical Investigation on the Influence of Different Parameters on a Vegetated Slope—A Case Study



G. Vishnu and Tadikonda Venkata Bharat

Introduction

Landslides are the downslope movement of the mass of rock, earth or debris down a slope. Natural and anthropogenic factors cause landslides. The natural causes that trigger landslides are earthquakes, heavy rainfall, forest fire and volcanoes, and anthropogenic causes include overdevelopment, deforestation and an inappropriate drainage system. Landslides are one of the most devastating and recurring natural disasters, and they have affected several mountainous regions across the globe. Yearly losses in Japan USA, Italy and India are estimated above one billion dollars or more [15]. In India, the great Himalayas in the north and northeast India, the Nilgiris and the other Western Ghats regions report many landslides every year [9, 18]. Many landslides in the Indian subcontinent are triggered by rainfall events. Rainfall-induced shallow landslides contribute to one-fifth of the total landmass [6]. The study of different aspects of global climate change indicated anomalous rainfall events and suggested higher rainfall intensities and lesser rainfall days—this harms natural and artificial slopes [5, 17]. Most of the rainfall-induced slides are shallow slides, and it occurs within the unsaturated soils having different geological settings like weathered residual or colluvium deposits [12, 16]. A rainfall-induced landslide's primary triggering mechanism is rainwater infiltration into the slope, decreasing the soil matric suction. The soil strength reduces and factor of safety (FOS) along with the potential failure surface.

G. Vishnu (✉) · T. V. Bharat
Department of Civil Engineering, Indian Institute of Technology, Guwahati, Guwahati 781039,
India
e-mail: g.vishnu@iitg.ac.in

T. V. Bharat
e-mail: tvb@iitg.ac.in

Vegetation and climatic factors like temperature, relative humidity and wind speed play an essential role in the stability of slopes against rainfall-induced slides. The studies considering these effects are scarce [10, 11]. Vegetation affects slopes' surficial and mass stability. Many hydromechanical mechanisms can be identified that explain vegetation's beneficial role in slopes [4]. The role of vegetation in the context of hydrological benefits had been studied widely. Experimental studies revealed that the presence of vegetation affects the hydraulic properties of soil [1]. The soil water characteristics (SWCC), the hydraulic conductivity function (HCF), runoff and infiltration characteristics are all affected due to the presence of vegetation [8]. The presence of vegetation incorporates transpiration, root cohesion and interception effects. The evapotranspiration effect is favorable to the slopes as it decreases the moisture content and helps to maintain a higher suction compared to the bare soil slope [11]. In the present study, a numerical model considers these effects to seepage and slope stability analysis of slope to predict a landslide event. The effects of various vegetation parameters such as root depth and soil cover fraction (SCF) were also studied.

Site Location

The study slope is 25.578°N latitude and 91.893°E longitude in the East Khasi district of Meghalaya, India. The region receives heavy rainfall from June to September. According to India Meteorological Department (IMD), the state has an annual average rainfall of above 3000 mm compared to around 1300 mm for India. The region comes under a high-risk zone in the landslide susceptibility map [2]. A landslide event was reported in the location in the last week of June 2019. The state map of Meghalaya is given in Fig. 27.1a.

Geology

The study region is surrounded by several faults. The mighty Brahmaputra River separates the region from the eastern Himalayas [13]. Digital Elevation Model (DEM) for the region was obtained from the Bhuvan portal. The DEM was used to derive slope, hill shade and contour map of the region (Fig. 27.1d). Also, lithology and geomorphological maps of location were also derived (Fig. 27.1b, c). The region consists of epidiorite and quartzite deposits. Boreholes were made in different locations of the affected area (Fig. 27.2). Boreholes were made at crest, slope and toe of the critical section. There was no mention of water table from any of the borehole data. It was also reported that the topsoil was loosely packed and SPT values were less (2–3). The vegetation present was pine trees.

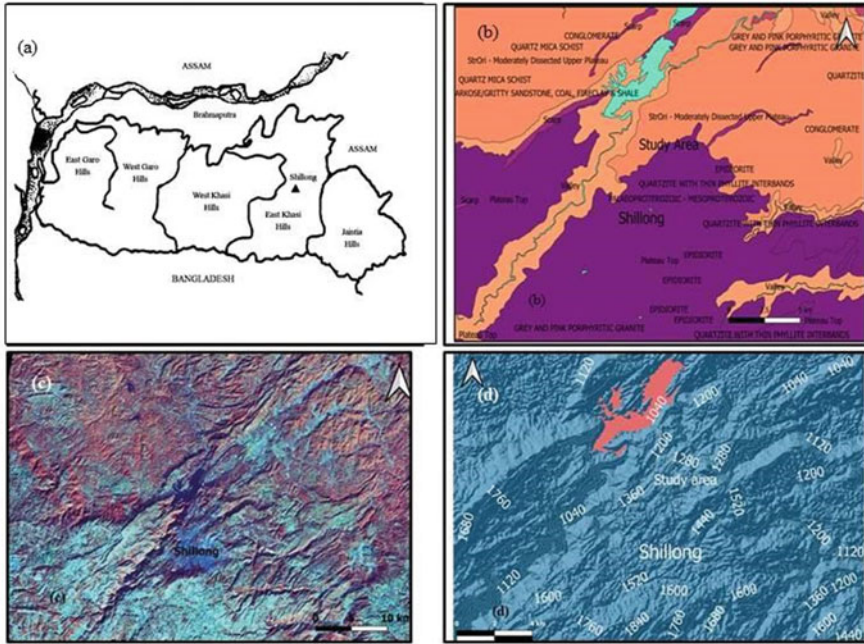
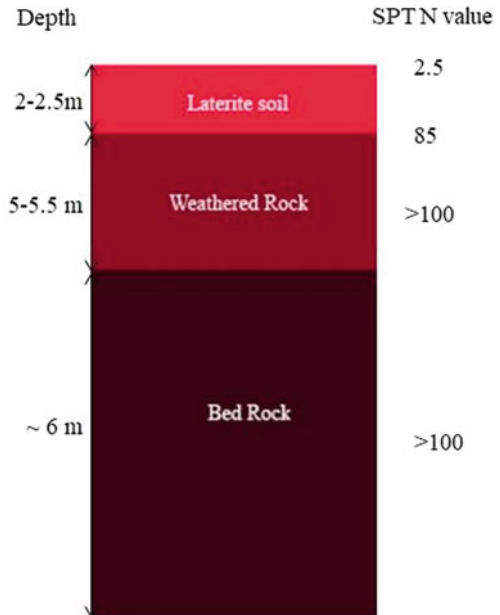


Fig. 27.1 a State map of Meghalaya, b rock types and age, c terrain map and d contour map

Fig. 27.2 Soil profile arrived from different borehole data



The borehole data provided the soil profile of the site. It consists of lateritic soil as the top layer for a depth of 2–2.5 m. Laterite soil is followed by a weathered rock layer (5–5.5 m) and then bedrock. The contour of the region was used to develop a simplified slope cross section for seepage and stability analysis.

Theory

A surface layer boundary condition is applied to the slope surface. The inclusion simulates a realistic analysis. It computes the net infiltration flux and root water uptake when vegetation details are provided along the slope. The net infiltration can be derived from the mass conservation equation.

$$(q_{\text{precipitation}} + q_{\text{snowmelt}})\cos(\alpha) + q_{\text{evaporation}} + q_{\text{runoff}} = q_{\text{netinfiltration}} \quad (27.1)$$

In the study area, snow cover is not encountered, so the flux corresponding to that is taken to be zero. The evaporation and runoff flux take water from the slope, so these are negative fluxes. An infiltration flux hence denoted the residual and was the boundary condition for the mass conservation equation. The precipitation flux is multiplied with the cosine of the slope angle as it is considered over a horizontal surface. The applied infiltration flux can lead to ponding at the surface. If this case happens, the pore pressure is set to zero, and the time step is resolved.

The presence of vegetation accounts for transpiration on surface layers which is absent if vegetation is neglected.

$$q_{\text{PT}} = q_{\text{PET}} \times (\text{SCF}) \quad (27.2)$$

where q_{PT} is the potential transpiration flux, q_{PE} is the potential evaporation flux, q_{PET} is the potential evapotranspiration flux, and SCF is the soil cover fraction. SCF denotes the vegetation cover, i.e., zero for bare land and one for slope covered with full vegetation [19].

The maximum root water uptake that can take place is calculated from q_{PT} [3]

$$q_{\text{root}}^{\text{max}} = \pi_{\text{root}} \times q_{\text{PT}} \quad (27.3)$$

where π_{root} is the normalized water uptake distribution, but the actual root uptake will be lesser than this due to dry, wet and osmotic (presence of salts). Therefore, the actual root uptake is given by [3]

$$q_{\text{root}} = \alpha_{\text{rw}} \times q_{\text{root}}^{\text{max}} \quad (27.4)$$

where q_{root} is the actual root water uptake; α_{rw} is the reduction factor for dry and wet conditions. The reduction factor due to salts is ignored. The plant moisture absorption

factor that considered root water uptake criteria is assumed from Jonas and Graham [7].

Van Genuchten (1980) proposed a model for SWCC of soils which is given by

$$\theta = \theta_r + (\theta_s - \theta_r) \times 1 / [1 + (\alpha|h|^n)^m] \quad (27.5)$$

where θ_s , θ_r , h and α are saturated volumetric water content, residual volumetric water content, suction head and reciprocal of air entry value, respectively, and the fitting parameters are n , m and α . The value of $n > 1$ for mathematical stability. Equation (27.5) is substituted in Mualem (1980) statistical conductivity model to obtain an analytical equation for HCF. The SWCC data were available for laterite soil, and values for the other two layers were assumed appropriately from Jonas and Graham [7]. HCF is predicted using Eq. (27.6).

$$k_r(\psi) = (1 - (\alpha\psi)^n)^{-m} / [1 + (\alpha\psi)^n]^{m/2} \quad (27.6)$$

here $k_r(\psi)$ is the relative hydraulic conductivity, and ψ is the soil suction.

Materials and Methods

Numerical Model

The numerical study was conducted on commercially available finite element (FE) software (Geostudio 2021). The modeled slope had a height of 67 m and extended horizontally for 116 m (Fig. 27.3). The slope angle was approximately 30°. The region consists of mainly pine trees. The potential evapotranspiration, root depth and limiting suction details of pine trees were assumed appropriately [14] for the numerical study. The surface boundary condition was applied on the slope face. A convergence study was performed to minimize numerical error and estimate the optimum mesh size for numerical analysis. Finer mesh size was used for the top two layers, while a coarser mesh size was taken for bedrock. The SWCC details of the bottom two layers were assigned according to an appropriate weathering class proposed by [7], and saturated hydraulic conductivities were assigned [4]. The slope consists of lateritic soil as the top layer for 2–2.5 m. The lateritic soil properties are summarized in Table 27.1.

A 9-month data (September 2018–May 2019) considering vegetation and climatic data set were used to generate the initial conditions for the critical event (June 1–July 15, 2019). The climatic data set used for critical rainfall events is given in the Fig. 27.4. The factor of safety variation with time with and without land–climate boundary conditions was compared. The influence of different vegetation parameters was also studied.

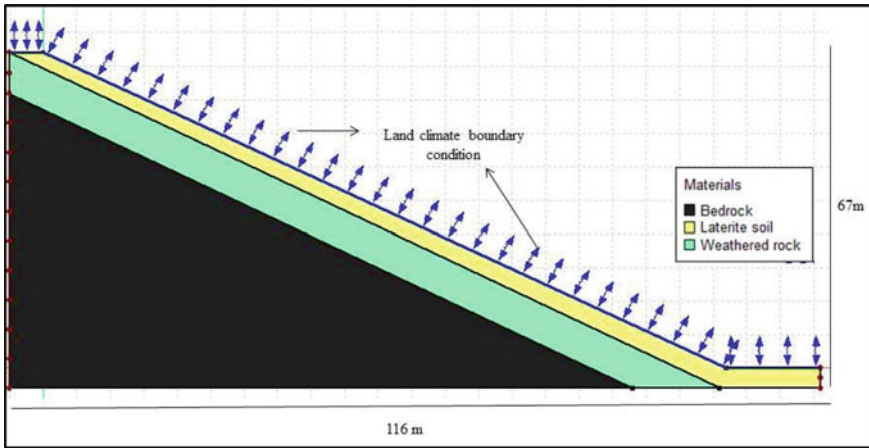


Fig. 27.3 Numerical model for coupled seepage and slope stability analysis

Table 27.1 Geotechnical properties of lateritic soil [2]

Properties	Value
	Lateritic soil
Specific gravity	2.71
<i>Particle size (%)</i>	
Sand	43.5
Coarse (4.75–2 mm)	0
Medium (2–0.425 mm)	0
Fine (0.425–0.075 mm)	43.5
Silt (0.075–0.002 mm)	39.07
Clay (< 0.002 mm)	17.43
<i>Consistency limits (%)</i>	
Liquid limit	42
Plastic limit	23
Shrinkage limit	19
Soil classification (ISCS)	CI

Results and Discussion

Coupled Seepage and Stability Analysis

The coupled seepage and stability analysis generated FOS variation with time for critical rainfall events (Fig. 27.5). It can be explicitly seen that vegetation had a considerable effect on slope stability. The analysis without vegetation FOS decreased

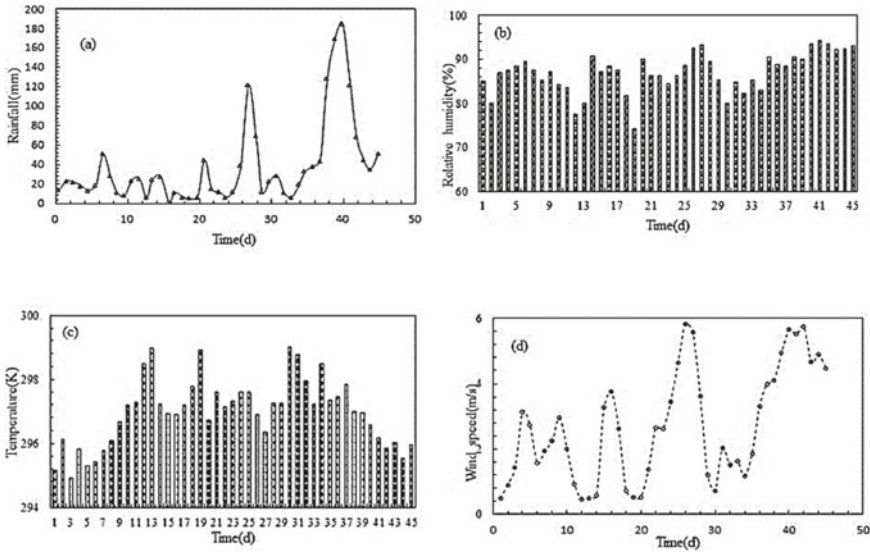


Fig. 27.4 Climatic data set used for critical rainfall event **a** rainfall, **b** relative humidity, **c** temperature and **d** wind speed (MEERA 2 weather data)

at a higher rate with higher rainfall intensity compared to vegetated cases. This can be accounted to interception and evapotranspiration effects.

The slope reached critical FOS in about 10 days when vegetation effects were ignored. The slope failure occurred on the 27th day when vegetation effects were introduced, which matched with the reported landslide event. Figure 27.6 shows the critical slip circle during initial and the time of landslide occurrence. This underlines

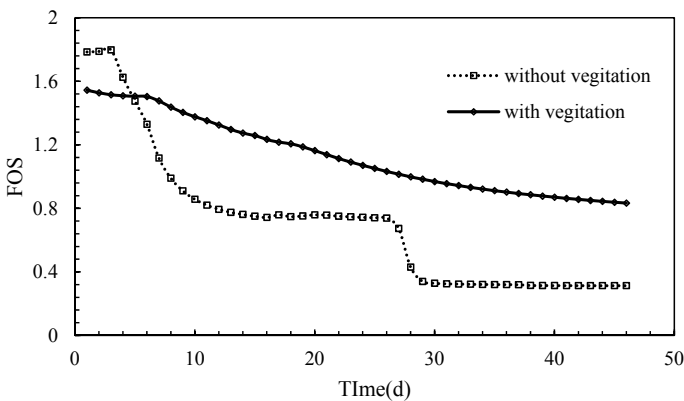


Fig. 27.5 FOS with time variation of critical rainfall event for vegetation and without vegetation scenario

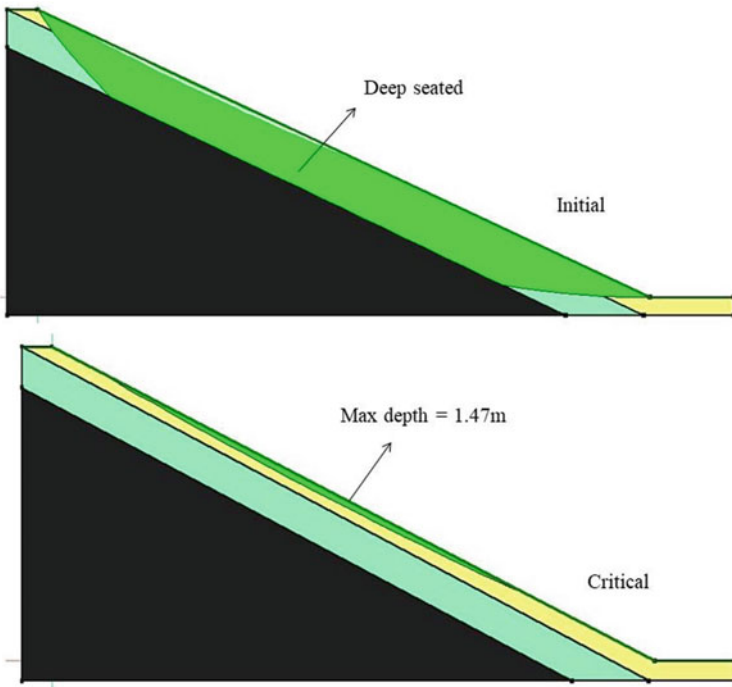


Fig. 27.6 Critical slip circle on initial and 27th day

the importance of land–climate interaction which considers vegetation and climatic details into analysis rather than assuming the total precipitation entering the slopes. The initial FOS for a vegetated slope was lesser in this case. It can be due to higher soil moisture content due to vegetation cover than bare land during the dry period. There are sharp decreases in FOS noticed in the case of no vegetation. This decrease corresponds to higher precipitation rates. The precipitation rates were higher in two sections in June of the critical event. The initial was on the 2nd week and the other on the 4th week. In between, there were fewer rainy days. The slope failed in the initial phase itself without vegetation due to higher water entry to slope decreasing matric suction, reducing the FOS along the potential failure surface. In the vegetated case, the FOS reduced gradually as the amount of water entered to slope increased relatively in lower amounts compared to other cases.

Parametric Study

The influence of different vegetation parameters on FOS variation with time was studied. The vegetation brings different parameters into consideration. The influence

of each parameter with keeping others constant was studied. The influences of root depth and soil cover fraction on FOS time variation were shown in Fig. 27.7a. Root depth had a significant influence on the FOS. As the root depth increased from 0.5 to 2 m, FOS increased, and a no failure case was observed at 2 m root depth. The influence of root depth also depended upon the failure surface. FOS sway was higher for shallow landslides.

The dependence on FOS solely on other parameters like SCF, LAI and PET was not that noticeable. Figure 27.7b depicts the FOS variation with SCF. In this case, critical FOS was attained marginally early at lower SCF. The trend was the same for LAI. The influence of other parameters as a sole contributor to FOS variation reflected in delay or early prediction of FOS by utmost 2 days.

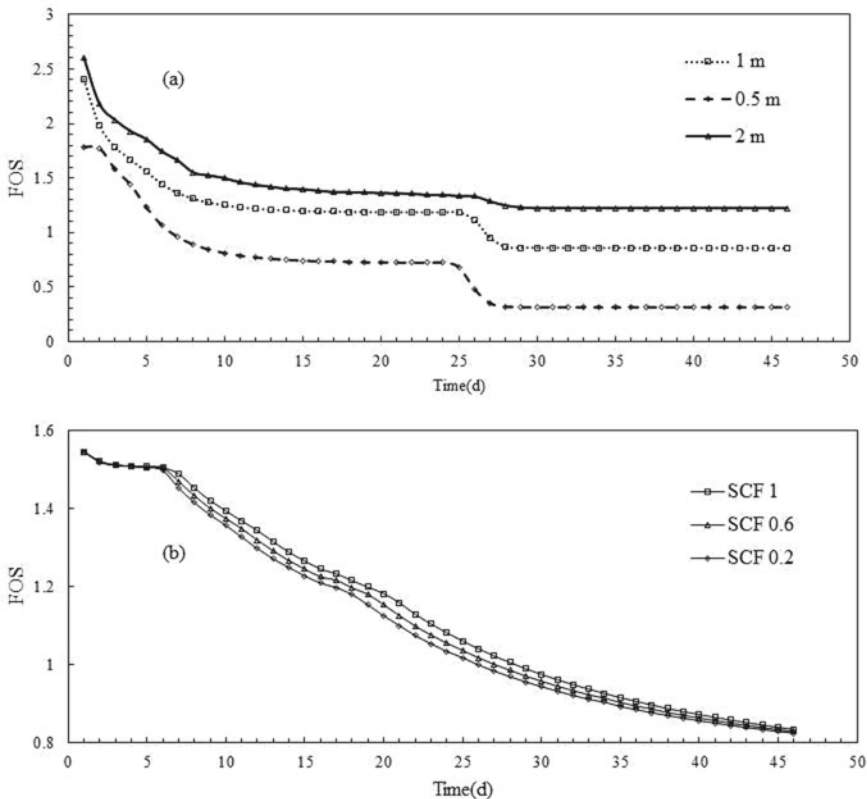


Fig. 27.7 FOS variations with time for a different root depths and b soil cover fraction variation

Conclusions

The study aimed to incorporate the effect of vegetation on the stability analysis of the slope. The various parameters that attribute to the stability of slopes due to the inclusion of vegetation were also studied. The following conclusions are drawn based on the analysis of the numerical study.

- The numerical study presented incorporated climatic and vegetation parameter into stability analysis of slopes which is done very rarely, and the model accurately predicted the landslide event. Earlier numerical models neglect runoff and evapotranspiration effect and assume the entire rainwater infiltration to the slope leading to false alarms
- The numerical model encompasses the shear strength modification due to vegetation effect to the slope and evapotranspiration effects due to climatic and root water uptake, thereby improving the FOS compared to bare soil slope analysis
- Root depth plays an important role in shallow landslides; in present study, shallow root depth of pine trees is one of contributing factor for landslide.

The incorporation of vegetation details for numerical analysis can improve the efficiency of Early Warning Systems (EWS) by reducing false alarms. Soil hydrological properties are altered by the effect of vegetation which is not accounted in the analysis. The FOS variation of critical slip circle changes with the location and depth of the slip circle. The influence of vegetation parameters on this can be worked out. The effect of interception and storage in canopies also need to be understood in future studies.

References

1. Bordoloi S, Ng CWW (2020) The effects of vegetation traits and their stability functions in bio-engineered slopes: a perspective review. *Eng Geol* 105742
2. Das P, Bharat TV (2020) Reconstruction of a wetting-induced shallow landslide in Shillong, India. *Proc Inst Civ Eng Forensic Eng* 173(2):48–53
3. Feddes RA, Hoff H, Bruen M, Dawson T, De Rosnay P, Dirmeyer P et al (2001) Modeling root water uptake in hydrological and climate models. *Bull Am Meteor Soc* 82(12):2797–2810
4. Gray DH (1995) Influence of vegetation on the stability of slopes. In: *Vegetation and slopes: stabilisation, protection and ecology*. Proceedings of the international conference held at the university museum, Oxford, 29–30 September 1994
5. Heath RC (1998) *Basic ground-water hydrology*, vol 2220. US Department of the Interior, US Geological Survey
6. Hong Y, Adler R, Huffman G (2007) Use of satellite remote sensing data in the mapping of global landslide susceptibility. *Nat Hazards* 43(2):245–256
7. Jones DP, Graham RC (1993) Water-holding characteristics of weathered granitic rock in chaparral and forest ecosystems. *Soil Sci Soc Am J* 57(1):256–261
8. Jotisankasa A, Sirirattanachai T (2017) Effects of grass roots on soil-water retention curve and permeability function. *Can Geotech J* 54(11):1612–1622

9. Kuriakose SL, Sankar G, Muraleedharan C (2009) History of landslide susceptibility and a chorology of landslide-prone areas in the Western Ghats of Kerala, India. *Environ Geol* 57(7):1553–1568
10. Leung AK, Garg A, Coe JL, Ng CWW, Hau BCH (2015) Effects of the roots of *Cynodon dactylon* and *Schefflera heptaphylla* on water infiltration rate and soil hydraulic conductivity. *Hydrol Process* 29(15):3342–3354
11. Ng CWW, Ni JJ, Leung AK (2020) Effects of plant growth and spacing on soil hydrological changes: a field study. *Géotechnique* 70(10):867–881
12. Pradhan AMS, Kim YT (2015) Application and comparison of shallow landslide susceptibility models in weathered granite soil under extreme rainfall events. *Environ Earth Sci* 73(9):5761–5771
13. Rajendran CP, Rajendran K, Duarah BP, Baruah S, Earnest A (2004) Interpreting the style of faulting and paleoseismicity associated with the 1897 Shillong, northeast India, earthquake: implications for regional tectonism. *Tectonics* 23(4)
14. Riekerk H, Numbers AAA (1982) Pine tree evapotranspiration. Florida Water Resources Research Center, University of Florida
15. Schuster RL, Fleming RW (1986) Economic losses and fatalities due to landslides. *Bull Assoc Eng Geol* 23(1):11–28
16. Sorbino G, Nicotera MV (2013) Unsaturated soil mechanics in rainfall-induced flow landslides. *Eng Geol* 165:105–132
17. Strauch AM, Mackenzie RA, Giardina CP, Bruland GL (2017) Climate driven changes to rainfall and streamflow patterns in a model tropical island hydrological system. *J Hydrol* 523:160–169
18. Vadivel S, Sennimalai CS (2019) Failure Mechanism of Long-Runout Landslide Triggered by Heavy Rainfall in Achanakkal, Nilgiris, India. *J Geotech Geoenviron Eng* 145(9):04019047
19. Wilson GW (1990) Soil evaporative fluxes for geotechnical engineering problems

Chapter 28

A Geotechnical Study on Failed Base Slab of Molasses Tank



Nandyala Darga Kumar and C. Lavanya

Introduction

The storage tanks are constructed mainly to store molasses, oil and gasses especially in the city outskirts and along the coastal areas. The size of the storage tanks can vary up to 100 m based on the storage requirement and 10–20 m in height. Tank construction activities are generally carried out on the surface or at certain depth below the ground surface. Due to unavailability of required construction sites, the engineers are utilizing the filled-up sites, including low-lying water-logged waste lands, creek lands with deep deposits of soft saturated marine clays having very low strength, with the confidence that the storage tanks in these sites can be provided with the special type of foundations or by improving the ground. There are plenty cost-effective foundation techniques, which can be utilized for the poor and marginal bearing capacity sites. The structures founded on difficult soil would suffer from problems of excessive settlement. The ground improvement methods can be effectively utilized to prepare the ground according to the project requirements rather than having to change the project to meet the limitations due to poor subsoil conditions prevailing at the site. Dewatering, densification, cementation, reinforcement, drying and heating are age-old techniques of ground improvement and are valid even today.

The foundations of the tanks are a form of reinforced concrete slab built sometimes on the soil improved with vertical drains. The settlement of storage tank can be measured using a horizontal inclinometer by placing it on the reinforced concrete slab and permanent geodetic points. The settlement values of tank foundations can

N. D. Kumar

JNTUH University College of Engineering Hyderabad, Hyderabad, Telangana, India
e-mail: ndkumar@jntuh.ac.in

C. Lavanya (✉)

Gokaraju Rangaraju Institute of Engineering and Technology, Hyderabad, Telangana, India
e-mail: lavanya.cc@gmail.com

be obtained either by numerical analyses or by actual measurements with the help of installed instruments. The settlements of tank foundations can be appropriately monitored during the stages of emptying and filling [1]. In-situ investigations including boreholes and cone penetration tests and laboratory tests have gained popularity to define the geotechnical profile of the construction site and the soil mechanical properties. Dissipation tests also carried out to evaluate the horizontal consolidation and permeability coefficients. Especially in the tank foundations, the differential settlements and distortions are to be maintained well below the allowable limits to envisaging a satisfactory performance of the tank under service conditions [2].

Structural failures which have occurred can be seen throughout history. The concerned engineers have studied the failures to identify the reasons and also to establish the failure prevention measures so as to not to repeat the same mistake in the future civil engineering construction. The Boston molasses tank failure is a famous incident in which 21 people lost their lives. Those days, there were no applicable structural codes available to use for design. From the simulation studies carried out [3], it is stated that the tank was wholly insufficient in point of structural strength to handle its load, insufficient to meet either legal or engineering requirements. The predominating cause of this accident was a bursting from internal pressure exceeding its structural strength. The heterogeneity and the compression of soft soil layers underlying the site can cause the excessive differential settlements of tank foundations. Adoption of deep foundation systems or improvement of soft soil can be the viable solutions to safeguard the tank structures on soft soils. For the construction of tank foundations in soft soils, consolidation by micro-piles can be best suited. The numerical simulations can help the engineers to design appropriate ground improvement technique in soft soil [4].

The surface layers of alluvial nature, mostly sandy clayey and heterogeneous soils will not reach sufficient degree of consolidation over time. These soils possess low bearing capacity and have tendency to undergo settlement. The structures such as tanks, bridge abutments and silos founded in alluvial soils have experienced tilt, settlement and collapse. In these soils, construction of deep foundations or adoption of soil improvement for heavy structures is the viable options [5]. The stability and settlement are the two factors to be considered to safeguard the oil storage tank foundation systems from rupture or even the complete failure of oil tanks. In the design of tank foundations, the differential settlement is given more importance than the absolute settlement [6].

Building performance during its lifetime can only be achieved by designing a suitable foundation with the consideration of loads acting on it and in-situ soil conditions. To avoid the foundation failure, it is required to see that its movement should not be more than the allowable value. Due to foundation failure, distortion and damage can be noticed in the superstructure. The failure of a foundation or structure has linked with the soil resistance. Generally, soils of low strength can cause foundation settlement. The soil which contains clay or silt material is unsuitable to carry the loads. Remedial works such as underpinning method, in-situ soil compaction and ground stabilization using pressure grouting can make the ground more resistant to sustain

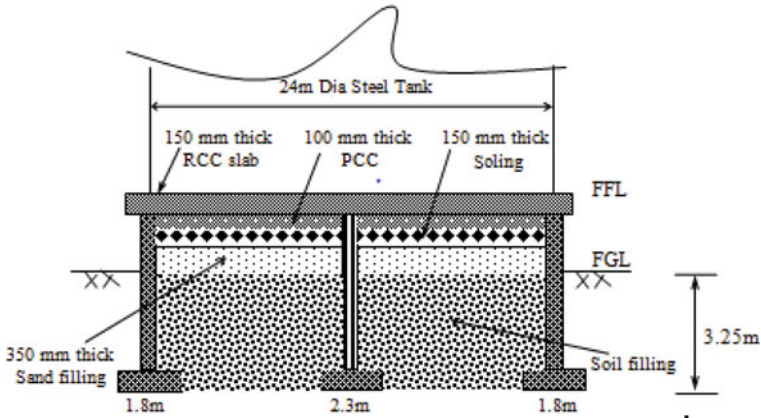


Fig. 28.1 Tank and foundation details

the loads. Execution of details present in the structural drawings is very important [7].

Foundation Details

The study was conducted at Sugar Complex and Cogen Plant at Tumkur village, Shahpur Yadgir dist., Karnataka, in India. As a part of the construction, two molasses tanks each of 24 m diameter and 9.7 m high were to be constructed. One of the tanks slabs of diameter 24 m failed during erection. The RCC base slab of thickness 150 mm is resting on the RCC ring wall of thickness 350 mm. The RCC ring wall is resting on a 1.8 m wide strip footing located at a depth of 3.25 m from the finished ground level (FGL). Also, the base slab at its center is supported by a steel column and in turn the steel column is resting on a RCC foundation of size 2.3×2.3 m. The foundations were laid at dense natural ground. The height from FGL to FFL is 0.75 m, and it consists of 150 mm thick RCC base slab, 100 mm thick PCC, 150 mm thick soling and followed by 350 mm thick sand layer as presented in Fig. 28.1.

Test Program

Laboratory Tests and Soil Description

The laboratory tests such as grain size distribution (IS 2720-Part 4, 1985), liquid and plastic limit (IS 2720-Part 5, 1985), free swell index (IS 2720-Part 40, 1977) and light compaction (IS 2720-Part 7, 1980) were conducted on the disturbed soil

samples as per the standard test procedures provided in the BIS codes. The test results are presented in Table 28.1.

The location of boreholes is presented in Fig. 28.2.

The borehole profiles for BH1, BH2, BH3, BH4 and BH5 are presented in Fig. 28.3. From these soil profiles, it is observed that the thickness of the filled-up soil from FGL to natural ground level (NGL) is varying from 2.4 to 3.8 m. The filled-up soil consists of 15% gravel, 61% sand and 24% silt and clay. Also, the optimum moisture content (OMC) and the maximum dry density (MDD) of filled-up soil are 9.5% and 19.50 kN/m³, respectively. The depth at which natural ground located at the tank area is varying from 2.4 to 4.5 m from the finished ground level, and it consists of 76% sand and 18% fines. The liquid limit of soil is 24%. Below this depth, there exist dense gravelly strata.

Table 28.1 Soil characteristics

Soil type/soil property	Filled-up soil	In-situ natural soil
% gravel	15.00	6.00
% sand	61.00	76.00
% fines (size < 0.075 mm)	24.00	18.00
Liquid limit (%)	28.00	24.00
Plastic limit (%)	18.00	18.00
Free swell index (%)	25.00	15.00
Optimum moisture content (%)	9.50	7.00
Maximum dry unit weight (kN/m ³)	19.50	20.50

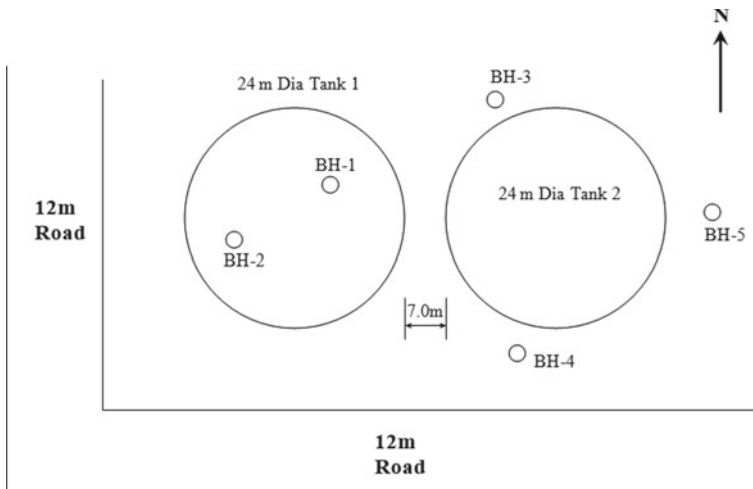


Fig. 28.2 Location of 24 m diameter molasses tanks and boreholes

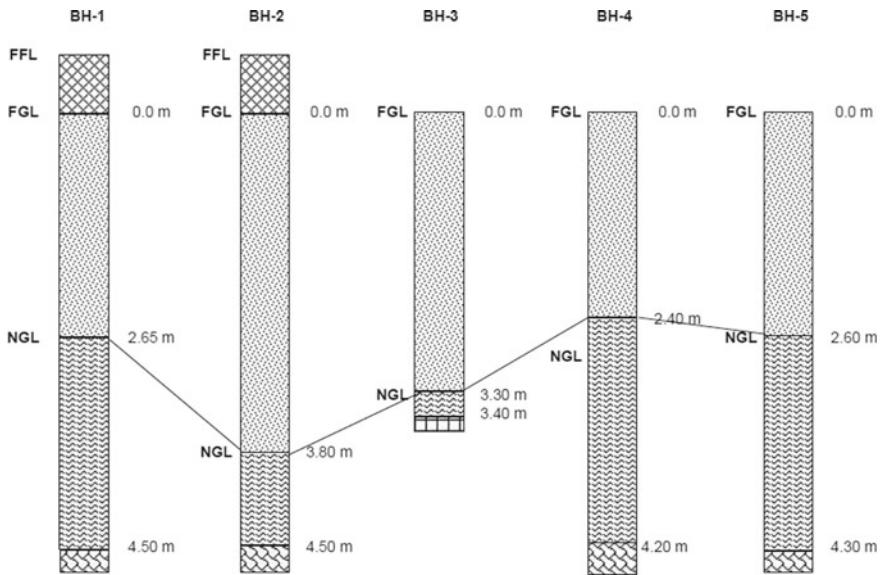


Fig. 28.3 Borehole profiles showing levels. *FFL* finished floor level, *FGL* filled-up ground level, *NGL* natural ground level

SPT Results

Standard penetration test (SPT) was conducted as per IS: 2131 (1981). The finished ground level (FGL) was taken as zero level, and test is continued through filled-up soil to till the natural ground is touched. The SPT was performed mainly to estimate the strength characteristics of soil. The variation of measured SPT *N* values is presented in Fig. 28.4 for boreholes BH1, BH2, BH3, BH4 and BH5.

The soil used for filling of depressed portion within the tank is from nearby area and possessing same characteristics as that of natural ground. The SPT '*N*' values are varying from 2 to 7 in the filled-up soil (Fig. 28.4). As per the values presented in Table. 28.2 [8], the filled-up soil is in very loose condition and proper densification is not carried out for the filled-up soil. Based on the SPT *N* value and from Table. 28.2, the relative density (D_r) of the filled-up soil would be below 35% confirming very loose to loose condition. In the natural strata, i.e., below the filled-up soil, the SPT '*N*' values are varying from 18 to 45, and therefore from Table. 28.2, it confirms that the natural stratum is in medium dense to dense state. From BH1, the SPT '*N*' value 18 is taken for the estimation of allowable bearing capacity of soil for a foundation depth of 3.25 m as it is the lowest among other values.

Fig. 28.4 Variation of SPT N corrected value

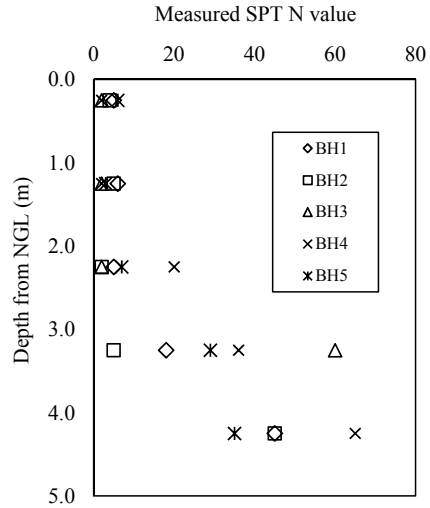


Table 28.2 Relation between SPT ‘ N ’, relative density (D_r) and the angle of internal friction, ϕ [8, 9]

SPT ‘ N ’	Compactness	Relative density (D_r), %	Angle of internal friction, ϕ , in degrees	Unit weight of soil (kN/m^3)
0–4	Very loose	0–15	< 28	12–16
4–10	Loose	15–35	28–30	14–18
10–30	Medium dense	35–65	30–36	17–20
30–50	Dense	65–85	36–41	17–22
> 50	Very dense	> 85	> 41	20–23

Allowable Bearing Capacity of Natural Soil

Calculation of Allowable Bearing Pressure at 3.25 m Depth

From the SPT data presented in Fig. 28.4, it is observed that the N values are varying from 18 to 45 for the natural strata. The lowest SPT N can be seen in BH1, i.e., $N_R = 18$ at a depth of 3.25 m in the natural soil. The filled-up soil is almost in loose state; hence, the unit weight of soil can be taken as $\gamma = 16\text{kN/m}^3$.

The corrected SPT ‘ N ’ value for overburden is,

$$N' = C_N N_R = \left[\frac{2}{1 + 0.01 \gamma z} \right] N_R \tag{28.1}$$

$$N' = \left[\frac{2}{1 + 0.01 \times 16 \times 3.25} \right] \times 18 = 23$$

As per the Teng [10], the equation for allowable bearing capacity for 40 mm settlement of footing is given as:

$$q_a = 55(N - 3) \left[\frac{(B + 0.3)}{2 \times B} \right]^2 \times R_w \times R_d \quad (28.2)$$

where $N = 23$, corrected value of SPT N , $B =$ width of footing = 1.80 m (taken from the drawings), $R_w =$ water reduction factor = 0.5, $R_d =$ depth factor = 1.

$$q_a = 55(23 - 3) \left[\frac{(1.8 + 0.3)}{2 \times 1.8} \right]^2 \times 0.5 \times 1 = 187.15 \text{ kN/m}^2 = 18.50 \text{ t/m}^2$$

The allowable bearing capacity works out to 18.50t/m² for a settlement of 40 mm.

Verification Against Bearing Capacity Failure

As per the structural drawings that are concerned, the load on the foundation is estimated as follows. Weight of the molasses to be stored = 6000 t.

Dead weight of the steel tank = 150 t.

Diameter of the molasses tank slab = 24 m.

Load intensity on the slab due to molasses and steel = Load/Area = 6150/[$\pi \times (12^2)$] = 13.59 t/m².

Dead weight of RCC circular slab = Unit weight of RCC \times Volume of slab.

As per the structural drawing the thickness of slab = 0.15 m and Dia. of slab = 24 m.

Dead weight of RCC circular slab = 2.5 ($\pi \times 12^2 \times 0.15$) = 169.64t.

Load intensity due to slab dead weight = Load/Area = 169.64/($\pi \times 12^2$) = 0.374 t/m².

Width of the RCC circular wall = 0.35 m.

Height of the RCC circular wall (average) = 3.25 m.

Dead weight of the RCC circular wall = Unit weight of RCC \times Volume of wall/m run = 2.5 \times (0.35 \times 3.25 \times 1) = 2.84 t/m run of wall.

The load intensity on the circular strip footing of width 1.85 m due to RCC circular wall = 2.84/(1.85 \times 1) = 1.53 t/m².

Therefore, the total load intensity on the circular strip footing of width 1.85 m = load intensity due to molasses and steel + load intensity due to RCC circular wall + load intensity due to RCC slab = 13.59 + 1.53 + 0.374 = 15.49 t/m² = 15.50 t/m².

The load intensity on the circular strip footing of width 1.85 m is 15.5 t/m², and it is less than the estimated allowable bearing pressure of 18.5 t/m² in the natural

soil at foundation depth of 3.25 m. Hence, the foundation is safe as per the bearing capacity is concerned.

Verification Against Degree of Compaction of the Filled-Up Soil

From Fig. 28.4, it can be noticed that the SPT 'N' values in filled-up soil are varying from 2 to 7. From Table 28.2, the average filed dry unit weight of the filled-up soil is found to be equal to 16 kN/m³. The maximum dry density obtained from the light compaction test is 19.5 kN/m³. The degree of compaction of a soil is the ratio of field dry unit weight to maximum dry density and is expressed in percentage. Therefore, the degree of compaction = (Field dry density/Maximum dry density) × 100 = (16/19.5) × 100 = 82%.

As per the specifications given in the structural drawings, the degree of compaction supposed to be achieved is 95% for the entire filled-up area. But actual value obtained as per the test conditions is only 82%. Hence, the filled-up soil compaction levels have not met the requirement. Also, there are no evidences seen about field compaction quality control. From the above aspects, it is understood that the failure of molasses tank base slab is merely due to settlement of filled-up soil and lack of support from soil beneath the slab.

Observations and Reasons for Failure of 24 m Diameter Molasses Tank Slabs

Observations at Site

The height of the molasses tank is 9.7 m from the finished floor level (FFL), and its RCC slab diameter is 24 m. The clear spacing between the two tanks is 7.0 m. Out of these two tanks, one is fully erected and the other was failed during erection steel. The 24 m diameter and 150 mm thick RCC slab of molasses tank has 8 mm diameter reinforcement bars in both ways, and the slab is almost simply supported on RCC wall and on central steel column. No structural connectivity is observed between the RCC circular wall and the slab. The slab portions between the circular wall and central column support have collapsed, and large gaps between the slab and the PCC are observed (Fig. 28.5).

The soil from the same site was used for filling. Filled-up soil at the site is not compacted well. The depressed area around the tank is filled up with silty sand which is of pervious in nature. Due to entry of water into the filled-up soil, it got settled and hence the RCC slab lost its support. It is also noticed that there was a 100–200 mm gap formation between bottom of the slab and the PCC (Fig. 28.5). The



Fig. 28.5 Orientation of failed slab and gap at the central portion of the tank

locations of levels taken on the top surface of failed slab are presented in Fig. 28.6, and respective levels are presented in Table 28.3. The levels are taken on top of the failed slab surface at its center and at distances of 3, 6 and 12 m around from the center. From the levels presented in Table 28.3, it is noticed that the levels at the center of the slab are varying from 366.775 to 366.830. At a distance of 3 m from center, the levels are varying from 366.610 to 366.665. At 6 m distance from the center, the levels are varying from 366.695 to 366.740, and at 12 m distance, i.e., at slab edge, the levels are varying from 366.810 to 366.815. From these average values of levels, the slab at 6 m distance sunk up to about 100 mm as compared to the edge of slab. The difference in average levels at the center and edge of slab is insignificant.

Reasons of Failure of RCC Slab of Molasses Tank

The reasons for failure are due to lack of structural rigidity and support for the slab in the form of ring beams and cross-beams. Improper compaction of filled-up soil and no evidences are found regarding the compaction quality control. Percolated water through the filled-up porous soil around the tank caused the soil to settle and in turn the RCC slab lost support from soil and soling.

Fig. 28.6 Position of levels taken

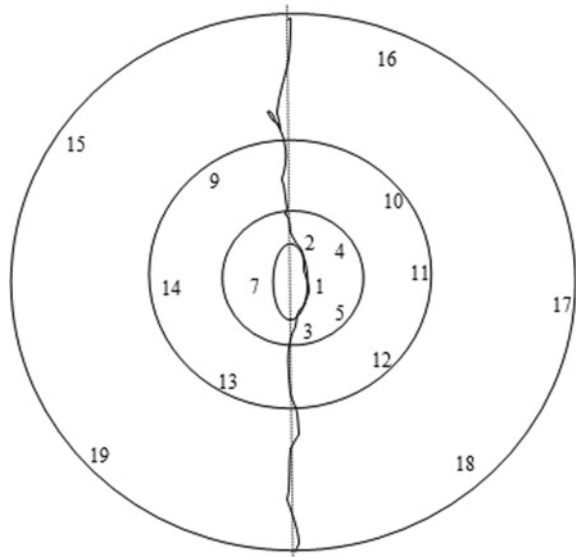


Table 28.3 Levels on the top surface of RCC circular slab after failure

Position	Level	Position	Level
1	366.830	11	366.720
2	366.805	12	366.730
3	366.775	13	366.695
4	366.610	14	366.725
5	366.655	15	366.815
6	366.640	16	366.815
7	366.665	17	366.815
8	366.660	18	366.810
9	366.740	19	366.805
10	366.715		

Conclusions and Remedial Measures

1. The allowable bearing capacity of natural ground where footings are placed is sufficient to sustain the loads.
2. The degree of compaction of the filled-up soil estimated is 82%, but as per the specifications, it should be 95%.
3. There is no proper structural connectivity between RCC slab, and the RCC circular wall and RCC slab are not supported by ring beams and cross-beams.
4. The workmanship is very poor in understanding the guidelines and implementing them during execution of work.

5. Remove the failed slab and before placing a new slab and construct the stone columns of diameter 0.3 m at spacing of 2 m in the filled-up soil below the slab till hard strata. This will give proper stable and compacted ground to support the slab.
6. Slab should be provided with ring and radial beam, and also its connectivity should be ensured properly.
7. If stone column support is not feasible, then replace the fill with compacted soil and place the tank over the compacted soil, but within the ring wall.
8. The ring wall should be designed for hoop tension.

References

1. Grget G, Ravnjak K, Szavits-Nossan A (2018) Analysis of results of molasses tanks settlement testing. *Soils Found* 58(5):1260–1271
2. Cascone E, Biondi G (2013) A case study on soil settlements induced by preloading and vertical drains. *Geotext Geomembr* 38:51–67
3. Mayville RA (2015) A new structural and metallurgical review of the great Boston molasses tank failure of 1919. In: *Forensic Engineering-7th Congress on Performance of the Built Environment*, Miami, Florida, USA, pp 1–8
4. Ramdane B, Boumediene H, Djahid A (2013) Differential settlements of cylindrical steel storage tanks: case of the marine terminal of Bejaia. In: *Seventh international conference on case histories in geotechnical engineering*, Missouri University of Science and Technology, USA, Paper No. 2.26, pp 1–11
5. Bahar R, Sadaoui O, Vincens E (2010) Settlements of silos founded on compressible soils reinforced by stone columns. In: *Proceedings of the international geotechnical conference—geotechnical challenges in megacities*, Moscow Russia, vol 3, pp 965–970
6. D’Orazio TB, Duncan JM (1987) Differential settlement in steel tank. *J Geotech Eng ASCE* 113(9):967–983
7. Salena IY (2016) A case study of foundation failure in the existing residential building. *J Teknik Sipil Fakultas Teknik* 2(1):91–103
8. Terzaghi K, Peck RB (1967) *Soil mechanics in engineering practice*. John Wiley and Sons, p 729
9. Bowles JE (1988) *Foundation analysis and design*, 4th edn. McGraw Hill Publishing Co., New York, p 1004
10. Teng WC (1969) *Foundation design*. Prentice-Hall Publishers

Chapter 29

Geotechnical Design and Execution of Driven Spun Piles in Estuarine Geology



Gouri Krishna, M. Jeevan Reddy, and Adak Pinaki

Introduction

Time becomes notably critical in private sector projects because the huge liquidity damages levied for delay in completion. In this context, development of port terminal in an offshore area becomes very crucial and therefore, adopting the driven spun piles system expedites the construction process. These are commonly adopted in foundations for offshore and onshore structures.

The extensive research and study on deep foundation design are limited to common ground conditions and adopting the conventional design approach might lead to huge loss for the contractor. Therefore, the designer can suggest extensive geotechnical investigation and suggest customized design approach for each of the structures based on the ground conditions. The paper discusses various ground challenges faced by the designer like thick soft clay deposits, highly varying ground, liquefaction, etc. and site constraints faced by the contractor while executing the deep foundation in estuarine ground conditions. Also, the paper details about the approach adopted to resolve these hurdles.

G. Krishna (✉) · M. Jeevan Reddy
AECOM India Pvt. Ltd, ASV Ramana Towers, 3rd floor, T Nagar, Chennai 600017, India
e-mail: gouri.krishna@aecom.com

M. Jeevan Reddy
e-mail: M.Reddy@aecom.com

A. Pinaki
ITD Cementation India Ltd, 'Godrej Water Side' Tower No-1, Office #802 and 803, 8th Floor,
Kolkata 700091, India
e-mail: Adak.Pinaki@itdcem.co.in

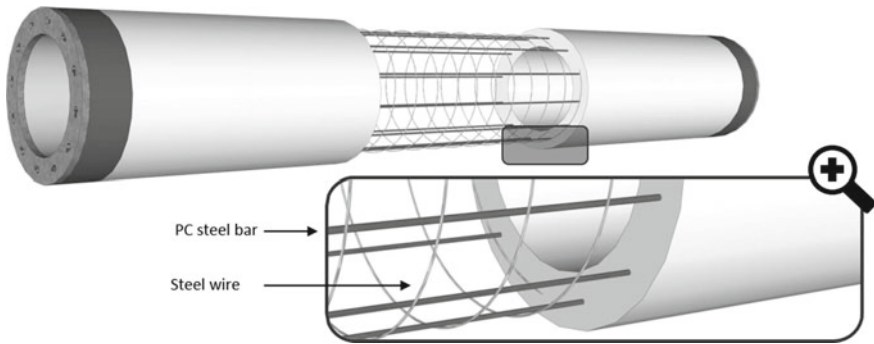


Fig. 29.1 Sectional details of a typical spun pile (VJP Co., Ltd. Catalogue)

Spun Piles

Overview

Spun piles are hollow, precast and prestressed concrete piles and offers an economical deep foundation system with superior quality and consistency compared to cast in-situ concrete piles (see Fig. 29.1). They generally vary in sizes ranging from 300 to 1200 mm outside diameter and the material of spun piles consists of high strength concrete 50–80 MPa and prestressed steel. They are usually 6–15 m long and can be easily joined to any combination of length as per design requirements and manufactured with steel end plates for splicing.

The spun piles are generally manufactured with reference to JIS A 5357 standards and modified to suit ACI 543 R–Recommendation for design, manufacture and installation of prestressed concrete piles. A compressive strength test and bending strength test are conducted to assess performance of the piles.

Site Execution

A spun pile can be driven within a very short time. In land or onshore structures, it is pressed by silent pile driver which is virtually noise and vibration free and therefore allows installation of piles as close as 50 cm to existing structures or services (see Fig. 29.2). One 12 m pile segment can be pressed in 5–7 min in land while a longer pile can be driven after splicing together few segments.

In case of offshore structure, the concrete spun piles are driven by diesel or hydraulic hammer like steel piles itself, along with an added cushion on the pile top to prevent the local damage (see Fig. 29.3). One 30–40 m pile can be typically installed within 40–60 min.



Fig. 29.2 Silent pile driver



Fig. 29.3 Diesel or hydraulic hammer

Application and Features

Application Spun piles are widely used as foundation pile for power projects, steel plants, marine structures, harbors, bridges, high-rise buildings, etc.

Advantages Since spun piles are hollow, the unit weight is quite low and hence lower cost. The high grade of concrete enables the piles to be driven through hard strata. The consistent quality under factory conditions and denser concrete with lower water cement ratio results in piles with high strength and high resistance to corrosion especially from sea water.

High rate of production ensures early completion of projects. The installation of concrete spun piles is environment friendly, i.e., free from noise (vibrations) and air pollution.

Disadvantages Although the hollow circular spun piles have a smooth appearance and low unit weight, the friction developed is lesser when compared to the square counterpart. Wang et.al. [1] found that the material cost is less and bearing capacity is high for a hollow square pile of same size as the pipe pile through performance analysis of actual construction of pile foundation.

Another downside is for structures with very high uplift loads, the hollow spun piles might not offer the required tensile capacity due to the low self-weight. Therefore, many projects end up using solid square piles or larger diameter pipe piles which in turn increases the project cost.

Also, the concrete spun piles have only lesser compressive strength than steel piles and are therefore subject to a high risk of fatigue damage due to the hammer blows.

Geotechnical Design Approach

The ultimate capacity of piles in compression is determined by equations in API RP 2GEO [2] as the sum of shaft friction and end bearing based on soil type, cohesive or cohesionless. The shaft friction and end bearing values are limited based on density of cohesionless soil as mentioned in the code.

The total resistance of pile is either the sum of external shaft friction, internal shaft friction and end bearing on the pile wall annulus (unplugged behavior) or the sum of external shaft friction and end bearing of annulus and plug (plugged behavior), whichever is less.

Challenges Faced in Geotechnical Design

Geology

An extensive geotechnical investigation campaign conducted in both offshore and onshore area revealed estuarine deposits of soft clay of thickness ranging from 5 to 20 m which was further underlain by medium dense to dense silty sand along the Yangon riverbank, Myanmar.

Soft Clay Deposits

Overview For onshore structures, the piles are taken through the fill and soft clay deposits ranging from 5 to 20 m in thickness to a suitable underlying bearing stratum (see Fig. 29.4). Because of the fill surcharge and its own self-weight, the soft clay deposits will undergo consolidation which usually lasts hundreds of years. Due to this, positive skin friction will not get mobilized over the length of pile shaft through these soft clay deposits.

When the settlement of pile is more than the settlement of soil, this initiates a frictional resistance in upward direction, which helps in carrying the vertical load coming on pile and hence it is called the positive skin friction. Contrary to this, when the soil settles at a higher rate than the pile, a downward drag is mobilized along the shaft and this acts as an extra load on pile, and hence called negative skin friction. The conservative approach is to negate the skin friction developed along the shaft length in soft clay from the total safe vertical pile capacity.

Design Approach Meyerhof [3] advises to calculate the negative skin friction, $|_{nsf}$ in terms of effective stress, σ'_{vo} from the equation:

$$|_{nsf} = \beta \sigma'_{vo} \tag{29.1}$$

The negative skin friction factor, β decreases with depth of penetration of pile. It is taken as 0.3 up to penetration of 15 m and thereafter reduces to 0.15 for a

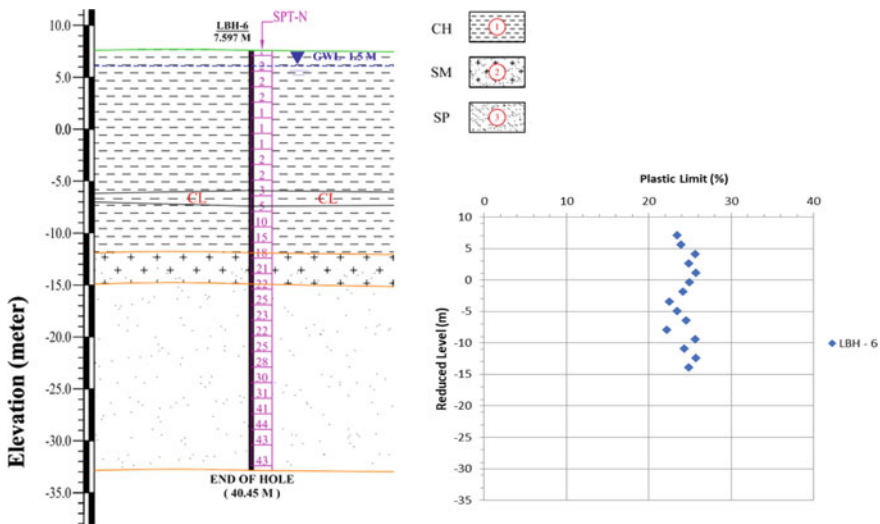


Fig. 29.4 Thick clay deposits found in Myanmar estuarine grounds—geological profile and plastic limit variation

penetration of 60 m. Since, the negative skin friction depends on many factors, it does not mobilize in equal magnitude over the total depth of the soft strata.

The relative movement between soft clay deposits and the pile takes place in a very slow rate. Also, the relative settlement is further nullified due to yielding of soil under pile toe. Thus, negative skin friction is not developed over a considerable portion of soft clay deposits and therefore, calculation of negative skin friction for the full layer of soft clay deposits is an overconservative approach.

The distribution of negative skin friction on piles terminated in compressible strata is described by Fellenius [4]. When the pile toe is resting into a compressible stratum, the drag down will initiate pile toe settlement to such an extent that the negative skin friction gets eliminated. Estimation of relative settlement and correctly identifying the depth until which negative skin friction mobilizes will result in a more economic design of driven piles.

Layered Soils

Overview The stratigraphy of estuarine soil deposits is highly variable spatially and vertically. Occurrence of soft soil deposits are usually found underlying a competent stratum (see Fig. 29.5). This poses another common challenge, especially while terminating the piles.

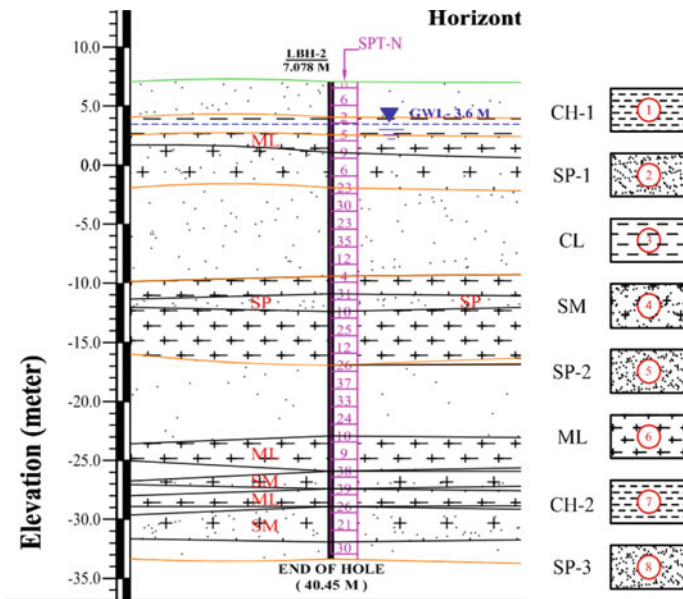


Fig. 29.5 Geological profile showing layered soil deposits found in Myanmar estuarine grounds

When the piles are subjected to their working loads, there exists a consequent risk of a breakthrough into the weaker soil underlying the bearing stratum. A common practice is to ignore the end bearing resistance of pile.

Design Approach In these situations, one can reduce the end bearing resistance of denser soil with respect to its proximity to the weaker layer. Meyerhof [3] has established a method for calculating the base resistance of a pile located in a stiff layer underlain by a weak stratum. He stated that the weaker layer influences up to 10 times of width of pile (B) into the denser strata. Hence, he suggested to interpolate the unit end bearing resistance in this $10B$ portion as shown in equation below.

$$q_p = q_0 + [(q_1 - q_0) H] / 10B \text{ limiting to } q_1 \quad (29.2)$$

where

q_0 = ultimate base resistance in the lower weak layer,

q_1 = ultimate base resistance in the upper stiff or dense stratum,

H = distance from the pile toe to the base of the upper layer, and,

B = width of the pile at the toe.

When the underlain weaker layer is thin, the influence might not be as large as $10B$. Therefore, proper establishment of thickness and strength parameters for both dense and weak strata are the first essentials. This can be done through extensive geotechnical exploration, in-situ tests like SPT and CPT at adequate number of boreholes. The thickness and extent of denser layers should be established reliably to ensure that the denser bearing stratum is not an isolated pocket.

To arrive at an economical design, trial and error can be performed on termination levels and structural load correlated to number of piles under each pier. For example, taking the pile deeper would be economical in case of thin underlain weaker strata. Similarly, increasing the number of piles and thereby a structural load reduction might be economical rather than taking piles deeper.

Spatial Variation

Overview As described in Sect. 3.3, the geology at estuarine environment tend to be heterogenous due to uneven settlement of layers, wave action, etc. The spatial variation of ground parameters poses as a challenge because usual number of boreholes proposed at sites might not give a reliable picture. Designing the foundations with the results derived from these scattered boreholes might result in unpredictable denser or softer layers and this hinders the pile driving process, and in turn results in time wastage and loss of money.

Design Approach The general design approach is to idealize the design parameters for an extensive area and perform the geotechnical design. But if spatial heterogeneity exists, then this might result in an over conservative design (see Fig. 29.6). This can

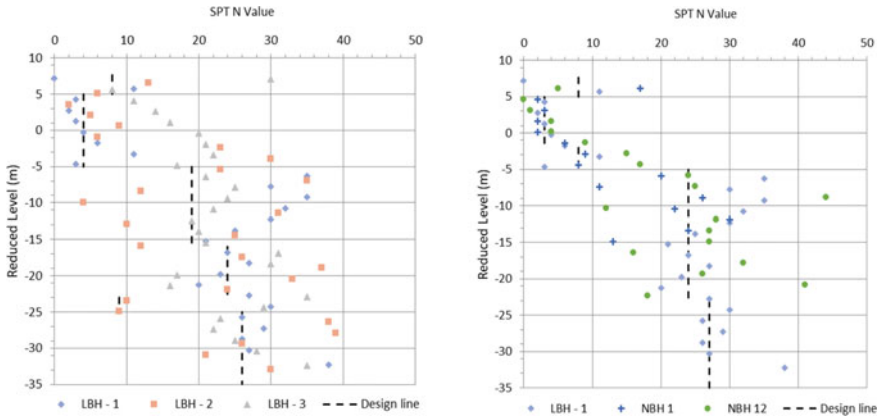


Fig. 29.6 Myanmar estuarine ground: SPT *N* variation for boreholes at 200 m interval on LHS and improved design with microzoning and confirmatory boreholes on RHS

be solved by identifying micro-zones within the site and performing confirmatory boreholes within these zones will give specific details about spatial variation of geology. Thereafter, estimation of parameters and performing the foundation design customized to each of the microzones will immensely cut down the construction time and cost.

Liquefaction

Overview Marcuson [5] defines liquefaction as the transformation of cohesionless material into liquefied state from a solid as a result of increased pore water pressure and reduced effective stress. The tendency of cohesionless soil particles with poor drainage to compact when subjected to cyclic shear deformations (Earthquake or other dynamic forces) induces an increase in pore water pressure. The reduced shear strength softens the soil which leads to large cyclic deformations and flow failure in varying degree depending on the density of soil.

The piles supporting the berth piers are usually terminated in the dredging slope of seabed. Chances of fine and non-plastic surface layers to liquefy is another challenge faced while designing the berth piles.

Design Approach The generally followed design approach to first estimate the liquefiable depth of soil as per and ignore it in the pile design. Various researchers suggest that this is an over conservative approach.

It is understood that liquefaction is a rare event which might occur in case of earthquakes. Hence, the design considering liquefaction need to cater only for seismic

or accidental loads and liquefaction phenomenon can be ignored in case of static pile design.

Liquefied residual shear strength estimation methods are suggested by few researchers. Idriss and Boulanger [6] computed the ratio of liquefied residual shear strength to effective overburden pressure. They came up with two cases, Case 1 is the condition in which void redistribution due to excess pore water pressure can be confidently judged to be negligible, while Case 2 is when excess pore water pressure dissipation is impeded due to very thick layer of liquefiable soil overlain by lower permeability soil. Kramer and Wang [7] have developed a procedure to determine the liquefied shear strength. Olson and Johnson [8] proposed a model to give normalized shear strength depending corrected SPT N value. The proposed model predicts the shear strength as a nonlinear function of both penetration resistance and initial effective stress. The liquefied angle of internal friction can be calculated from the above methods and critical value can be used for estimating the skin friction of pile in the liquefaction zone.

Estimating the parameters for liquefaction assessment reliably through field tests along the length and width of site (berth) will assist in arriving at an economical liquefaction design.

Site Constraints

Overview

It is evident from the geological profiles presented in Figs. 29.4 and 29.5 that the site geology is highly variable both vertically and horizontally. When the site execution of piles is commenced based on the idealized design, there exists chances of encountering unpredictable hard or soft strata while driving.

The preferred method of the spun pile installation is as a single piece after splicing the segments to the desired length, but this method has drawbacks as discussed in Sect. 4.3.

Spatial and Vertical Variation of Geology

When the shallow layers are soft and thick, the pile must be terminated into the underlying hard strata to satisfy both ultimate and serviceability limit states. The number of hammer blows are increased to drive the pile into the hard stratum. But the industry guidelines suggest restricting the blow count to 2000 to avoid fatigue damage of pile. Usually, the pile driving gets difficult once the N value increases beyond 30. If it is not possible to drive piles with the maximum number of blows,

then site engineer can recommend either redesigning after microzoning the area or the pile is terminated shallower than the recommended design level.

It is difficult to predict the actual founding level of pile at the time of construction; hence judicious decision shall be taken by designer about the pressing load factor in case of press pile.

Similarly, there could be circumstances under which the pile gets terminated deeper than the recommended level which becomes critical when the underlying stratum is weak. As explained above, the spun piles are terminated based on industry guidelines and this might result in disagreement between employer, designer and contractor. Hence, judicious decision shall be taken by designer about the pressing load factor in case of press pile. Also, pile load tests like high strain dynamic pile test can be proposed for validating the site termination levels.

Welding and Jointing of Pile Segments

The main purpose of splicing the pile before driving is to avoid in-situ welding and thereby maintaining the quality control. Other added benefits are higher self-weight which eases the driving process, maintains verticality and prevent the soil setting which occurs during in-situ welding process. But the main constraint of longer pile is its strenuous transportation. The leader should be long and strong enough for holding long piles in its proper position, i.e. the center of gravity of pile and hammer should be aligned. Even a slight tilting will result in huge damage of pile during the hammer fall.

Considering the difficulties faced while using long piles, it is a common practice to perform in-situ cutting and welding of pile segments. The pile cutting must be performed if shallow termination occurs and pile segments are welded if pile is terminated deeper than the design level. During pile cutting, necessary precautions need to be taken such that the worker can stand on the suitable platform to operate the cutting machine. When welding is inevitable, then the strength of welding shall be designed to be more than the ultimate structural strength of pile. It is advisable to perform a strength check of welding in a designated laboratory or in some cases the pile manufacturer facilitates the testing in their own workshop. Site welding shall be performed by certified welder and it shall be checked thoroughly by the quality control team at site before the driving the pile. Site welding is very critical procedure and required lot of patience and care. The site photographs captured of cutting and welding of pile segments are shown in Fig. 29.7.

Conclusion

It can be concluded that the first essentials to deal with the challenges are identifying them and reliably establishing the thickness and strength parameters of the subsoil



Fig. 29.7 Site photographs of **a** site setup for cutting of pile segment, **b** site setup for welding of pile segment, **c** welded pile segments and **d** enlarged view of pile welding joint

through extensive geotechnical exploration. Thereafter, the design approach must be modified using the obtained test results. A value engineering comparative study can be conducted to ascertain the way forward, either construction with idealized generic design or extensive literature review and modification of design on economic grounds.

The site constraints can be either avoided or dealt with cautiously by the quality control team at site. It is difficult to predict the actual founding level of pile at the time of construction; hence, judicious decision has been taken by designer with two times of working load for pile pressing in case of press pile. Factor of pressing load shall be in range of the geotechnical safety factor and pile structural strength shall be adequately strong enough to counter the pressing load.

When welding is inevitable, then the strength of welding shall be designed to be more than the ultimate structural strength of pile and the same is verified with the necessary strength tests.

References

1. Wang R, Li Y, Liu X, Zhang S, Zhang C, Li Z, Wang P (2021) Research on advantages and disadvantages of prestressed concrete hollow square pile and pipe pile in pile foundation selection. *IOP Conf Ser Earth Environ Sci* 787(1):012022
2. ISO 19901-4:2003 (Modified) (2011) Petroleum and natural gas industries—specific requirements for offshore structures, part 4—geotechnical and foundation design considerations. API recommended practice 2GEO, Washington, USA
3. Meyerhof GG (1976) Bearing capacity and settlement of pile foundations. *J Geotech Eng Div* 102(3):197–228
4. Fellenius BH (1972) down drag on piles in clay due to negative skin friction. *Can Geotech J* 9(4):323–337
5. Marcuson WF III (1978) Definition of terms related to liquefaction. *J Geotech Eng Div ASCE* 104(9):1197–1200
6. Idriss IM, Boulanger RW (2008) Soil liquefaction during earthquake. *Earthq Eng Pap* 291(10). Research Institute, EERI Publication MNO-12
7. Kramer SL, Wang CH (2015) Empirical model for estimation of the residual strength of liquefied soil. *J Geotech Geoenviron Eng* 141(9):04015038
8. Olson SM, Johnson CI (2008) Analyzing liquefaction-induced lateral spreads using strength ratios. *J Geotech Geoenviron Eng* 134(8):1035–1049